THE UNIVERSITY OF HULL

Laser Structuring of Materials for Biomedical Applications

being a Thesis submitted for the Degree of

Doctor of Philosophy

in the University of Hull

by

Bibi Safia Haq, M.Phil (University of Peshawar)

July 2012

Abstract

Laser processing methods have become very appealing for the fabrication of micro/nano structures. To fabricate 3D structures with high resolution and arbitrary complexity, several material deposition processes are in use. By using appropriate moulding techniques, these structures can be fabricated out of a variety of materials such as polymers, ceramics and composites. In this work different lasers have been investigated regarding their suitability for additive and subtractive patterning of small features for biomedical applications. The main focus is on a technique based on two-photon polymerisation of photosensitive materials; this is a nonlinear optical stereo lithography which allows direct-writing of high-resolution three dimensional structures. During the two-photon absorption process, temporal and spatial overlap of photons leads to nonlinear absorption in a highly localized volume. Absorbed photons induce chemical reactions which cause a polymer to form. Due to the quadratic intensity dependence of the process, resolutions of less than 100nm in polymerized structures can potentially be achieved because of the well-defined polymerization threshold. Here, we have emphasised another regime whereby deep structures (~300μm) can be generated in a single pass. This allows rapid fabrication of structures suitable for cell scaffolds where the length scales are small (~10μm) and are required over long ranges (~cm). A Ti: sapphire femtosecond laser at 800nm wavelength with 150fs pulse duration and 1kHz repetition rate was used to determine the two-photon absorption cross section of photoinitiators. This approach was used to initiate two-photon polymerization of resin allowing the fabrication of cell scaffolds suitable for biomedical applications. Diffraction calculations for the imaging optics employed, show that spherical aberration plays a significant role in determining the feature sizes achieved.

For subtractive patterning of materials, a femtosecond laser system and an ArF excimer laser have been used. Using ablative techniques keratin films were processed to investigate physical realisation of the commonly used theoretical bricks-and-mortar description of skin. This structure was successfully fabricated and is being used for skin cream research. Also the threshold fluence for ablation of Polyimide Kapton (HN) foils has been measured at oblique angles as an analogue for corneal sculpturing based on beam scanning.

Dedicated

To my father Mian Zafar-ul-Haq

His prayers, inspiration and encouragement

in pursuit of excellence, will continue to linger on.

Acknowledgements

In the name of Allah, the Most Gracious and the Most Merciful

Alhamdulillah, all praises to Allah who keep me compose when I shatter in the moments of grief and despair, for answering my prayers, for giving me the strength to plod on and for His blessing in completing this thesis.

First and foremost, my utmost gratitude to Dr. Howard V. Snelling for his constant support and guidance he extended throughout the work and whose sincerity and patience I will never forget. Dr. Snelling has been my inspiration as I hurdle all the obstacles in the completion of this research work.

I am sincerely grateful to the University of Peshawar, government of Pakistan for their financial support in the form of a scholarship to undertake this study.

My acknowledgement also goes to all the staff of Physics department, University of Hull for their co-operations. I would like to express my gratitude to all those who made it possible to complete this thesis.

My deepest gratitude goes to my beloved parents; who are no more in this world but their everlasting love, endless prayers and inspiration led me to the highest pursuits of life. I would like to pay special tributes to my great father who was praying for my success throughout this period till his last moments.

I thank my entire family for always being there for me. Knowing that they always held me in their thoughts and prayers gave me strength to go on. Especially, I would like to give my special thanks to my husband Jehan Bahader whose patient love, moral and financial support enabled me to complete this research work. Without his sincere support and encouragement it would not have been possible for me to conduct this study. Also it would be unfair if I do not mention my sweet children Ayesha Jehan, Muhammad Saad and Muhammad Ammar who spare their lovely time and share their innocent feelings throughout this period. My brother, sister-in-law, aunties and cousins deserve my wholehearted thanks as well.

I would like to thank Dr. Naiz Shah for his valuable suggestions and encouragement he extended throughout this period. Sincere thanks to all my friends especially Mah-e-rukh Ahmad, Shafqat Shah, Iram Batool and others for their kindness and moral support during my study. Thanks for their friendship and memories.

Last but not the least, to those who indirectly contributed in this research, your kindness means a lot to me. Thank you very much.

Contents

Glossary

CCD	Charge-coupled device
DEF	Diethyl fumarate
EBPADMA	Ethoxylated bisphenol A dimethacrylate
ECM	Extracellular matrix
HA	Hypocrellin A
HB	Hypocrellin B
LIFT	Laser Induced Forward Transfer
LSR	Lateral spatial resolution
MAPLE-DW	Matrix assisted pulsed laser evaporation - direct write
MEMS	Microelectromechanical systems
NEMS	Nanoelectromechanical systems
NIR	Near Infra Red
NLT	Nonlinear transmission
ORMOCER	ORganically Modified CERamic
PDT	Photodynamic therapy
PEGda	Poly(ethylene glycol) diacrylate
PLD	Pulsed laser deposition
PPF	Poly(propylene fumarate)
TPA	Two-photon absorption
TPE	Two-photon excitation
TPEF	Two-photon excited fluorescence
TPP	Two-photon polymerisation
WLC	white-light continuum

Chapter 1 Introduction

This thesis sets out to study the use of lasers in material structuring for bio-medical applications. We have chosen the term “biomedical” as opposed to “biological” or “medical” to encompass the field of applied research that contributes to the development of new treatments rather than clinical trials. In this way, the thesis explores the use of lasers in such treatments or in the production of structures required for research into new procedures. Laser processing can generate structures on the micron scale (and in some cases, nanometre scale) in metals, dielectrics and semiconductors. In order to form surfaces and volumes that are suitable for biomedical applications, the action of the laser radiation can be subtractive or additive. Subtractive patterning is largely accomplished by laser ablation but might also be achieved through laser induced changes in reactivity followed by chemical etching. In additive processing, material is built up into the required shape. This may be achieved by laser controlled deposition via physical vapour, forward transfer, photopolymerisation, sintering and other techniques.

As indicated above, subtractive surface structuring is often an ablative process in which high irradiance laser light causes explosive ejection of species from a well-defined volume. Various mechanisms have been proposed for this, such as photothermal decomposition [1] photochemical decomposition [1], phase explosion [1], coulomb explosion [1] and, when the temperature excursion is long-lived, evaporation. The resolution of such patterning should be considered not only in terms of lateral (across the surface) features but also the depth. The lateral resolution depends strongly on the method used to define the pattern. In point-by-point direct writing the size of the focal spot coupled with any spreading due to heat flow limits the minimum feature size that can be realised. Thus laser parameters (e.g. wavelength, beam quality, pulse duration) which affect the minimum spot size and material properties (e.g. thermal conductivity, heat capacity, reactivity) which control the range of laser-induced material removal must be considered together. For projection etching techniques the optical system, together with the laser wavelength, primarily controls the minimum feature size and, in general, heat flow will tend to compromise this. Depth resolution is often dictated by the optical absorption depth except in the case of long pulse irradiation where, again, heat flow must be considered. An

increasingly common ablative medical procedure is corneal sculpting. In most cases this can be considered a bulk material interaction. In this thesis we will also explore thin film on substrate ablation for the manufacture of model skin surfaces.

In additive patterning, the surface relief is formed by depositing material, normally on a support or substrate. There are a number of ways that this can be achieved using laser radiation and some techniques have the additional advantage of being spatially selective. For example, pulsed laser deposition has been shown to allow stoichiometric transfer of complex materials [2] but this technique normally requires post deposition patterning to increase the functionality of the film. However, laser-induced forward transfer techniques can be used to form functional components directly, for example circuit-elements [3]. In the biomedical arena, direct write techniques have been used to carefully deposit sensitive materials that are damaged by other techniques. Such methods provide an ideal way to transfer chemically, physically and biologically complex materials by allowing the laser interaction to propel the majority of the desired material to the substrate without harm. These methods have been used to transfer electrochemical materials such as multicomponent, nanostructured oxides whilst maintaining their electrochemical performance and physically porous structure. Biomaterials such as proteins, bacteria, DNA and stem cells can be deposited in a similar manner without compromising the viability of these delicate structures. Liquids can also be transferred by laser-based techniques; direct writing has been used to transfer water-based solutions of proteins and a single cell suspension with small volume droplets of the order of 10fL successfully onto solid substrates [4]. In this way, laser direct write transfer is an exciting tool for applications such as manufacturing of miniaturized biosensors, implantable drug delivery systems, tissue engineering studies and placement of cells [4].

As well as material transfer, additive material structuring can be achieved by photopolymerisation. With the help of using a two-photon polymerization process, 3D structures of very high resolution can be fabricated using light curable resins. The liquid is polymerised by the simultaneous absorption of two photons in the longer wavelength infrared spectral region. Compared to conventional prototyping due to single photon absorption, a two-photon

polymerisation process has certain advantages. The transparency of the light-curable resin in the infrared spectral region allows the long wavelength radiation to penetrate into the material and induce polymerization process at the focal point. The focal position where polymerization occurs can then be placed a significant depth below the surface. Another advantage of the two-photon polymerisation process over single photon absorption is its quadratic dependence on the light intensity enabling 3D patterning with high resolution [5].

To delineate different themes, the thesis is divided into a number of chapters that cover background information, together with experimental studies and analysis of the data. In chapter 2, a literature review is presented that covers the current status of research related to this thesis. This includes deposition techniques, patterning and the requirements of biomedical research so as to put the work presented here in context.

Chapter 3 describes the laser systems used and quantifies their performance via their output characteristics. Particular emphasis is given to the femtosecond laser and the possibility of frequency doubling the output to allow both 800nm and 400nm wavelength interactions to be studied. Integration of this laser into a 3-D translation stage “workstation” is discussed along with the resolution and limitations achieved.

The main sections of the remainder of the thesis broadly fall into two categories already mentioned; additive and subtractive material processing. In chapter 4, additive photopolymerization is presented. Here the choice of materials is discussed with a view to forming cell scaffolds that have the additional feature of being optically transparent, thus allowing microscopy for biomedical studies using these structures. In order to fully characterise the interaction, two-photon absorption cross-sections have been measured for the photosensitizers used. This data was not previously available. Additionally, so as to optimise the speed at which structures can be fabricated, particular attention has been paid to deep (10’s μm) solid formation in a single pass. This is contrary to usual two-photon polymerisation that has been shown to achieve very small structures at high resolution. Utilising that approach here for these large scaffold

arrangements, would result in a prohibitively slow process and so a new regime has been explored.

Subtractive patterning based on the ablative process is covered in chapter 5. Distinct but related applications are studied. Firstly, both direct write and projection etching of keratin films is presented. This has application in forming model skin surfaces to allow the study of the effect of applying creams to human skin. Secondly, laser interactions at oblique angles, such as would be encountered in corneal sculpting are explored.

The final chapter of the thesis draws conclusions from the preceding sections and shows their inter-relation supporting the use of laser material structuring as an enabling technique for biomedical research. The areas of study that would benefit from further exploration are identified in a “future work” section.

Chapter 2 Literature Review

In this chapter we will discuss the need for laser based techniques for material structuring in biomedical research and the requirements of various applications in terms of feature size and material properties. Techniques for deposition and patterning will then be reviewed and the reasons for the choice of which to study here explained.

2.1 Requirements of biomedical research

The properties required from laser-based procedures for biomedical research fall into two broad categories. Those where the laser performs the procedure itself and those where it is used to manufacture devices or structures to aid a procedure. For example, corneal sculpting and photodynamic therapy have both been improved by the use of lasers and represent the laser as an intrinsic part of the therapy. On the other hand, laser micromachining of stents and photopolymerisation to manufacture cell scaffolds both illustrate the use of lasers as an enabling technology in the medical sphere. It can be seen that each of these two types of function may require material removal or material deposition.

Natural tissues consist of an extracellular matrix (ECM) where cells are embedded in a three dimensional fibrous network of biopolymer. This extracellular matrix provides structural integrity and influences cell growth and metabolic processes. Fabrication of 3D scaffolds is required for physiological cell cultivation in biomedical applications [6]. A porous, degradable 3D structure made of natural materials (collagen, fibrin) or synthetic polymers is known as a cell scaffold. For the fabrication of such structures with a resolution ranging from 300µm to 10µm injection moulding, 3D-printing techniques and micro syringe methods have been used [7]. Complex 3D micro structures with high resolution can be fabricated in a single step with potential applications in tissue engineering and other biomedical applications using two-photon polymerisation techniques. Two-photon polymerisation techniques have been used to fabricate medical devices, including microneedles for transdermal drug delivery, ossicular (ear bone) replacement prostheses, and tissue engineering scaffolds [8]. Typically these applications all require relatively coarse structures with long range order. Laser processing has already been shown to easily exceed the

resolution required (for example, cell sizes are of the order of 10μm and so supports for them can be of this size).

2.2 Laser-based techniques for additive surface structuring

As stated earlier, this chapter includes the needs of the project and the different techniques in use today and for the current research to process organic and inorganic materials using femtosecond and other lasers. The laser is distinguished from other sources of electromagnetic radiation in terms of its coherence, spectral purity and collimation. As a result of these characteristics it has a wide range of applications in each and every field of life. A large variety of materials can be deposited from gaseous, solid and liquid states using laser techniques. There are many sophisticated applications and the choice of deposition technique used will depend on the type of material to be deposited together with the properties of the substrate.

The application of different types of lasers began shortly after their discovery. As a result, new and enabling techniques have been developed to process thin films and biomaterials. These biomaterial and thin film processing techniques include pulsed laser deposition (PLD) which makes biocompatible thin layer production possible, Laser Induced Forward Transfer (LIFT), and matrix assisted pulsed laser evaporation - direct write (MAPLE DW) technology, which has also been successfully applied to cell and biomaterial patterning. Polymeric thin films can be fabricated by different techniques such as vacuum evaporation, plasma polymerization, electrochemical polymerization, spin coating, and photodecomposition.

2.2.1 Laser induced forward transfer – LIFT

Laser Induced Forward Transfer (LIFT) techniques have become important Direct Write methodologies for generating high resolution patterns. In these techniques a substrate that is transparent at the laser wavelength is coated with the material of interest and is known as the donor substrate. Laser pulses are used to transfer material from the target substrate onto another substrate which is placed close to or in contact with the target as shown in Figure 2-1. The distance between target and the receiver substrate can be varied from near contact to several micrometres. Laser pulses propagate through the transparent

substrate and are absorbed by the film. Above an incident laser energy threshold, material is ejected from the source and transferred towards the receiving substrate preserving the properties of the transferred material rather than relying on a chemical reaction or other material modification to induce the deposition. This added versatility, in comparison with other printing methods, manages to transfer complex materials for which it is critical to maintain the delicate physical, chemical or biological properties in the resulting patterns.

LIFT was first reported for the deposition of a Cu metal pattern inside a vacuum chamber using excimer laser pulses of wavelengths 193nm with a pulse duration of 15ns [9]. The LIFT technique is simple and has been used with a variety of solid film materials, mainly metals such as Cu, Ag [10], Al [11] and Cr[12]. Reports of LIFT for other materials such as Al_2O_3 [13], In_2O_3 [12, 13] and even high temperature superconductors [14] are also available, although the quality of the transferred ceramics was not as good as those achieved by traditional techniques.

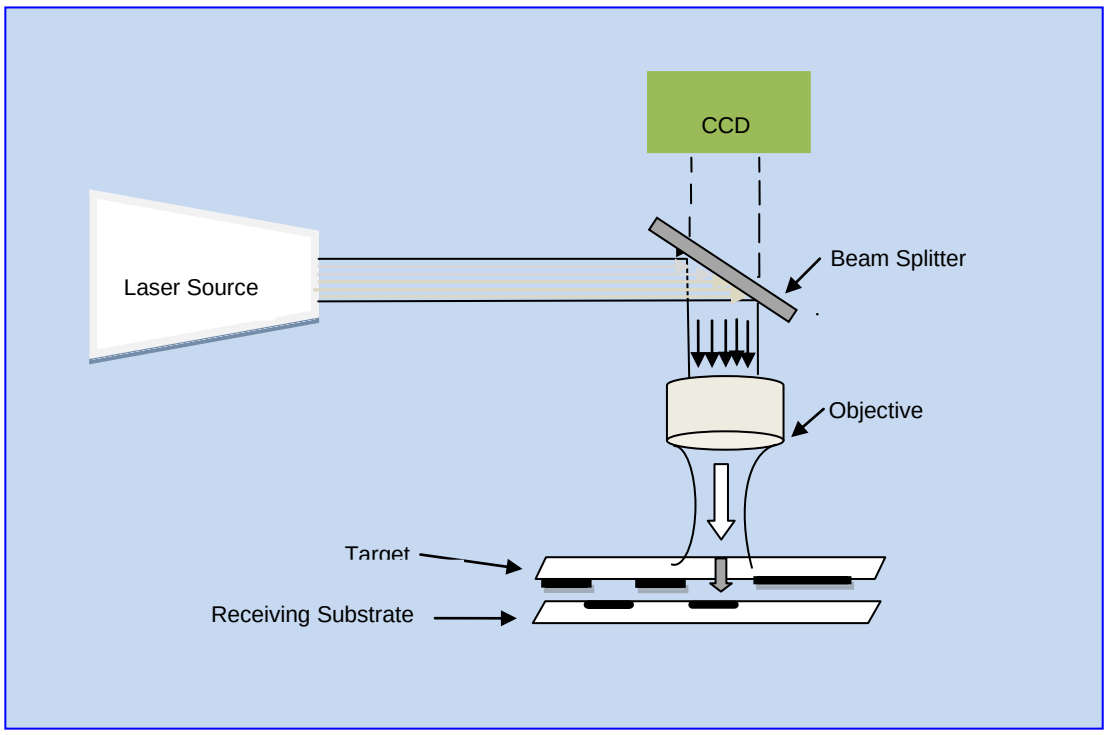

Figure 2-1 Experimental set up for Laser Induced Forward Transfer (LIFT)

This method can be used to transfer living or active biomaterials in such a way that the desired properties of the biomaterials are preserved. The biomaterials

after deposition onto the receiving substrate have been shown to remain alive or active [15].

2.2.2 Pulsed laser deposition – PLD

PLD is a thin film deposition technique where a high power pulsed laser beam is focussed inside a vacuum chamber on an elementary or alloy target at a small angle as shown in Figure 2-2

Material is then vaporised from the target and the atoms and molecules ablated from the target are condensed on the substrate. Substrates are placed parallel to the target surface at a target to substrate distance of typically 2-10 cm.

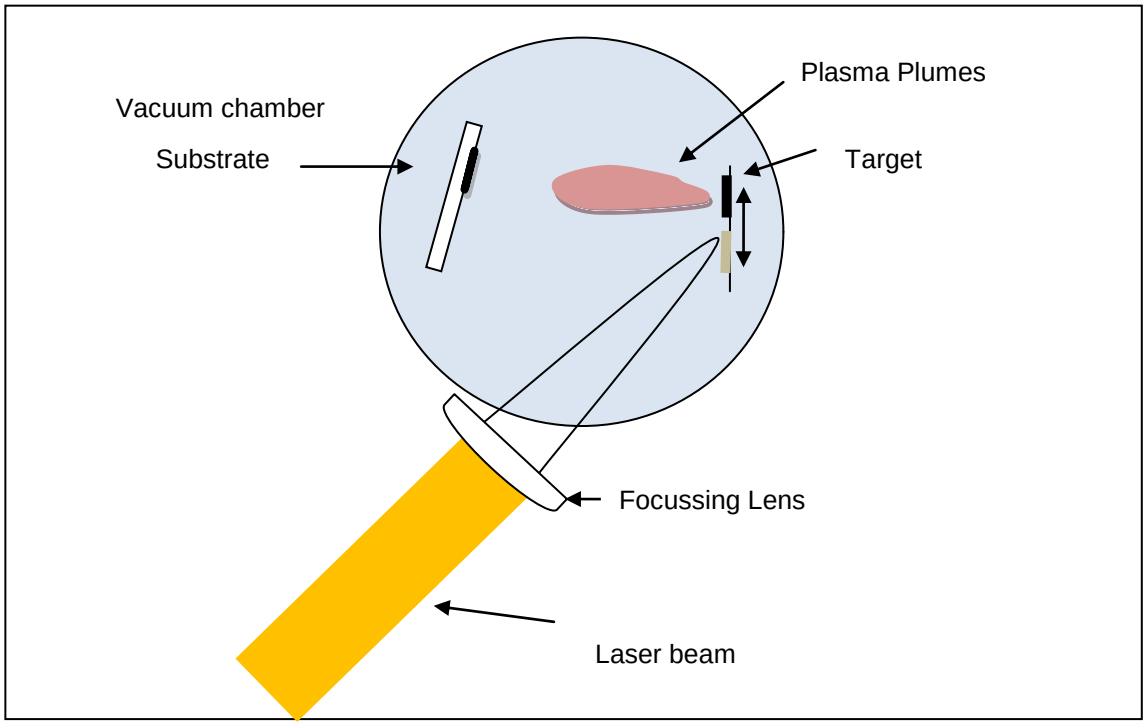

Figure 2-2 Schematic diagram to show an example of a typical PLD system of configuration

Pulsed laser deposition is for many reasons a versatile technique. With this method the energy source is placed outside the chamber, therefore the use of ultrahigh vacuum as well as ambient gas is possible. This technique allows deposition all kinds of different materials, e.g., high temperature superconductors, oxides, nitrides, carbides, metals and even polymers. The

PLD process even allows complex polymer-metal compounds and multilayer to be prepared [16].

2.2.1 Photopolymerization

Since the age of the semiconductor, photolithography has been the conventional method used for the fabrication of microstructures and wafer patterning. UV lasers as well as several photo mask resolution-enhancement technologies have been used to produce submicron level patterns. To reduce the cost of photo masks and lithographic equipment, an alternative technique such as maskless femtosecond laser lithography was introduced. The important feature of material processing with infrared femtosecond laser systems is the ability to fabricate structures far smaller than the diffraction limit. If the peak laser fluence is chosen to be slightly above the threshold value only the central part of the beam can modify the material and the diffraction limit can be overcome. Due to the ultrahigh peak power along with very short pulse width and central wavelength of approximately 800 nm which is close to half the wavelength of polymerisation, femtosecond lasers are widely used for inducing two-photon absorption processes. In 2009 Ik-Bu Sohn et al [17] used maskless femtosecond lithography for the fabrication of submicron patterns on a spin coated UV photoresist and observed the lithographic widths for various pulse energies and number of pulses. They concluded that direct femtosecond lithography is an efficient tool to produce submicron level patterns using photoresist and can be used to fabricate diffractive optical elements and photonic band gap structures.

Material deposition processes have become very appealing methods for the fabrication of 3D-microstructures which is of great importance for various mechanical, optical and electronic devices and for the production of three dimensional (3D) scaffolds for many tissue engineering applications and bone replacement. Some results were obtained in the field of molecular engineering for two-photon polymerisation relating optical power limiting in the visible range and micro fabrication. This study was based on observing the two-photon absorption (TPA) efficiency and making comparisons with different photoinitiators [18].

A laser technique based on two-photon polymerisation of photosensitive materials is nonlinear optical stereo lithography which allows the direct-writing of high-resolution three dimensional (3D) structures. Stereo lithography, based on layer-by-layer photo polymerization, allows the fabrication of cellular structures with defined pore sizes and geometries using an acrylate containing resin formulation [19]. A major focus of this study involves nonlinear optical absorption, wherein a molecule absorbs two or more photons at once. This process is intensity dependent; for two-photon absorption the absorption rate increases quadratically with intensity. This allows activation of photo-chemical or photo-physical processes with high spatial resolution in 3-D. To fabricate three dimensional complex micrometre sized structures, photo polymerization initiated by two-photon absorption is an interesting process. The fabrication of structures, difficult to obtain by any conventional single photon 3D microfabrication techniques, can be carried out by two-photon lithography, which is intrinsically a 3D lithography technique. Polymerization reactions leading to the formation of solid structures can be chemically activated when the photo initiators (chromophores) are excited by the nonlinear absorption of two photons by focusing the beam of a femtosecond infrared laser tightly within the volume of a material. 3D structures can be fabricated by moving the laser focus through the resin in three dimensions. To construct photonic crystal templates, mechanical devices, plasmonic structures, biomolecular scaffolds and microscopic models, a large number of acrylate and epoxy materials are in use[20]. 3D structures with high resolution and arbitrary complexity produced by this method should find applications in 3D integrated optical components, biomedical micro devices, microelectromechanical systems and micro fluidics[21].

2.2.1.1 Two-photon absorption (TPA)

Two-photon absorption phenomena, first predicted by Goeppert–Mayer in 1931, involve the excitation of molecules from their ground state to the higher energy state by simultaneous absorption of two photons. Two possible phenomena, namely sequential excitation and simultaneous two-photon excitation, give rise to two-photon absorption. Sequential excitation involves the absorption of a photon leading to the population of a real intermediate state that has a well defined life time of 10^{-4} to 10^{-9} sec (Figure 2-3a). A small number of electrons in

the first intermediate state then go on to absorb a further photon to complete the two-photon absorption process while the majority of electrons relax back to their ground state. The energy of each photon absorbed by the chromophores is equal to half the energy of the energy difference between ground and excited state. In both sequential excitation and simultaneous two photon excitation, fluorescence is emitted which is a three step phenomenon. In the first step photons supplied by a laser source are absorbed by the photoinitiator molecules and create an excited singlet state $S_{1`}$ which exists for a short interval of time (1-10nsec) during which the fluorophores interact with other molecules. In the second step as a result of this interaction the energy of the excited state $S_{1`}$ is partially dissipated and converted into a relaxed singlet excited state $S_{1.}$ In the third step the excited singlet state S_1 emits a photon in the form of fluorescence.

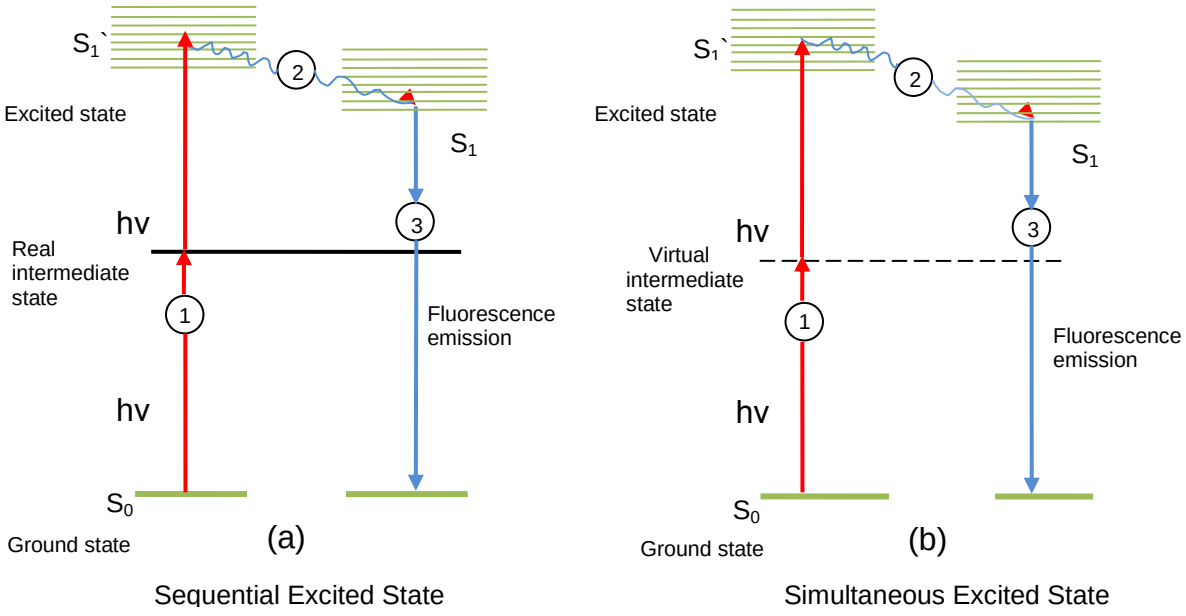

Figure 2-3 Two different mechanisms leading to a TPA process (a) sequential excitation and (b) simultaneous excitation [22]

During the second mechanism i.e., in simultaneous two photon excitation, a virtual state is created by the interaction of the first photon and the second photon is absorbed only if it arrives within the virtual state life time which is 10^{-15}sec (Figure 2-3b). This mechanism needs high intensity laser radiation that ensures the arrival of a second photon within the life time of the virtual state. The use of a femtosecond laser can fulfil this condition. To enable easy control of the polymerisation threshold energy, Ti:sapphire lasers having ultrahigh peak powers within a very short pulse width of approximately 100 femtosecond (fs) or

less and a wavelength of 800nm which is close to the half of the wavelength of polymerisation, are widely used for two-photon polymerisation processes [22]. In two-photon absorption the chromophores excitation takes place inside a volume anywhere due to the deep penetration of the long wavelength as compared to one photon excitation where molecules are excited on the surface of the resin where the beam strikes. This process has a wide range of applications and one of the most common is two-photon polymerisation process used for the fabrication of micrometre and nanometre scale 3D structures [23].

Three dimensional micron size structures with high spatial resolution can be fabricated by making use of two-photon absorption polymerization processes. To initiate two-photon absorption polymerisation processes, chromophores with an efficient two-photon absorption (TPA) property are required as photosensitizer. In the last few years intense study has been carried out for the development of two-photon chromophores with high two-photon absorption cross section in the field of 3D microfabrication. Chris Xu et al., in 1996, measured the two-photon fluorescence excitation (TPE) spectra for 11 common molecular fluorophores in the excitation wavelength range 690 nm to 1050 nm. They used ~100-fs pulses of a mode-locked Ti: sapphire laser for excitation and the results obtained were confirmed by single-mode cw Ti: sapphire excitation data in the range 710 nm to 840 nm. They calculated the TPE cross section for Rhodamine B and Fluorescein by comparing two photon excitation signals to one photon excitation signal. They found that with both pulsed and cw excitation the fluorescence emission intensities are strictly proportional to the square of the excitation intensity to within ±4% for excitation intensities sufficiently below excited-state saturation. They concluded that good agreement between cw and pulsed measurements indicates that the considerable spectral spread of ultrashort pulses does not alter the excitation spectra significantly. The peak TPE cross sections for the fluorophores were measured and found to be between ~10^{-50} and10^{-48} cm^4s/photon [24].

In 1999 Song et.al, [25] determined the two-photon absorption cross-section of fluorescein at 800nm by comparing the intensity ratio of one-photon absorption to two-photon absorption using a mode locked Ti:sapphire laser. They used the second harmonic of this laser as a light source for single photon excitation. They reported that compared to cw laser excitation, the high peak power of the

Ti: sapphire laser at low average laser power is more suitable for the determination of two-photon absorption cross-sections. The accuracy of the measurement of the two-photon absorption cross section increases due to the reduced decomposition of the fluorophore at low average laser power.

In spite of a much smaller cross section for two-photon absorption as compared to one-photon absorption, two-photon absorption processes are still an important emerging technique for photodynamic therapy (PDT) because of its site-specific irradiation with more accurate operation, great penetration depth within cells and body tissues and less damage compared with one photon excitation. For this purpose, in 2002 Liu et al. examined the photophysical and photochemical properties of hypocrellins (HA and HB) with two-photon excitation at 800 nm using femtosecond pulses from a Ti: sapphire laser. They measured the two-photon excitation cross sections of HA and HB at 800 nm as 34.8×10^{-50} cm^4 s /photon and 21.3×10^{-50} cm^4 s / photon, respectively. Their results showing the two-photon excitation of hypocrellins with large two-photon excitation cross sections, suggest potential two-photon PDT applications of hypocrellins involving in both photodynamic type I and type II reactions. They also examined the cell-damaging effects of HA upon two-photon illumination. Their results indicate that hypocrellins can effectively damage the Hela cells under two-photon illumination [26].

In 2003 Schafer et al., reported the TPA properties of common, commercially available photoinitiators often used in TPA-based polymerizations and typically utilized in conventional radiation curing science and technologies. They measured the two-photon absorption cross-sections (δ_{2a}) of the photoinitiators using Z-scan and white-light continuum (WLC) pump–probe techniques. Their results show good agreement between the two methods for most of the compounds studied. They found that most of the photoinitiator studied posses a low value for δ_{2a} indicating a need for the development of new photoinitiators with improved properties optimized for TPA applications. They prepared a compound (7-benzothiazol-2-yl-9,9-bis-decyl-fluoren-2-yl)-diphenyl-amine DPABz ($\delta_{2a} \leq$ 120GM, λ=390nm) exhibiting high TPA which was found to be useful as a two-photon free-radical photoinitiator [27].

Cao et al, in 2004, [28] synthesized and structurally investigated donor-π-donor (D-π-D), acceptor-π-acceptor (A-π-A), and donor-π-acceptor (D-π-A) types of organic compounds with fluorine as a π bridge and a dimesitylboryl group as an electron acceptor. These organic compounds showed strong two-photon excited blue fluorescence. Blue–violet or blue two-photon excited fluorescence (TPEF) demonstrates that the dimesitylboryl group is a good fluorophore and a blue-shift group. The shortest wavelength of TPEF at $\lambda_{em=}$ 405 nm under the excitation wavelength of λ_{ex} = 730nm was exhibited by a symmetric A-π-A type of compound. The most intense TPEF at blue region (λ_{em}=484 nm) with a two-photon absorption cross-section of 425 GM under λ_{ex} = 800 nm was exhibited by the unsymmetrical D-π-A type of compound with diphenylamino as a donor compound. This work used a two-photon fluorescence method for the measurement of TPEF cross-section δ_{2ef} and (TPA) cross-section δ_{2a}. A synthesized compound, bis(N,N-diphenylamino)-9,9-diethyl-fluorene and bis(dimesitylboryl)-9,9-diethyl-fluoren show quasi-symmetric and π-conjugated structure at their ground state. When in the excited state, quadrupolar charge transfer takes place for bis(N,N-diphenylamino)-9,9-diethyl-fluorene and bis(dimesitylboryl)-9,9-diethyl-fluoren. This suggests that these geometric and electronic structure features may have a close relationship to their TPEF properties.

In 2005, [29] Werts et al used near infrared femtosecond laser pulses for the study of four different luminescent lanthanide complexes with respect to multiphoton excitation. They investigated their luminescence under two-photon excitation by measuring two-photon excitation cross section and emission spectra. They reported the necessities of two refractive index related corrections, one for the excitation process and the other for the detection of emission. They investigated two-photon excited lanthanide luminescence in the 700–1000 nm range under less than 20mW excitation power. The report shows that (2,4,6-trimethoxyphenyl)dipicolinic acid and Michler's ketone are reasonable sensitizers of two-photon excited lanthanide luminescence in solution, whereas two-photon excited lanthanide luminescence of dipicolinic acid and carbostyril-124 are not detectable as shown in Figure 2-4.

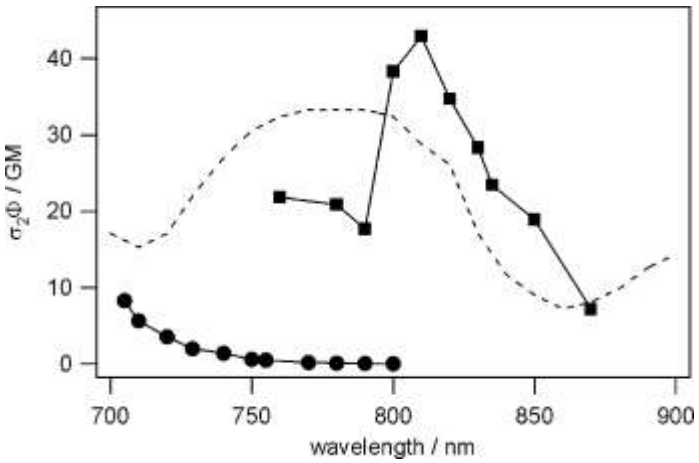

Figure 2-4 Action cross section spectra for two-photon excited luminescence. Circles: Tb (TMP-DPA) 33– (2×10^{-4} M in 2 mM TRIS buffer pH 8.3), squares: Mk–EuFOD (10^{-4} M Michler's ketone + 10^{-3} M EuFOD in toluene). A solution containing only EuFOD does not generate any detectable multiphoton-excited luminescence. The dashed line is the spectrum of fluorescein in 0.1 M NaOH, shown here for comparison [29].

In 2007 Atif et al.[30] used a femtosecond laser delivering pulses of wavelength 800nm and 124 fs duration at rates of 1 kHz to investigate the two photon excited fluorescence of a photoinitiator m-THPC. They used laser pulses of relatively high energy (up to ~1 mJ) but delivered at a lower repetition rate of 1 kHz making this system efficient for two photon excitation without strong beam focusing. They measured the two-photon excitation cross-section, δ_{2e}, derived from the ratio of the fluorescence rates at 800 and 400nm (generated using a frequency doubling crystal) for single photon excitation. They also reported two-photon induced PDT (Photodynamic therapy) activity of m-THPC in an epithelial cell line.

Signorini et al [31] studied the linear and nonlinear optical properties of the heteroaromatic push-pull-push two-photon absorbing dye *N*-methyl-2,5-bis[1-(*N*-methylpyrid-4-yl)ethen-2-yl]-pyrrole ditriflate (PEPEP) in 2008. They used femtosecond TPA-white light continuum probe experiments, two-photon-induced fluorescence, and open aperture Z-scan measurement techniques using both nanosecond and femtosecond laser pulses for the determination of the TPA cross-section spectrum. They determined the TPA cross sections and

found that their wavelength dispersion show a marked dependence on the parameters of the laser pulses and on the measurement technique employed. They also reported that the TPA-white light continuum probe (TPA-WLCP) technique is less efficient than the two-photon-induced fluorescence (TPIF) technique in detecting the TPA maxima.

Martineau et al [32] determined the TPA cross-section of a new compound for the wavelength range (800–1100 nm). A symmetrical conjugated ketone with terminal amino groups was presented in their work which appears as an efficient initiator for the photo polymerization of triacrylates at 1.06µm. They obtained (E,E,E,E,E,E)-1,13-bis-[4-(diethylamino)phenyl]-trideca-1,3,5,6,8,10,12-hexaen-7-one by a cetolisation–crotonisation reaction from (E,E)-5-[4-(diethylamino) phenyl]penta-2,4-dienal and acetone in basic conditions. They used a Nd-YAG laser pumped optical parametric oscillator supplying 2.6ns pulses in the 780–1120 nm spectral range with 10 Hz repetition rate and obtained TPA spectra by up-conversion fluorescence measurements. As compared with commercial UV-Vis initiators, their study presents a high two-photon absorption cross-section ($100x10^{-50}cm^4$ s $photon^{-1}$). Its polymerization efficiency was characterized by the determination of the threshold absorbed energy density ($5.5kJcm^{-3}$) and threshold incident exposure dose (2.05 kJ cm^{-2}). They used a common and inexpensive Nd-YAG microlaser source for the polymerisation and demonstrated experimentally that owing to the design of such initiators with improved TPA properties, TPA polymerization can be performed for the fabrication of 3D microstructures in a single step. Samples obtained using TPA polymerization for 10 ms and 100 ms exposure times show an increase in length due to the extended dwell duration as shown in Figure 2-5.

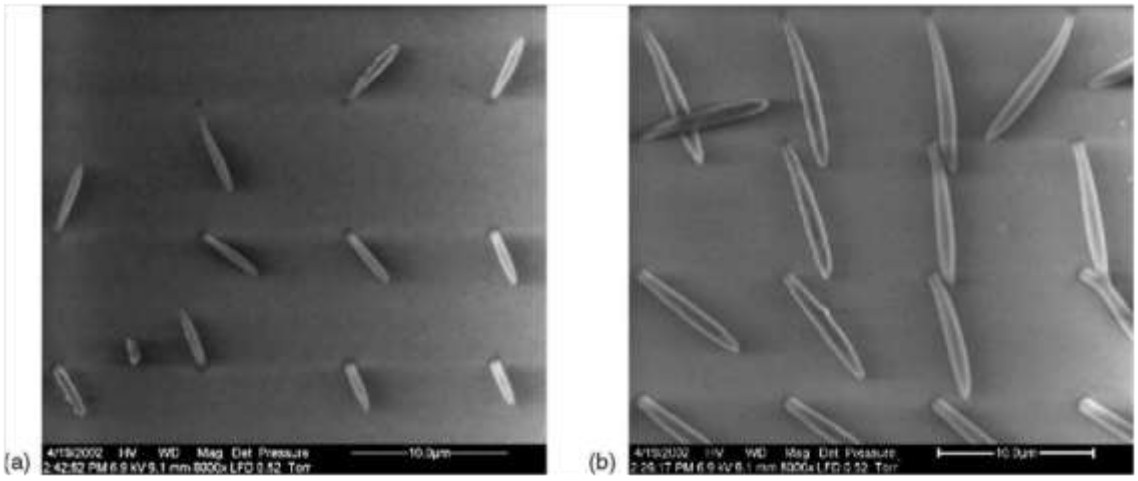

Figure 2-5 Polymer studs obtained after: (a) 10 ms; and (b) 100 ms irradiation [32] showing the dependence of their length on the exposure time.

2.2.1.2 Two-photon polymerization (TPP)

Two-photon polymerisation is initiated by the absorption of photons and is a photochemical process. During this process monomers are cross linked with other molecules in the presence of chromophores to form a chain-like polymer. Sufficient cross linking of the polymer is required during the process to avoid re-dissolving of the polymerised material back into the liquid monomer [33].

When a high intensity laser beam is focused into the volume of the liquid resin, the photosensitizer chromospheres are excited by a TPA mechanism. The photoinitiator is then excited and can give rise to radicals which react with monomer, producing monomer radicals. These monomers propagate in the form of a chain reaction in the targeted area and terminate when two radicals meet. The interaction between photosensitizer (P) photoinitiator (I), radical (R•) and the monomer (M) can be describe in the following equations [22] .

Chromophores Excitation $P \xrightarrow{hv,\ hv} P^*$ (1)

Initiation $P^* \longrightarrow I^* \longrightarrow R\bullet$ (2)

Association $R\bullet + M \longrightarrow RM$ (3)

Propagation $RM + M..... \longrightarrow RM_n\bullet$ (4)

Termination $RM_n\bullet + RM_m\bullet \longrightarrow RM_{n+m}R$ (5)

P* and I* in equation (1) and (2) indicate the excited states of the photosensitizer which after excitation initiates the reaction and act as a photoinitiator. Photoinitiator I* after two-photon absorption generates radicals R• and initiates the polymerisation process. Radicals R• combine with monomer M in the next step to form monomer radicals RM (association) expanding in a chain reaction (propagation) to form the polymer. The propagation of the monomer radicals continues until two monomer radicals meet together (termination) [22]. During radical formation, one bond of the atom ruptures, leaving one unshared electron on each atom. An atom with an unpaired electron is very reactive and is known as free radical. In equation (5) RM_n shows the polymerised material. To initiate the process ultra short laser pulses are employed in the photosensitive material. This process is a non linear process and the triggered reactions are strongly confined to the focal point. Thus 3D structures are fabricated just by moving the focal point through the photosensitive material which therefore is a single step process [34] as illustrated in Figure 2-6. A sufficient degree of cross linking is required as the fabricated polymerised structures should survive during the developing stage when it is washed to get rid of the unexposed resin [21].

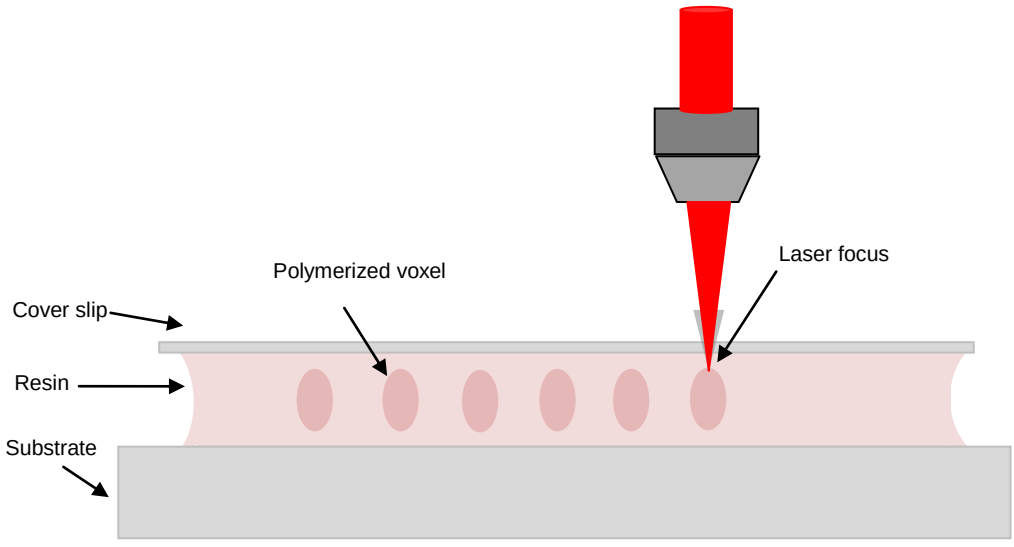

Figure 2-6 Schematic diagram shows that Polymerization take place only at the laser focus during two-photon polymerisation process.

Two-photon polymerization is an exciting microfabrication process, which can be used for simple and fast fabrication of microstructures using computer aided design to control the position of laser irradiation. Two-photon polymerization

provides several advantages over conventional techniques and offers state of the art resolution and can fabricate true 3D structures [35]. Using TPP microstructured medical devices in different shapes and sizes can be fabricated with high reproducibility.

Of particular current interest is the production of assemblies on scales of the order of the wavelength of light. These so-called photonic bandgap structures have optical properties that are modified as compared to the native material purely due to their size and shape.

Two component composite sol gel materials (zirconium/silicon composite) and a copolymer of photosensitive silicon alkoxide with a nonlinear optical (NLO) alkoxysilane were structured by a two-photon polymerisation process. This was reported by Ovsianikov et al in 2008[36]. The materials investigated by them exhibited ultra-low shrinkage. They used two different Ti: sapphire femtosecond lasers for the processing of MAPTMS: SGDR1 and MAPTMS: ZPO composites, with laser characteristics of 60 fs, 90MHz, <450mW, 780 nm, and 140 fs, 80MHz, 780 nm respectively. They fabricated 3D structures in a layer by layer form using an *x-y* galvanometric mirror scanner. Photonic crystals were fabricated choosing a woodpile geometry as shown in Figure 2-7 and Figure 2-8. The refractive index of the material was found to be approximately 1.497 (10% w/w SGDR1 content) and the experimentally obtained smallest feature size was 250nm [36].

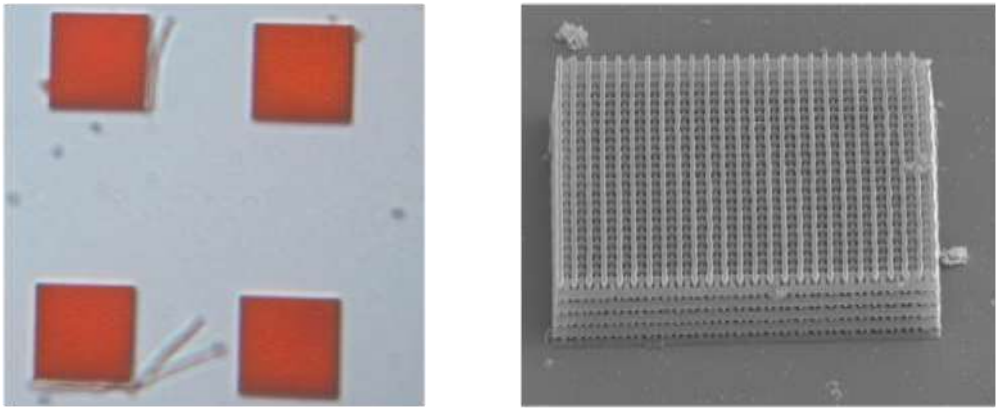

(a) (b)

Figure 2-7 Images of photonic crystals of MAPTMS: SGDR1 (a) Optical microscope and (b) SEM [36]. The red colour in (a) is a result of the structure being doped with the chromophore SGDR1 (Disperse Red 1).

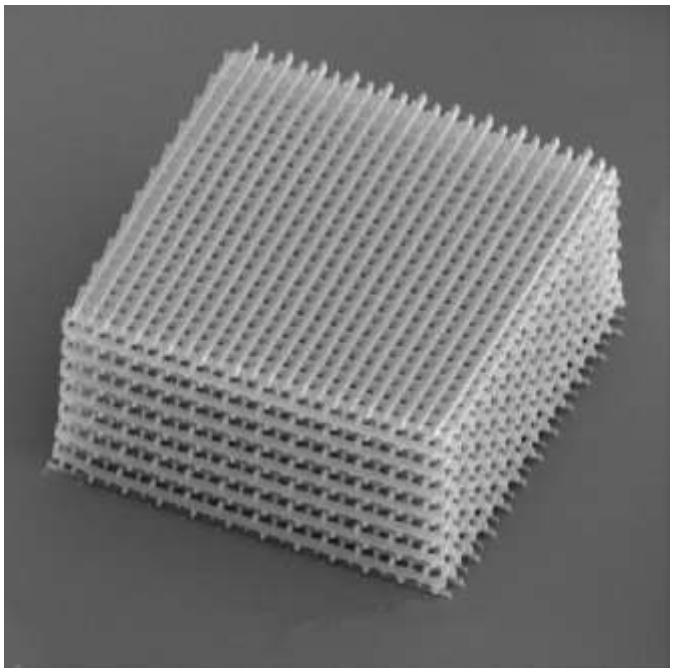

Figure 2-8 SEM image of a Zr-containing photonic crystal structure [36]

Using two-photon polymerisation techniques photonic crystal structures were built up from individual rods with a diameter of 200nm and a spacing of 250nm between the rods as shown in Figure 2-9. The time required for the fabrication of this structure was 10 minutes. They concluded that for low-cost fabrication of artificial microstructures and nanostructures two-photon polymerisation

techniques in ORMOCER (ORganically Modified CERamic) will be useful for different applications in optics, medicine, and biology [37].

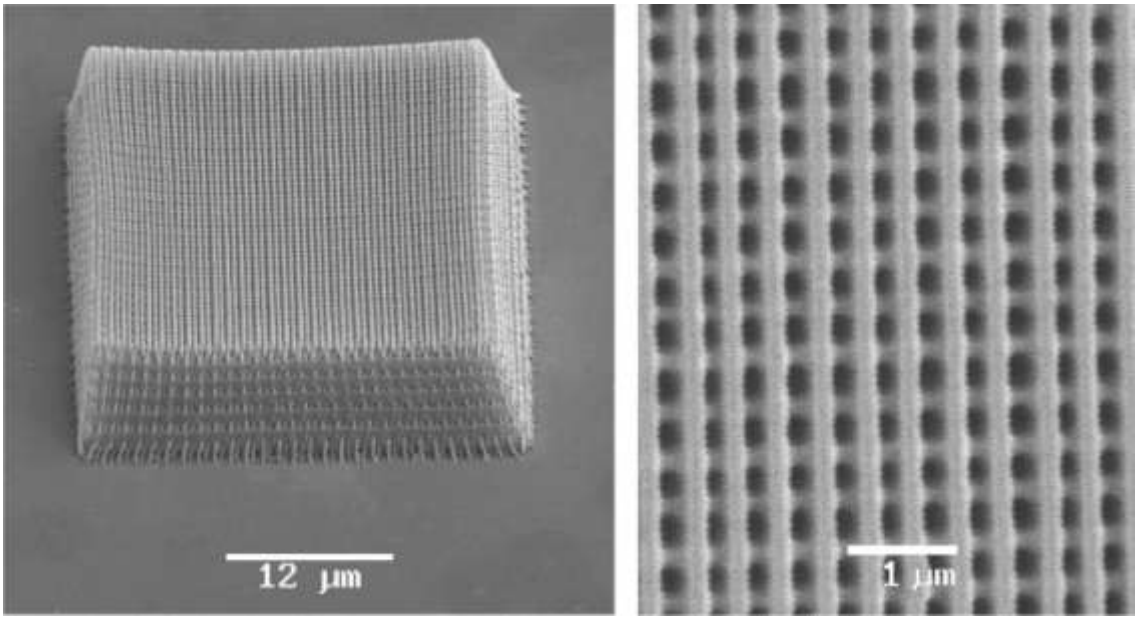

Figure 2-9 SEM image of a photonic crystal structure fabricated by 2PP [37]

Bhuian et al. [38] investigated a Zr-based material produced by solgel synthesis using a silicon alkoxide species that possessed methacrylate functionality. Hydrolysis of an organo-silane precursor with zirconium alkoxide was used for the preparation of resin. They demonstrated that this resin is suitable for a two-photon polymerisation process. To promote the condensation reaction between hydrolysed precursors, water was added to the resin followed by adding a photoinitiator to cross link the polymer. Effects of zirconium content on polymerisation behaviour were studied using a series of samples with 1, 5 and 10 mol% of zirconium concentration. They also investigated laser scanning speed as a function of photoinitiator concentration (1.33, 2.0, 2.66 and 3.33 wt. %) at 54mW average power and suggested that increased photoinitiator concentration accelerates the fabrication process.

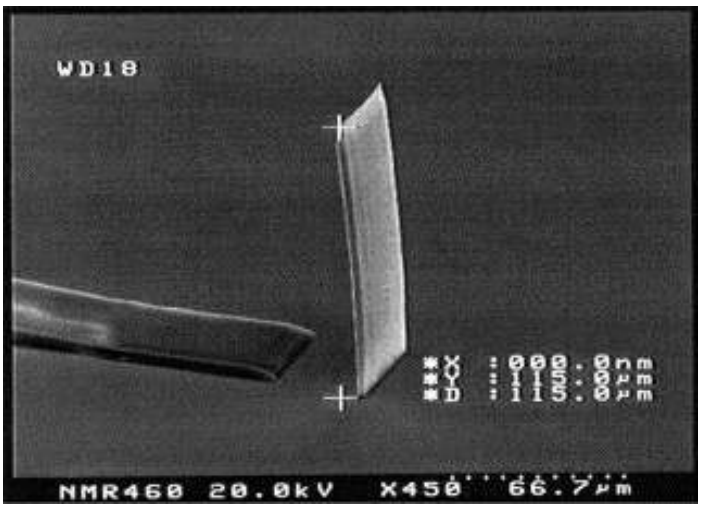

Figure 2-10 Pillar structure from reference [38]

A thin film sample with Zr content of 5 mol% and photoinitiator concentration of 2 wt.% was prepared. A vertical pillar at 90mW power and with a velocity of 100µm/sec was built up with 60µm width and 4µm thickness as shown in Figure 2-10 and Figure 2-11. To find the roughness of the thin film, the pillar was then analysed. It was laid horizontally to give 150µm x 60µm surface area for analysis. The sampling area for analysis was 10µm x 10µm. For average over three sampling areas the roughness of the film was found to be 14nm thus illustrating its suitability as an optical structure.

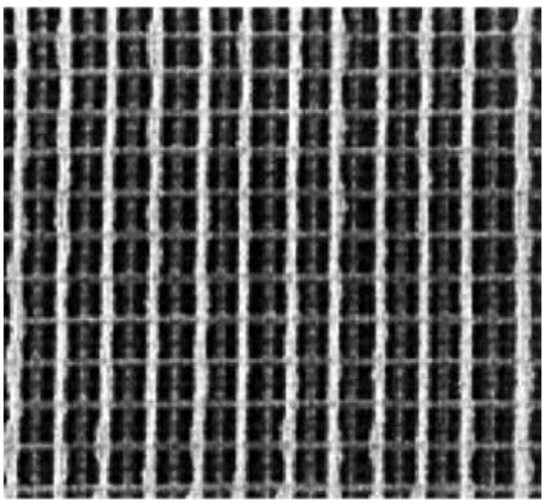

Figure 2-11 Woodpile structure with 2.5µm period [38]

Tailored structures with intentional defects have also been reported [39]. The paper presents the fabrication of photonic crystal woodpile structure using

negative and positive photoresist as shown in Figure 2-12. Defects were introduced at the particular location desired for the application. A 90^{o} waveguide-like woodpile structure has been fabricated in SU8 photoresist with a defect at the top of the structure as shown in Figure 2-12a. In order to remove the unexposed resin SU-8 resist has been used as the developer. They also fabricated an inverse woodpile in a positive resist material S1813 shown in Figure 2-12b and the illuminated area has been washed using acetone.

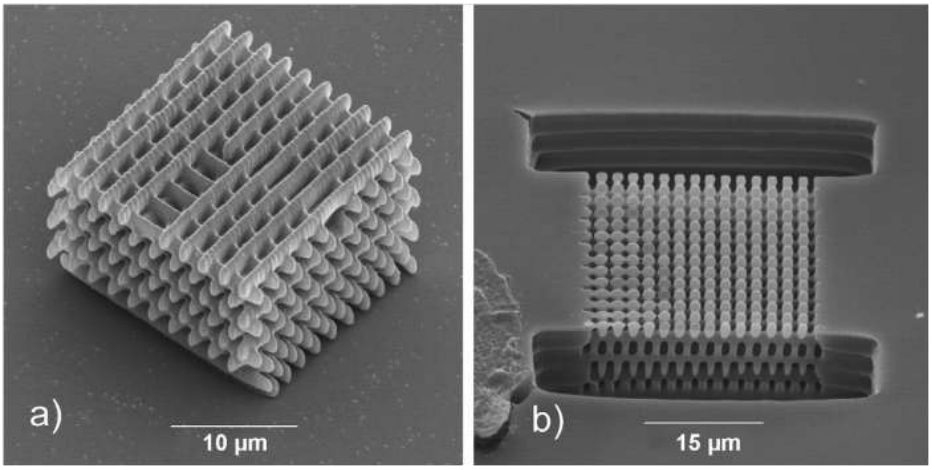

Figure 2-12 Photonic crystal woodpile structures fabricated by 2PP: (a) negative photoresist SU8 and (b) positive photoresist S1813 [39]

Others have prepared example structures such as a 20 µm diameter Euro coin and a micrometer sized Archimedes' screw [18]. The minimum structures fabricated to date are around or below 100nm. However due to the limitations of the focussing optics and long fabrication time, fabrication of large size biomedical cell scaffold structures are challenging and the structured dimensions are restricted to small size [40].

2.2.1.3 Examples of TPP in the biomedical arena

In 2002 Serbin et.al used ORMOCER, an inorganic-organic hybrid polymer produced by solgel synthesis which has an adjustable refractive index (in the range 1.47–1.56) and high optical transparency, to fabricate 3D microcapsules as shown in Figure 2-13. As the ORMOCER is a biocompatible material, these capsules can be used for biological and medical applications [37].

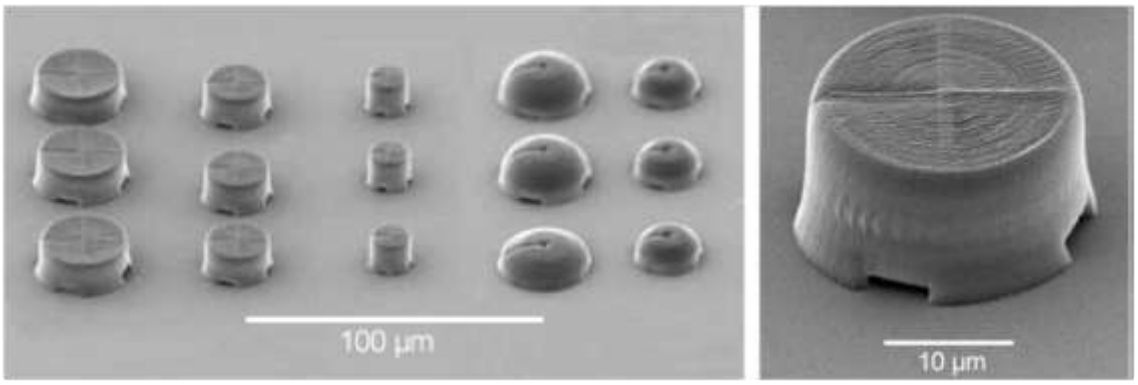

Figure 2-13 Fabrication of microcapsules using the TPP technique. Here, the biocompatible inorganic-organic hybrid polymer ORMOCER has been used. [37]

In 2006 Landis et.al [41] prepared a tissue engineering scaffold for optical imaging studies of cell attachment. The scaffold was based on photo activated ethoxylated bisphenol A dimethacrylate mixed with sodium chloride (NaCl) crystals that had been sieved to average diameter of 390, 300, 200 and 100µm. The resin mixture with sodium chloride crystals was photo-cured to form a cross linked composite. After the cross-linking process, the composite was soaked in water to remove the salt and leave the porous scaffold with desirable optical properties as shown in Figure 2-14. The scaffolds were analysed using scanning electron microscopy and X-ray micro computed tomography which indicated that the surface and internal morphology of the scaffolds were very similar in size and shape to the salt crystals used in the formulation. They concluded that the mechanical properties of the scaffolds can be changed from a rigid, hard material to flexible, soft foam if the smallest salt crystals are used instead of largest. Due to sufficient mechanical integrity, the scaffolds prepared were utilized in the cell seeding process. Due to the glassy nature of the material, these scaffolds were more transparent than crystalline polymer based scaffolds which scatter light and limit penetration. Confocal microscopy showed that cells at depths of over 400µm below the surface of the scaffold could be imaged.

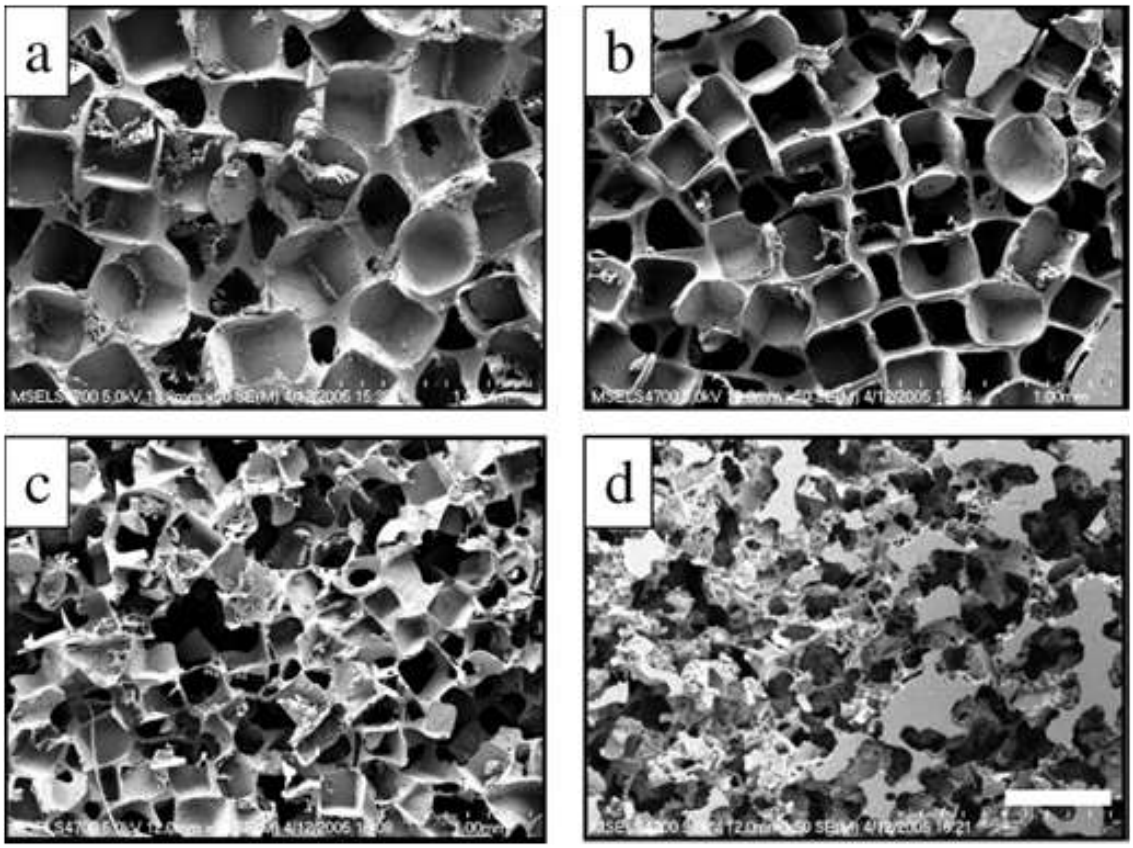

Figure 2-14 Scanning electron micrographs of the surface of (a) EBPADMA-390, (b) EBPADMA-300, (c) EBPADMA-200, and (d) EBPADMA-100. The scale bar represents 500μm and applies to all of the images [41].

In 2007, Lin-Gibson et al [42] prepared tissue engineering scaffolds by salt leaching of a photopolymerized dimethacrylate and investigated how to control the scaffold structure (porosity, pore size, etc.). Scaffolds were prepared using Ethoxylated bisphenol A dimethacrylate (EBPADMA) with the photoinitiator system of camphorquinone (CQ) and ethyl 4-*N,N*-dimethylaminobenzoate (4E) as shown in Figure 2-15 and Figure 2-16. They also investigate detailed morphometric parameters and mechanical responses of two series of scaffolds structure prepared with (1) the same polymer-to-salt ratio but different salt sizes (ranging from average size of 100 to 390 μm) and (2) the same salt size but different polymer-to-salt ratios (ranging from salt mass of 70 to 90%). The scaffold parameters, such as porosity, pore size, and strut thickness and their size distributions, and pore interconnectivity were determined using techniques of X-ray microcomputer tomography (μCT), mercury porosimetry, and gravimetric analysis. Their study suggests that the size and the amount of

porogens used in the fabrication of the scaffold could tailor the structure and properties of the scaffold. Their experimental results indicate that mechanical properties are affected by strut thickness and porosity, with the dominant contribution being porosity.

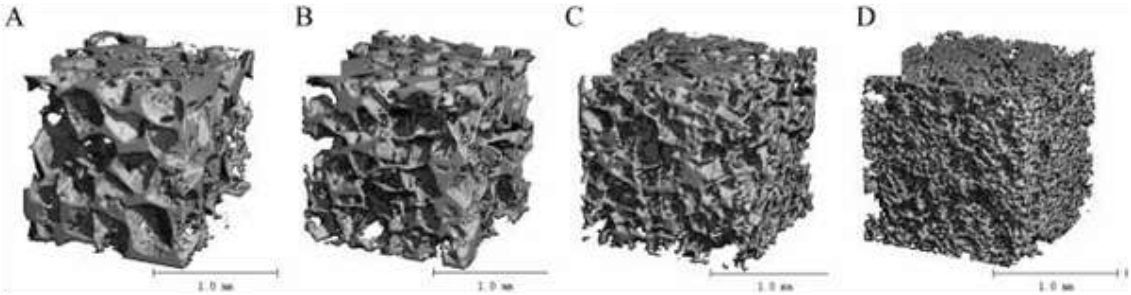

Figure 2-15 3D renderings from µCT analysis of scaffolds prepared with a constant polymer-to-salt ratio but varying salt crystal sizes: (A) DMA-74p-100, (B) DMA-74p-200, (C) DMA-74p-300, and (D) DMA-74p-390. Each cube represents a volume of 1.7 mm^3. [42].

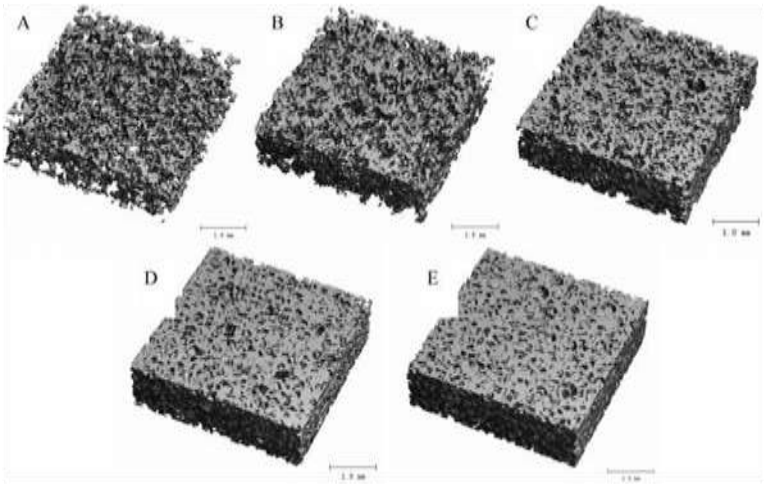

Figure 2-16 3D renderings from µCT analysis of scaffolds prepared with varying 200-µm salt contents: (A) DMA-83p-200, (B) DMA-76p-200, (C) DMA-69p-200, (D) DMA-62p-200, and (E) DMA-56p-200. Each cube represents a volume of 15 mm^3. [42]

In 2009 Frederik et.al [43] used the biodegradable triblock copolymer poly (*ε*-caprolactone-*co*- trimethylenecarbonate)-*b*-poly(ethylene glycol)-*b*-poly(*ε*-caprolactone*co*- trimethylenecarbonate) with 4,4′-bis(diethyl amino)benzophenone as the photoinitiator for the fabrication of three dimensional structures. Their study indicated the potential of two-photon polymerisation for the fabrication of three dimensional microstructured tissue engineering scaffolds as shown in Figure 2-17.

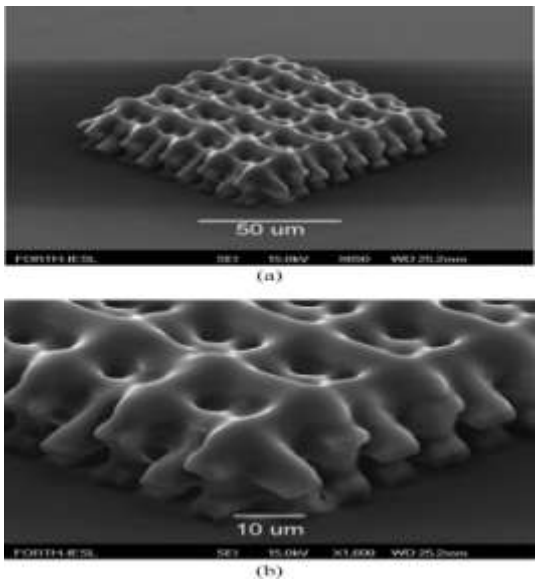

Figure 2-17 3D microstructured tissue engineering scaffolds (a) Overview (b) and detail structure [43]

Ostendorf and Chichkov [44] reported in an article issued by Laser Zentrum Hannover eV, the preparation of some photonic crystals with full photonic bandgap created in high refractive index materials using two-photon polymerisation process. Photonic crystals created in SU 8, Shipley photoresist S1813 and ORMOCERS are shown in Figure 2-18 .

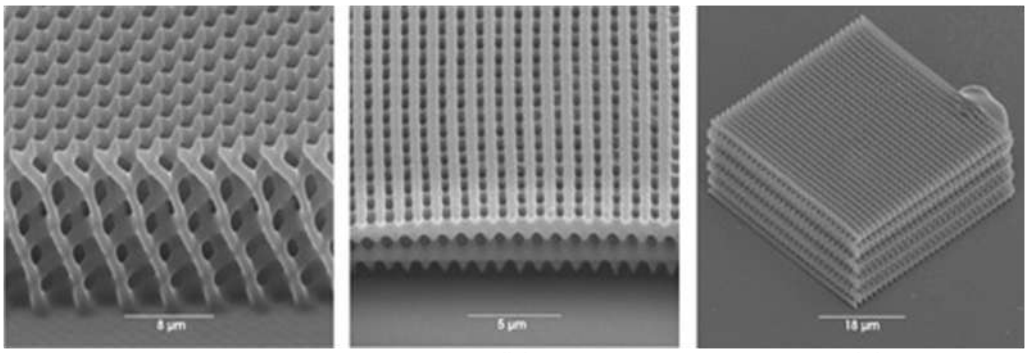

Figure 2-18 SEM images of photonic crystal created in (a) SU8 (b) Shipley photoresist S1813 (c) and ORMOCER [44].

They also report the fabrication of 3D scaffold structures required to artificially fabricate living tissue. Fabrication for the manipulation of drug delivery devices e.g., micro needles is also presented in the report as shown in Figure 2-19 . As ORMOCER was found to be the most suitable material for application in biomedicine, therefore it was used for the fabrication of scaffolds and micro needles [44].

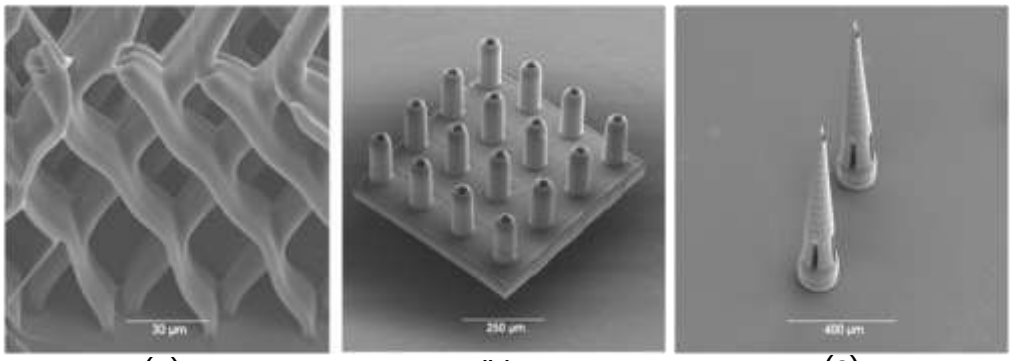

Figure 2-19 SEM images of (a) scaffold structures (b) a free-standing Lego-type structure for cell growth experiments (c) micro needles for drug delivery. [44]

In 2009 Gittard et al [45] also reported the fabrication of microneedles with antimicrobial functionality using two-photon polymerisation, micromolding and pulsed laser deposition. To reduce the risk of infection associated with microneedles, antimicrobial coatings i.e., silver, were applied to the microneedles surfaces using pulsed laser deposition. Pulses from a Ti:sapphire femtosecond laser with 60fs pulsed duration, 780nm wavelength and 300mW laser power were focused on SR 259 polyethylene glycol dimethacrylate with 2% weight Irgacure 369 initiator. The structure of the micro array was fabricated on a silanized glass cover slip as shown in Figure 2-20.

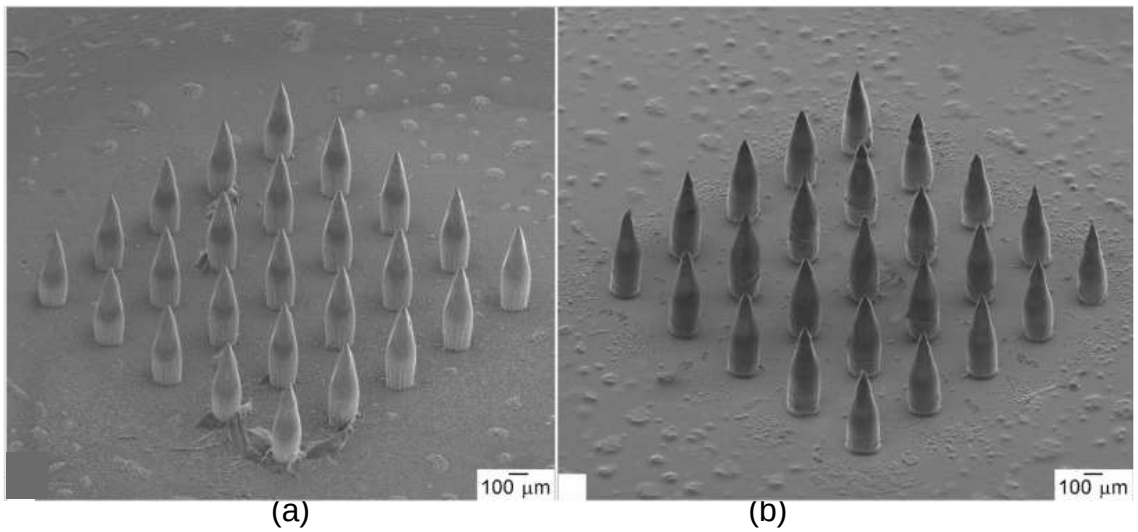

Figure 2-20 SEM of (a) SR 259 polyethylene glycol dimethacrylate microneedles array serve as a master structure (b) SEM of a silver-coated ORMOCER [45].

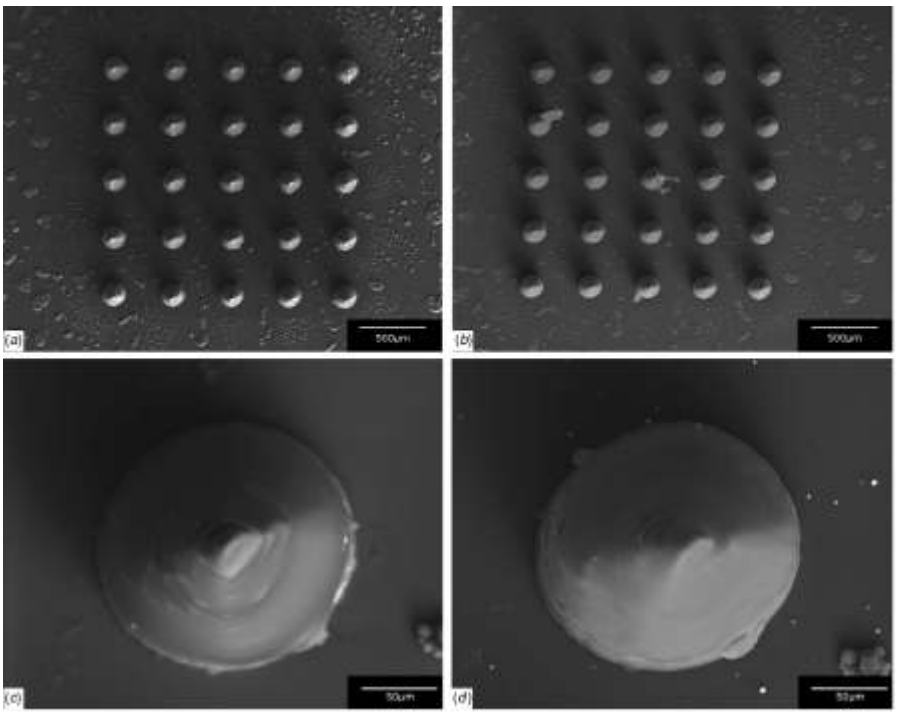

Figure 2-21 SEM images of (a) uncoated Ormocer microneedle array (b) silver-coated Ormocer microneedle array (c) an individual uncoated Ormocer (d) an individual silver-coated Ormocer needle [45].

Their study indicates [45] that pinhole-free and pore-free silver coating can be deposited on ORMOCER microneedle arrays with the help of pulsed laser deposition as in Figure 2-21. They anticipated that antimicrobial functional microneedles will be widely used as compared to conventional microneedles for transdermal delivery of protein and nucleic-acid-based pharmacologic agents.

Stereolithography has been the conventional method for the fabrication of structures. Microstereolithography (μSL) has evolved from the conventional method and has been used by Choi et al [46] for the fabrication of three-dimensional tissue engineered scaffolds with controlled biochemical and mechanical micro-architectures. They developed a mask projection μSL system and synthesised a biodegradable/biocompatible polymer, poly (propylene fumarate) (PPF) for the fabrication of 3D structures. They demonstrated the ability of the system by fabricating a miniature 3D human kidney scaffold with interconnecting pores and also fabricated a simple PPF/DEF cubic scaffold which illustrated that both horizontal and vertical channels can be successfully fabricated. Examples are shown in Figure 2-22.

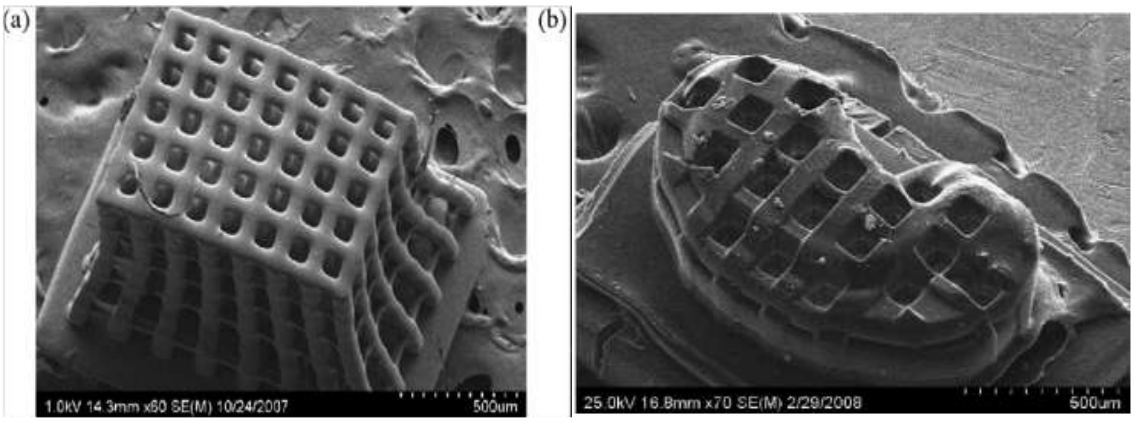

Figure 2-22 (a) Fabricated PPF/DEF cubic scaffold with more pores (b) SEM image of fabricated kidney scaffold using the commercial resin [46].

Ovsianikov et al [39] created middle-ear bone replacement prostheses using TPP as shown in Figure 2-23(a). This shows that two-photon polymerisation can successfully create micro structured medical devices on a large scale with different sizes and shapes as compared to other conventional fabrication techniques. The material used in this study was ORMOCOMP, containing 1.8% of Irgacure 369 photoinitiator. They successfully implanted the Ormocer ossicular replacement prostheses and removed it from the site without any damage or fractures as shown in Figure 2-23(b) [35]. The material ORMOCOMP belongs to ORMOCERs and its mechanical properties can be changed by means of chemical design.

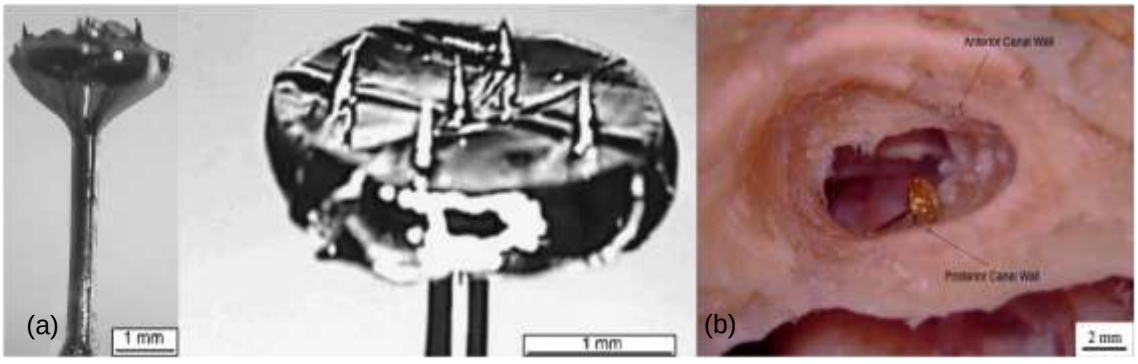

Figure 2-23 (a) Optical micrographs of a total ossicular replacement prosthesis fabricated by two-photon polymerization (b) Insertion of an Ormocer ossicular replacement prosthesis into a commercially obtained un-frozen human head. In this image, the Ormocer ossicular replacement prosthesis lies against the posterior canal wall. A tympanomeatal flap was raised prior to acquiring this image [35].

Also scaffold systems for tissue engineering, based on three-dimensional polymeric structures, have been fabricated by two-photon polymerization technique as shown in Figure 2-24. The material used for the fabrication of scaffold and drug delivery systems was ORMOCOMP due to its biocompatibility. Another biocompatible and biodegradable material reported in this review for the fabrication of tissue engineering scaffold and drug delivery was poly(ethylene glycol) diacrylate (PEGda). Using PEGda a scaffold has been fabricated for cartilage tissue repair shown in Figure 2-24b. The scaffold fabricated was able to sustain vertical load and allow cell migration and growth in the lateral direction [39].

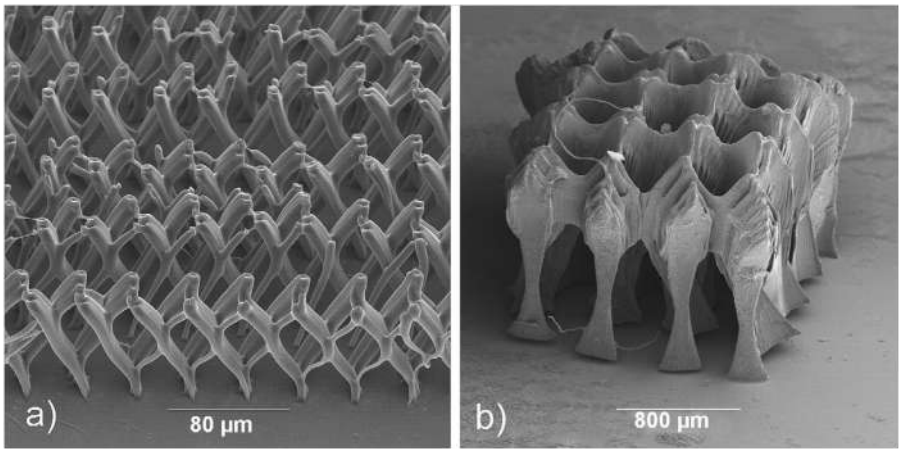

Figure 2-24 Scaffolds fabricated by 2PP: (a) from ORMOCER structure and (b) from PEGda [39]

Recently fabricated microneedles arrays, for transdermal drug delivery using two-photon polymerisation (TPP) techniques were also included in this review. They fabricated flat-top microneedles and single hypodermic-like microneedles shown in Figure 2-25. As suggested the fabricated microneedles are suitable for in vivo applications and also for MEMS- and NEMS-based drug delivery devices[39].

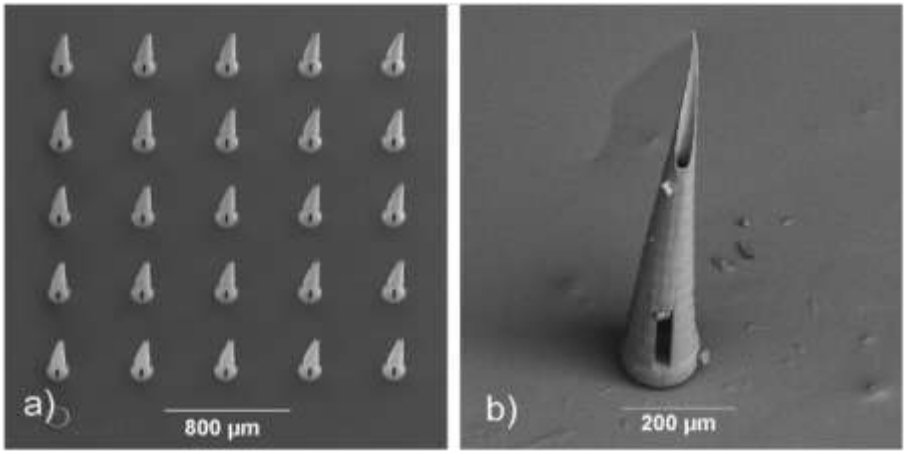

Figure 2-25 Microneedles fabricated by 2PP: (a) conventional flat-top microneedles array and (b) micro needle with off-centre channel [39]

2.3 Laser-based techniques for subtractive surface structuring

Whilst cutting sheet material could be considered subtractive patterning, this process will not be discussed here as it is usually on a larger scale than of interest for inducing bio-functionality to a surface. In order to operate on the micron scale, heat flow will normally dictate that short pulse lasers are necessary. Lasers of this type fall into two broad categories; those with highly multimode beams that have near uniform transverse profiles and those with low order mode structure (typically Gaussian). The poor focussing properties of multimode beams make them more suitable for mask illumination systems [47-50]. Sophisticated step and repeat systems together with mask scanning have enabled high resolution, repetitive, structures to be manufactured over large areas [51]. Strong absorption gives excellent depth resolution (~ 50nm) whilst short wavelengths give high lateral resolution (typically micron level but 100nm has been achieved). In contrast, Gaussian beams lend themselves to focussing to small spots limited by the wavelength of light. These high irradiance beams can then be scanned over the sample to give a direct-write capability. However, the speed is limited by a combination of the laser repetition rate and the spot size due to overlap requirements. This has led to the development of very high repetition rate laser that can now operate at 100's of kHz or even MHz for mode-locked pulse trains.

Chapter 3 Characterisation of the laser systems

This chapter describes the laser systems that have been used for the experimental work and gives details of measurements of their characteristics. The lasers used in this work were either a nanosecond ArF ultraviolet excimer laser or ultrashort pulses from a femtosecond titanium sapphire (Ti:sapphire) laser. Due to the smaller heat affected zone and reduced plasma screening effect, the femtosecond laser has certain advantages over longer pulses [52]. Precise laser machining and 3D micro and nano structure fabrication can be achieved by using point-by-point processing with the femtosecond laser system, whereas the excimer laser is more suitable for large area projection patterning.

Most of the work in this study has been based around the femtosecond titanium sapphire laser system for the fabrication of micro structures and surface patterning of materials. Two-photon absorption cross sections have been determined using the femtosecond laser at a wavelength of 800nm and also along with second harmonic generation to convert to a wavelength of 400nm. For the fabrication of three dimensional cell scaffolds, femtosecond laser irradiation at 800nm was used. The femtosecond laser system was also used to fabricate a bricks and mortar structure in keratin films to investigate skin structures for different cream absorption. The ArF excimer laser was also used for the surface patterning of keratin in order to investigate the resolution that could be obtained.

Laser beams can have varying degrees of monochromaticity, can be temporally and spatially coherent and may propagate with a variety of irradiance profiles. It is important to have knowledge of these characteristics to be able to predict the transport of the beam through various optical elements and also to analyse the subsequent interaction with materials. Here, measurements have been made of the beam parameters and a summary of the laser performance given for both the Ti: sapphire and ArF systems.

3.1 The femtosecond titanium sapphire laser

The laser characterised here is a Spectra Physics, Hurricane X. This is a complex laser system consisting of a seed laser and a regenerative amplifier. Chirped pulse amplification is utilised to avoid optical damage to the amplifier;

the seed pulses are stretched in time, amplified, and then compressed back to nearly their original duration. The seed laser is a mode-locked Ti: sapphire oscillator pumped by a frequency doubled, diode-laser pumped, Nd: YVO4 laser. This system gives ~100fs duration pulses at 80MHz repetition rate. As the regenerative amplifier is excited at 1kHz by a diode-laser pumped, frequency doubled, Nd: YLF laser (527nm), seed pulses are selected and introduced into the amplifier by a Pockels cell at this lower repetition rate. A second Pockels cell allows the timing of the exit of the amplified pulse relative to the Nd:YLF laser excitation pulse (~100ns in duration) to be altered and therefore the output energy of the femtosecond pulse. However, leaving the pulse circulating in the amplifier leads to pulse broadening and so it is often better to time the switching of the Pockels cell so that it coincides with the peak of the gain and then attenuate the beam outside of the laser if less energy is required. In this way, the Hurricane X system can nominally deliver 1mJ pulse energies in 100fs pulses at 800nm wavelength with a repetition rate of 1 kHz. This is an average power of 1W but each pulse has a peak power of ~ 10^{13}W (10TW). Measurements of the laser characteristics are given in the following sections.

3.1.1 Beam profile

The whole optical intensity profile in two dimensional space of a laser beam i.e. across the beam radius and its detailed shape can be measured with the help of a diagnostic device known as a beam profiler (or beam analyser). The beam analyser used here is based on a silicon CCD sensor (OPHIR Beam Star profiler V-PCI), with a sensor size of 6.4mm x 4.8mm corresponding to 320 x 240 pixels in both dimensions respectively. This device has useful sensitivity in the visible and near infrared spectral regions. The pixel size and hence the spatial resolution, is of the order of 5µm. Different parameters such as beam radius, beam position, ellipticity and Gaussian fits are displayed via software on a PC to which the CCD array is connected.

As the CCD sensor is very sensitive to light, it was necessary to attenuate the beam to prevent saturation. This was achieved by placing the beam profiler behind a dielectric beam turning mirror which had a nominal reflectivity of approaching 100%. The distance from the laser output to the CCD was of the order of 2m. As the sensor has a fixed frame rate of 25Hz it is difficult to

synchronise the data capture with the arrival of a laser pulse. Therefore, the laser was allowed to run at 1kHz and the software adjusted to reject blank frames. In this way the figures shown represent a typical frame that contained pulse data. Figure 3-1 shows the measured vertical and horizontal profiles through the centre of the beam together with Gaussian beam fits at an emission wavelength of 800nm. In Figure 3-2 the 2-D profile is given with the highest intensity coloured yellow and the background light level blue. Table 3-1 summarises the beam diameters in the different directions as measured using the raw data or the Gaussian fits. The CCD pixel values are proportional to the irradiance and therefore it is appropriate to use the $1/e^2$ point to evaluate the beam width (diameter); this is given as the 13.5% width. For completeness the 1/e width is also given which represents the equivalent beam size in electric field. It is also possible to see in Figure 3-2 small dark spots with concentric rings. These were found to move with the CCD sensor and are therefore thought to be associated with dust and not intrinsic to the beam itself. The concentric rings illustrate the coherence of the beam as these are thought to be Newton's rings formed from the scattered light. The beam can also be seen to be slightly wider in the horizontal direction than the vertical. Defining the elliptcity of the beam as $\sqrt{\frac{major^2 - minor^2}{major^2}}$ [53] gives a value of 0.56 for this beam.

Table 3-1 Horizontal and Vertical beam diameter of the femtosecond laser beam at 800nm wavelength.

	Horizontal		Vertical	
	Beam	Gaussian	Beam	Gaussian
Width (μm) 1/e (36.5%)	3145.18	3020.16	2498.83	2487.41
Width (μm) $1/e^2$ (13.5%)	4248.25	4257.11	3726.30	3506.16

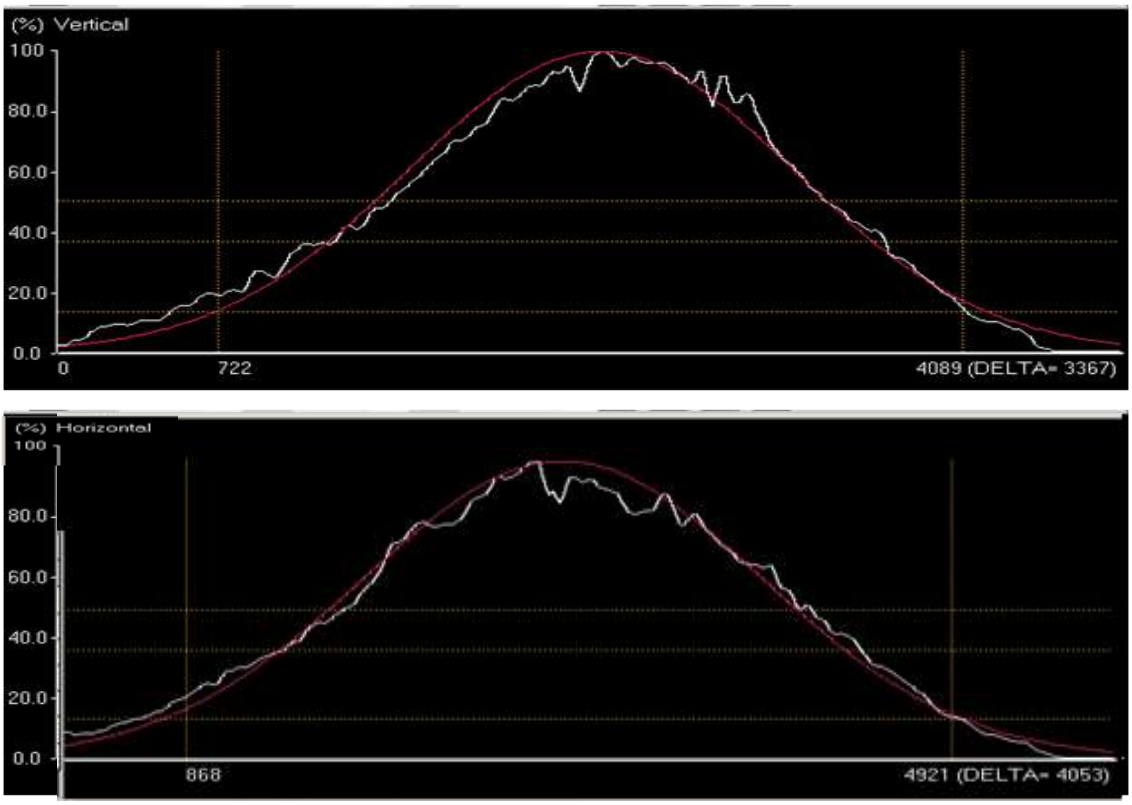

Figure 3-1 Vertical and horizontal line profiles through the centre of the beam. The raw data is shown in white together with a Gaussian fit in red. The laser was operating at 800nm wavelength and 1kHz. The intensity was attenuated by placing the sensor behind a dielectric turning mirror of near 100% reflectivity.

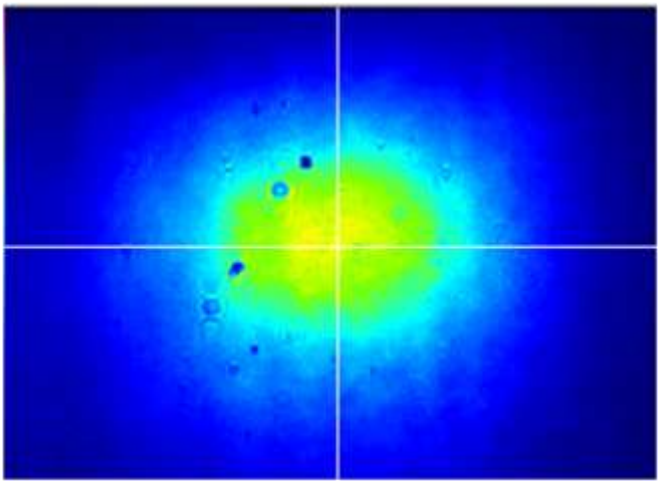

Figure 3-2 Colour coded 2-D intensity pattern showing in white the position that the line profiles in Figure 3-1 were measured through. Yellow areas are high intensity with blue regions being the background level.

It is possible to use the high intensity 800nm wavelength beam to create 400nm wavelength pulses via second harmonic generation. A commercial system from Spectra Physics was used for this purpose. The conversion efficiency, coupled with the transmission loss of the optical elements gave approximately 20% of the input power at 800nm as 400nm output. Figure 3-3 shows the vertical and horizontal Gaussian beam fits for the 400nm wavelength beam approximately 30cm after the output of the second harmonic generator. The 2D view and 3D view of the shape of this beam is shown in Figure 3-4 and Figure 3-5 respectively while Table 3-2 indicates the vertical and horizontal beam sizes at 400nm. It can be seen that the 400nm output is smaller in size than the 800nm input. This can be attributed to two reasons; the second harmonic generation is controlled by the irradiance and so the wings of the Gaussian distribution will not undergo conversion and also, the second harmonic generator includes focussing and collimating optics that may change the beam divergence. The beam can also be seen to contain fewer fluctuations in irradiance (i.e. it is “smoother”) and as a result has a better correlation to the Gaussian fit (Figure 3-3). However, the 400nm wavelength beam pointing stability was not as good as the 800nm output from the laser and could be seen to move from the centre of the CCD by approximately 100µm from pulse-to-pulse.

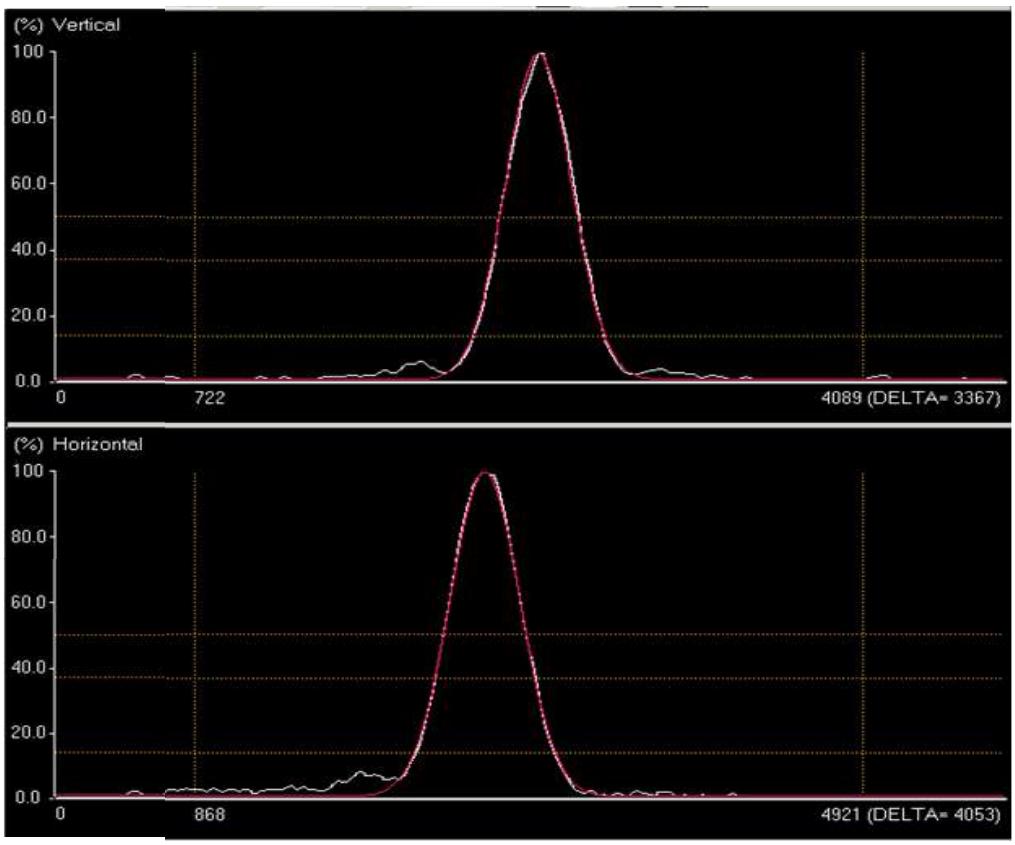

Figure 3-3 Vertical and horizontal line profiles through the centre of the beam. The raw data is shown in white together with a Gaussian fit in red. The laser has been frequency doubled to a wavelength of 400nm wavelength. The repetition rate was 1kHz.

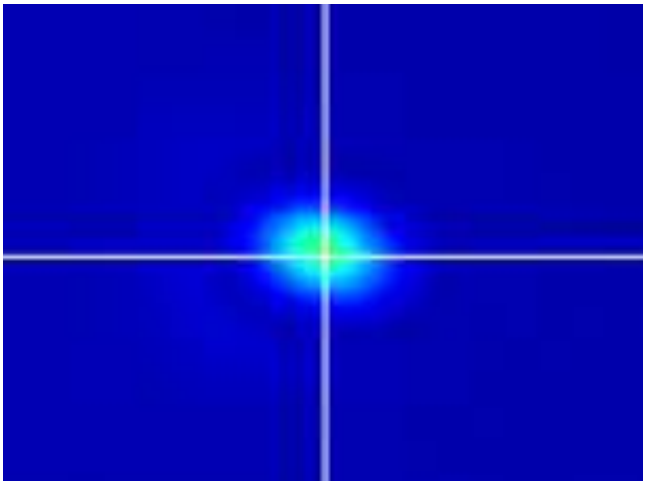

Figure 3-4 Beam shape of the femtosecond laser beam at 400nm wavelength generated using the frequency doubling crystal (2D view)

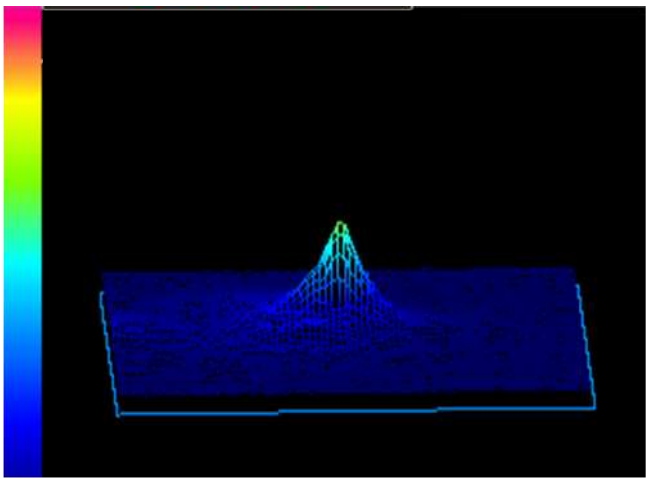

Figure 3-5 3D structure of the laser beam at 400nm wavelength measured with the CCD sensor.

Table 3-2 Horizontal and Vertical beam diameter of the femtosecond laser beam at 400nm wavelength.

	Horizontal		Vertical	
	Beam	Gaussian	Beam	Gaussian
Width (μm) 1/e (36.5%)	610.69	605.14	473.95	473.38
Width (μm) $1/e^2$ (13.5%)	840.18	852.99	657.25	667.25

3.1.2 Divergence of the beam

The lowest order Gaussian beam is characterized by the spot size ω_o known as the beam waist at $z=0$ and a planar wave front ($R_0 = \infty$) at this point. The beam waist ω_o is given by the equation

$$\omega_o = \frac{f\lambda}{\pi \omega_L} \qquad 3.1$$

where f is the focal length of the lens, λ is the wavelength of the laser beam and ω_L is the size of the beam entering the lens. The beam size as a function of distance, z, can be found from equation 3.2. Here, the beam size $\omega(z)$ is related to the beam waist, ω_o, by the ratio z/z_R [54].

$$\omega(z) = \omega_0 \sqrt{1 + \left(\frac{z}{z_R}\right)^2} \qquad 3.2$$

An ideal Gaussian beam expands due to diffraction spreading as it propagates away from the waist region as shown in Figure 3-6. It remains approximately collimated over a short distance in the near field and diverges in the far field. The distance over which the beam travels from the waist before the beam diameter increases by $\sqrt{2}$ (i.e. its area doubles) is given simply by the parameter

$$z = z_R = \frac{\pi\omega_0^2}{\lambda} = \text{Rayleigh range}$$

In terms of the Rayleigh range, the wave front radius of curvature can be written as,

$$R(z) = z\left[1 + \left(\frac{z_R}{z}\right)^2\right]$$

Substituting the value of the Rayleigh range, equation 3.2 can be written as

$$\omega(z) = \omega_0\left[1 + \left(\frac{\lambda z}{\pi\omega_0^2}\right)^2\right]^{\frac{1}{2}} \qquad 3.3$$

Here z is the distance propagated from the focal plane and λ is wavelength, ω_o is the radius of the 1/e electric field contour at the plane where the wave front is flat and $\omega(z)$ is the radius of the beam when it has propagated a distance z . For large z, $R(z)$ asymptotically approaches z and $\omega(z)$ asymptotically approaches the value [55]

$$\omega(z) = \frac{\lambda z}{\pi\omega_0} \qquad 3.4$$

where z is presumed to be much larger than $\pi\omega_o^2/\lambda$ so that the 1/e electric field contour ($1/e^2$ in irradiance) approaches a cone of angular size

$$\theta = \frac{\omega(z)}{z} = \frac{\lambda}{\pi\omega_0} \qquad 3.5$$

The Rayleigh range is the dividing line between near field divergence and mid-range divergence. Far field divergence must be measured at a point $>z_R$.

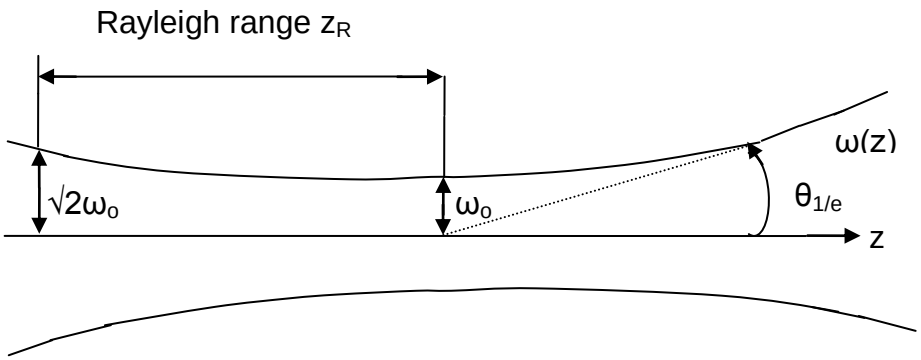

Figure 3-6 Here the approximately collimated waist region of the Gaussian beam is shown together with the Rayleigh range.

The beam diameter of the train of femtosecond laser pulses was measured with the help of the CCD system placed at different positions along the optical path. This data is plotted in Figure 3-7. The graph indicates that at this point in the optical path the beam is slowly converging and that the laser system, with its series of cavities (one for the seed laser and another for the regenerative amplifier) and stretcher/compressor (which includes a focussing mirror) results in a waist outside of the enclosure. The slightly elliptical nature of the beam can be seen as the horizontal axis has a larger diameter but this does not result in an appreciable difference between the horizontal and vertical divergence angles as the lines of best fit are quite parallel (Figure 3-7). In order to quantify the beam divergence, a lens was placed in the beam path (plano-convex, focal length 300mm) and measurements taken of the beam diameter as a function of distance before and after the geometric focal point. It was not possible to measure the focal spot size directly as the irradiance was too high and damage to the CCD would result. In addition, as the beam waist predicted from equation 3.1 is approximately 20μm in diameter and the CCD pixel size is ~12μm, there is insufficient resolution to observe it accurately. By interpolating the data back towards the focal point the beam waist can be inferred and the divergence taken as the ratio of this size to the focal length.

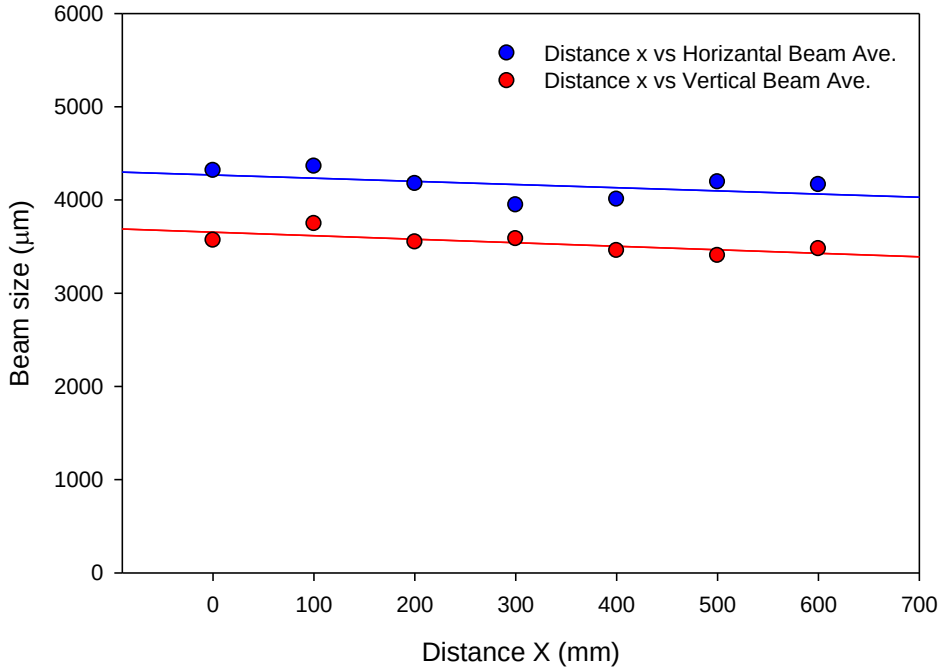

Figure 3-7 Graph between the distance and beam size without using lens.

Horizontal and vertical beam diameters were plotted against distance as shown in Figure 3-8 and Figure 3-9 respectively. The graph obtained shows that the size of the beam decreases towards the focus and is smallest near 275mm which is close to the geometrical focus of the lens. This is in accordance with the fact that when a beam is focused by the ideal lens, a slight shift in position between the geometrical focus of the lens and the actual waist of the focused Gaussian beam is always present [56]. The theoretically calculated values of $\omega(z)$ were plotted against distance and shown in the same Figure 3-8 and Figure 3-9 for horizontal and vertical beam diameters. Experimental data and theoretically calculated data for both horizontal and vertical beam diameters do not show symmetry after focus point. This is due to high irradiance at focal position which changes the refractive index and disturbs propagation of the beam beyond the focal point.

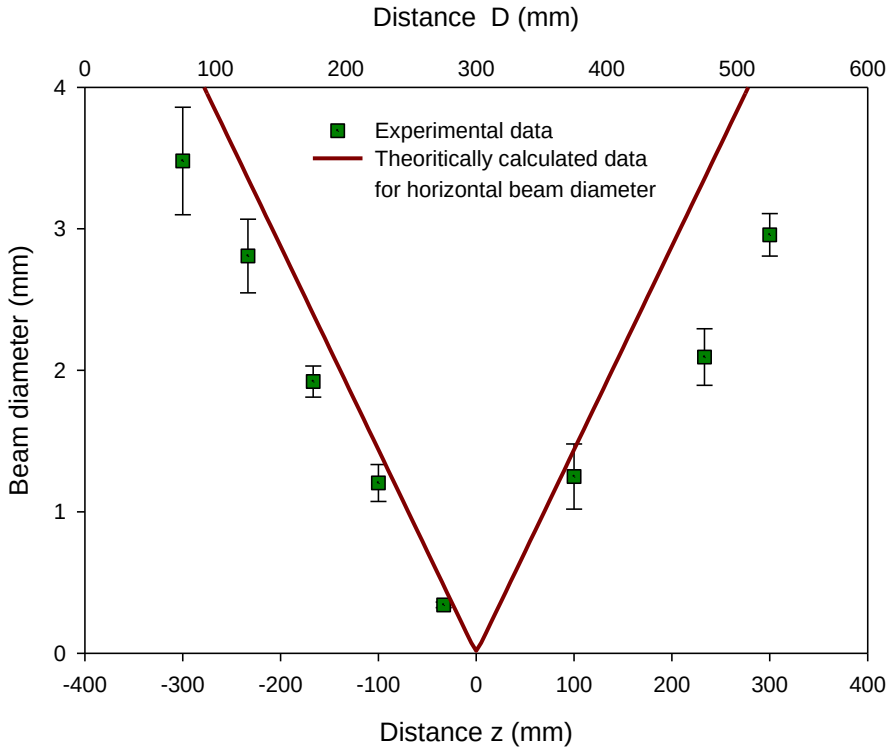

Figure 3-8 Experimental data for the beam size as a function of distance using a 300mm lens for horizontal beam diameters. The calculated beam diameter ω(z) vs. distance is also plotted.

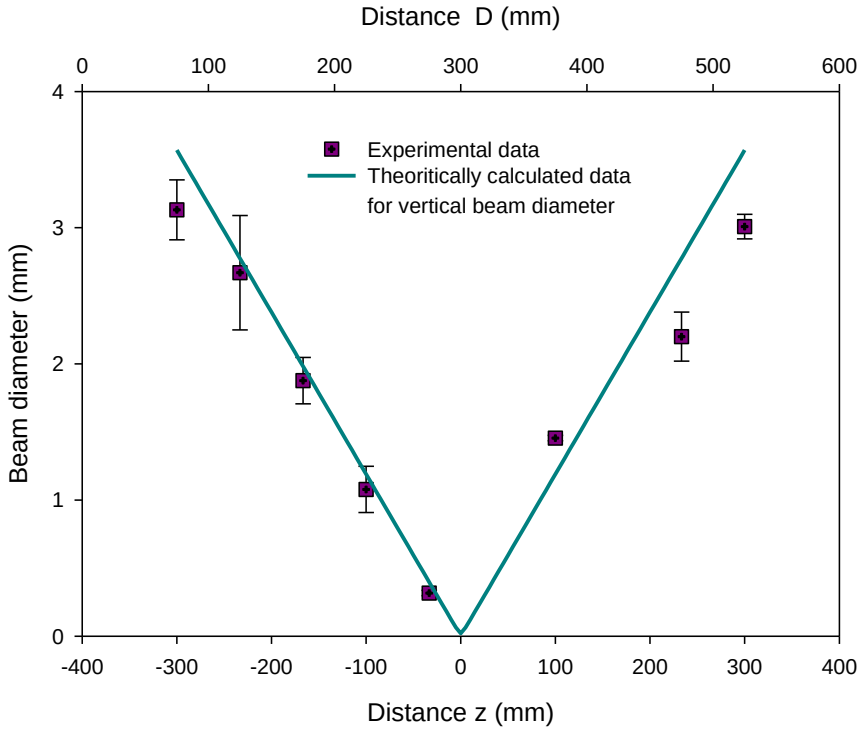

Figure 3-9 Experimental data for the beam size as a function of distance using a 300mm lens for vertical beam diameters. The calculated beam diameter ω(z) vs. distance is also plotted.

The experimental values obtained for horizontal and vertical beam waists were found to be 17.7μm and 21.4μm respectively. The fit to the expected curve is not that good and the beam quality should be considered to explain this departure. The next section discusses this.

3.1.3 M^2 Factor

The M^2 Factor or the beam propagation factor is a measure of the beam quality. M^2 is a numerical quantity which compares the focused diameter of a pure Gaussian beam with the diameter of the real focused beam in the far field. The concept of M^2 is useful in measuring the mode quality of a laser beam. Knowing M^2, it becomes possible to align laser mirrors or adjust the aperture of the beam to produce the desired quality. It is defined as the beam parameter product ($\omega_o\theta$) divided by λ/π, the latter being the beam parameter product for a

diffraction-limited Gaussian beam with the same wavelength or it is related to the half angle beam divergence given by

$$\theta = M^2 \frac{\lambda}{\pi \omega_o} \qquad 3.8$$

For a pure Gaussian beam the M^2 value is 1, and higher values indicate poorer quality (higher mode content) beams [57].The propagation equations for $\omega(z)$ and R(z) of a mixed mode beam are given by

$$\omega(z) = \omega_0 \left[1 + \left(\frac{M^2 \lambda z}{\pi \omega_0^2}\right)^2\right]^{\frac{1}{2}} \qquad 3.9$$

$$R(z) = z\left[1 + \left(\frac{\pi \omega_0^2}{M^2 \lambda z}\right)^2\right] \qquad 3.10$$

Using the experimental data from the previous section and by choosing suitable values for M^2 and substituting into equation 3.9, theoretical values $\omega(z)$ have been calculated. Experimental and theoretically calculated data can be compared as shown in Figure 3-10 for the horizontal beam diameter and in Figure 3-11 for the vertical beam diameter.

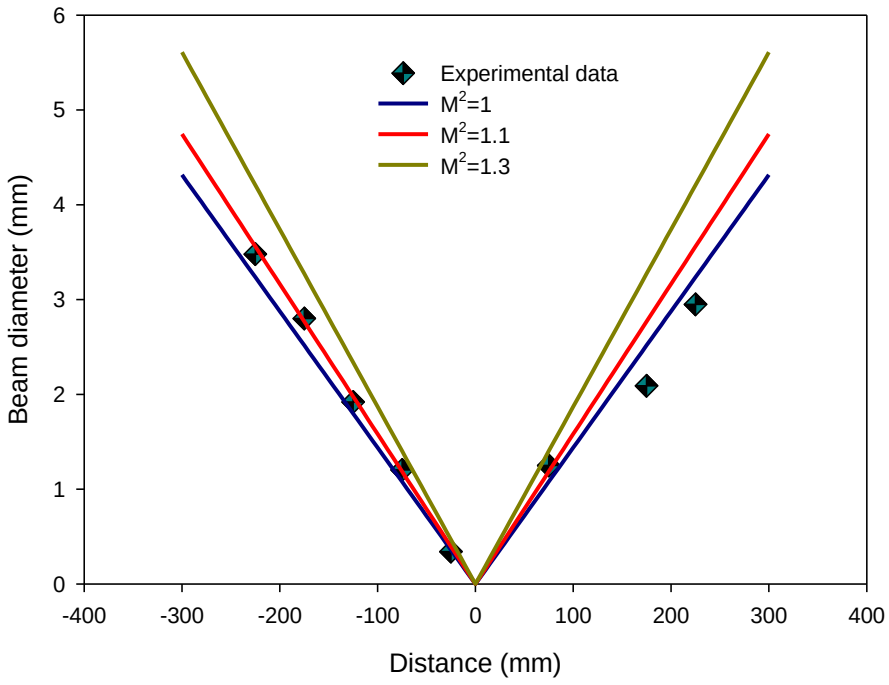

Figure 3-10 Comparison of the experimental and theoretical data for M^2 values for horizontal beam diameter

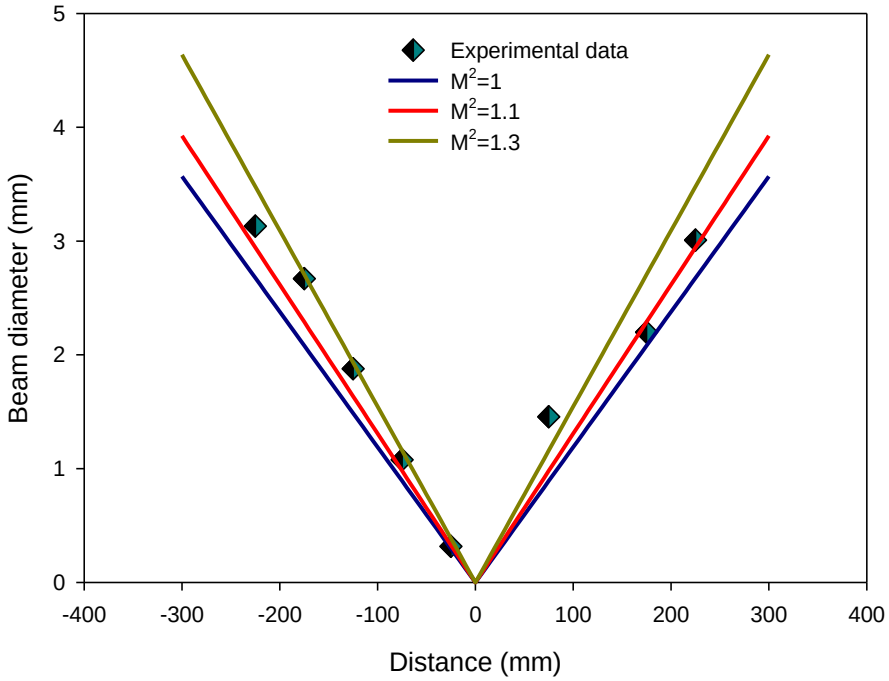

Figure 3-11. Comparison of the theoretical and experimental data for different M^2 values for vertical beam diameter.

It can be seen that the horizontal data has a good fit to M^2 = 1.1 before the focal point. This agrees with manufacturer's data. After the focal point the correlation is poorer. This may be partly due to refractive index disturbances in the air caused by the much higher intensity in the region of the focus even though the beam had been attenuated and no visible breakdown was observed.

3.1.4 Wavelength

The wavelength of the femtosecond laser beam was measured with the help of a computer controlled spectrometer type S2000 visible to NIR (Near Infra red Radiation) manufactured by Ocean Optics with serial no. HR2A0734. This system has a resolution of 0.5nm which was deemed sufficient as the output of the femtosecond laser was expected to be relatively broad. Scattered light from the laser beam was delivered to the spectrometer by a multimode fibre optic and an integration time of 30ms was used to improve the signal to noise ratio and also to average over several laser pulses. The calibration was checked using a HeNe laser operating at 632.8nm and the spectrometer was found to be reading 2nm too long. This has been corrected for in the data shown. The corrected wavelength measured was 802nm and the full width at half maximum was 13nm as shown in Figure 3-12. This is slightly longer than the expected

800nm output although the seed laser does have a scanning function with a range 790 – 810nm. The scanning control software reported the wavelength as being set to 800nm.

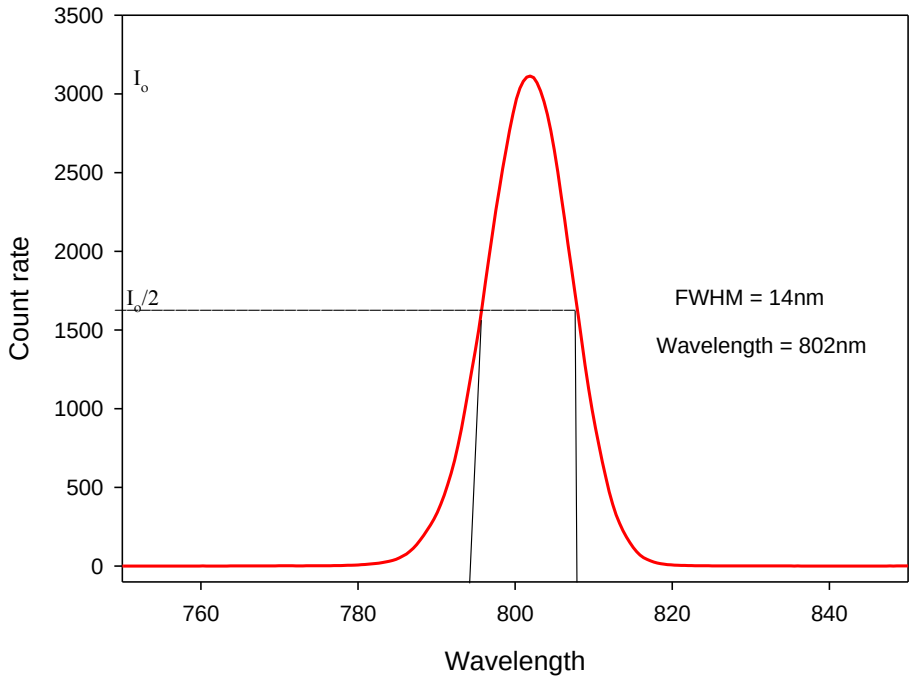

Figure 3-12 Fundamental emission of the femtosecond laser at 802nm wavelength measured using a fibre coupled spectrometer.

Using the fundamental output of the laser, a second harmonic generator was used to give an output around 400nm as described in section 3.1.1 and scattered light was again measured with the fibre coupled spectrometer. The same integration time of 30ms was used. The wavelength of femtosecond laser after passing through frequency doubling crystal was measured as 402nm and the full width and half maximum was 10nm as shown in Figure 3-13.

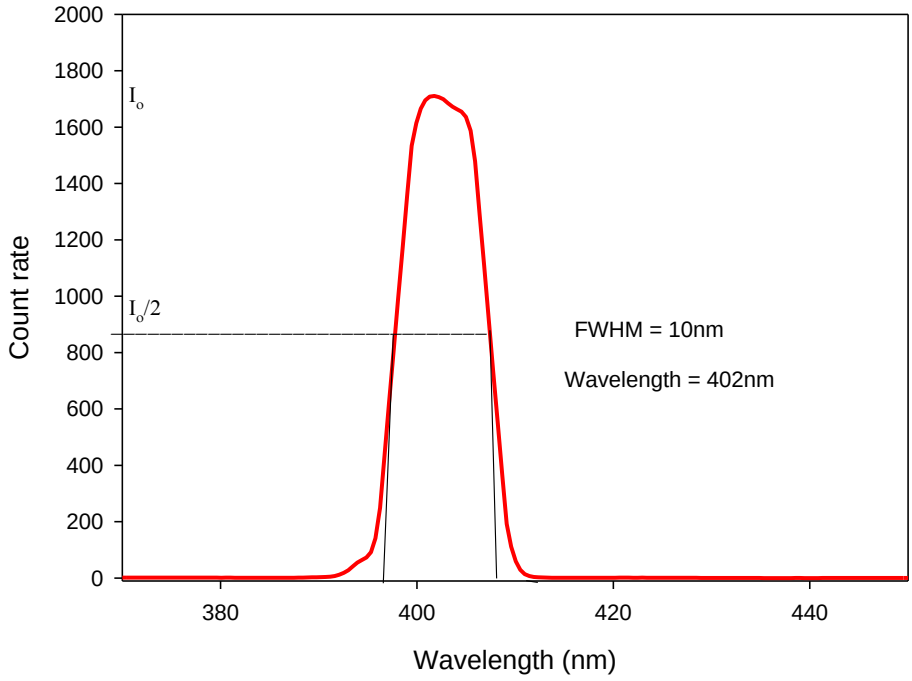

Figure 3-13 Wavelength spectrum of the frequency doubled femtosecond laser beam at 402nm.

3.1.5 Pulse Duration

The minimum duration of an individual pulse from the laser is related to the bandwidth of the output and hence the data from section 3.1.4 can be used to estimate the shortest pulse that could be expected. A so-called *bandwidth limited optical pulse* or one reaching the *Fourier transform limit* has the lower limit for pulse duration that is possible for the optical bandwidth of that pulse. A pulse at this limit is called *transform limited*. To calculate the transform limited pulse the minimum time-bandwidth product should be calculated when there is no chirp. The Fourier transform of a Gaussian pulse is a Gaussian function and the spectral width and the duration of a pulse are related quantities. From the uncertainty principle we know that

$$\Delta t\, \Delta E \geq \frac{\hbar}{2}$$

As

$$E = h\nu = \hbar\omega$$

Therefore

$$\Delta t\, \Delta\omega \geq \frac{1}{2} \qquad 3.6$$

The equality in equation 3.6 is only reached for pulses that have an electric field envelope in time that is Gaussian. Making this assumption but using a more convenient width measurement at the half maximum point (FWHM) and frequency (rather than angular frequency) changes the constant from 0.5 to 0.441 [58]. Equation 3.6 is now written as,

$$\Delta t\, \Delta\nu \geq 0.441 \qquad 3.7$$

Other pulse shapes require different constants but here we continue with the Gaussian assumption as the autocorrelator used to measure the duration also makes this assumption.

The emission width measured in the previous section was 14nm at a central wavelength of 802nm. This corresponds to a frequency bandwidth of 6.5×10^{12} Hz and therefore minimum pulse duration of 68fs.

Current technology for measuring optical pulses directly is limited by the response time of a photodetector and oscilloscope combination. For a repetitive waveform this can be as fast as 10's of ps. For example, Hamamatsu offer a metal-semiconductor-metal (MSM) photodiode with a rise-time of 30ps and LeCroy can supply oscilloscopes with 100GHz bandwidth. However, this is still much longer than the transform limited pulse calculated above. Therefore an indirect method must be used. Streak cameras are one option but here an optical autocorrelator has been used. There are also techniques such as FROG (frequency resolved optical gating) or SPIDER (spectral phase interferometery for direct electric field reconstruction) [59] that can be used to obtain much more information on the real pulse shape in time but their complexity and cost precluded their use here.

Fundamental wavelength laser pulses were sampled by using a flat glass plate to direct ~5% of the main pulse train into an APE Pulse Check autocorrelator (APE ser.03/3A211). It was ensured that only the reflection from the front face of the plate was allowed to enter the device so that a double pulse was not measured. Attenuation of the main pulse train was additionally required and

was achieved using neutral density filters. The optical path length of the stretcher-compressor can be adjusted using a motorised stage and this was optimised for the shortest output pulse. In addition, the alignment of the regenerative amplifier together with the Pockel cell timing affects the gain build-up time and therefore how long the seed pulse circulates in the system. Due to dispersion, this has an effect on the pulse duration as well [60]. A cleaned and freshly aligned system (i.e. just after manufacturer servicing) was measured as having a pulse duration of ~120fs. As the system becomes lossy (e.g. absorption in the stretcher-compressor section) and less well aligned, the pulse extends in time. Consequently, brief re-alignment, as achievable for daily use, gave usual pulse durations in excess of this and measurement at the start of each experiment was required. It will be seen that the pulse durations used throughout the rest of the thesis broadly fall into an interval of not being shorter than 120fs and not exceeding 180fs with the most prevalent timescale being ~160fs.

3.2 The argon fluoride excimer laser

An excimer laser is a form of ultraviolet laser widely used in deep-ultraviolet photolithography [61] for the manufacturing of microelectronic devices, micromachining and eye surgery. The ultraviolet light emitted from the excimer laser can successfully remove surface layers without damaging and burning of the remaining material.

ArF and KrF are types of excimer laser and are widely used in high-resolution photolithography machines. The argon fluoride laser has a deep ultraviolet wavelength of 193 nm [62] and is used in the production of semiconductor integrated circuits, eye surgery, and micromachining. An excimer laser contains a mixture of halogen gas (fluorine or chlorine) and noble gas (argon, krypton, or xenon). A pulsed electrical discharge generates excited species that bond to form excited complexes (exciplexes). These states are unstable and decay rapidly (~nanoseconds) releasing the excess energy as an ultraviolet photon. As the ground state is dissociative, population inversion is maintained and high gains can be achieved. Although the UV wavelengths that can be generated by excimer lasers are becoming available from solid state systems, these gas lasers still uniquely offer large area, short pulse and beams that make them suitable for projection mask illumination.

3.2.1 Divergence of the ArF excimer laser

A number of focal plane divergence measurement techniques can be used. The National Institute of Standards and Technology recommends measuring the beam diameter at the focal point of an imaging lens.[63] The ideal focal point of a lens is defined as the point in space where a beam size is at minimum when it passes from the lens as shown in Figure 3-14.

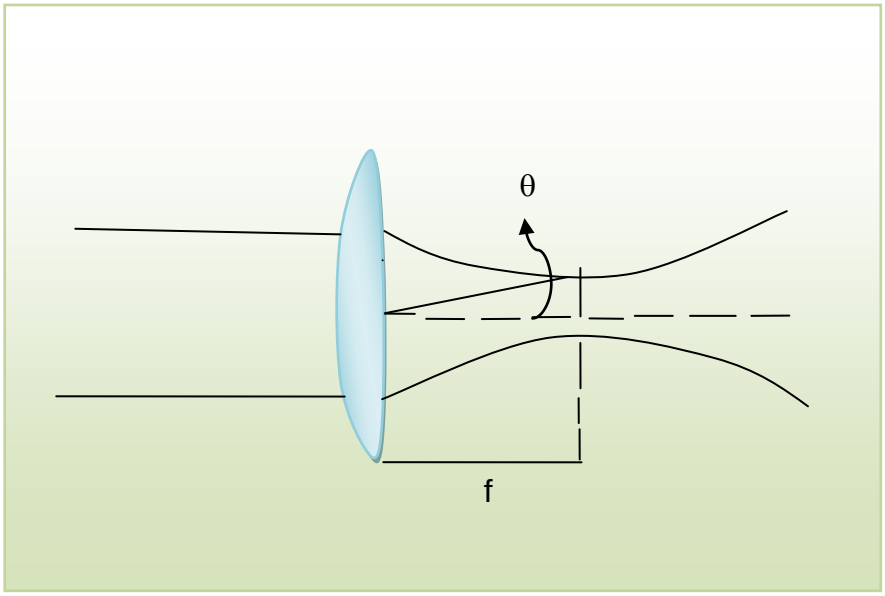

Figure 3-14 Schematic diagram for measuring divergence of argon fluoride excimer laser beam using plano convex lens.

From a burn pattern taken at the minimum spot size position beam diameters were measured both for the horizontal and vertical directions. Horizontal beam diameters are denoted by D(x) and the vertical beam diameters are denoted by D(y). The divergence for the laser beam in the horizontal(x) and vertical(y) directions can be calculated by the formula:

$$\theta = \frac{D_{x,y}}{F} \qquad 3.17$$

where $D_{x,y}$ represents the horizontal and vertical beam diameters depending upon which axis is being measured and F is the distance to minimum spot size of the lens used.

Figure 3-15 Transverse beam profile of the argon fluoride excimer laser obtained by irradiating thermal paper (fax paper) with 5 pulses of the raw beam. The beam can be seen to be approximately rectangular due to its highly multimode nature. In the vertical axis it is ~11mm in size and the irradiance distribution is roughly Gaussian. However, in the long, horizontal, axis it is ~27mm with uniform irradiance (the so-called "top-hat" distribution).

A plano-convex lens of nominally 23cm focal length at a wavelength of 193nm and 50mm diameter was illuminated with the beam from an ArF excimer laser Questek (Model 2860) shown in Figure 3-15. The smallest burn pattern was found at a distance of 230mm from the lens and was measured using an optical microscope and software to have dimensions 1.4mm by 0.64mm. As shown in Figure 3-14 this data can be used to find the beam divergence in the horizontal, θ_x, and vertical, θ_y, directions. In this way the following values were obtained; θ_x =3mrad, θ_y = 1.4mrad. As is common with high gain, short-pulse, lasers, the beam size at the output is defined by the electrode separation in one dimension and the discharge width in the other. It is usual for excimer lasers to have an electrode spacing of 2cm and discharge widths that rarely exceed 1cm [62]. As the burn pattern in Figure 3-15 was taken at a distance of ~50cm from the output coupler of the laser, this beam size is commensurate with the typical characteristics of a laboratory scale device.

Within the beam, areas will be correlated to each other in phase. The physical size of these patches is known as the spatial coherence of the beam and is given by $l_c = \lambda/\theta$ [64]. Therefore, the coherence patch size will be longer in the lower divergence axis and of approximate dimension 107μm and shorter in the other with a size of 64.3μm. This is an important consideration when using interference methods to pattern surfaces as there is no phase correlation across the whole beam unlike a true Gaussian (TEM_{00}) profile. Although not measured here, an ArF excimer laser has a linewidth of the order of 10^{13}Hz [65]

corresponding to a coherence length of 30μm. Whilst this is relatively short, it does make possible the use of self aligned optical interference schemes such as a phase mask in the near field.

3.2.2 Pulse duration for ArF excimer laser

The pulse duration was measured using a reverse biased avalanche photodiode (FND 100Q with -90V bias). Light was back-scattered from the front surface of a UV lens into the photodiode so as to avoid saturation. In order to preserve the nanosecond rise time of the detector, a fast oscilloscope (HP Infiniium, 500MHz bandwidth, 2 GSa/s) was used and the coaxial cable from the FND100Q to the input was terminated into 50Ω. The waveform was averaged over 64 pulses and the result is shown in Figure 3-16. It can be seen that the optical pulse has a rapid rise followed by a longer decay with an overall FWHM duration of 16.3±0.2ns. As the laser is capable of generating up to 200mJ of output energy at this wavelength, this sets a limit on the peak power available of 12MW. Similarly, as the pulse repetition rate has a maximum value of 10Hz, average powers of 2W can be extracted.

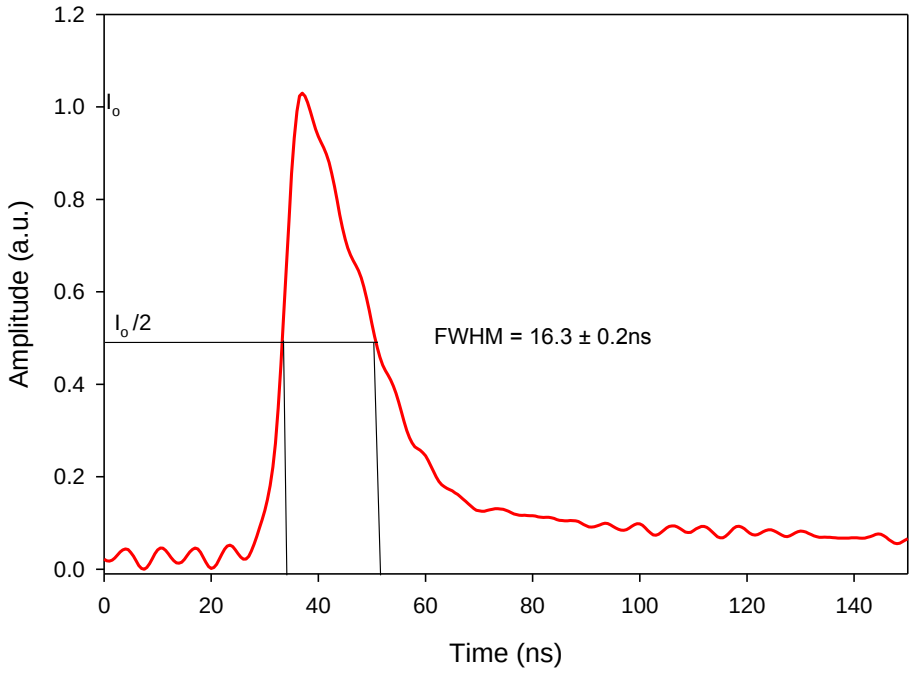

Figure 3-16 Amplitude vs. time graph shows pulse shape of the ArF excimer laser. The laser pulse length (FWHM) is approximately 16.3 ± 0.2ns.

In practice, it is common to select a uniform part of the beam using an aperture. This greatly reduces the available pulse energy but the fluence is broadly similar to the average of the full beam, i.e. ~100 mJ cm^{-2}. Given that it is relatively straightforward to construct an optical system to give ~10x reduction in beam size, this sets, as a rough estimate, the upper limit of fluence available at the sample to be ~10 J cm^{-2}.

Chapter 4 Additive material structuring by two-photon polymerisation

Laser direct writing additive techniques have been receiving significant attention in recent years and have been extensively used for the fabrication of 3D micro/nano structures. In this technique material is added to the substrate. Laser-based fabrication using laser direct writing techniques has been used for the production of medical devices, as they do not damage material by heating and no “wet” chemicals are involved in the process [66]. For the deposition of materials several techniques are in use nowadays.

The Pulsed Laser Deposition (PLD) technique has been used for the deposition of high quality thin films and has been successfully used to grow epitaxial films of ceramic materials i.e., ferroelectrics, ferrites, colossal magnetoresistance materials, transparent conductors, and biomaterials. Unfortunately PLD is not suitable for more fragile and temperature sensitive organic material where due to breakage of chemical bonds the surface chemistry of the thin film changes and thus changes the phase and electronic properties of the organic thin film [67].

Another material deposition technique, laser induced forward transfer (LIFT) process, is used to transfer thin films from an optically transparent substrate onto another substrate close to it. Patterning is achieved by projecting the thin film in a spatially selective manner. The thickness of the thin film on the target substrate should be less than a few 100nm and its absorption should be high otherwise morphology, spatial resolution, adherence to the substrate and the transferred pattern will be affected. Other disadvantages are poor line width, ablation of the substrate and impurities in the thin film [67]. Usually LIFT is used for the deposition of microelectronics and display products [68]. For the fabrication of a cell scaffold, material deposition by the LIFT technique is not suitable due to the low volume of material that can be transferred.

3D structures with high resolution can be fabricated using nonlinear optical microstructuring technique based on two-photon polymerization of organic materials [69]. Two-photon absorption process, applied to photon polymerisation is used for many advanced applications such as fabrication of 3D microstructures, 3D integrated optical components and optical data storage

[27] and is also getting attention because of the potential for two-photon excitation for bimolecular imaging, two-photon photodynamic therapy [26] and two-photon laser scanning fluorescence microscopy [70].

Therefore, in the present study, for the fabrication of cell scaffolds, two-photon polymerization processes have been used. LIFT can be successfully used on metallic target films; therefore this method can be used in the future for the deposition of antimicrobial material i.e., silver onto the scaffold to reduce the risk of infection.

Two-photon absorption is a process in which two photons of identical or different frequencies are absorbed for the excitation of molecule to a higher energy state. Photoinitiators upon exposure to laser light simultaneously absorb two-photons to access an excited state that each photon alone has insufficient energy to do so. These processes have unique characteristics for applications such as (a) the square power dependence of laser irradiance which improves spatial resolution, (b) increased penetration depth, and (c) fast temporal responses [71].

Two-photon excitation studies of various photosensitizers are presented in this chapter to enable determination of two-photon absorption cross sections. Fluorescence spectra of the photoinitiators Bis(diethylamino)benzophenon and Thioxanthone were recorded for excitation at wavelengths 400nm and 800nm using a Ti:sapphire femtosecond laser. The second harmonic of this laser has been used as light source for single photon excitation. Due to the use of a second harmonic generator for the femtosecond laser system the method used in this study is experimentally and theoretically more clear and simple as compared to other methods so far used [25]. No differences between one-photon and two-photon-excited fluorescence emission spectra were observed. The peak intensities of emitted fluorescence spectra at 800nm and 400nm wavelength were at the same wavelength i.e., approximately around 500nm and no difference in the shape of the spectrum was observed.

4.1 Choice of materials and their characteristics

4.1.1 Liquid polymer resin – EBPADMA

3D structures can be fabricated in photosensitive materials which are divided into two classes: negative and positive tone photoresists. Negative resist materials are available in solid and liquid form. Most of the negative resist liquid materials are acrylate-based [3]. Polymerization processes are initiated by radically reacting photoinitiators during laser exposure in acrylate-based negative resist liquid materials. To generate a micron scale 3D structure, two-photon polymerisation (TPP) of photo-cross-linkable Ethoxylated Bisphenol A Dimethacrylate (EBPADMA) (6EO) monomers was used. This form of EBPADMA has 6 units of ethoxylation. Units of ethoxylation indicate the number of EO (ethylene oxide) added to the chain starter material (compounds containing an active hydrogen atom). By increasing the ethoxylated chain length the mobility of the molecule increases and thereby increases the reactivity and degree of conversion. This material was obtained from Esstech [72] available in the form of clear viscous liquid with unpleasant odour. The material has negative resist behaviour and can be used as a liquid photo-polymerizable resin. This material has been chosen for its biocompatibility and optical transparency [72]. Other potential material choices form scattering solids that often appear white and preclude studies of cell proliferation via optical microscopy (conventional and confocal). In order to make it photosensitive chromophores were added to the material. When Ti: Sapphire femtosecond laser pulses are tightly focused into the volume of this resin they can initiate two-photon polymerization processes transforming the liquid into solid state. Two-photon polymerization (TPP) has many advantages when applied to the fabrication of 3D micron sized structures with nano-scale resolution. After curing, the EBPADMA has properties like a rigid, optically transparent polymeric glass. Polymerisation occurs along the trace of the laser focus when it is moved through the resin in three dimensions. This process is confined to a highly localized area at the focal point due to the quadratic dependence of the two-photon absorption rate on the laser intensity. Any computer generated 3D structure can be fabricated by direct laser recording into the volume of the EBPADMA. The non–irradiated liquid resin can be removed by washing the

sample a few times with deionised water. The structure of the monomer employed in this work is shown in Figure 4-1.

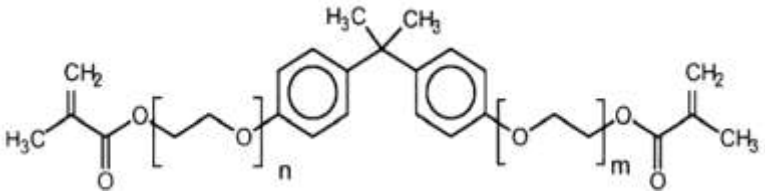

Figure 4-1 Chemical structure of Ethoxylated Bis Phenol A Dimethacrylate (EO=6) with molecular weight of 628.7 and molecular formula as $C_{35}H_{48}O_{10}$.

4.1.2 Photosensitizers

The use of efficient TPA chromophores can contribute to the fabrication of fine 3-D patterns with high resolution under low laser power and short periods of illumination thus optimising the speed of the process. Chromophores act as photosensitizers absorbing light of a particular wavelength and yield free radicals upon irradiation thus initiating the reaction. The photosensitizers used in the current study are *4, 4'-Bis(diethylamino)benzophenon* and *Thioxanthone*. The chromophores of *4, 4'-Bis(diethylamino)benzophenon* were used as the photosensitizer as well as photoinitiator while Thioxanthone only act as photosensitizer and cannot initiate reaction in the absence of coinitiator. Solutions of these materials were exposed to the femtosecond laser beam at 800nm and 400nm to obtain the fluorescence at one and two photon excitation. The fluorescence spectra were compared and the two-photon absorption cross sections were calculated.

4.1.2.1 4, 4'-Bis(diethylamino)benzophenon

Usually, photoinitiators are added to the monomer to initiate the photopolymerization process. In order to start radical polymerization, electron transfer is required from chromophores to the polymerizing monomer. Therefore electron-rich molecules capable of transferring electrons should be used. The transfer of electrons to the monomer generates active species and initiates the polymerization. The TPA cross-sections of photoinitiators have been extensively studied [24, 25, 27, 29]. This work presents the study of *4, 4'-Bis (diethylamino) benzophenon* which is used for the photosensitization of the liquid monomer *Ethoxylated Bis Phenol A Dimethacrylate (EO=6)*.

The photoinitiator 4, 4'-Bis(diethylamino)benzophenon is in the form of yellowish powder obtained from Aldrich. It has a molecular formula $C_{21}H_{28}N_2O$ with a molecular weight of 324.46 and its chemical structure is shown in Figure 4-2. To measure the single and two-photon absorption cross section of the 4, 4'-Bis(diethylamino)benzophenon ethyl state, solutions were prepared with several solvents; ethanol, ethyl acetate and Ethoxylated Bis Phenol A Dimethacrylate (EO=6). A stock solution of 4, 4'-Bis(diethylamino)benzophenon ($3.1x10^{-2}$M) was prepared in EBPADMA. To prepare the stock solution, 0.1546g of 4, 4'-Bis(diethylamino)benzophenon was mixed with 5ml of EBPADMA contained in a 14ml glass bottle. The materials were mixed with help of a stirrer and the glass bottle containing the resin was cover with foil to protect from light. It was left overnight allowing the photosensitizer to completely dissolve in the resin. The sample solution with $3x10^{-3}$M was prepared by successive dilution of the stock solution and was placed in a 10mm cuvette to obtain the absorbance at 400nm wavelength. The absorption spectrum of EBPADMA was determined by a Perkin Elmer UV/Vis spectrometer lambda 40 in the wavelength range 200nm to 900nm. The absorption spectrum in Figure 4-3 shows, that EBPADMA is transparent in the visible region. In order to achieve efficient photosensitization of the polymerizable resin, TPA chromophores are employed as photosensitizer. It is significant from the figure that resin EBPADMA without photosensitizer shows absorption in the wavelength range 200nm to 400nm while after adding photosensitizer it shows absorption in the visible range. With increasing concentration of the chromophores, absorbance of the material increases in the visible range while it still shows very little absorbance in the 800nm region.

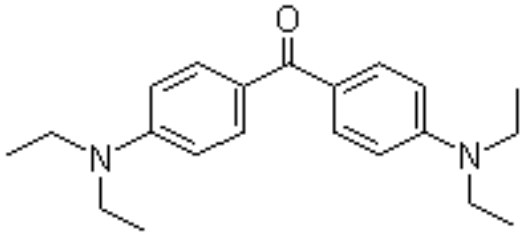

Figure 4-2 Chemical structure for 4, 4'-Bis(diethylamino)benzophenon

Different concentrations were used to find the best photosensitization of the EBPADMA mixture for two-photon polymerisation in the 400nm wavelength region. For this purpose $3.1x10^{-2}$M stock solution was diluted and less

concentrated solutions were prepared and the absorption spectra were obtained as shown in Figure 4-3. Absorbance of 4, 4'-Bis(diethylamino)benzophenon at different concentrations was measured using a UV/Vis Spectrometer Lambda 40 (Perkin Elmer) were plotted against molar concentration to calculate the molar absorbance coefficient as shown in Figure 4-4.

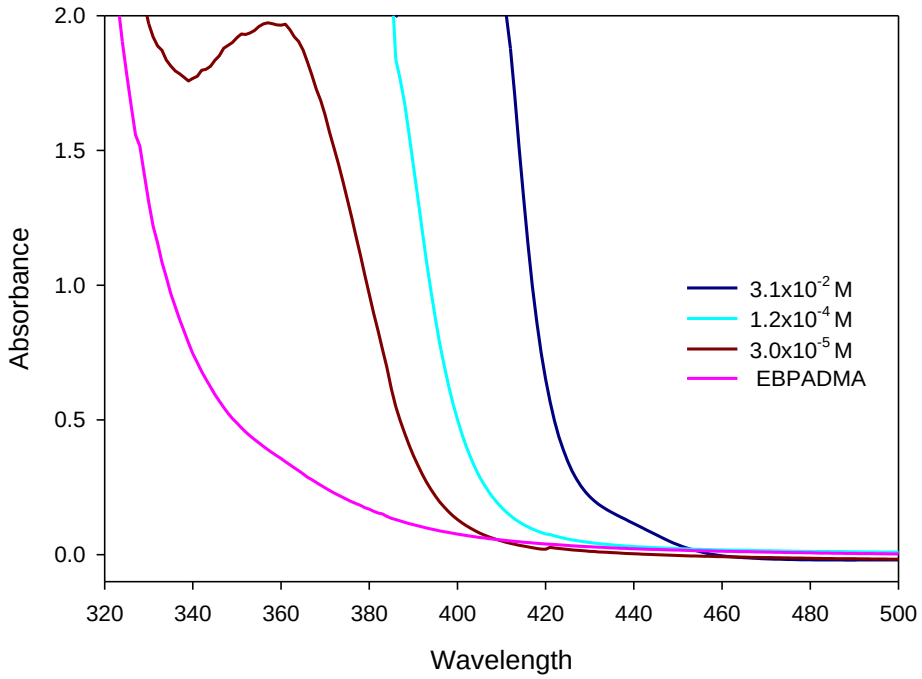

Figure 4-3 Absorbance curves of Ethoxylated Bis Phenol A Dimethacrylate (EBPADMA) with and without photosensitizer. It is significant from the figure that resin EBPADMA without photosensitizer shows absorption in the wavelength range 200nm to 400nm while by increasing the concentration of the photosensitizer absorption in the visible range increases.

The relation between incident intensity I_o and transmitted intensity I is given by

$$T = \frac{I}{I_o}$$

and the absorbance is given by

$$A = \log \frac{1}{T}$$

The measured intensity I transmitted through a material with thickness z is related to the incident intensity I according to the inverse exponential law known as the Beer-Lambert law:

$$I = I_o e^{-\alpha z} \qquad 4.1$$

$$\ln \frac{I}{I_o} = -\alpha z$$

$$2.302 \log_{10} \frac{I_o}{I} = \alpha z$$

As $A = \log_{10} \frac{I_o}{I}$

Therefore $2.302\, A = \alpha z$

and $\alpha = \frac{2.302\, A}{z} \qquad 4.2$

The absorption coefficient α can be calculated using the above equation at different wavelengths once the absorbance at different wavelength has been found from the absorbance spectrum shown in Figure 4-3. Here z is 1cm which is width of the cuvette containing the resin. The absorbance of the material A is directly proportional to the thickness of the sample and to the concentration of the absorbing species in it and can be written as

$$A = \varepsilon c z \qquad 4.3$$

where ε is the molar absorption coefficient and c is the concentration of the absorbing species. To determine molar absorbtivity ε, accurate measurements of A and c are required. The measurement of A is straightforward and can be determined using the UV/Vis spectrometer. The concentration c was prepared using weight-in-volume (W/V) solutions. A graph was drawn between the absorbance A and concentration of the absorbing species c, to find the molar absorbtivity from the gradient of the graph. The molar absorption coefficient ε for *4, 4'-Bis (diethylamino) benzophenon* was determined from the graph as 4450M^{-1}cm-1, shown in Figure 4-4. The single photon absorption cross section at 400nm wavelength was also calculated from the value of molar absorption coefficient. The molar absorption coefficient for *4, 4'-Bis (diethylamino) benzophenon* at different wavelengths was also calculated and a graph between wavelength and molar absorbtivity shows a decrease with increasing wavelength as shown in Figure 4-5.

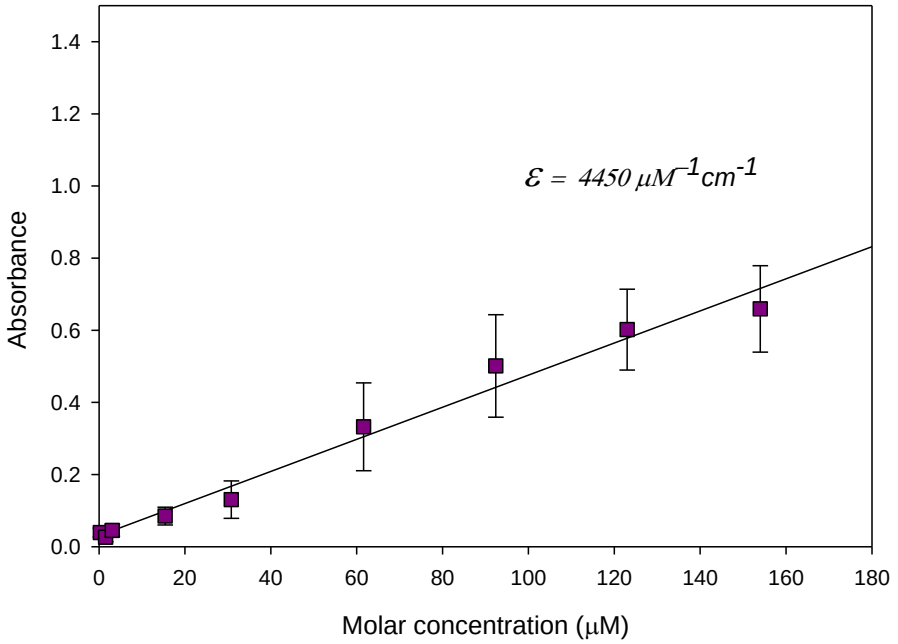

Figure 4-4 Graph is drawn between absorbance of light and different concentration of 4*, 4'*-Bis(diethylamino)benzophenon in Ethoxylated Bisphenol A Dimethacrylate. Gradient of the graph shows molar absorption coefficient ε for *4, 4'*-Bis(diethylamino)benzophenon at 400nm wavelength .

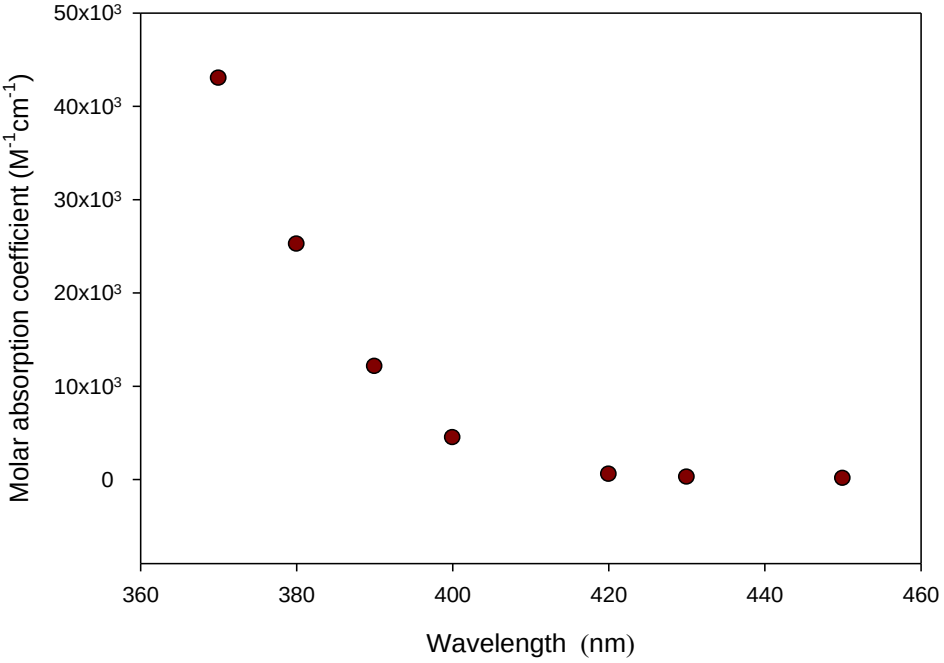

Figure 4-5 Molar absorption coefficient ε at different wavelength are calculated for 4*, 4'*-Bis(diethylamino)benzophenon in Ethoxylated Bisphenol A Dimethacrylate.

In order to measure the molar absorbtivity, single photon absorption cross section and two-photon absorption cross section of *4, 4'-Bis (diethylamino) benzophenon* in a different solvent i.e., ethyl acetate, a new stock solutions of 3. 1x 10^{-2}M was prepared. The stock solution was diluted to different concentration and its absorption at 400nm wavelength was determined using UV/Vis spectrometer as shown in

Figure 4-6. The molar absorption coefficient ε was calculated from the graph drawn between absorption A of the photoinitiator at 400nm wavelength and molar concentration c as shown in Figure 4-7. The value of ε was found to be 65.4$M^{-1}cm^{-1}$and maximum light was absorbed at 350nm wavelength.

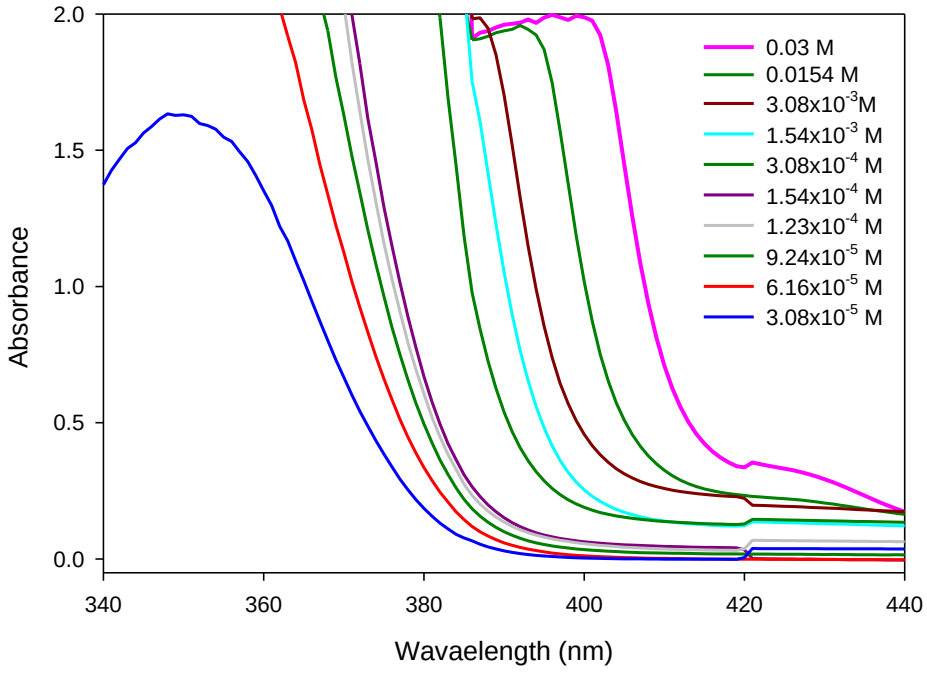

Figure 4-6 Shows the absorbance curves of *4, 4'-* Bis(diethylamino)benzophenon in ethyl acetate at different wavelength using UV/Vis spectrometer. Absorbance is maximum at 350nm wavelength.

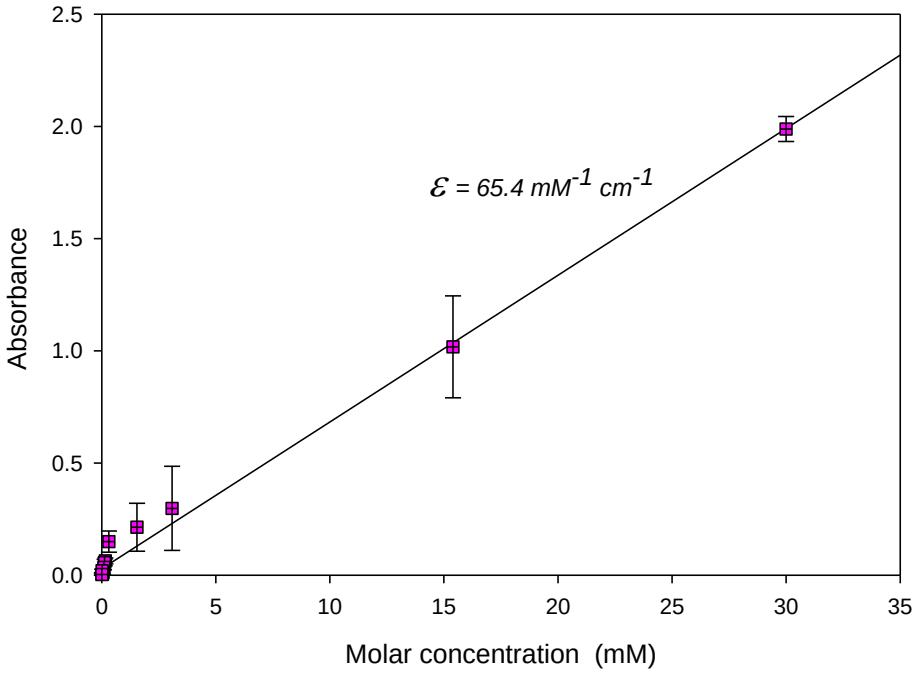

Figure 4-7 Graph is drawn between absorbance of light at 400nm wavelength and different concentration of 4, 4'-Bis(diethylamino)benzophenon in ethyl acetate. Gradient of the graph shows molar absorption coefficient ε=65.4mM^{-1} cm^{-1} for 4, 4'-Bis(diethylamino)benzophenon in ethyl acetate at 400nm wavelength.

Finally, the same procedure was followed as above but using ethanol as the solvent. The absorbance curve of *4, 4'-Bis(diethylamino)benzophenon* in ethanol is shown in Figure 4-8. The peak of the curve shows maximum absorbance at 375nm wavelength. The absorbance of light at 400nm wavelength was plotted against concentration of 4*, 4'-*Bis(diethylamino)benzophenon in ethanol. The molar absorption constant ε was calculated from the slope of the graph as 11366M^{-1}cm^{-1}as shown in Figure 4-9.

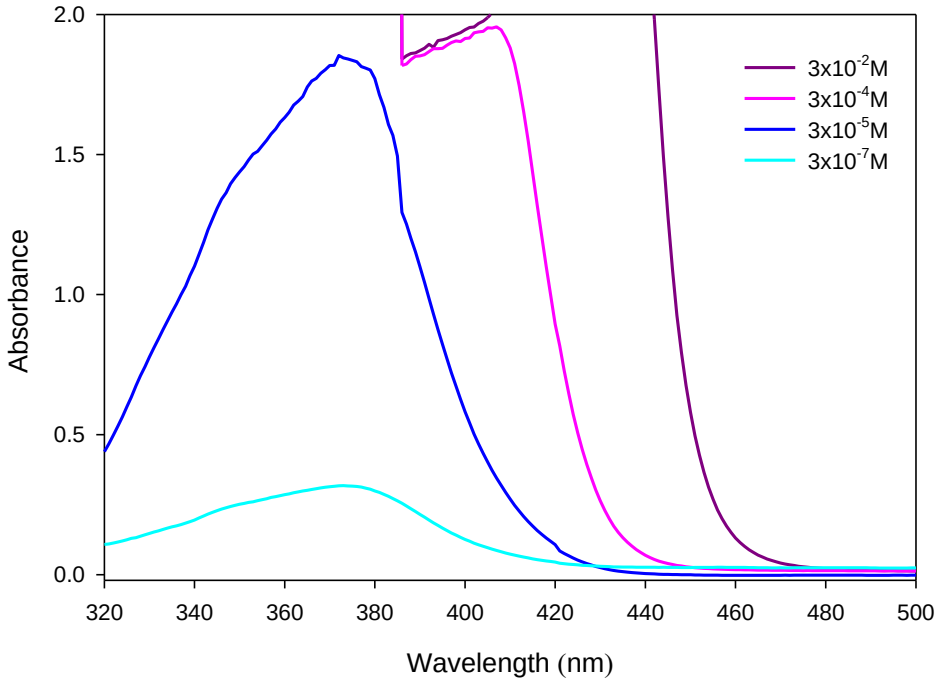

Figure 4-8 Shows the absorption spectra of *4, 4'*-Bis(diethylamino)benzophenon in ethanol at 400nm. Peak of the curve shows maximum absorbance at 375nm wavelength.

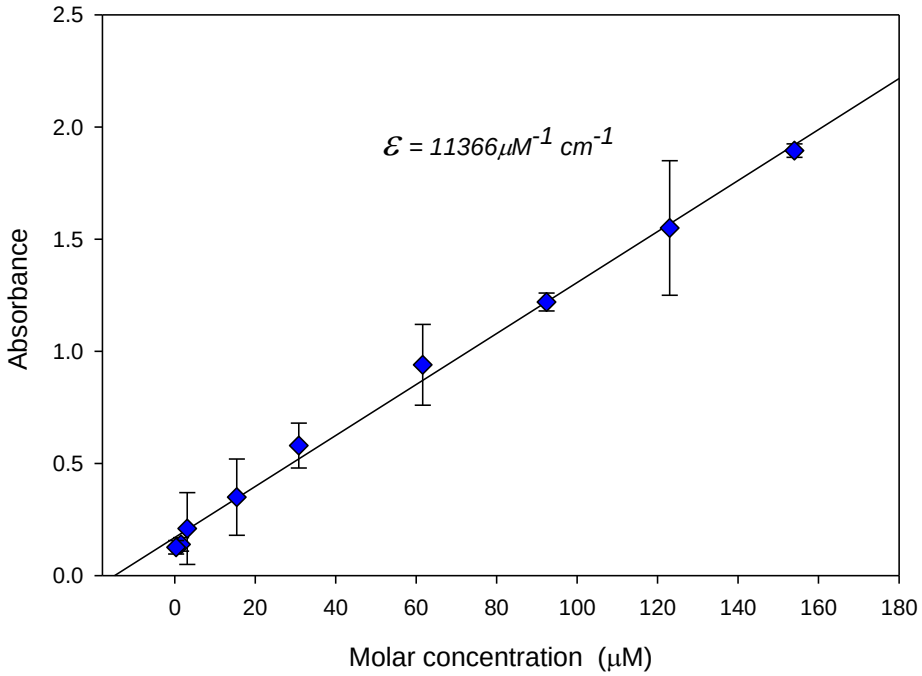

Figure 4-9 Graph is drawn between absorbance of light and different concentration of 4, *4'*-Bis(diethylamino)benzophenon in ethanol. Gradient of the graph shows molar absorption coefficient ε for *4, 4'*-Bis(diethylamino)benzophenon in ethanol at 400nm wavelength.

4.1.2.2 Thioxanthone (Speed cure CPTX)

Thioxanthone is a Type II photoinitiator in the form of a yellow powder. Its chemical name is *1-chloro-4-propoxythioxanthone* ($C_{16}H_{13}ClO_2S$) having molecular weight 304.79. The molecular structure of *1-chloro-4-propoxythioxanthone* is shown in Figure 4-10. Type II photoinitiators are those compounds which only initiate reactions and is not consumed during the reaction. They produce an initiating radical when the triplet excited states of the material react with hydrogen donors and are generally slower than type I photoinitiators which are based on unimolecular formation of radicals [73].

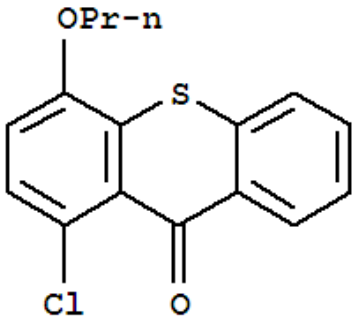

Figure 4-10 Molecular structure for 1-chloro-4-propoxythioxanthone

In order to calculate the single and two-photon absorption cross section of the photosensitizer, absorbance at different concentrations was measured for *1-chloro-4-propoxythioxanthone* using a UV/Vis Spectrometer Lambda Bio 10 (Perkin Elmer). A stock solution of *1-chloro-4-propoxythioxanthone* (0.1M) was prepared in ethanol. By diluting the stock solution, different concentrations of the photoinitiator were obtained and were exposed to the light source in a 10mm cuvette. The spectrum of the photoinitiator shows that the absorbance of the material increases with increasing concentration and the peak absorbances are at 313nm and 385nm wavelength as shown in Figure 4-11.

The molar extinction coefficient ε was calculated to be 2870 $M^{-1}cm^{-1}$ from the gradient of the graph drawn between absorbance and molar concentrations at 400nm wavelength as shown in Figure 4-12.

The appearance of several absorption peaks or shoulders for a given photosensitizer is common and may depends on the solvent used as has appeared in Figure 4-11 where the solvent is ethanol.

The photoinitiator *1-chloro-4-propoxythioxanthone* was added to *Ethoxylated Bis Phenol A Dimethacrylate (EO=6)* and 0.1M solution was prepared. The solution was exposed to the femtosecond Ti: Sapphire laser source in a 10mm cuvette to analyse the ability to initiate polymerisation of the monomer used. No polymerization was observed when Thioxanthone derivative was used as photoinitiator. This shows that *1-chloro-4-propoxythioxanthone* is not an efficient initiator in the absence of a co-initiator.

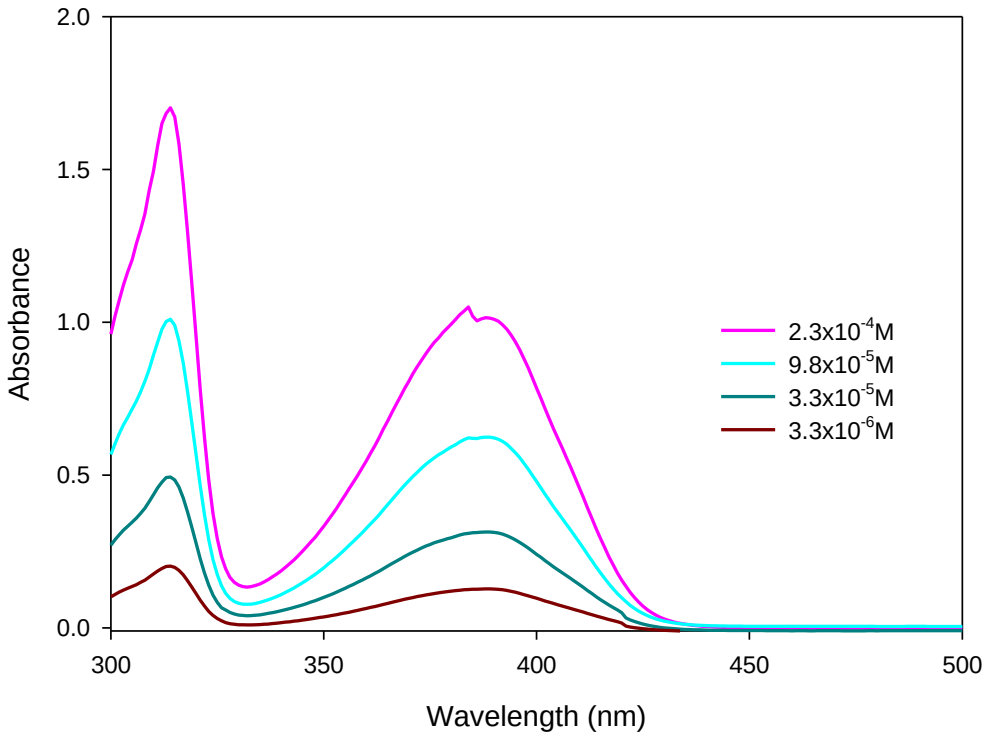

Figure 4-11. Absorbance spectra of 1-chloro-4-propoxythioxanthone in ethanol. Figure shows absorbance at different concentration.

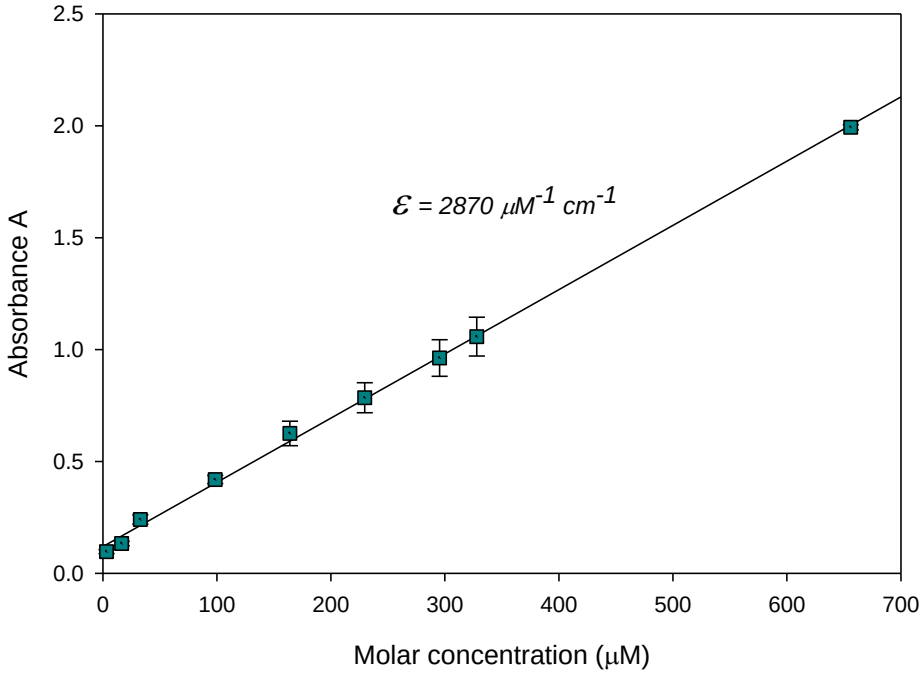

Figure 4-12 Graph shows molar absorption coefficient ε for 1-chloro-4-propoxythioxanthone at 400nm wavelength.

4.2 Single photon absorption cross section measurements

Single photon absorption cross-sections, σ, can be calculated from the molar absorption coefficient ε, as they are related via the Avogadro's constant N_A (number of molecules per Mole) [74].

$$\sigma = 1000 \ln(10) \frac{\varepsilon}{N_A}$$

Using Beer Lambert's law, the above relation can be established where the amount of light, dI absorbed per thickness dx is proportional to the effective cross-section for absorption per molecule σ and number of light absorbing molecules n present per cm^3.

$$\frac{dI}{dx} = -I \sigma n \qquad 4.4$$

$$\frac{dI}{I} = -\sigma n \, dx$$

$$\int_{I_o}^{I} \frac{dI}{I} = -\sigma n \int_0^d dx$$

$$\ln I - \ln I_o = -\sigma n d$$

$$\ln \frac{I}{I_o} = -\sigma n d$$

$$\ln \frac{I_o}{I} = \sigma n d$$

As from equation 4.3

$$\log \frac{I_o}{I} = A = \varepsilon c d$$

Therefore the equation can be written as

$$2.303 \log \frac{I_o}{I} = \sigma n d$$

And

$$2.303\, \varepsilon c d = \sigma n d$$

Therefore

$$\sigma = \frac{2.303 \varepsilon c}{n} \qquad 4.5$$

n is the number of light absorbing molecules/cm^3 and can be written as

$$n = \frac{N_A c}{10^3}$$

Substituting the value of n in equation 4.5 the absorption cross section can be calculated using the molar absorption coefficient ε which is related via Avogadro's number N_A and now can be written as

$$\sigma = 3.82 \times 10^{-21} \varepsilon \ (\text{cm}^2\ \text{molecule}^{-1}) \qquad 4.6$$

4.3 Two-photon absorption cross-section measurements

Two-photon absorption is a second-order process, several orders of magnitude weaker than single photon absorption. It is a non-linear process and is only significant at high irradiance level such as available from picosecond and femtosecond duration lasers.

The method of perturbation theory can be applied whenever there is weak interaction of light and molecules. Using this approach the cross section for single photon absorption can be estimated based on quantum mechanical perturbation theory as applied to multi photon ionisation. Using this, the ionisation rate per molecule is given as [75]

$$U = \left(\frac{V_i}{2\,\pi\,h\,\omega}\right)^{\frac{3}{2}} \left(\frac{e^2E^2}{8\,m\,\omega^2\,V_i}\right)^n \qquad 4.7$$

where ω is the angular frequency of the laser radiation, V_i is the ionisation potential of the fluorophore used, E is the perturbing electric field strength of the radiation felt by the fluorophore and m is mass of the excited electron. For two-photon absorption process the value of n is 2 as n indicates the order of multi photon process.

The irradiance of the beam I, can be related to the electric field E using $I = \varepsilon_o c E^2$ where ε_o is the permittivity of free space and c is the velocity of light. Substituting this relation in the above equation we get:

$$U = \left(\frac{V_i}{2\,\pi\,h\,\omega}\right)^{3/2} \left(\frac{e^2I}{8\,c\,\varepsilon_o m\,\omega^2 V_i}\right)^n \qquad 4.8$$

Making use of equation 4.8, an effective two-photon absorption cross section δ can be calculated taking $n=2$ and assuming that excitation to the real level is similar to the excitation above the ionisation limit. As the process involves the absorption of two photons, the ionisation potential $V_i = 2h\nu$ and using a Ti: Sapphire femtosecond laser at λ=800nm, the energy of a single photon $h\nu$= 2.4x10^{-19}J and ω=2.3x10^{15} rad/s. By substituting these values the ionisation rate per molecule U can be written as

$$U = 1.7 \times 10^{-21} I^2 \qquad 4.9$$

Where I is the irradiance of the laser radiation and has units of W/m^2. Equation 4.9 shows that the ionization/excitation rate is proportional to the square of radiation intensity. Equation 4.9 can be further modified and by introducing photon arrival rate $P = I/h\nu$, it can be written as

$$U = 1.7 \times 10^{-21} (h\nu)^2 P^2 \qquad 4.10$$

Substituting the value of $h\nu = 2.4x10^{-19}$J at 800nm wavelength, we get

$$U = \delta_{2a} P^2 \qquad 4.11$$

From the above equation the value of δ_{2a} calculated is $1x10^{-50}cm^4s$. This value is in close approximation with the experimentally measured value of two-photon absorption cross sections using different techniques for a variety of molecules. It is often convenient to introduce units named after Goeppert-Mayer where 1 GM is 10^{-50} cm^4 s $photon^{-1}$.

4.3.1 Techniques

Several techniques have been used to determine the two-photon excitation cross sections of various materials for over two decades [76]. Two-photon excited fluorescence (TPEF), nonlinear transmission (NLT), white-light continuum pump–probe technique and z-scan techniques are few of the commonly used methods.

Various studies reveal that two photon excited fluorescence is essentially identical with that found for one photon excited fluorescence. A relatively simple method for measuring the values of two-photon absorption cross sections has been used based on comparing the intensity ratios of one photon excited fluorescence to two photon excited fluorescence. By using low laser power the decomposition of the fluorophore is reduced and the accuracy of the two-photon absorption measurement increases [25]. As compared to other techniques i.e., the Z-scan method, this technique is highly sensitive however controversy exist about the determination of the collection efficiency and fluorescence quantum yield [31]. This difficulty can be overcome if the measurement for two-photon absorption cross section is based on the comparison of one-photon excited fluorescence to two photon excited fluorescence under same physical and geometrical arrangement using same optical system [25].

In this study the two-photon absorption cross sections of photoinitiators *4, 4'-Bis (diethylamino) benzophenon* and *1-chloro-4-propoxythioxanthone* have been determined by comparing the amplitude of the fluorescence of a sample under one and two photon excitation using a mode locked Ti: sapphire laser. The second harmonic of this laser was used as the source of one photon excitation.

This makes the present study more simple and efficient for two photon excitation without strong beam focusing.

As the two-photon absorption cross section of a molecule is much smaller than that for one-photon absorption, direct measurement is still difficult. For the measurement of two-photon absorption cross sections, a sample with high concentration is required due to its small efficiency and the emitted fluorescence may be susceptible to self absorption [25].

Following the approach of Song et al [25] we can develop a formulation that will allow measurement of the two-photon absorption cross-section by quantifying the intensity ratio of the single and two-photon induced fluorescence signals. This method is outlined below.

The average excitation rate per molecule per second for a pulse train delivered at a pulse repetition rate of f with each pulse of duration τ is given by

$$\mathrm{E_{2p}} = \mathrm{U\,f\,\tau} \qquad 4.12$$

$$\mathrm{E_{2p}} = 1.7 \times 10^{-21} \mathrm{I^2 f \tau}$$

$$\mathrm{E_{2p}} = 1.7 \times 10^{-21} \left(\frac{\mathrm{F_o}}{\tau}\right)^2 \mathrm{f\tau}$$

$$\mathrm{E_{2p}} = 1.7 \times 10^{-21} < I >< \mathrm{I_p} > \qquad 4.13$$

where $< \mathrm{I_p} > = \mathrm{F_o}/\tau$ is the peak power of an individual pulse in the train and $< \mathrm{I} > = \mathrm{f\,F_o}$ is the average beam irradiance.

The excitation rate per molecule per second at an average irradiance $< \mathrm{I} >$ for one-photon absorption cross section σ in a single photon process can be written as

$$\mathrm{E_{1p}} = \sigma \frac{<I>}{\mathrm{h}\,\nu'} \qquad 4.14$$

where $h\nu' = 2h\nu$ is the photon energy required for the excitation of a molecule by single photon absorption. At this stage it is informative to consider what the magnitude of the ratio of equation 4.13 and 4.14 is likely to be. Substituting the value of a typical molecular cross section σ = $2\text{x}10^{-20}\text{m}^2$/molecule ($10^{-18}\text{cm}^2$/molecule), and considering a typical un-focussed irradiance from the

femtosecond laser of ~ 10^{15} Wm^{-2} then E_{2p}/E_{1p} ~$5x10^{-5}$. Therefore, it can be seen that experimentally we should expect that the emission spectra excited by 400nm pulses will be easier to collect than the same spectra excited by two-800nm photons as they will be of the order 10^5 times brighter. By focussing, this can be improved upon. For example taking the 4mm beam size down to 0.04mm, increases the predicted ratio by 10^4 but it is likely that breakdown of the material will begin to occur and limit the irradiance that can be used.

Using equation 4.13 and 4.14 the two-photon absorption cross section δ (cm^4 s $photon^{-1}$ $molecule^{-1}$) can be calculated. The single-photon excitation rate as given in equation 4.14 is $E_{1p} = \sigma < I_1 > /(h\nu)_{1p}$ where σ is absorption cross section (cm^{-2} $molecule^{-1}$), $< I_1 >$ is the mean irradiance and $(h\nu)_{1p}$ is single photon energy at 400nm. The subscript 1 corresponds to a one photon process and 2 to the two photon process. If quantum efficiency for fluorescence is Φ_1, and the geometrical factor due to collection geometry is g_1, then the single photon emission fluorescence F_{1p} is given by

$$F_{1p} = \Phi_1 E_{1p} g_1$$

$$F_{1p} = \sigma < I_1 > /(h\nu)_{1p}\, \Phi_1 g_1 \qquad 4.15$$

Using equation 4.13, the two-photon emission fluorescence signals can be written as

$$F_{2p} = \Phi_2 E_{2p}\, g_2$$

$$F_{2p} = \Phi_2\, U f \tau g_2$$

$$F_{2p} = \delta_{2a} P^2\, f \tau \Phi_2 g_2$$

$$F_{2p} = \delta_{2a} \left(\frac{I}{(h\nu)_{2p}}\right)^2 f \tau \Phi_2 g_2$$

$$F_{2p} = \delta_{2a} \left(\frac{1}{(h\nu)_{2p}}\right)^2 < I_2 >< I_{2p} > \Phi_2 g_2 \qquad 4.16$$

Here Φ_2 and g_2 are the quantum efficiency and geometrical factor for two-photon absorption and which are assumed to be the same as the single-photon values if the spectral recording geometrical conditions for the induced

fluorescence are kept constant. The mean irradiance is $< I_2 >$ and $< I_{2p} >$ is the peak irradiance with $(\mathrm{h}\nu)_{2\mathrm{p}}$ as the photon energy at 800nm wavelength. Comparing the two-photon emission signals in equation 4.16 to single photon emission in equation 4.15, we get

$$\frac{\mathrm{F_{2p}}}{\mathrm{F_{1p}}} = \frac{\delta_{2\mathrm{a}} <\mathrm{I_2}><\mathrm{I_{2p}}>}{\sigma<\mathrm{I_1}>/(h\nu)_{1\mathrm{p}}\,(\mathrm{h}\nu)^2_{2\mathrm{p}}} \qquad 4.17$$

Finally, in this approach from Song et al [25], rearranging equation 4.17 allows the two absorption cross section δ to be calculated from:

$$\delta_{2\mathrm{a}} = \frac{\sigma<\mathrm{I_1}>(\mathrm{h}\nu)^2_{2\mathrm{p}}}{(\mathrm{h}\nu)_{1\mathrm{p}}<\mathrm{I_2}><\mathrm{I_{2p}}>}\left(\frac{\mathrm{F_{2p}}}{\mathrm{F_{1p}}}\right) \qquad 4.18$$

Measurements were made of the two photon excited fluorescence amplitude at 800nm and single photon excitation fluorescence at 400nm under same geometrical conditions to give $\left(\frac{\mathrm{F_{2p}}}{\mathrm{F_{1p}}}\right)$ and the laser parameters were found from measurements of the time averaged power incident on the sample, pulse duration and repetition rate.

4.3.2 Confirmation of a two-photon process

The fluorescence of the material was found with the help of an Ocean Optics, HR2000CG-UV-NIR High Resolution spectrometer. The material was exposed in a cuvette to the laser source without focusing. The integration time was 10s and the peak intensity of the fluorescence was measured for different laser powers. A short pass filter was used to minimise saturation of the spectrometer by the laser excitation and to allow only the fluorescence of the material to reach the spectrometer. The material, EBPADMA with 1% concentration of photosensitizer 4, 4'-Bis (diethylamino) benzophenon, when exposed to the femtosecond laser of wavelength 800 nm, shows blue fluorescence (i.e. at a shorter wavelength than the excitation beam) which indicates multi-photon absorption is likely to be taking place. The peak of the intensity of the fluorescence depends upon the laser power. The laser excitation can be seen in Figure 4-13 along with two-photon absorption fluorescence.

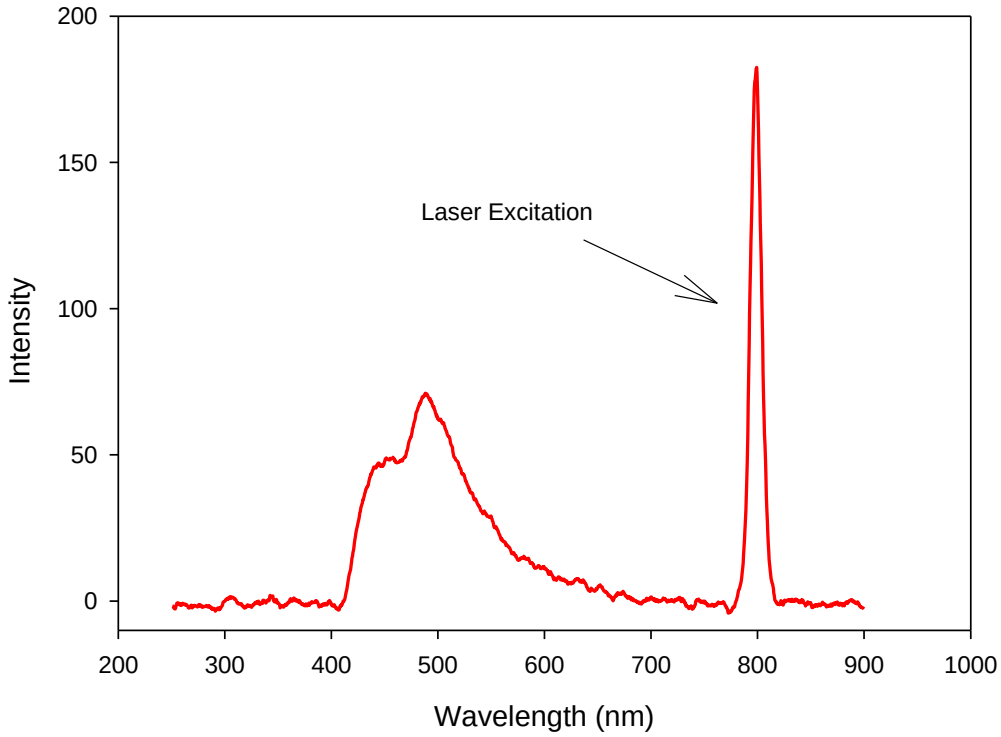

Figure 4-13 Emission spectrum showing the fluorescence emission from EBPADMA with 1% concentration of photosensitizer 4, 4'-Bis (diethylamino) benzophenon. Incomplete blocking of the laser excitation can be seen around 800nm. The laser excitation power was 680mW with pulse duration of 180fs, pulse repetition rate 1 kHz.

It is obvious from the two-photon absorption fluorescence spectra that the maximum emission is near 500nm wavelength. At different laser powers the peak intensity of the curve was found to change in height. High laser power is required to excite a fluorophore-containing specimen therefore with increasing laser power the fluorescence intensity *I* increases giving a relation

$$I = CP^{n}$$

so that

$$\log I = n\log P + \log C$$

A plot of log*I* as a function of log*P* will yield a gradient whose value will be equal to n and can be used to verify the order of the interaction. Here, the expectation is that n=2 indicative of a two-photon process. Therefore for two-photon absorption process, the above relation can be written as

$$\frac{\log I}{\log P} = 2 \qquad 4.19$$

The power-squared dependence of two-photon excited fluorescence for photoinitiator *4, 4'-Bis(diethylamino)benzophenon* and *1-chloro-4-propoxythioxanthone* was determined in this study at 800nm excitation wavelength. The emitted fluorescence was recorded at different laser power using the spectrometer as mentioned earlier. In both cases nearly perfect power squared dependence of two-photon-excited fluorescence was recorded. According to the above relation two-photon-excited fluorescence should obey the square-law dependence on the excitation intensity. However slight deviations from the square-law dependence of two-photon-excited fluorescence can be observed due to stimulated emission, excited-state saturation and excited-state absorption [24]. Higher fluxes and long duration laser exposure may give rise to saturation effects or in some cases switching to cubic dependence as a result of three-photon excitation may be observed. In this study only data taken in the quadratic regime is included for the calculation of the two-photon absorption cross section.

The power dependence of the fluorescence detected at 500 nm was determined from a plot of the fluorescence signal peak versus the incident power as shown in Figure 4-14 for EBPADMA with 1% 4, 4'-Bis (diethylamino) benzophenon. Plotting the peak height of the fluorescence as a function of laser power reveals a power law dependence of order 2 showing that this is most likely a two-photon process. The gradient of the graph confirms the two-photon absorption process.

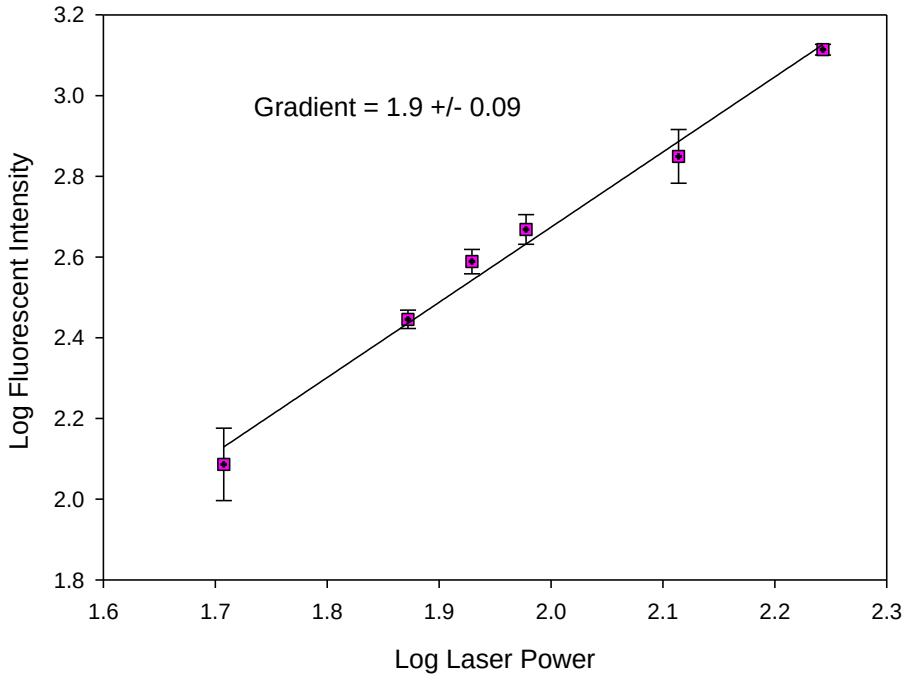

Figure 4-14 Log-log plot of the fluorescence emission of EBPADMA with 1% concentration of photosensitizer 4, 4'-Bis (diethylamino) benzophenon versus the incident power of the femtosecond laser.

A log-log plot of the emitted fluorescence versus incident laser power was also obtained for *1-chloro-4-propoxythioxanthone.* A sample containing $1.6x10^{-2}$M solution was exposed to 800nm wavelength laser light using femtosecond laser source with 146fs pulse duration at the repetition rate of 1kHz and average power of 650mW. The fluorescence emitted using 800nm irradiation was focused through a lens to optical fibre coupled spectrometer (USB 4000 Ocean optics) and fed to the computer via the fibre. The output of two photon excited fluorescence was recorded. The fluorescence intensity detected at 492nm was measured as a function of the excitation power and a log-log plot of the emitted fluorescence versus incident laser power was obtained. The gradient of the graph is approximately 2 which shows two-photon absorption processes and confirms power squared dependence.

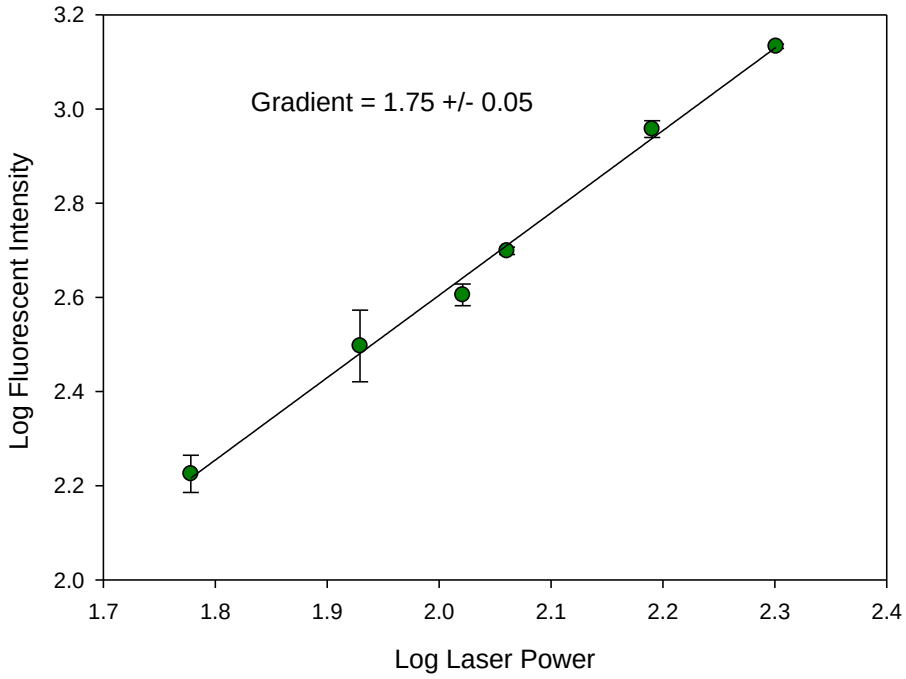

Figure 4-15 Log-log graph for two-photon absorption in *1-chloro-4-propoxythioxanthone* The linear fit to the data has a gradient of 1.75±0.05

The excitation intensity dependences of the two-photon fluorescence are shown in Figure 4-14 and Figure 4-15 with the plots on log–log scales. It is obvious that two-photon excited fluorescence obeys the square-law dependences, where the fitted slope for *4, 4'-Bis(diethylamino)benzophenon* is 1.9+/-0.09. This confirmed the quadratic dependence of the two photon excited fluorescence on the incident laser power as given in equation 4.19. While the fitted slope for that of *1-chloro-4-propoxythioxanthone* is 1.75±0.05 which might indicate square-law dependence together with other processes which have not been identified here. Significant deviation from the square law dependence of the two photon excited fluorescence has been observed due to various factors such as stimulated emission, excited state absorption, saturation, intensity dependent 2PE cross section, lack of correction for 1PE, etc [77].

4.3.3 Experimental arrangements and Methods

As stated earlier in this study a frequency doubling crystal was used to determine the two-photon absorption cross section of different photosensitizers therefore laser pulses of 800nm wavelength from a mode locked Ti: sapphire laser source were focused on a frequency doubling crystal for second harmonic

generation (400nm). The two-photon absorption cross section of the photosensitizer was measured by comparing single photon excited fluorescence and two photon excited fluorescence.

Upon exposure to laser pulses the fluorescence emitted from the sample during two photon excitation and one photon excitation are shown in Figure 4-16. The sample contained 1% by weight *4, 4'-Bis (diethylamino) benzophenon* dissolved in *Ethoxylated Bis Phenol A Dimethacrylate (EO=6).* The difference in single photon excitation and two photon excitation fluorescence is obvious. The 800nm wavelength laser pulses penetrate into the resin and the emitted fluorescence in the form of blue light spreads along the width of the cuvette. Due to deep penetration of the 800nm wavelength the fluorophore inside the cuvette absorb two photons and emit light in the visible region.

The fluorescence emission excited by 400nm wavelength is confined to a single point where the laser light strikes the surface and yellow resin can be seen in Figure 4-16 in the cuvette without fluorescence. The experimental apparatus is shown schematically in Figure 4-17.

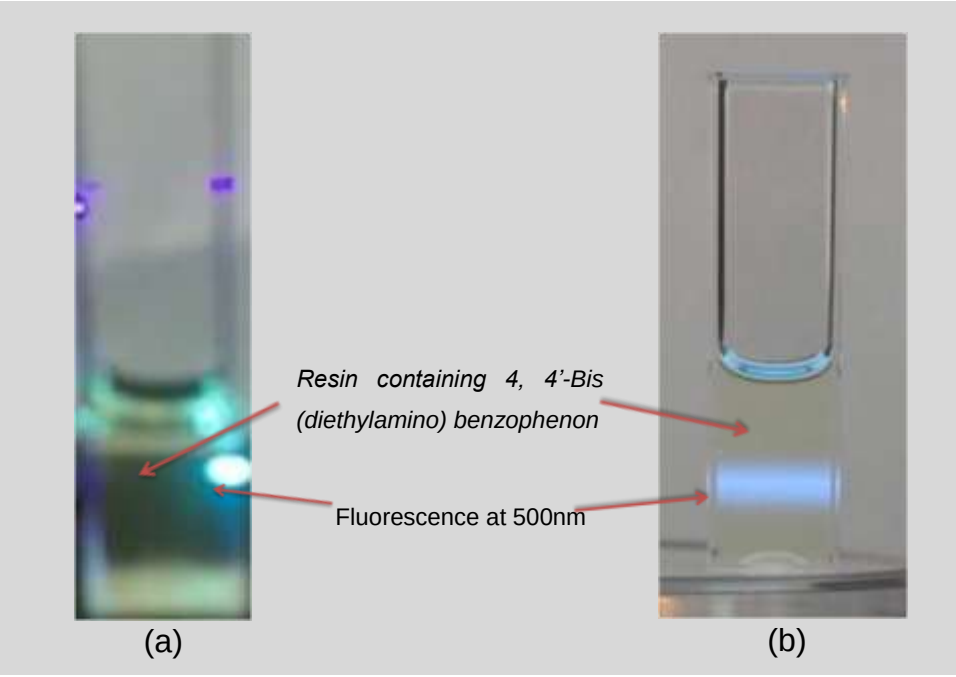

Figure 4-16 Shows (a) single photon absorption fluorescence when resin containing 4, 4'-Bis (diethylamino) benzophenon was exposed to 400nm femtosecond laser light. (b) Two-photon absorption fluorescence when resin containing 4, 4'-Bis (diethylamino) benzophenon was exposed to 800nm femtosecond laser light.

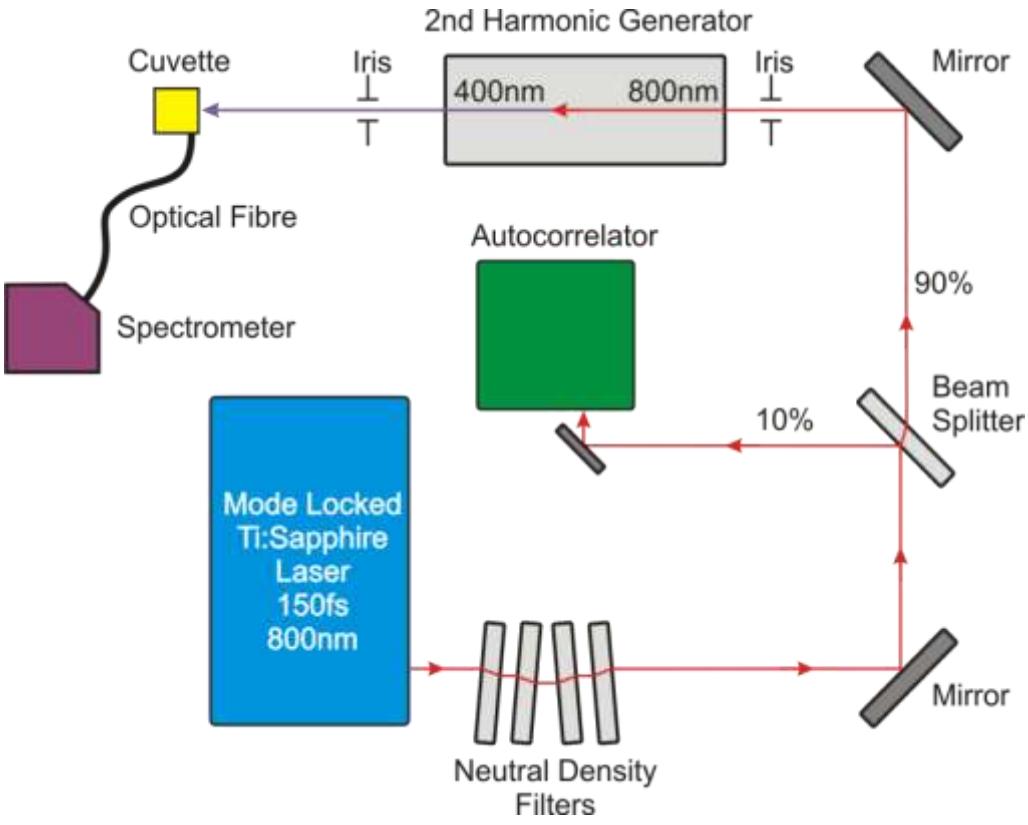

Figure 4-17 Schematic diagram showing experimental arrangement for the calculation of two-photon absorption cross-section

The sample solution with $3x10^{-3}$M was prepared by a successive dilution of the stock solution and was placed in a 10mm cuvette to obtain the fluorescence at 800 and 400nm wavelength. The laser beam was directed at the middle of a fused silica cuvette through irises of different diameter placed in front of the laser output to produce quasi uniform irradiance removing the extended wings of the Gaussian beam. The excitation beam size at the cuvette was restricted to 3mm diameter using a circular aperture. An iris of diameter 3mm was located at a distance of approximately 4cm from the centre of the cuvette containing the sample solution of *4, 4'-Bis (diethylamino) benzophenon* in ethanol with $3x10^{-3}$M concentration. The femtosecond laser beam with 800nm wavelength was allowed to fall on the cuvette containing the sample solution. The fluorescence produced using 800nm irradiation was focused through a lens to a fibre coupled spectrometer (USB 4000 Ocean optics) and data fed to the computer. The two

photon excited fluorescence spectrum was recorded. For the analysis of single photon excitation fluorescence, 400nm wavelength laser light was allowed to fall on the cuvette under the same geometrical and experimental conditions. Fluorescence spectra for single and double photon excitation were recorded, and their normalised fluorescence intensity for single photon (400nm) and two photon (800nm) pumping were plotted. The fluorescence intensity of the photosensitizer *4, 4'-Bis(diethylamino)benzophenon* and *1-chloro-4-propoxythioxanthone* was measured and compared for single photon excitation to two photo excitation. Using the equation 4.6 and equation 4.18 single photon and two-photon absorption cross section of photoinitiator, *1-chloro-4-propoxythioxanthone* in ethanol and *4, 4'-Bis(diethylamino)benzophenon* in ethanol, EBPADMA and ethyl acetate were calculated. When taking the ratio of the fluorescence peaks, account was taken of any changes to the integration time used for the spectrometer. This was necessary due to the much weaker emission when 800nm excitation was used.

A $3x10^{-3}$M solution of *4, 4'-Bis(diethylamino)benzophenon* in ethanol was exposed to laser light at 800nm wavelength and 400nm wavelength in a 10mm cuvette at 200mW and 415µW laser power respectively. The fluorescence intensities of the photoinitiator were measured and compared; one-photon excitation to two-photon excitation. Recorded fluorescence spectra for single and double photon excitation are shown in Figure 4-18, while normalised fluorescence intensity for single photon (400nm) and two photon (800nm) pumping is shown in Figure 4-19. A peak fluorescence signal of approximately 1793 counts at 200mW laser power was recorded over a 2s integration time. With 215µW laser power at 400nm wavelength, a count of approximately 4537 was obtained with 2s integration time. Making use of equation 4.6, the single photon absorption cross section was calculated from the molar absorption coefficient ε as $43.4X10^{-18}$ cm^2 $molecule^{-1}$. The two-photon absorption cross section was calculated by comparing fluorescence intensity in equation 4.18 and was found to be $14X10^{-50}$ cm^4 s photon $^{-1}$. The main peak of the fluorescence intensity is centred at 494nm wavelength.

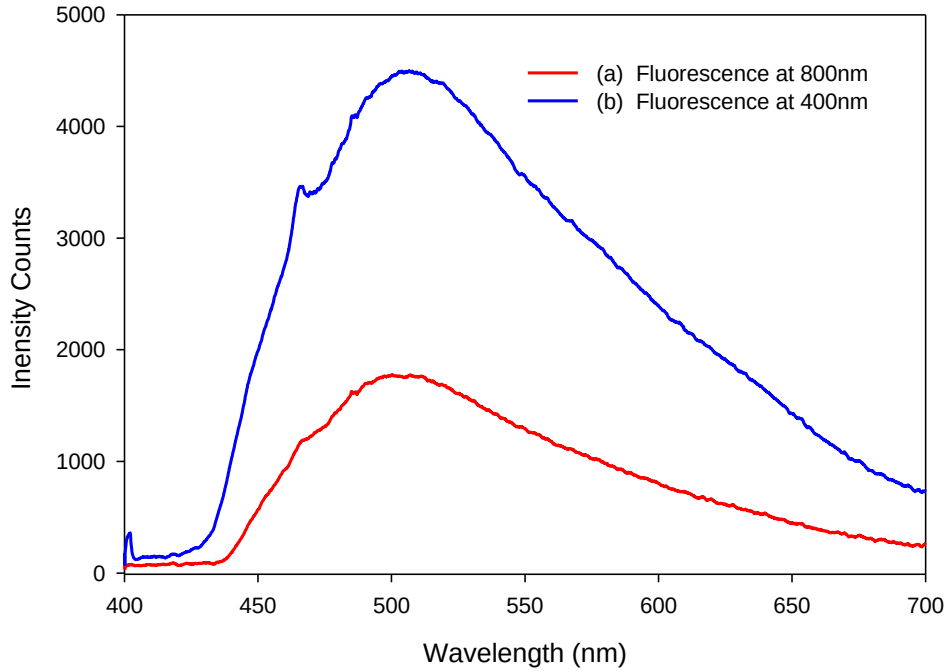

Figure 4-18 Fluorescence curve for *4, 4'*-Bis(diethylamino)benzophenon in ethanol in the form of main peak centred at 500nm. Laser parameters are (a) 800nm wavelength at 200mW laser power and (b) 400nm wavelength at 215µW laser power.

Excitation of the photosensitizer at different wavelengths (800nm, 400nm) does not change the emission profile but only produces variations in fluorescence emission intensity. This can be seen from the normalised fluorescence curve shown in Figure 4-19. The fluorescence emission spectra for single and two photon excitation are similar irrespective of the excitation wavelength. This is due to the relaxation of the fluorophore which upon excitation to the high energy level quickly dissipates its energy in about 10^{-12} s and returns to the lowest vibrational level of S_1 [74].

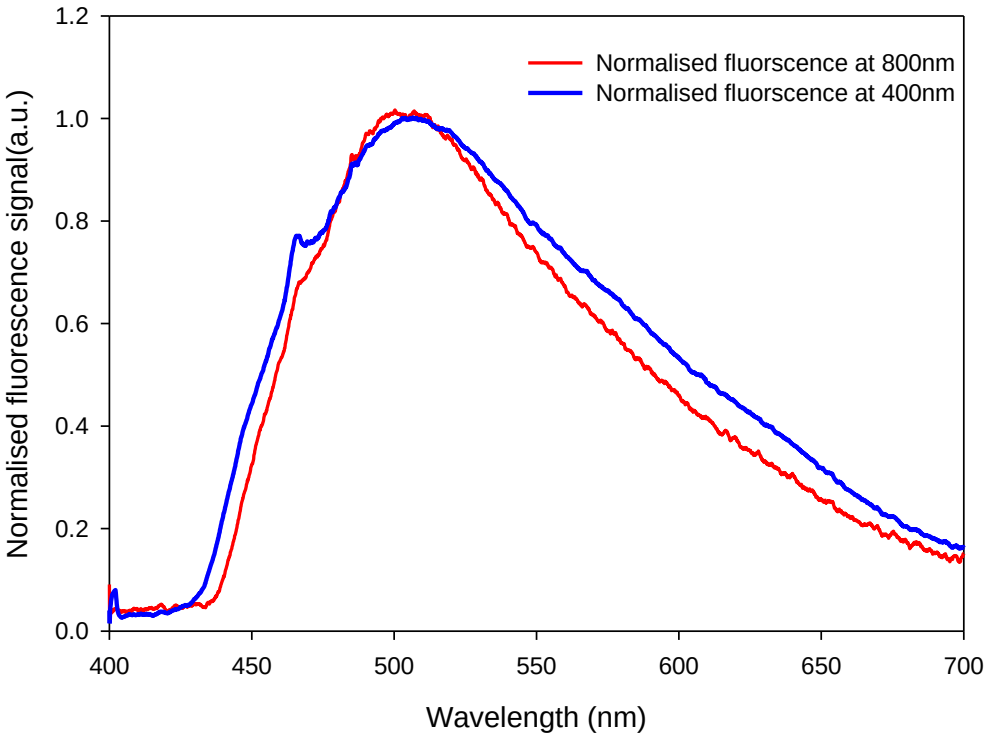

Figure 4-19 Normalised excited fluorescence spectra for *4, 4'-*Bis(diethylamino)benzophenon in Ethanol using femtosecond laser pulse trains at single photon excitation(400nm) and two photon excitation(800nm).

In order to find one-photon and two-photon absorption cross sections of *4, 4'-Bis(diethylamino)benzophenon* in *Ethoxylated Bis Phenol A Dimethacrylate* (EO=6), a solution with the same molar concentration($3x10^{-3}$M) was exposed to the femtosecond laser beam at 800nm wavelength and at 400nm wavelength using harmonic generator with 200mW and 215µW laser power respectively. The fluorescence spectra for single and two-photon absorption were recorded and are shown in Figure 4-20 and its normalised fluorescence spectrum is shown in Figure 4-21. A peak fluorescence signal of approximately 3902 counts at 200mW laser power was recorded over a 2s integration time. With 215µW laser power at 400nm wavelength, a count of approximately 49760 was obtained with 2s integration time. The one-photon-absorption coefficient σ on the basis of equation 4.6 from the molar absorption of coefficient of *4, 4'-Bis (diethylamino)benzophenon* was determined to be 17.0 x $10^{-18}$$cm^2$/(molecule) and the two-photon absorption cross section was calculated as 1X10^{-50} cm^4 s photon $^{-1}$.

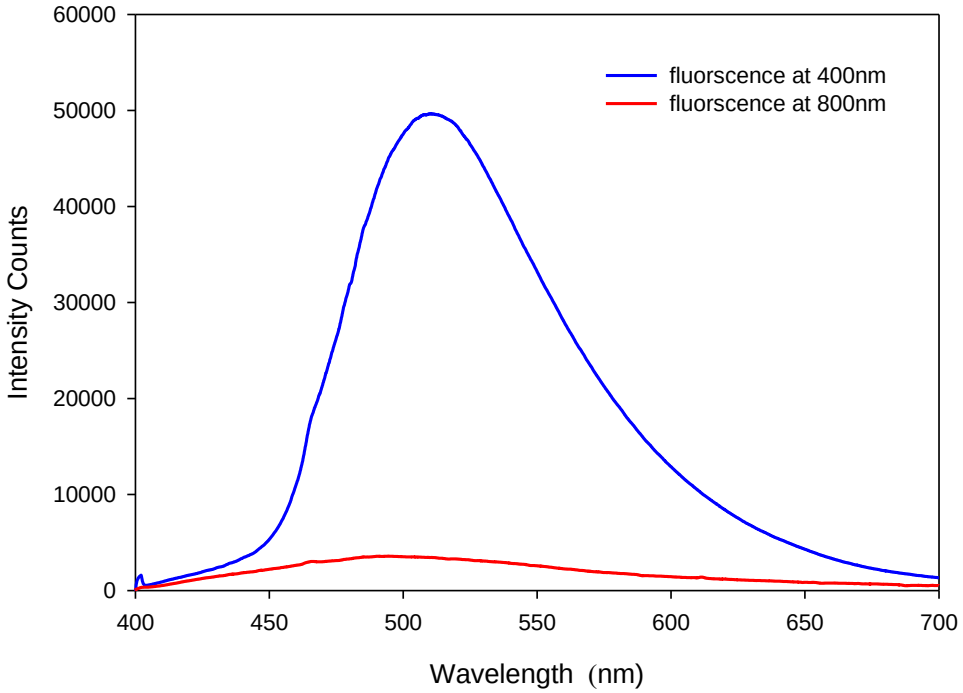

Figure 4-20 Fluorescence curve for 4,4'-Bis(diethylamino)benzophenon in EBPADMA at 215µW laser power when exposed to 400nm and at 200mW laser power when exposed to 800nm wavelength. Wavelength of the fluorescence emitted in the form of main peak centred around 500nm.

The main peak of the fluorescence is centred nearly at 500nm wavelength. Although the fluorescence curve for one-photon excited fluorescence and two-photon excited fluorescence of *4, 4'-Bis(diethylamino)benzophenon* in Ethanol coincide quite well, it is not the case for *4, 4'-Bis(diethylamino)benzophenon* in EBPADMA solvent. Peak signals of one-photon excited fluorescence and two-photon excited fluorescence do not exactly coincide. This indicates that one-photon and two-photon absorption may populate different excited states on account of different selection rules involved and the subsequent relaxation may take place to a slightly different lower energy level. Wavelengths of the peak signals emitted due to one-photon and two-photon excited fluorescence lie in the range of 492nm to 510nm and therefore blue fluorescence was observed in both cases.

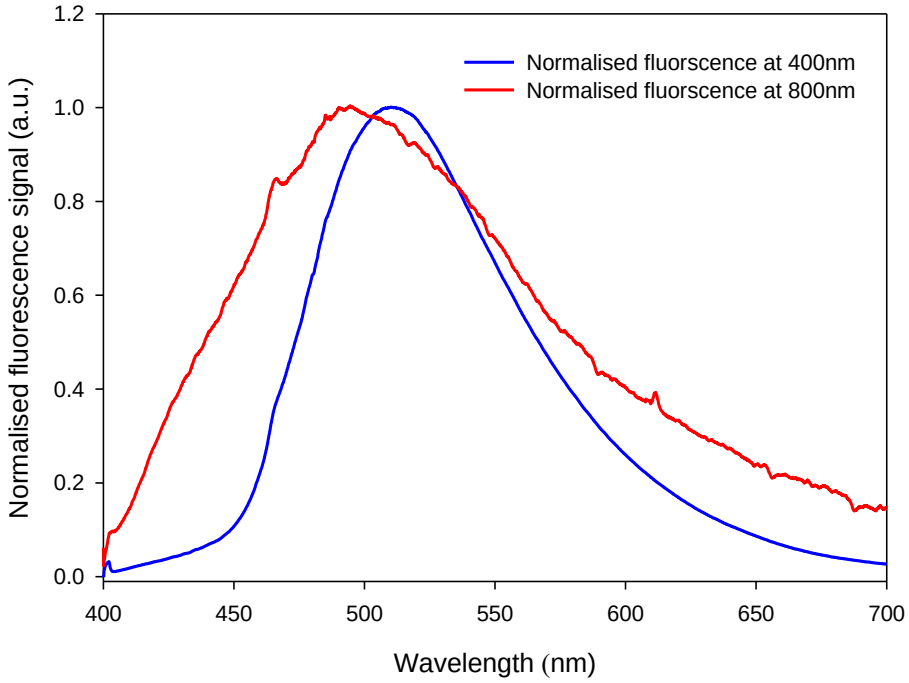

Figure 4-21 Normalised excited fluorescence spectra for *4, 4'*-Bis(diethylamino)benzophenon in EBPADMA using femtosecond laser pulse trains at single photon excitation (400nm) and two photon excitation(800nm).

Also ethyl acetate was used as solvent to find one and two-photon absorption cross sections for *4, 4'*-Bis(diethylamino)benzophenon. A $3x10^{-3}$M solution was exposed in a 10mm quartz cuvette to 800nm wavelength at 200mW laser power and to 400nm wavelength at 215µW laser power as above. The fluorescence at 800nm and 400nm wavelength were recorded and compared as shown in Figure 4-22 and Figure 4-23. A peak fluorescence signal of approximately 996 counts at 200mW laser power was recorded over a 2s integration time at 800nm wavelength. With 215µW laser power at 400nm wavelength, a count of approximately 14714 was obtained with 2s integration time. The peak intensity of the emitted fluorescence coincides at 466nm wavelength. The single and two-photon absorption cross sections were calculated as $0.25X10^{-18}$ cm^2 $molecule^{-1}$ and $1.2X10^{-52}$ cm^4 s $photon^{-1}$respectively.

Solvent effects on the absorption and fluorescence spectra of the photoinitiator *4, 4'*-Bis(diethylamino)benzophenon were compared. Comparisons of the

absorption and fluorescence spectra using different solvents indicate the influence of solvent on the chemical and physical properties of the solute. Solute-solvent interaction in the ground and excited states induce changes in electronic transitions of the solute. This is significant as from these effects it can be seen that excited state dipole moments are greater than those in the ground state and indicate a strong intramolecular charge transfer character of solute in the excited state [78].

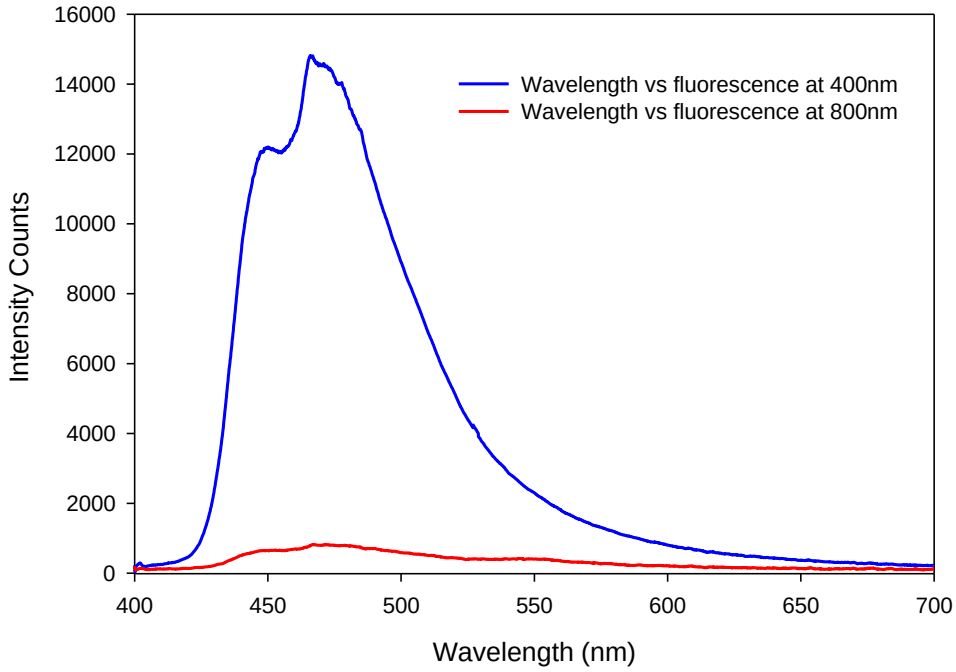

Figure 4-22 Fluorescence curve for *4, 4'*-Bis(diethylamino)benzophenon in ethyl acetate at 215µW when exposed to 400nm wavelength and fluorescence curve for *4, 4'*-Bis(diethylamino)benzophenon at 800nm at 200mW wavelength in the form of main peak centred at 466nm.

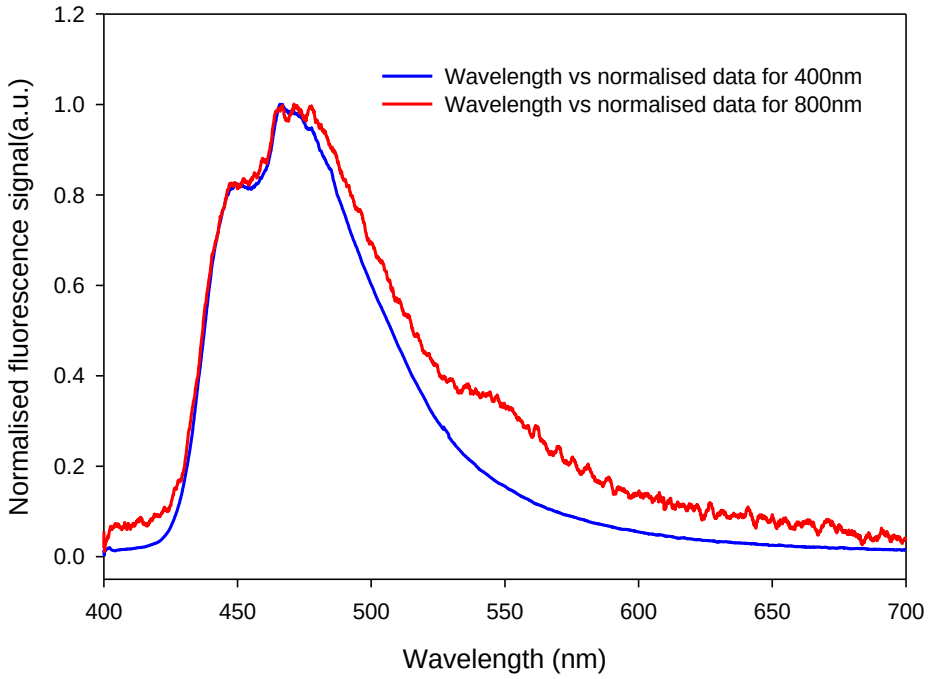

Figure 4-23 Normalised fluorescence spectra for *4, 4'*-Bis(diethylamino)benzophenon in Ethyl acetate excited using femtosecond laser pulse trains at single photon excitation (400nm) and two photon excitation (800nm).

The two-photon absorption cross section was also calculated for *1-chloro-4-propoxythioxanthone* and the power-squared dependence of two-photon excited fluorescence was determined. The sample solution of the photosensitizer with $1.6x10^{-2}$M concentration in ethanol was exposed in 10mm cuvette in front of the femtosecond laser with 650mW average power and 146fs pulse duration with a repetition rate of 1 kHz. The laser power was filtered and only 200mW at 800nm or 381µW at 400nm was allowed to fall on the cuvette passing through an iris of 3mm without focussing. The result is shown in Figure 4-24 and the normalised data in Figure 4-25. The fluorescence spectra excited at 800nm and 400nm wavelength both peak at 490nm. The single-photon absorption cross section was calculated from the value of molar absorption constant as $11X10^{-18}$ cm^2 $molecule^{-1}$ and the two-photon absorption cross section was calculated to be $7x10^{-50}$ cm^4 s $photon^{-1}$.

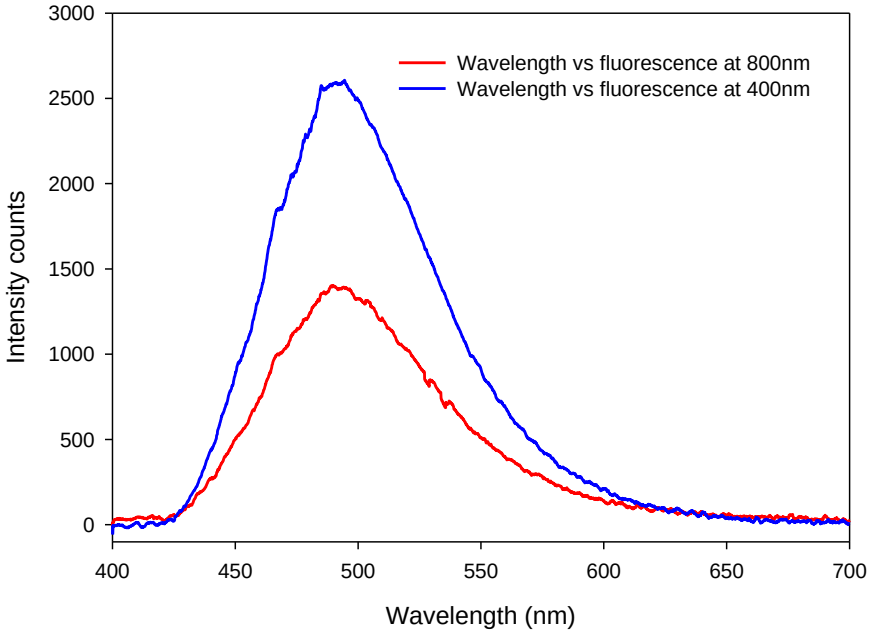

Figure 4-24 Fluorescence spectra for *1-chloro-4-propoxythioxanthone* in Ethanol at 400 and 800nm wavelength in the form of main peak centred at 490nm.

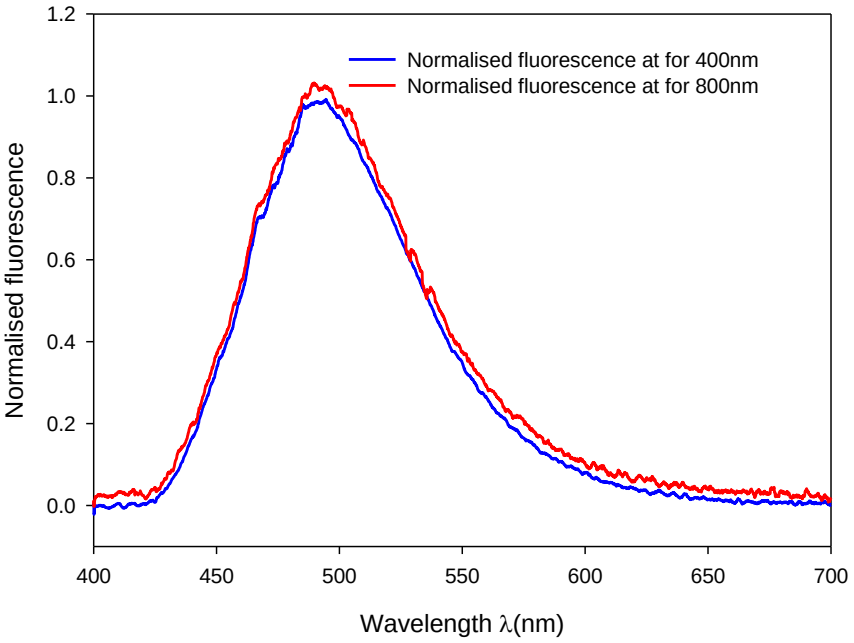

Figure 4-25 Normalised fluorescence spectra for *1-chloro-4-propoxythioxanthone* in Ethanol excited using femtosecond laser pulse trains at single-photon excitation (400nm) and two-photon excitation (800nm).

In addition, the system was checked for systematic errors by measuring the absorption cross-sections of a well characterised dye. In this case, Fluorescein was used as the standard sample. The sample solution for Fluorescein ($1x10^{-6}$M) was prepared in 20mM Potassium Phosphate buffer at pH 11. The TPA cross section of Fluorescein was calculated by comparing the fluorescence intensities and the result obtained was compared with the two-photon absorption cross section δ determined by Song *et al* [25] and Xu *et al* [24]. Song *et al* measured the two-photon absorption cross section for Fluorescein as $5.4x10^{-49}$ cm^4 s $photon^{-1}$ while Xu *et al* measured as $3.8x10^{-49}$ cm^4 s $photon^{-1}$ at 800nm wavelength laser source. In the present study the two-photon absorption cross section δ for Fluorescein was measured as $3.04x10^{-49}$ cm^4 s $photon^{-1}$ which is close to the previously calculated values.

4.3.4 Summary of cross-section results

A femtosecond system laser with pulse duration of 146fs at the rate of 1kHz has been used to investigate single and two-photon absorption cross section of photoinitiators *4, 4'-Bis (diethylamino) benzophenon* and *1-chloro-4-propoxythioxanthone* using different solvents. The one-photon and two-photon absorption cross section have been determined on the basis of equation 4.6 and 4.18. The derived one-photon and two-photon absorption cross sections for photoinitiators using different solvents are presented as a summary in Table 4.1. The one-photon absorption cross-section, for the 3×10^{-3} molar solution was based on the measurement of molar absorption coefficient ε and was found to be $43.4X10^{-18}$ cm^2 $molecule^{-1}$for *4, 4'-Bis (diethylamino) benzophenon* and $11X10^{-18}$ cm^2 $molecule^{-1}$ for *1-chloro-4-propoxythioxanthone* at 400nm.The molar absorbtivity ε = $11366M^{-1}cm^{-1}$ was determined for *4, 4'-Bis (diethylamino) benzophenon* in ethanol while for *1-chloro-4-propoxythioxanthone* it was found to be $2870M^{-1}cm^{-1}$. A value for the two-photon absorption cross-section $\delta_{2a} = 14\times10^{-50}$ cm^4 s $photon^{-1}$ and $\delta_{2a} = 7\times10^{-50}$ cm^4 s $photon^{-1}$ for *4, 4'-Bis (diethylamino) benzophenon* and *1-chloro-4-propoxythioxanthone* in ethanol was derived by comparing the fluorescence signals excited by 800nm and 400nm wavelengths respectively. The two-photon absorption cross section for photoinitiator *4, 4'-Bis (diethylamino) benzophenon* in ethanol was found to be twice that of *1-chloro-4-propoxythioxanthone*. Single and two-photon absorption cross sections of *4, 4'-Bis (diethylamino) benzophenon* were further

investigated using ethyl acetate and *Ethoxylated Bis Phenol A Dimethacrylate* (EBPADMA) as solvent. The two-photon absorption cross section δ_{2a} for the photoinitiator was found to be $1.2X10^{-52}$ cm^4 s $photon^{-1}$ in the ethyl acetate using single photon absorption cross section $\sigma = 0.25x10^{-18}$ cm^2 $molecule^{-1}$ and molar absorption constant $\varepsilon = 65.4M^{-1}cm^{-1}$. When *Ethoxylated Bis Phenol A Dimethacrylate* (EBPADMA) was used as the solvent for *4, 4'-Bis (diethylamino) benzophenon*, the two-photon absorption was measured to be $\delta_{2a} = 1\times10^{-50}$ cm^4 s $photon^{-1}$ based on the one-photon absorption cross section $\sigma = 17x10^{-18}cm^2molecule^{-1}$ and molar absorbtivity $\varepsilon = 4450M^{-1}cm^{-1}$. In spite of the low two-photon absorption cross section of *4, 4'-Bis (diethylamino) benzophenon* it was found to polymerize the liquid monomer *Ethoxylated Bis Phenol A Dimethacrylate* as will be shown in the next section. By tailoring the optical system for a photoinitiator with such a weak two-photon absorption cross section, 3D structures can be fabricated using two-photon absorption polymerization processes over large (deep) ranges giving rapid material structuring when resolution requirements can be relaxed (as is the case for cell scaffolds).

Table 4-1 showing the photoinitiators used in this study together with its concentration, single and two-photon absorption cross sections and wavelength of the excited fluorescence.

Photoinitiator	*4,4'-Bis(diethylamino)benzophenon*	*1-chloro-4-propoxythioxanthone*
Solvent	*Ethanol, EBPADMA* and *Ethyl acetate*	*Ethanol*
Concentration	*$3x10^{-3}$ M*	*$16x10^{-3}$ M*
Molar absorbtivity ε	*11366 $M^{-1}cm^{-1}$ in Ethanol* *4450$M^{-1}cm^{-1}$ in EBPADMA* *65.4$M^{-1}cm^{-1}$ in ethyl acetate*	*2870$M^{-1}cm^{-1}$*
One photon cross section	*43.4 x 10^{-18} cm^2 $molecule^{-1}$ in Ethanol* *17 x 10^{-18} cm^2 $molecule^{-1}$ in EBPADMA* *0.25 x 10^{-18} cm^2 $molecule^{-1}$ in Ethyl acetate*	*11 x 10^{-18} cm^2 $molecule^{-1}$*
Two photon cross section	*14 x 10^{-50} cm^4 s photon $^{-1}$ in Ethanol* *1 x 10^{-50} cm^4 s photon $^{-1}$ in EBPADMA* *1.2 x 10^{-52} cm^4 s photon $^{-1}$ in Ethyl acetate*	*7 x 10^{-50} cm^4 s photon $^{-1}$*
Excited fluorescence Wavelength	*494nm in Ethanol* *492nm to 510nm in EBPADMA* *466nm in Ethyl acetate*	*490nm*

4.4 Scaffold formation

Tissue engineering approaches are currently being extensively investigated to develop biological substitutes that restore, maintain, or improve tissue function or a whole organ. A matter of considerable interest is the creation and structuring of biocompatible materials which can be used as the mechanical framework for attachment of cells and proliferation to enable the integration of living cells [42]. Metals, ceramics, synthetic polymers, and biopolymers can be selected as scaffold materials that are not rejected by the body upon implantation. Creating an engineered tissue requires the identification of a suitable material to fabricate a scaffold for a specific tissue engineering application. Also structuring of the scaffold material and cell seeding into the scaffold for cell culturing is required [43].

Many different techniques such as fused deposition modeling, 3D printing, stereo lithography, and methods that use porogens, phase separation, gas foaming, or supercritical fluid to form less ordered pore structures have been developed to fabricate scaffolds for tissue engineering applications [42].

The distinction between the two-photon polymerisation (TPP) and stereo lithography (SL) technologies is the use of infra red laser pulses for TPP while in the case of SL, UV laser radiation is used for curing photosensitive materials. Polymerisation processes can be initiated in multi photon (IR) or single photon (UV) absorption. Photosensitive materials are usually transparent in the IR region and highly absorptive in the UV range. Photo-polymerisation in the IR region can be initiated by focusing laser pulses within the volume of the liquid to fabricate 3D structures whereas in the case of UV laser radiation, due to single photon absorption, polymerization usually occurs at the surface. Therefore SL is considered as a planar technology with layer by layer polymerisation steps for the fabrication of 3D structures while TPP is a truly high resolution 3D technology [79].

Photo-polymerization initiated by a two-photon absorption process is used in the present study to fabricate three dimensional (3D) micrometer sized structures and to rapid-prototype tissue engineering scaffolds. Two-photon polymerization is an effective technique for the fabrication of complex polymeric 3D micro/nano features using ultrashort pulses from a NIR laser source. The use of 3D laser nonlinear lithography techniques based on the phenomenon of two-photon polymerization (TPP) process has been demonstrated for the fabrication of 3D structures with high resolution capabilities. The polymerization process can be initiated by a two-photon absorption process, when the beam of an ultrashort infrared laser is tightly focused into the volume of a photo sensitive material. By absorbing photons a chain polymerization reaction is initiated in the photosensitive material and the interaction of laser pulses creates a voxel (volumetric pixel) in the liquid photosensitive resin which defines the resolution of the TPP process [80]. By moving the laser focus three-dimensionally through the photosensitive material, arbitrary 3D structures can be fabricated. Recently, the photosensitive organic-inorganic hybrid sol-gel ORMOCER and the negative photoresist SU8 have been used for the construction of permanent scaffolds exploring the techniques based on the phenomenon of two-photon polymerization [43].

Two-photon-polymerization (TPP) techniques have been used to rapid-prototype various medical devices e.g., microneedles for drug delivery, bone replacement prostheses, and tissue engineering scaffolds [8]. The TPP process

involves both temporal and spatial overlap of photons, leading to nonlinear absorption in a highly localized volume. Absorbed photons induce chemical reactions between chromophores and monomers within a transparent medium. This initiates the polymerization process which results in localized solidification of the liquid material. This process is intensity dependent and the absorption rate increases quadratically with intensity for two-photon absorption (TPA). The interaction of the laser radiation with matter is confined within the focal volume. The focal volume does not have well defined edges. Theoretically the Gaussian beam will extend to ±∞ transverse to the propagation direction and the beam is also not finite along the optical axis. However, the strength of the TPA is highly irradiance dependent and so outside of the focal region the absorption (and therefore, interaction) is so weak as to be zero to a good approximation. Therefore for TPA processes, the boundary between where we consider significant interaction will take place and where the material is effectively untouched is more abrupt. By moving the laser focus within such photosensitive materials, a trace of polymerized material is produced. This allows the fabrication of computer generated three dimensional structures by direct laser writing into the volume of photosensitive material. The quadratic intensity dependence of the two-photon-absorption probability and the well-defined polymerization threshold has allowed other workers to achieve sub wavelength resolution [39, 81]. Here the resolution requirements are much lower (μm) and are more readily achieved.

Beer's law relates the absorption of light to the properties of the material through which the light is travelling. According to this law there is a logarithmic dependence between the transmission, T of light and the product of the absorption coefficient of the substance, α and the distance, x which light travels through the material. The absorption coefficient α can be written as a product of molar absorbtivity, ε of the material and the concentration, c of the absorbing species in the material. Here, ε is a constant for particular substance and is a measure of the amount of light absorbed per unit concentration as discussed in the previous section. If light is travelling in the x-direction through a slab of thickness dx then according to Beer's law for single photon absorption the amount of light absorbed through small thickness dx is given by

$$dI = -\sigma c I\, dx \qquad 4.20$$

or $$\frac{dI}{dx} = -\sigma c I \quad (4.21)$$

And therefore $$I(x) = I_o \exp(-\sigma c x) \quad (4.22)$$

where I is intensity of incident light, σ is the one-photon absorption cross section and c is the concentration of the absorbing species in the material. For a two-photon absorption process, Beer's law changes to

$$\frac{dI}{dx} = -\beta c I^2 \quad (4.23)$$

Giving $$I(x) = \frac{I_o}{1 + \beta c I_o x} \quad (4.24)$$

where I_0 is the intensity at x=0, I is the intensity of the incident light and β is the two-photon absorption coefficient.

To initiate polymerisation, a threshold irradiation fluence has to be overcome for all photosensitive material [79]. Because of the non-linear nature, its dependence upon the square of the irradiance from the laser and the threshold behaviour required for the particular material, a resolution beyond the diffraction limit can be realised by controlling pulse energy and number of applied pulses as shown in Figure 4-26 for a Gaussian laser pulse.

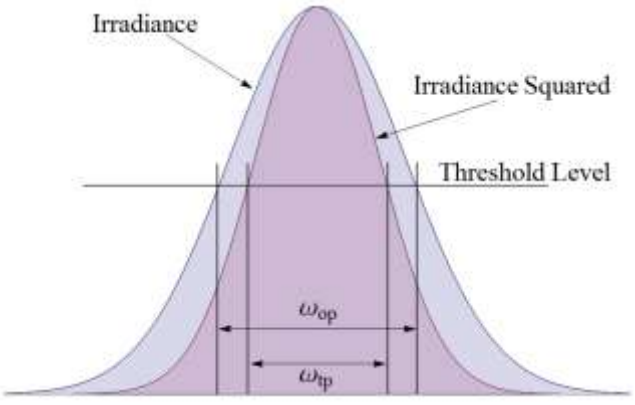

Figure 4-26 A Gaussian beam intensity distribution and voxel resolution at a well defined threshold level. Threshold effects combined with the intensity squared dependence give two-photon polymerisation a high degree of spatial selectivity.

Good control of the TPP resolution process can be achieved but a thorough understanding of the resolution achieved for combinations of various process parameters is required. The resolution of TPP processes partially depends on

the applied laser power, writing speed, concentration of the photoinitiators, and on the numerical aperture (N.A.) of the objective lens. To achieve high resolution, generally high N.A. objective lenses with irradiances close to the threshold conditions are used but the interaction of various factors with each other in defining the high resolution polymerized voxel size is not completely understood. Here, experiments have been performed to understand how the width of the polymerised line changes with different laser power and writing speeds.

For the fabrication of 3D micro/nano structure in 2PP process, knowledge of size and shape of the polymerized material and its dependence on various process and materials parameters provides a good platform. Experiments were performed to characterize the voxel size of the polymerized material at different laser power and writing speed. It is difficult to measure the voxel dimensions if the focal position is not at the surface of the substrate during a TPP polymerisation process. The polymerised voxel can get flushed away during development if it is not firmly attached to the surface of the substrate and focused too far above the substrate. On the other hand it can be truncated if the laser focus is inside the substrate. In this case it adheres to the surface but the dimensions cannot be fully measured [23]. In 2002 an ascending scan method has been proposed by Sun et al to measure the accurate voxel dimensions [82]. They used a urethane acrylate monomer and free-radical-type initiators as a media to record two-photon-excited (TPE) focal spots in three dimensions. To characterise the voxel size of the polymerised material at different laser power and exposure time, the ascending scan method has been used by many researchers [80]. The ascending scan method is shown schematically in Figure 4-27.

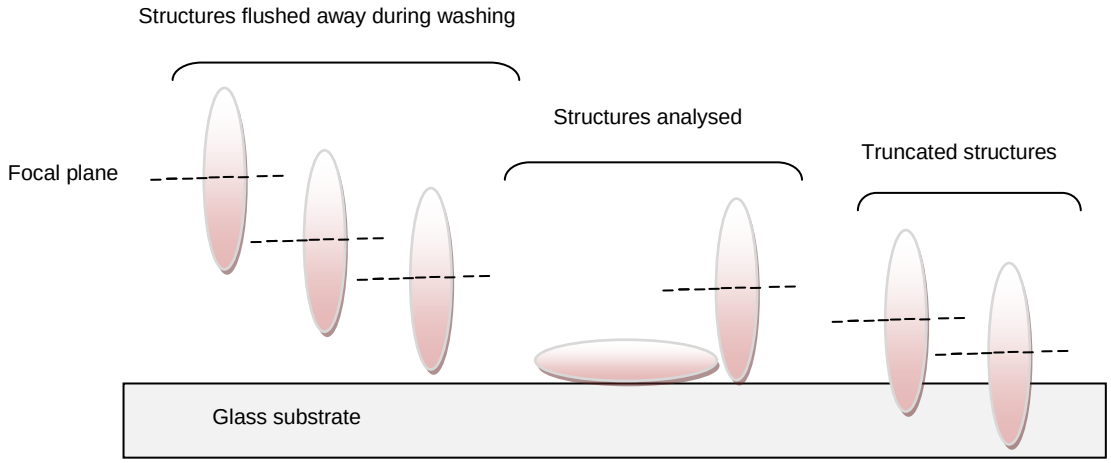

Figure 4-27: Single structure (voxel) and their appearance in a negative photoresist depending on the focal position and distance to the substrate. Structures above the substrate are flushed away during washing while structures fabricated in the substrate are truncated. Structures on the surface of the substrate can be analysed [23].

In order to measure the correct dimensions of the fabricated scaffold the ascending scan method was also used in this work. The laser focus was scanned in a direction from below to above the substrate surface. At each position the laser light was switched on for a short interval of time and a line was drawn at the same laser power but at different z-positions and illumination time. A single voxel is too small to survive post processing and therefore to study the resolution a polymerised line has been used in this study.

4.4.1 Material synthesis:

To initiate the photopolymerization process, photoinitiators are added to the monomer. In order to start radical polymerization, electron transfer is required from chromophores to the polymerizing monomer. Therefore electron-rich molecules capable of transferring electrons should be used. The transfer of electrons to the monomer generates active species and initiates the polymerization. This work presents the study of *4, 4'-Bis (diethylamino) benzophenon* which is used for the photosensitization of the liquid monomer *Ethoxylated Bis Phenol A Dimethacrylate (EO=6)* and has been discussed in detail in the previous section. The two-photon absorption cross section of the initiator was measured to be 14GM (1GM= 1×10^{-50} cm^4 s $photon^{-1}$) in ethanol and 1GM in EBPADMA as discussed in section 4.3.4. In spite of the low two-

photon absorption cross section this photoinitiator is found to polymerise EBPADMA used as the monomer in this study.

The absorption spectrum of EBPADMA was recorded by a Perkin Elmer UV/Vis spectrometer Lambda 10 in the wavelength range 200nm to 900nm. The absorption spectrum for the uncured resin used in this investigation is shown in Figure 4-28. The sample of EBPADMA is transparent in the visible region and shows little absorption at the laser wavelength of 800nm. In order to achieve efficient photosensitization of the polymerizable resin, TPA chromophores are employed as photosensitizers. The use of efficient TPA chromophores can contribute to the fabrication of fine 3-D patterns with high resolution under low laser power and short exposure time. The photosensitizer 4, 4'-Bis (diethylamino) benzophenon used in the current study is a type I photoinitiator which acts as a TPA sensitizer and also plays the role of initiator. This photo-initiator was chosen for its strong single photon absorption in the 320–420 nm regions. The advantage of using a longer wavelength photo-initiator is that it should work more efficiently with the 800 nm laser employed. The photoinitiator was added to the liquid resin and the mixture was stirred until the powdered 4, 4'-Bis (diethylamino) benzophenon was dissolved. The mixture was allowed for two days to become smooth and completely dissolve the photosensitizer in the viscous solution of the monomer. The resin EBPADMA activated with blue light with different concentrations of 4,4' Bis(diethylamino)benzophenon was then stored in a dark place wrapped in aluminum foil covering the bottle. The absorption spectra of EBPADMA containing 1% by weight 4,4' Bis(diethylamino)-benzophenon is shown in Figure 4-29. It can be seen from the figure that EBPADMA without photosensitizer shows absorption in the wavelength range 200nm to 400nm while after adding photosensitizer it additionally shows absorption in the visible range.

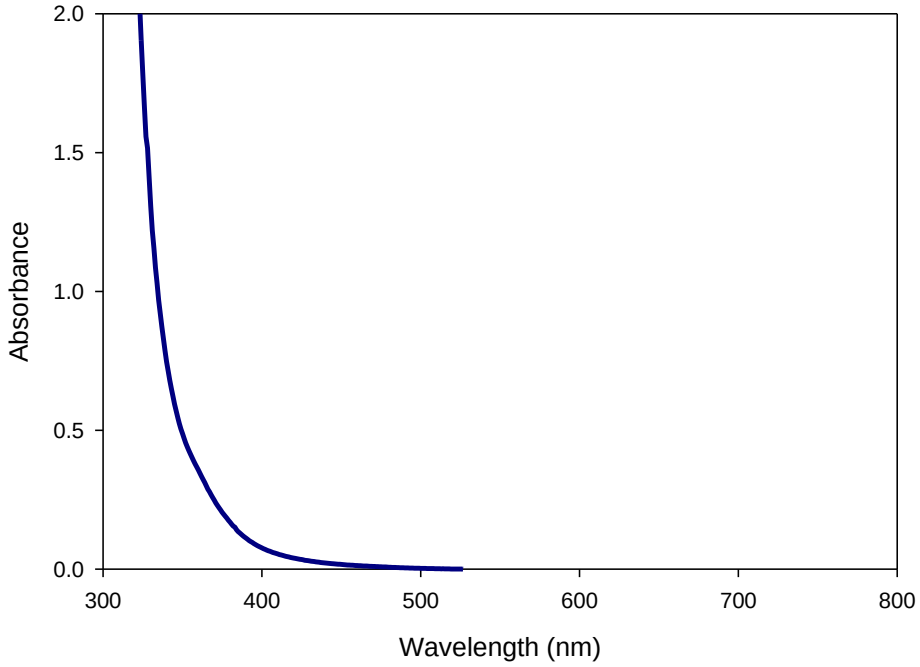

Figure 4-28 UV absorption spectrum of Ethoxylated Bis Phenol A Dimethacrylate (EBPADMA) taken over an optical path length of 10mm.

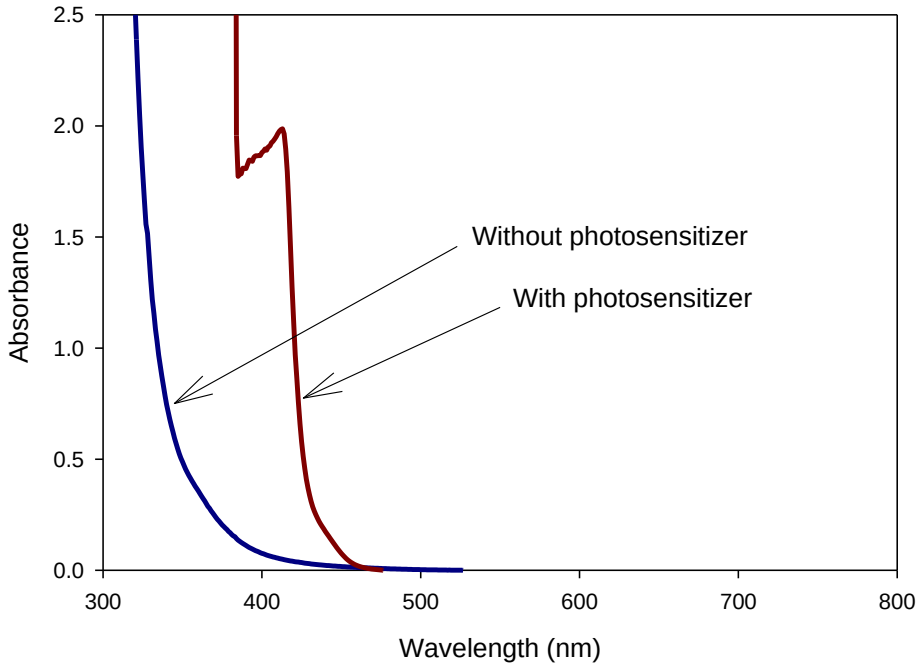

Figure 4-29 UV absorption spectra of monomer EBPADMA with and without photosensitizer 4,4' Bis(diethylamino)benzophenon

4.4.2 Experimental arrangements:

We used a near infrared mode-locked Ti: Sapphire femtosecond laser of wavelength 800nm with 150fs pulse duration and 1 kHz repetition rate for 3D material processing. A drop of activated EBPADMA was placed in the middle of a hole reinforcer placed on a clean microscope slide to act as a spacer as shown in Figure 4-30. The sample was warmed to 50^{o}C on a hot plate to allow the liquid resin to flow. After a while a cover slip of thickness 100µm was placed on the drop of the material to ensure that the surface upon which the laser light is incident was flat. The sample was mounted on a computer controlled X-Y-Z translation stage (Aerotech linear motor stages with NPAQ controller) to allow translation of the sample through the laser beam with preset velocity. Software (Automation 3200) was used to control the movement of the stage in three dimensions. The computer controlled stage has a resolution of 10nm and a maximum travel of 50mm. The power of the radiation incident on the sample at the rate of 1 kHz was measured after focus using a Newport (model 840 IRVINE CA) optical power meter. The incident power on the sample was controlled with the help of attenuation filters and powers in the range of 380µW to 450µW were allowed to be focussed on the sample. The femtosecond laser pulses were tightly focused onto the liquid resin by a plano-convex lens of 30mm focal length. The laser was made incident on the sample in the desired pattern by moving the computer controlled stage.

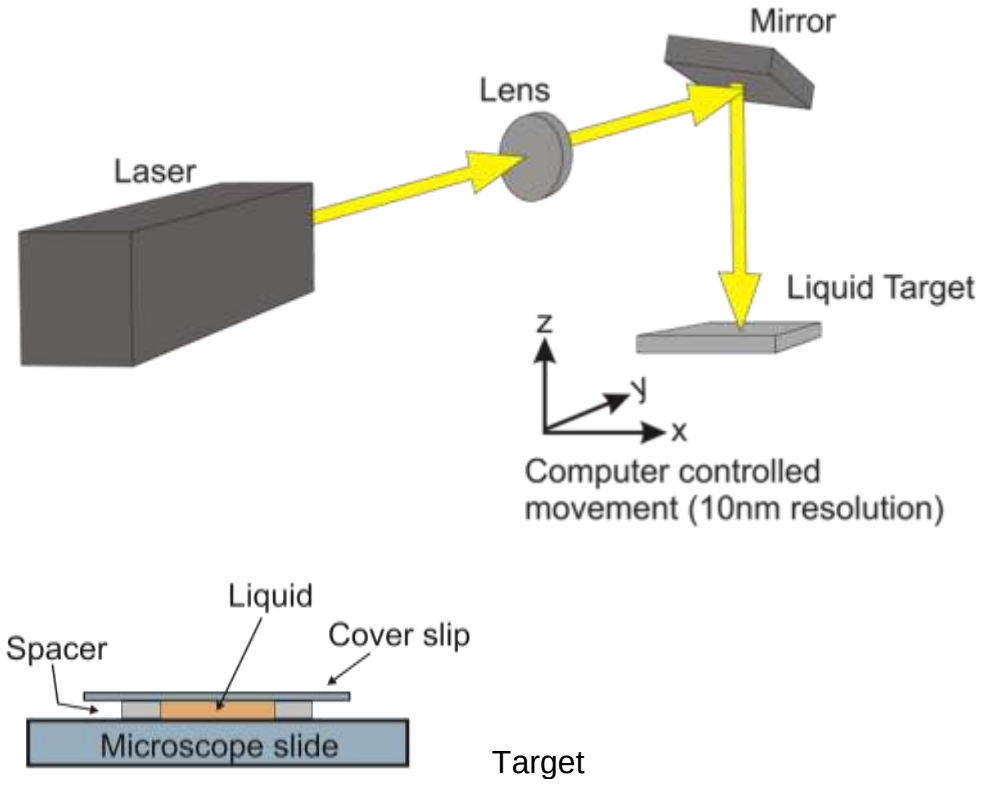

Figure 4-30 Experimental arrangement for the preparation of three dimensional (3D) structures using Ethoxylated Bisphenol A Dimethacrylate (EBPADMA) (6EO) monomers.

4.4.3 Fabrication techniques

As discussed earlier, in order to measure the dimensions of the polymer 3D structures accurately, the ascending scan method proposed by Sun et al has been used. For the fabrication of 3D structures liquid drops were used in the middle of ring reinforcer. An intrinsic shortcoming of using a resin droplet is that fabricated 3D structures may move and may be easily displaced during post fabrication washing. If the fabricated structure is not firmly attached to the substrate surface, it may flush away during washing. Therefore in order to get firmly attached 3D features two-photon polymerisation scanning should start from substrate surface [5].

Polymerized lines were fabricated in Y and Z directions by gradually decreasing the laser power while the sample was moved in the Y-Z direction using a computer controlled x-y-z translation stage as shown in Figure 4-31. The laser power was attenuated with the help of filters. The laser power was decreased gradually and it was observed that with the reduction of power the polymerised line become narrower and disappeared when the power was below the

threshold level of intensity where the polymerisation terminates and photochemical reactions vanish [81]. The fine polymerised line after which there is no polymerisation observed shows the achievable spatial resolution.

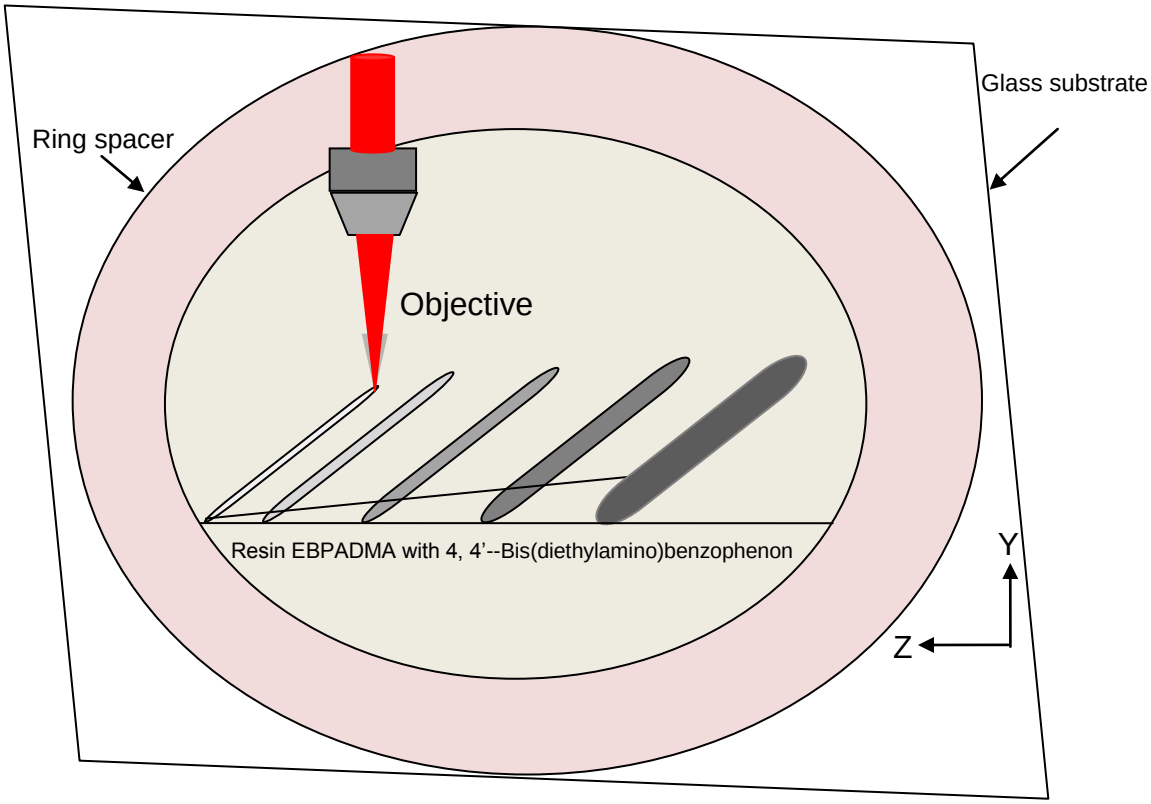

Figure 4-31 Schematic diagram shows the fabrication of lines in Z and Y directions at different laser power. The sample was moved from lower to upper position to find the focal position.

The polymerization properties were studied in detail as a function of writing power and speed as well as the NA of the objective lens used to focus the laser light. To measure the line width and axial dimensions of the polymerised features, cell scaffolds at different laser power and writing speeds were fabricated. To achieve best resolution and best shape of the polymerized voxel, it is required to work with low laser threshold and short irradiation time. Therefore to improve lateral spatial resolution (LSR), laser intensity and exposure time are the main factors to be controlled. Exposure time influences the number of radicals produced by TPA while laser intensity affects initial radical generation in the two-photon absorption region. A low laser threshold, reducing the size of the region where radicals are initially generated and short

exposure times, decreases the diffusion and number of radicals generated due to two-photon absorption and results in localized polymerization in a tiny region [83]. Pulses from the mode-locked Spectra Physics, Hurricane X laser system with a centre wavelength of 802 nm, a pulse width of 170fs, and a repetition rate of 1 kHz were used for two-photon induced polymerisation experiments here. Figure 4-32 shows the TPP laser patterned line dimensions written at various velocities for several laser powers (0.4mW, 1.0mW and 1.3mW). The laser output average power was 730mW before attenuation and so only a small percentage of the available power was used. The width of the polymerized lines decreases with increasing speed. As the speed increases, the exposure time decreases and the number of generated radicals is reduced. Therefore the dimension of the polymerized lines decreases. A resolution of ~10µm i.e., of cell size, was obtained at a writing speed of 200mm/min using 0.4mW laser power. These conditions give the resolution required for the fabrication of a cell scaffold.

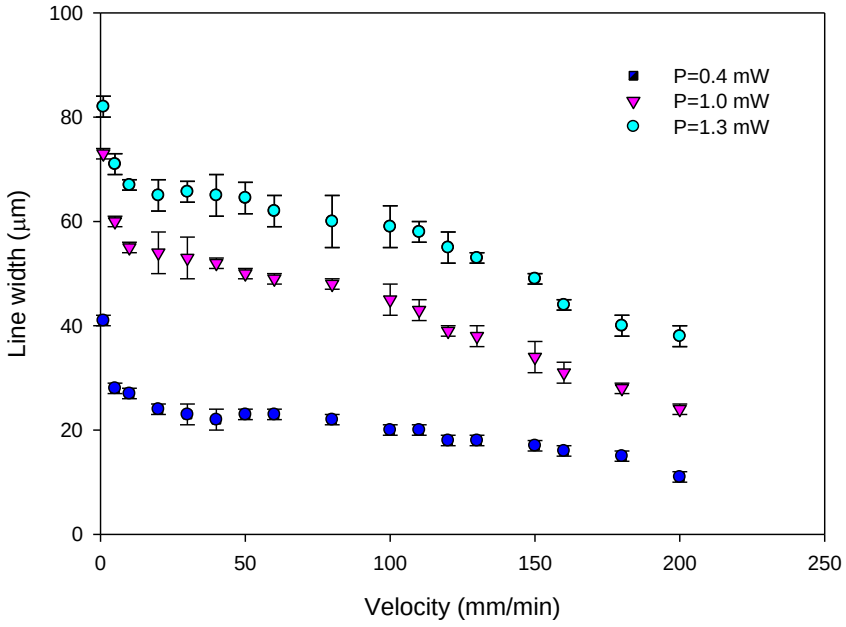

Figure 4-32 Graph shows characteristics of EBPADMA at different speeds as a function of laser power at 800nm wavelength using the TPP technique.

Figure 4-33 shows the TPP laser patterned line dimensions written as a function of laser power for two writing speeds (1mm/min, 50mm/min). The pulse duration of the Ti: sapphire femtosecond laser system used for the experiment was

160fs at the rate of 1 kHz and the laser output average power was 740mW. The figure indicates that the width of the polymerized lines fabricated show an increase with high laser power and it is obvious that the width is reduced as the power decreases and therefore at low laser power and large writing speed features less than 5µm size can be fabricated. Resolution measurements obtained in this study show that structures down to 1 µm can be fabricated using this technique for the monomer selected here for the fabrication of cell scaffolds. The lowest average laser power, measured before the objective lens, that can guarantee fabricating a solid line with a linear scan speed of 10mm/min was 80µW and was defined as the threshold of TPP for Ethoxylated Bis Phenol A Dimethacrylate.

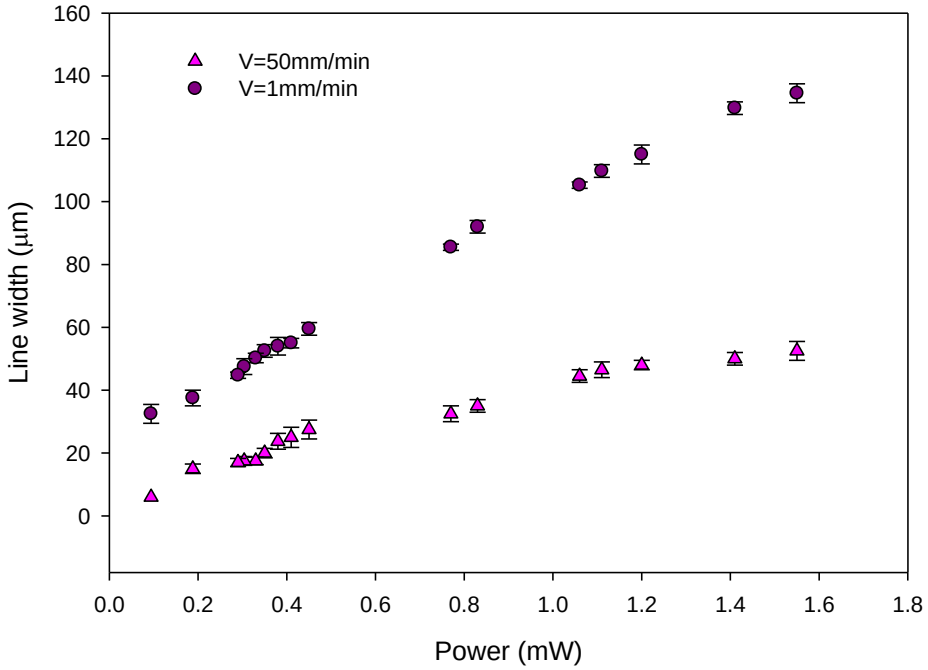

Figure 4-33 Graph shows increase in line width with increase in power using 800nm wavelength. At low laser power and high velocity small size of the polymerized line width has been achieved for Ethoxylated Bis Phenol A Dimethacrylate monomer.

It can be concluded that at low laser power and large scanning speed the size of the polymerized line width can be minimized and the lateral spatial resolution desired for the fabrication of a cell scaffold with different pore size can be improved. This is in agreement with previous studies [80].

In a two-photon polymerisation process, as discussed earlier, the photosensitizer chromophores are excited by the absorption of photons and give rise to radical formation. The active radicals react with the monomers and a chain reaction is initiated. As the monomer starts converting into larger molecular weight polymer the concentration of photosensitizer chromospheres present in the resin changes. The polymerisation process will continue with the absorption of photons and will terminate only in the absence of irradiance. If the resin is exposed to high irradiance for a long time, all of the chromophores present in the material will convert into radicals thereby reaching a saturated state. At that point the rate of polymerisation becomes constant [79]. Figure 4-34 shows an example of time dependent polymerised line width. It can be seen in the graph drawn that for all the laser powers studied a slight increase in exposure time initially results in a significant increase in line width. On the other hand at large exposure times the polymerised volume almost becomes constant due to the excitation saturation that takes place in the central portion where maximum intensity exists. Therefore no significant self focusing effect, which is non local in time, was observed in this study as observed in case of single photon absorption [84]. This confirms two-photon polymerisation processes which are non linear and the polymerisation is confined to the focal point only in the presence of high irradiance. It can be seen in Figure 4-34 that the size of the polymerized voxel varied and thus the smallest features can only be obtained by carefully controlling the exposure time and intensity. High spatial resolution can be achieve only if the two-photon polymerisation process takes place in near threshold region for short exposure times[85].

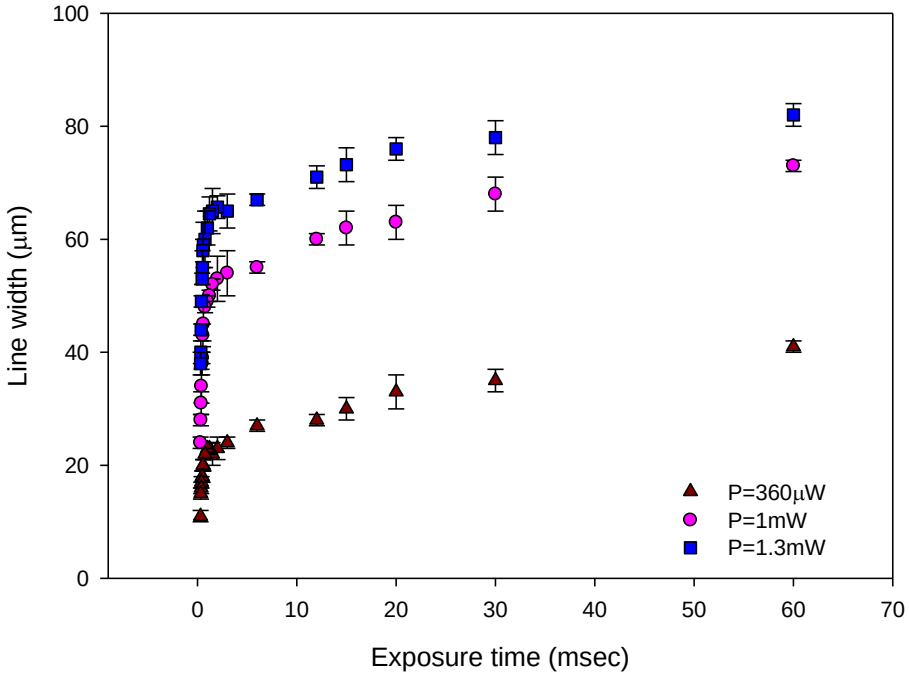

Figure 4-34 Graph shows exposure time dependent polymerisation. When the resin is exposed to high irradiance for a long time, all of the chromophores present in the material absorb photons and convert into radicals thereby reaching a saturated state and the rate of polymerization becomes constant.

The resolution limit of 3D two-photon materials processing with a femtosecond laser can be affected by many factors. The first factor is the material composition i.e., the properties of the material used for the fabrication of features, while laser characteristics can be considered as a second factor which determines how close one can achieve the TPP threshold. Linear or multiphoton processing is the last factor affecting the resolution limit. Laser wavelength and numerical aperture of the imaging optics define the classical resolution limits as can be seen by the following relations [79].

$$\mathrm{CD} = \mathrm{k}_1 \frac{\lambda}{\mathrm{NA}} \qquad 4.25$$

and

$$\mathrm{DOF} = \mathrm{k}_2 \frac{\lambda}{\mathrm{NA}^2} \qquad 4.26$$

where CD is the critical dimension of the fabricated features size and DOF is the depth of focus representing axial features dimensions, λ is the wavelength of

the laser light used and NA is the numerical aperture of the lens. In addition, k_1 and k_2 are constant factors and depend upon characteristics of the experimental techniques applied and properties of the material used. The resolution limits for multiphoton polymerization can be written as

$$\mathrm{CD} = k_1 \frac{\lambda}{\sqrt{q}\mathrm{NA}} \qquad 4.27$$

$$\mathrm{DOF} = k_2 \frac{\lambda}{\sqrt{q}\mathrm{NA}^2} \qquad 4.28$$

where q represents the multiphoton process and for two-photon polymerization can be written as $q=2$ [79].

In order to investigate the effect of changing the N.A. of the optical system on the feature sizes produced a stop was placed close to the entrance of the lens (Figure 4-35). The lens had a fixed focal length of 30mm and the effective N.A. was varied by using adjusting the stop size. TPP laser patterned line dimensions written at various N.A. of the lens as a function of writing speed (1, 10, and 50mm/min) are shown in Figure 4-36.

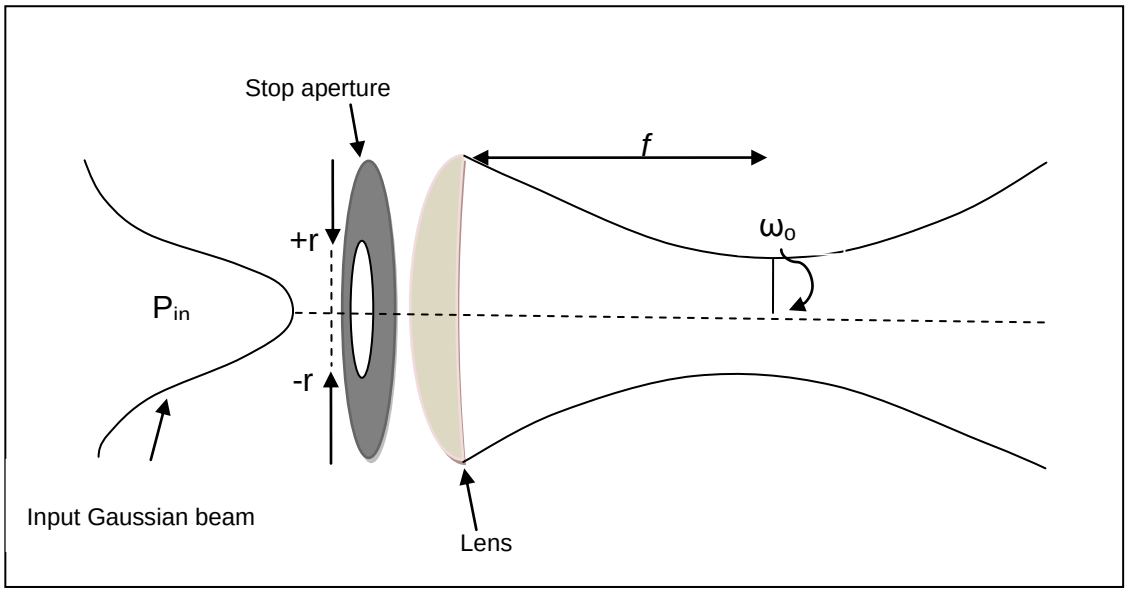

Figure 4-35 Experimental arrangement for varying the entrance pupil diameter to write TPP laser patterned line dimensions at various N.A of a lens as a function of writing speed.

The lowest average laser power measured before the objective lens was 930μW. Unexpectedly, the feature size increases with increasing N.A. This is

counter to equation 4.27 which predicts that by increasing the N.A. it should be possible to generate smaller features.

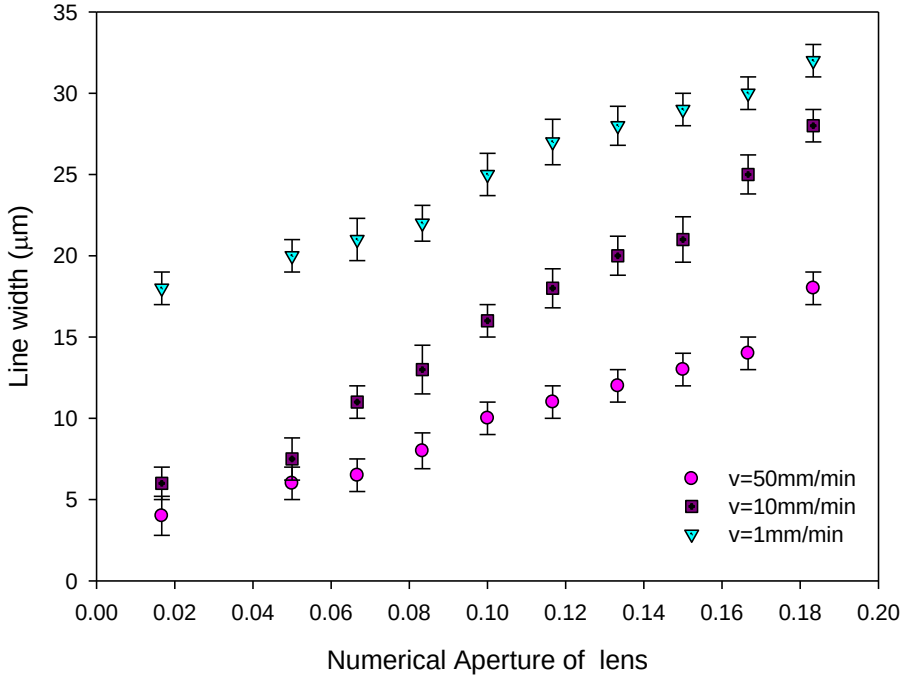

Figure 4-36 Graph shows an increase in line width with increase in N.A. of the lens used at 800nm wavelength and at a constant laser power of 930µW.

It is hypothesized that there are two competing processes at play. Firstly, the increase in N.A. does produce smaller focal spot sizes. However, as the N.A. is simply varied here by the stop diameter, the power transmission of the system changes as well. Added to this, the threshold for the TPP must be accounted for. An analysis to include these features is now given.

For a TPP process, variation of feature size with the numerical aperture of the focusing lens depends on the square of irradiance compared to some irradiance threshold for the process. This threshold will depend on the concentration of the chromophores present in the resin and on the two-photon absorption cross section of the photosensitizer used. The corresponding time-averaged intensity (or irradiance) distribution for a Gaussian beam is given by

$$I = I_o e^{-2r^2/\omega^2} \qquad 4.29$$

where $I_o = I_{(0,0)}$ is the intensity at the centre of the beam at its waist. Therefore the square of the irradiance can be written as

$$I^2 = I_o^2 \, e^{-4r^2/\omega^2} \qquad 4.30$$

Threshold effects combined with the intensity squared dependence gives the size of the feature i.e., r can be found by solving equation 4.30 when $I^2 = I_{th}^2$. Therefore

$$\ln \frac{I_{th}^2}{I_o^2} = -\frac{4r^2}{\omega^2}$$

and

$$r = \sqrt{\frac{\omega^2}{4} \ln \frac{I_o^2}{I_{th}^2}} \qquad 4.31$$

The formula indicates that the feature size depends on the beam waist radius ω and the ratio I_o^2/I_{th}^2. For any changes in the numerical aperture of the system, the focal spot size will be affected and therefore a change in I_o will also take place. In general, increasing N.A. reduces the spot size and therefore I_{th} is reached at a smaller width. However the peak intensity I_o also depends on the power in the spot, therefore the effect of N.A. alone cannot be discovered by varying the entrance pupil diameter as both power and spot size have been varied.

If the irradiance of the Gaussian beams entering the lens is denoted by I_{in} then the power P of the incident radiation is given by

$$P_{in} = I_o \int_{-\infty}^{+\infty} \int_{-\infty}^{+\infty} e^{-2(x^2+y^2)/\omega_{in}^2} \, dx \, dy \qquad 4.32$$

$$P_{in} = \frac{I_o \pi \omega_{in}^2}{2} \qquad 4.33$$

$$I_o = \frac{2P_{in}}{\pi \omega_{in}^2} \qquad 4.34$$

The peak intensity is thus exactly twice the average intensity, obtained by dividing the total power by the area within the radius ω_{in}.

The power P passing through an aperture of radius *d* in the transverse plane is given by

$$P_{out} = I_o \int_{-d}^{+d} \int_{-d}^{+d} e^{-2(x^2+y^2)/\omega_{in}^2} \, dx \, dy \qquad 4.35$$

The result of this integration can be written in terms of an error function and so P_{out} can be written as

$$P_{out} = I_o \frac{1}{2} \pi \omega_{in}^2 \, Erf\left[\frac{d.\sqrt{2}}{\omega_{in}}\right]^2 \qquad 4.36$$

or

$$P_{out} = P_{in} \, Erf \left[\frac{d.\sqrt{2}}{\omega_{in}}\right]^2 \qquad 4.37$$

Let us also consider changes in the beam waist size that result from varying the size of the beam at the lens entrance. It is assumed that a Gaussian beam propagating in free space is incident on the lens and is transmitted. The truncation effects during transmission are ignored and also the paraxial ray approximations are assumed with no lens aberrations. Then the beam waist ω_o is given by

$$\omega_o = \frac{\lambda f}{2\pi\omega_L} \qquad 4.38$$

The “f-number” expresses the diameter of the entrance pupil in terms of the focal length of a lens for an optical system and is defined as

$$f^{\#} = \frac{f}{D}$$

where f is the focal length and D is the entrance pupil diameter. Hence,

$$f^{\#} = \frac{f}{2\omega_L}$$

Also the numerical aperture of the lens in terms of f-number can be expressed as

$$N.A. = \frac{1}{2f^{\#}} = \frac{\omega_L}{f} \qquad 4.39$$

$$\omega_L = f \, N.A. \qquad 4.40$$

Substituting the value of ω_L from equation 4.40 in equation 4.38 we can write ω_o as

$$\omega_o = \frac{\lambda}{2\pi \text{N.A.}} \qquad 4.41$$

The intensity profile of a laser beam at its waist is known as the focal point irradiance, I_{fp} and for a Gaussian distribution at the lens is given by another Gaussian function at the focus:

$$I_{fp} = I_{ofp}\, e^{-2r^2/\omega_o^2} \qquad 4.42$$

where I_{ofp} is the peak irradiance at the focal point. Taking the integral of equation 4.42, the central (peak) irradiance I_{ofp} can be related to the total power in the beam. Therefore

$$P_{out} = \int_{-r}^{+r}\int_{-r}^{+r} I_{fp}\, dx\, dy$$

and

$$P_{out} = I_{ofp}\int_{-r}^{+r}\int_{-r}^{+r} e^{-2(x^2+y^2)/\omega_{in}^2}\, dx\, dy$$

$$P_{out} = I_{ofp}\frac{\pi\omega_o^2}{2}$$

Therefore now I_{ofp} can be written as

$$I_{ofp} = \frac{2P_{out}}{\pi\omega_o^2} \qquad 4.43$$

Substituting the value of ω_o^2 from equation 4.41 in equation 4.43, we get

$$I_{ofp} = \frac{8\pi(\text{N.A.})^2}{\lambda^2} P_{out}$$

By substituting the value of power P_{out} passing though an aperture of radius d from equation 4.37 in the above equation, we get

$$I_{ofp} = \frac{8\pi(\text{N.A.})^2}{\lambda^2} P_{in}\, \text{Erf}\left[\frac{d.\sqrt{2}}{\omega_{in}}\right]^2 \qquad 4.44$$

In terms of numerical aperture, $\text{N.A.} = d/f$, equation 4.44 becomes

$$I_{ofp} = \frac{8\pi(\text{N.A.})^2}{\lambda^2} P_{in}\, \text{Erf}\left[\frac{f(\text{N.A.})\sqrt{2}}{\omega_{in}}\right]^2 \qquad 4.45$$

The feature size at the focus of the lens is given by equation 4.31, this is now equivalently written as

$$r = \sqrt{\frac{\omega_o^2}{4} ln \frac{I_{ofp}^2}{I_{th}^2}}$$

$$r = \sqrt{\frac{\omega_o^2}{4} 2\left[lnI_{ofp} - lnI_{th}\right]} \qquad 4.46$$

Substituting the value of I_{ofp} in the above equation, we can get the feature resolution for different N.A. values as

$$r = \frac{\omega_o}{\sqrt{2}} \left\{ ln \left[\frac{8\pi(N.A.)^2}{\lambda^2} P_{in}\ Erf\ \left(\frac{f(N.A.)\sqrt{2}}{\omega_{in}} \right)^2 \right] - ln\ I_{th} \right\}^{1/2}$$

where $I_{ofp} \geq I_{th}$ and $\omega_o = \frac{\lambda}{2\pi N.A.}$. This equation has been plotted for various threshold intensities in Figure 4-37. At low N.A. the aperture is small and the power transmitted is low. Although the focussing will be weak resulting in relatively large spot sizes, the width of the irradiance distribution above threshold will be small. Thus small features are obtained. At large N.A. the focal spot will be small and most of the power is transmitted by the lens resulting in high irradiances. However, the narrow distribution means that although a lot of the irradiance is above threshold, the width is still small and TPP features will also be small. Whilst these are interesting theoretical regimes to work in, the fit to the experimental data is poor as the general upward trend found in Figure 4-36 is not predicted. Varying the unknown parameters such as the threshold irradiance over wide ranges did not result in the trend being followed even if the order of magnitude of feature size could be predicted.

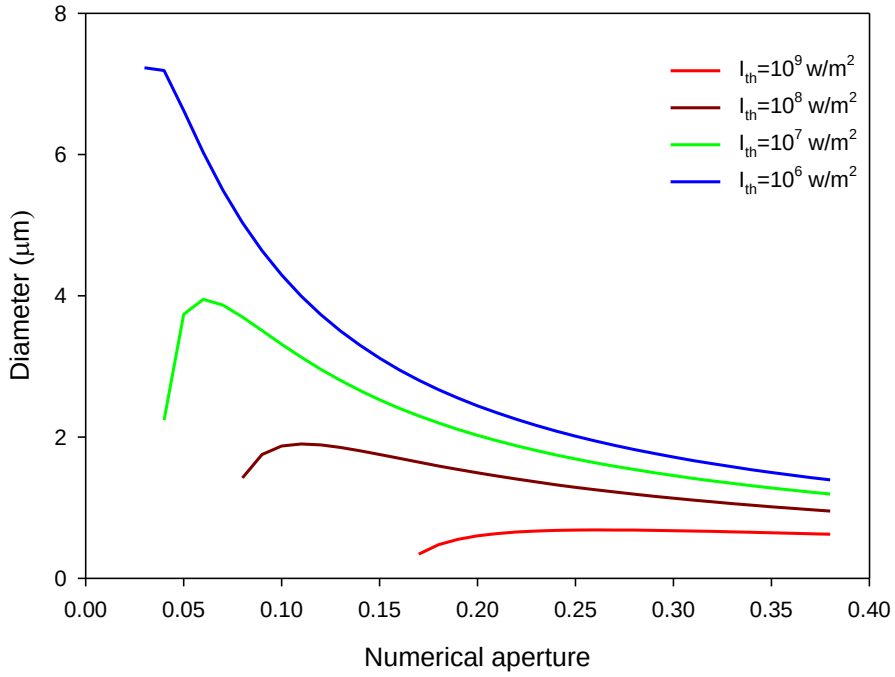

Figure 4-37. Theoretical predictions of the diameter of the TPP features for various threshold intensities as a function of numerical aperture. Reducing the threshold results in larger features. The variation with N.A. is more complex as this is achieved by varying an aperture and therefore the transmitted power as well.

In the above analysis it has been assumed that the lens is aberration free. At large N.A. this is unlikely to be the case and should be accounted for. The diffraction theory of aberrations is discussed in Born and Wolf [86] and also extensively covered by Stamnes [87]. From the analysis by Stamnes it is possible to include all the 3 of the Seidel aberrations; spherical, astigmatism and coma. This leads to a lengthy numerical integration and so spherical aberration was primarily included as this is most affected by aperture size. Aaron et al [88] have given a functional form for the degree of spherical aberration in terms of illumination radius for a plano-convex lens as used here. The displacement between an ideal converging spherical wavefront and the distorted wavefront is given by:

$$\phi(\rho) = \frac{-(a\,\rho)^4}{32\,f^3}\left[\frac{n^2}{(n-1)^2} - \frac{n}{n+2} + \frac{(2n^2-n-4)^2}{n(n+2)(n-1)^2}\right] \qquad 4.47$$

Here $\rho = (r/a)$ and r is the radial coordinate and a radius of the lens with focal length f and refractive index n. The focal irradiance distribution is found by

propagating this wave front through a circular aperture. This can be achieved mathematically by using the Fresnel-Kirchhoff integral which in this case is in the form [88],

$$I(u,v) = \frac{16\,\pi\,a^4\,P}{\lambda^2\,f^2\,D^2}\left|\int_0^{D/2a} \exp\left[i\left(k\,\phi(\rho) - \frac{u\,\rho^2}{2}\right)\right] J_0(v\rho)\rho\,d\rho\right|$$

4.48

The additional parameters in this equation are: P is optical power, D is the illuminated diameter, λ is the wavelength of light, k is the wave number and J_0 is the zero-order Bessel function. The irradiance has been cast as a function of the so-called optical coordinates which are given by,

$$u = \frac{2\pi}{\lambda}\left(\frac{a}{f}\right)^2 z$$

and

$$v = \frac{2\pi}{\lambda}\frac{a}{f} z$$

For the glass lens (presumed to be BK7) the refractive index at 800nm was taken to be 1.51078 [89] and the focal length was 30mm. The useable diameter of the lens was ~2cm.

The irradiance distribution was calculated by means of a program written in the Mathematica language (version 7, Wolfram Research Inc). For convenience, the power was set to 1W and as the other, spatial, units were defined in metres, the calculated intensity will be in Wm^{-2}. Restricting the stop diameter to 1mm diameter (N.A. = 0.017) minimises spherical aberration and a smooth increase in irradiance is observed as the beam is brought to a focus (Figure 4-38). The small amount of aberration coupled with the fact that equation 4.48 assumes a uniform irradiance at the pupil, does give a low spatial frequency oscillation either side of the focal region. The peak intensity coincides with the geometric focal point at $z=0$. When the aperture is opened, N.A. increases along with the degree of spherical aberration. In Figure 4-39 the pupil diameter has been increased to 11mm (N.A. = 0.18). Now the focal region is highly oscillatory. The peak intensity is higher even though the transmitted power remains set at 1W. It can also be seen that the peak intensity no longer coincides with the

geometric focal plane and has shifted towards the lens. Note that the horizontal scale is quite different in these two regions; the depth of field for the higher N.A. is much shallower.

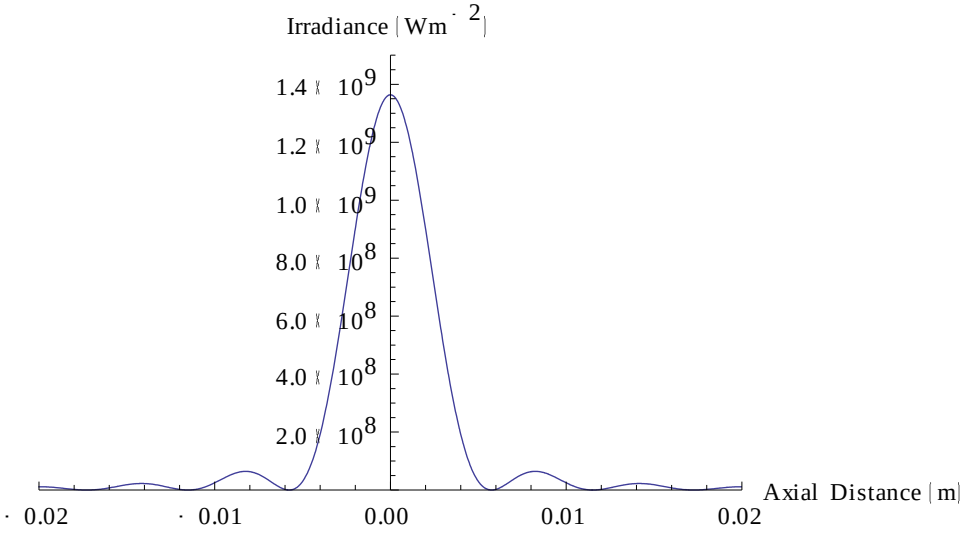

Figure 4-38 Calculated intensity profile along the optical axis in the region of the geometrical focus. The lens pupil has been restricted to a diameter of 1mm to give an N.A. of 0.017.

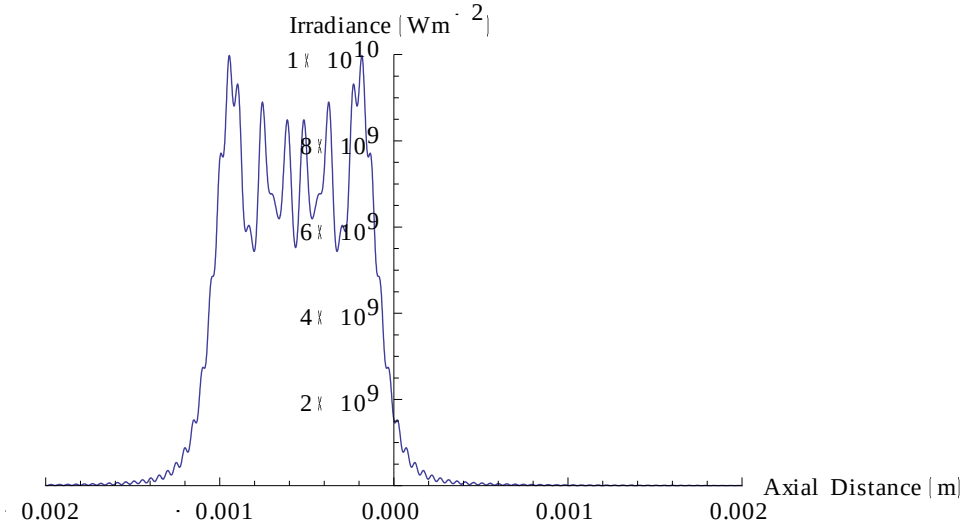

Figure 4-39 Calculated intensity profile along the optical axis in the region of the geometrical focus. The lens pupil has been opened to a diameter of 11mm to give an N.A. of 0.18. Note that the scale of the horizontal axis is 10 times smaller than Figure 4-38 illustrating the much shallower depth of field. There is also a marked increase in the peak intensity value and a shift towards the lens.

In order to compare spot sizes for these two N.A. values it is necessary to plot the irradiance in the radial axis. For the low N.A. this has been done for $z=0$

(the geometric focus) but for the high N.A. the centre of the focal distribution was chosen as this is likely to dominate the TPP process. This position was taken to be -676μm (i.e. closer to the lens). In addition, the power transmitted has been reduced for the low N.A. plot by a factor equal to the ratio of the aperture areas (1:121). These plots are shown in Figure 4-40 and Figure 4-41.

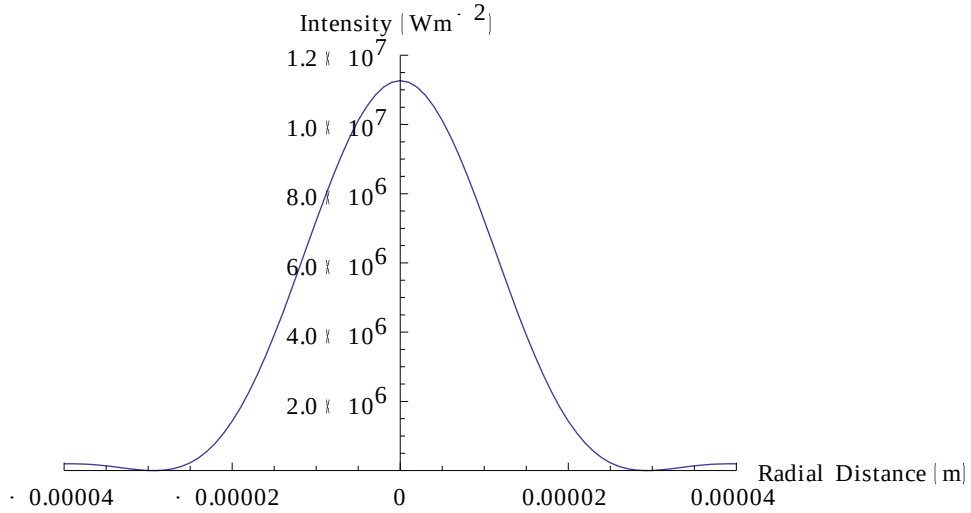

Figure 4-40 Calculated radial intensity distribution in the geometric focal plane (z=0) for a numerical aperture of 0.017. The total power has been reduced due to the pupil size by a factor equal to 1/121.

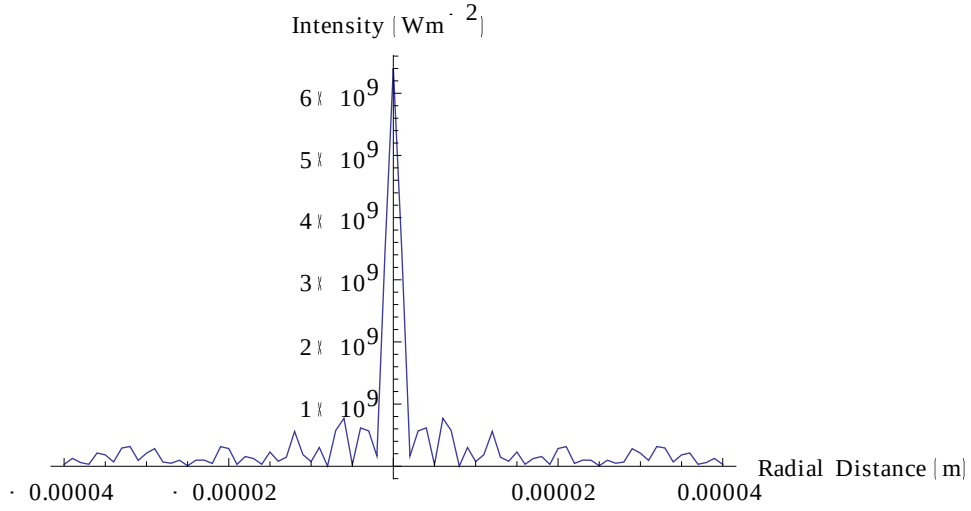

Figure 4-41 Calculated radial irradiance distribution in a plane 676μm closer to the lens than the geometric focus. From Figure 4-39 this can be seen to be the middle of the aberrated focal region. Here the total power is 1W and N.A. = 0.18

By comparison to the experimental data, the irradiance distribution in Figure 4-40 is expected to give rise to a feature size of ~ 5μm (Figure 4-36). From Figure 4-40 this corresponds to a threshold intensity of $1.1x10^{7}$ Wm^{-2} (this is a relative value as the real power through the system has not been used). Applying this value to the irradiance profile in Figure 4-41 predicts a TPP feature size of 16μm. Therefore, the analysis that includes the aberration of the focal spot as the N.A. is increased, not only predicts that the feature size will increase as the aperture stop is opened but also gives results of comparable magnitude to the experimental data.

4.4.4 Fabrication of cell scaffold structures

A desired tissue shape and a porous interconnected micro-architecture structure are required for biodegradable and biocompatible scaffolds for tissue engineering. In order to encourage cells to build an artificial living tissue, an appropriate environment exactly resembling that of a particular tissue type has to be created. Porous scaffold geometries are required to have high surface area for initial cell attachment and a specific micro-scale pore size depending on cell/tissue types. The pore sizes depend on the desired cell/tissue type and values ranging from ~5μm to hundreds of microns are reported according to the cell/tissue types used in various research [46]. 2D and 3D environments are required for the cell type to preserve tissue specific features. TPP techniques used with the right material allows the fabrication of 3D scaffolds with precise control over geometry to reproduce microcellular environments and provide control over cell organisation inside the scaffold and over the cell interaction [79].

A femtosecond laser beam of wavelength 800 nm at 420μW power having pulse duration of 180fs with repetition rate of 1 kHz was made incident on the sample with a writing speed of 1mm/min. The sample was analyzed with a Leica DM LM optical microscope which showed the presence of a scaffold covered with liquid resin. The scaffolds obtained were rinsed many times in deionised water to remove the liquid EBPADMA from the slide to get cell scaffolds as shown in Figure 4-42. The scaffold obtained contains pores of approximately 47μm, a pore size suitable for the liver tissue [46]. The size of the ridges between these

large sized pores was approximately 37µm wide due to fabrication at low speed i.e., at v=1mm/min.

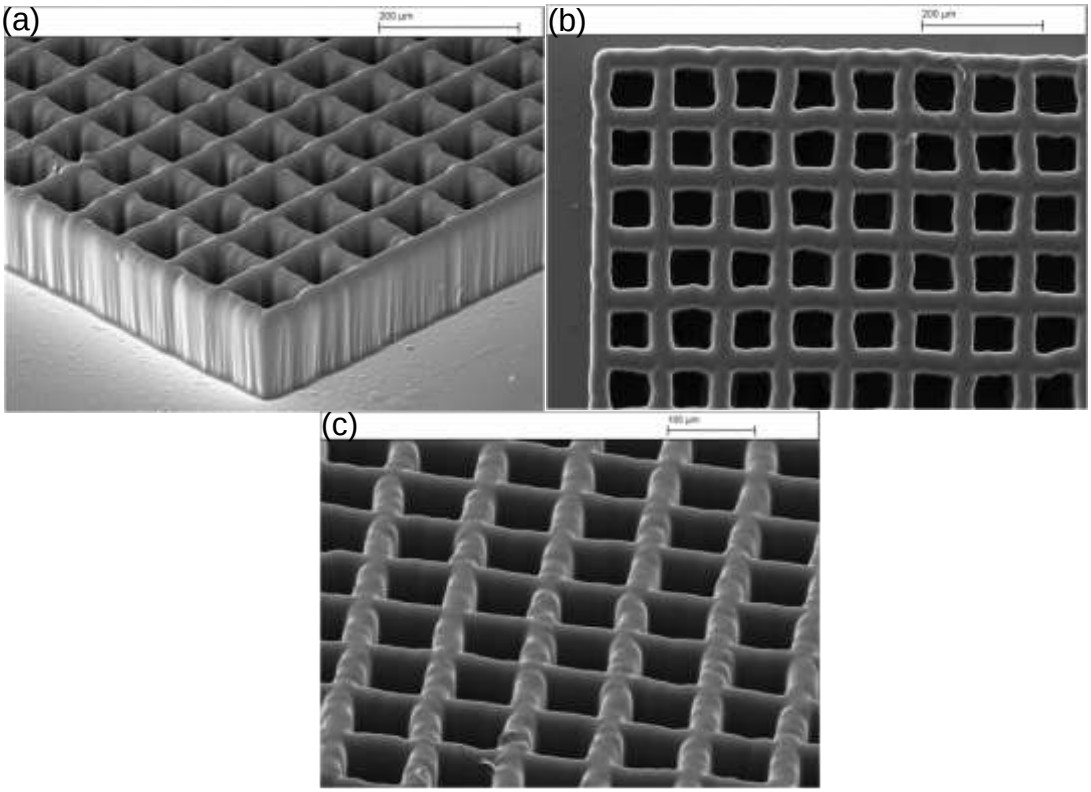

Figure 4-42 SEM image of large-scale cell scaffold fabricated with 47µm pore size and 37µm thick ridges suitable for the liver tissue [46]. SEM images (a) side view at 60^{o} (b) Top view at 0^{o}(c) Top view at 60^{o}

Figure 4-43 shows a cell scaffold obtained when a laser beam at 800nm wavelength of 380µW power having pulse duration of 170fs with repetition rate of 1 kHz was made incident on the sample with a velocity 100mm/min. After fabrication the structure was washed several times with deionised water and to get a clean scaffold, ethanol and acetone were used for the final rinses of the structure. Due to the chemicals used on the structure produced it was deformed, distorted and detached slightly from the substrate. The pore sizes of the scaffold obtained was large with approximately 10µm ridges between the pores. Thin ridges between the pores were obtained due to high speed scanning.

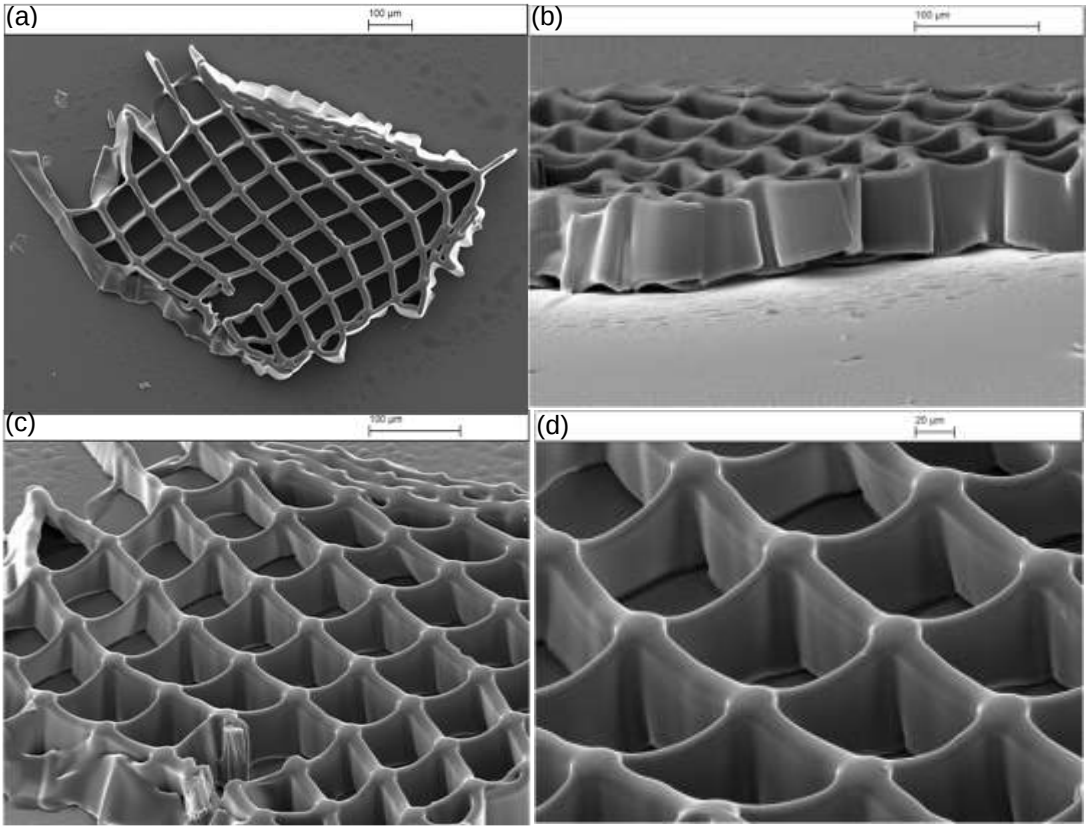

Figure 4-43 SEM images of cell scaffold structure with large pore size and thin ridges washed with acetone and ethanol. The SEM images show (a) deformation and distortion of the cell scaffold (b) detachment from the substrate surface (c) broken pores (d) depth of the scaffold.

Usually TPP is achieved using high N.A. objective lenses to achieve high resolution in the microfabrication processes [7]. Here we are interested in generating coarser structures but also optimising the speed. Therefore it is useful to increase the depth that can be polymerised in a single pass. The combination of employing a small N.A. objective lens to obtain a much longer depth of focus (DOF) and a photosensitizer with small two-photon absorption cross-section allows longer range TPP. With this approach we have fabricated approximately 100µm deep cell scaffolds with single pass.

In order to obtain even deeper structures for cell scaffolds, the height of the liquid was increased on the sample by using three reinforcement rings on top of each other. Step-and-repeat building strategy was used in this case. This method was used to duplicate a structure and to create rows and columns on the same position but one step above on top of the scaffold. The laser beam of 800nm wavelength at 413µW power having pulse duration of 166fs with

repetition rate of 1 kHz was made incident on the sample with a speed of 100mm/min. The distance between the lines of the scaffold was 0.03mm. After fabricating the structure, the sample was lowered approximately 100µm using computer controlled stage and was again exposed to the laser beam for laser writing. The structures were washed with deionised water several times. Due to the depth of these structures the non polymerized material was still standing inside the holes and therefore was soaked in water for two days. The height of the structure obtained was determined using Scanning Electron Microscopy at an angle of 90^{o} and was found to be approximately 310µm. The pore size was approximately 10-11µm. The uncured resin that was not removed from the scaffold completely can be seen and the longer rinsing time contributed to the distortion of the scaffold as shown in Figure 4-44. Furthermore, deformation and distortion in the scaffold appears during drying process due to the presence of surface tension and capillary forces [46]. The scaffold has $1mm^2$ area with 310µm height and the fabrication time was ≈ 1 minute and 19 seconds. If the overall dimensions of the fabricated scaffold is of the order of few mm then it will require more time, for example to fabricate a $1cm^2$ cell scaffold the time required will be approximately 10 minutes.

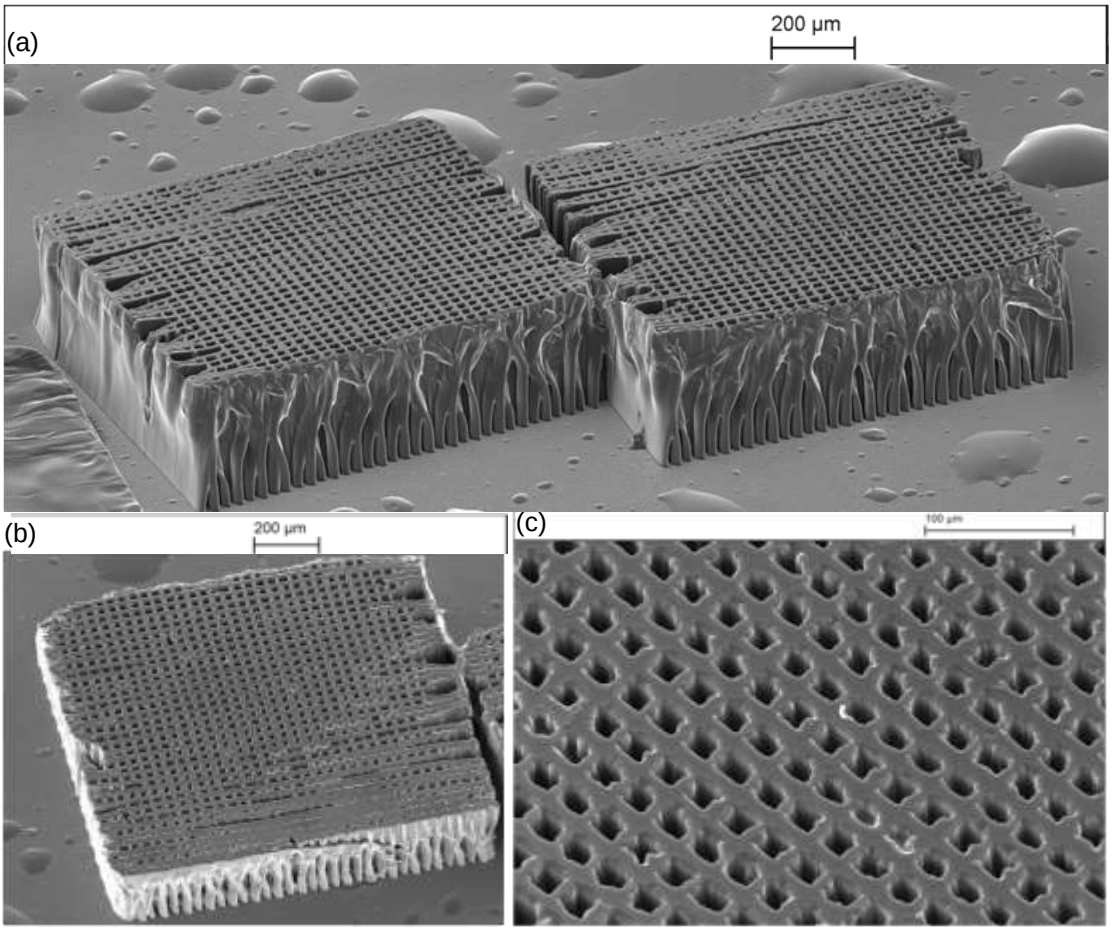

Figure 4-44 SEM images of a cell scaffold with 10-11µm pore size and 310µm depth. (a) 60^{o} tilted side views and (b) 30^{o} tilted side views (c) detail view at 30^{o}.

The purpose of the cell scaffold fabrication is to prepare structures which can provide temporary support for tissue regeneration and therefore should degrade later after healing. Keeping this in mind it is necessary to fabricate cell scaffolds using biodegradable photosensitive materials that can be fabricated with TPP techniques. Figure 4-45 shows SEM images of 305µm deep cell scaffold structures fabricated by two-photon polymerization process of Ethoxylated Bis Phenol A Dimethacrylate monomer used in this study. After fabrication the non polymerized material was washed away with deionised water and the samples were dried at room temperature. Wrinkles on the side of cell scaffold and slight breakage of the structures can be seen in the figure due to capillary forces [46]. This slight deformation and wrinkles indicate that the produced structures are elastic and shrink during water evaporation. The monomer used in this study has 6 units of Ethoxylation and therefore has lower cross-linking density [90] as the degree of conversion depends upon the level of ethoxylation. When the

fabricated structures were allowed to soak in water for a few days they showed disintegration and deformation. This mechanical instability of the structures upon soaking indicates weak cross-linking. Therefore it can be recommended that this weakly cross linkable dimethacrylate based monomer is a suitable material for the fabrication of support structures as biodegradable scaffolds.

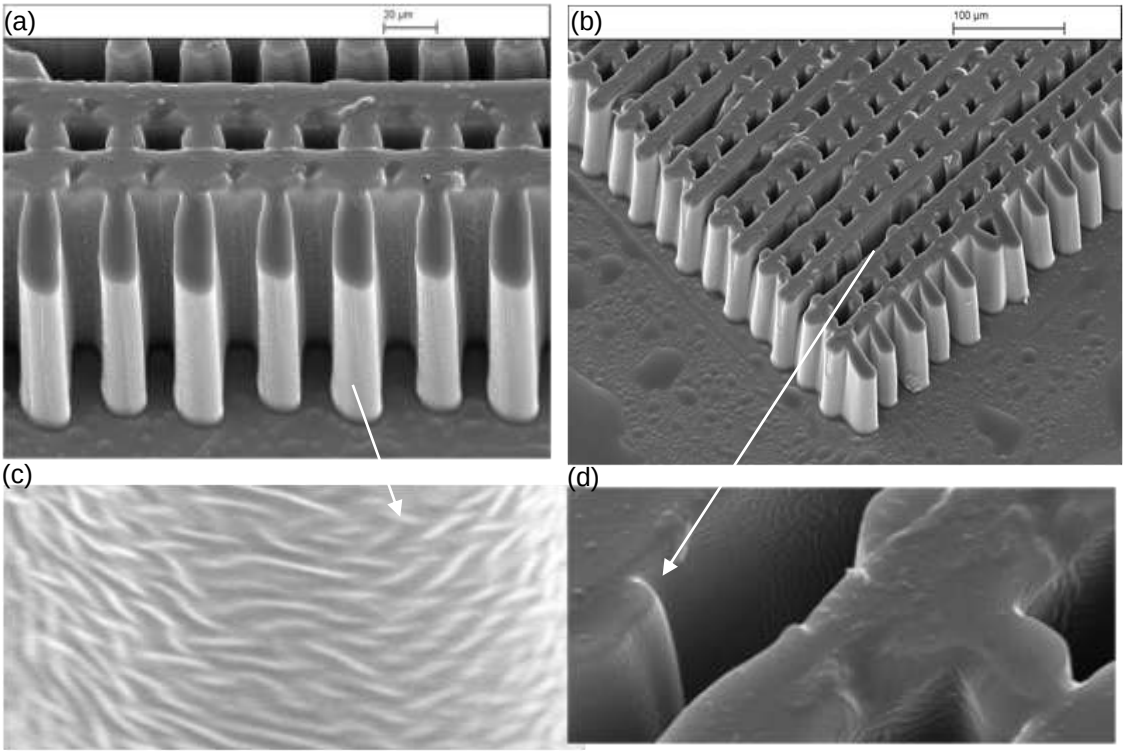

Figure 4-45 A 305µm deep and 15-16µm wide pore size cell scaffold structure fabricated by two-photon polymerization. Cell structure fabricated using a “step-and-repeat” building strategy. Structures show (a) wrinkles and shrinkage (b) breakage and deformation (c) detailed view of wrinkles on the scaffold (d) detailed view of breakage of the scaffold.

All the above scaffolds were fabricated in a layer by layer manner and the features were fabricated on the basis of desired geometry and pore sizes by choosing appropriate dimensions. These features were fabricated at 413µW with 100mm/min scanning speed using 160fs laser pulses from the Ti: sapphire laser source at 710mW average laser power. In order to get deep scaffold the height of the liquid on the substrate was increased using three ring spacer instead of one. The features fabricated were 1mm^2 in size and 305µm in height and the fabrication time was short i.e., ≈ 1 minute.

SEM images of approximately 85µm deep structures produced are shown in Figure 4-46. These 1mm^2 cell scaffold structures were fabricated with a speed of 100mm/min. The distance between each line drawn in the scaffold is 0.04mm which made it possible to get pores size of approximately 13µm horizontally and 12µm vertically with approximately 10 to 14µm ridges between them as can be seen in Figure 4-47. Small pore sizes are chosen in order to provide structures where cells might adhere and flourish. Cell scaffolds with such pore size are suitable for the cell possession and growth especially for the generation of fibroblast [46].

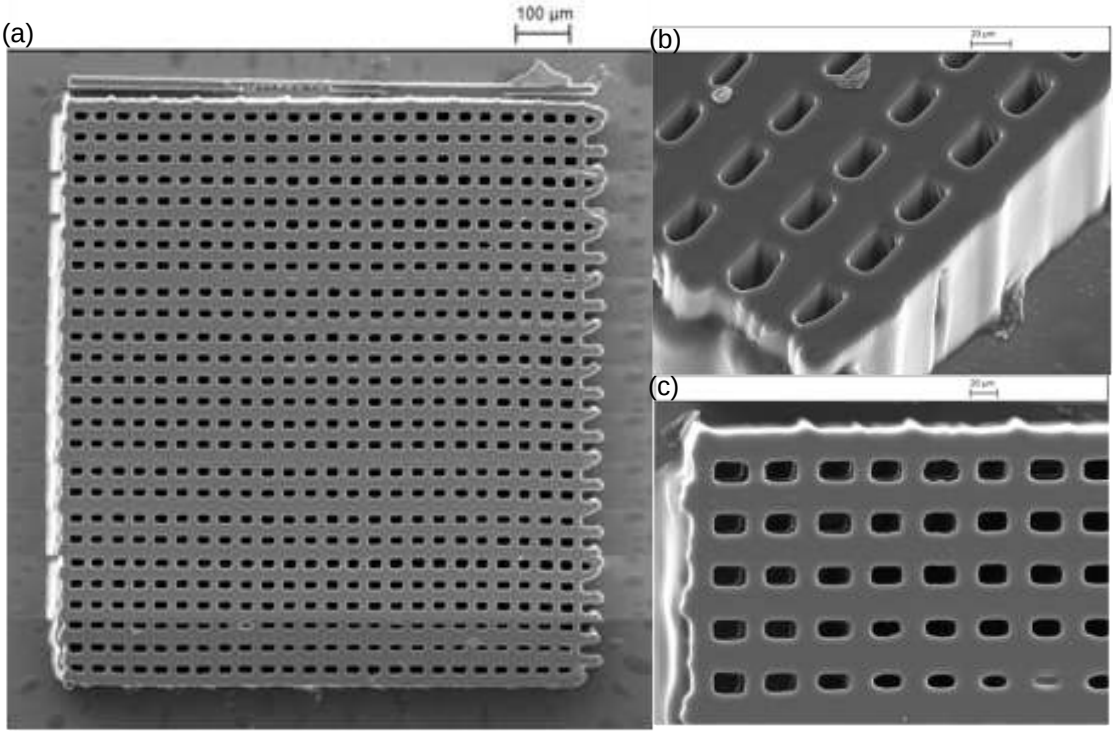

Figure 4-46 (a) Top view (b) side view and (c) detail view of a 3D structure fabricated using two-photon polymerization. Cell scaffolds with small pore size suitable for the cell possession and growth especially for the generation of fibroblast.

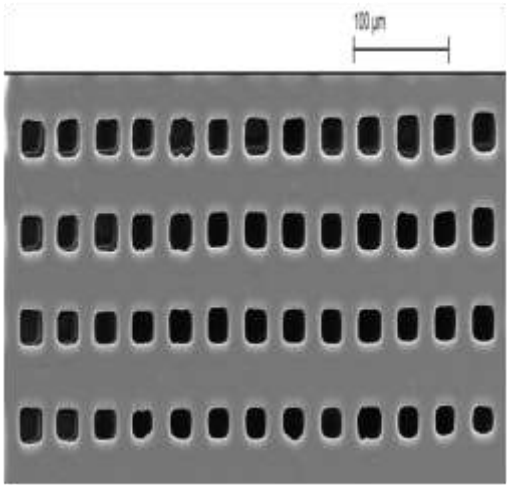

Figure 4-47 Top view of the tissue scaffold having 14µm pore sizes with 10µm ridges suitable for liver as well as fibroblast

Compared to conventional photo-lithography which is a planar processing, two-photon polymerization is a real three-dimensional volume microfabrication technique. These technologies can be used for rapid prototyping and low-cost fabrication of artificial micro- and nanostructure components which are required for different applications in optics, medicine, and biology.

Chapter 5 Subtractive patterning

Lasers are often used in different experimental configurations and processes, for just to remove material following a desired pattern. Laser ablation is removal of material due to light interaction and depends on many parameters such as, beam characteristics and surrounding conditions. Key features of the beam characteristics are choosing a wavelength that has strong absorption in the target material corresponding to a minimum absorption depth, short pulse duration, rapid pulse repetition rate, and good beam quality. Removal of material by this method involves both photochemical and photophysical mechanisms [91].

In order to ablate a surface, the maximum laser fluence must exceed some threshold value required to bring about change in the material surface. This modification threshold fluence depends on the material characteristics, number of applied pulses and the angle of incidence of the radiation [92]. When a laser beam of Gaussian intensity profile is made incident on a material, the size of the damaged site depends on the threshold level for that material relative to the peak intensity. When laser pulses from a Gaussian spatial beam profile are made incident on a material, the maximum laser fluence F_o on the sample surface and the radius r of the profile are related as

$$F(r) = F_O\, e^{-2r^2/\omega_0^2} \qquad 5.1$$

For a process with threshold fluence, F_{th}, the radius of the damaged site can be found by equating F_{th} to equation 5.1 and solving for, r. This gives:

$$r^2 = \frac{1}{2}\omega_o^2 \ln\frac{F_o}{F_{th}} \qquad 5.2$$

As it is easier experimentally to measure the diameter of laser induced material removal or surface changes, it is helpful to recast this equation in terms of a "damage" diameter, D, so that,

$$D^2 = 2\omega_o^2 \ln\frac{E_0}{E_{th}} \qquad 5.3$$

Here, the common areas of F_0 and F_{th} have been cancelled to give the equation in terms of pulse energy which, again, is experimentally easier to determine.

Noting that by integration it can be seen that the peak fluence or energy is twice the average value for the Gaussian distribution it is possible to write

$$F_{th} = \frac{2E_{th}}{\pi\omega_0^2}$$

Now by plotting D^2 as a function of ln E_o it is possible to obtain the laser spot size from the gradient and threshold fluence from the intercept with the energy axis.

The studies in this chapter consider the ablation of two material systems. Firstly the patterning of thin keratin films has been explored in order to manufacture model skin surfaces based on the "bricks and mortar" view of the relationship between keratin and lipids. Also, ablation at oblique angles has been studied. Such interactions are found during laser procedures with the eye that require scanning of the beam. Polyimide has been used as an analogue for the eye in this case.

5.1 Direct-write ablation of keratin thin films

Laser processing has been used for microfabrication, thin film deposition, particle formation, etching and cleaning in the field of organic / inorganic materials. In the field of biomimetics and bioelectronics, interest in laser processing of biomaterials has increased [93]. This chapter describes laser processing of keratin films of different thicknesses. Keratin is an extremely strong protein found in skin, hair, nail and teeth. Solid keratin can be extracted to produce a solution for sample preparation [94]. The keratin of the outer layer of human skin refers to a family of fibrous structural proteins. The unique properties of the protein are due to different levels of amino acids which combine to form keratin. The levels of amino acids present dictate whether the keratin will be soft and smooth. The protein content in these keratinized structures is about 80% of the total mass [94]. Epidermis, the outer most layer of human skin, is composed of keratinocytes where keratin filaments are abundantly present.

The skin is a complex human organ and acts as a barrier to protect the body from serious health problems. For example

- It prevents loss of moisture

- Provides protection against thermal, physical, and mechanical injury
- Regulates temperature
- Provides protection against infection
- Protects from the harmful effects of UV radiation
- Produces Vitamin D
- Is a sensory organ [95]

In the epidermis, cells are arranged like a brick wall structure. Due to the degradation of the cells the outer most skin cells are continuously being replaced by new skin cells. During this renewal process keratinocytes at the bottom rise to the top and the old cells shed from the surface in the form of dead cells [96].

To understand the barrier function of the skin, the outer most layer of the skin can be considered as a brick wall. Keratinizing epithelium together with their intercellular lipid surroundings protects the body from water loss and protects from mechanical, chemical and physical injury. Keratin forms the bricks and the gaps between these keratin bricks are filled with a double layer of lipids and water which act like mortar [97]. This extremely tough protein/lipid polymer structure provides a barrier [98] as shown in Figure 5-1. Without moisture and enough oil the skin structure is weak, and water can get through making it dry, itchy and sometimes red. Applying an emollient to skin fills up the gaps like mortar and makes it strong and water tight as shown in Figure 5-2 (a) and (b).

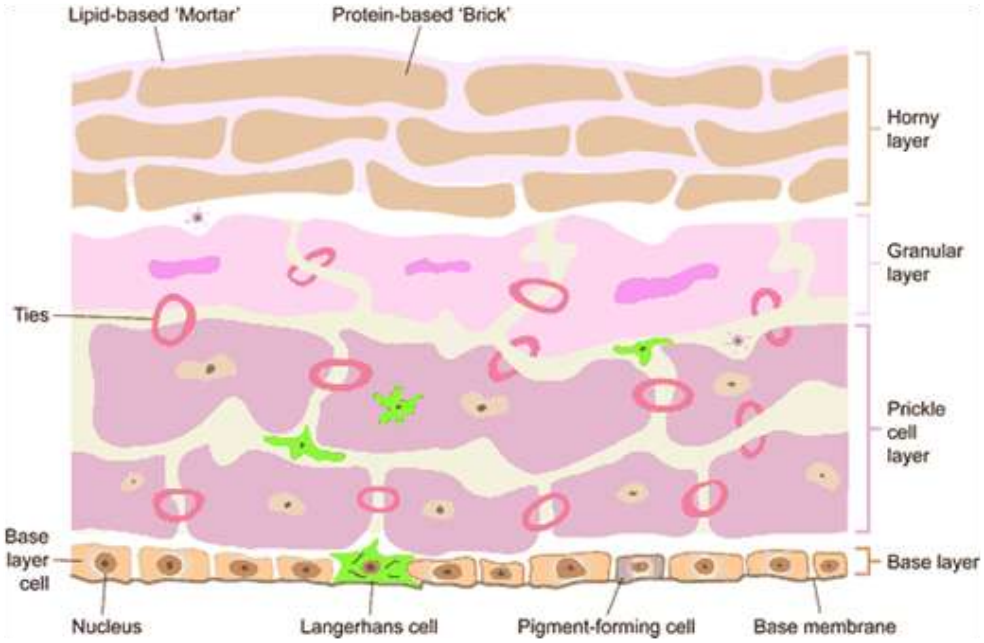

Figure 5-1 Schematic diagram of the structure of skin. The outer most layers are composed of Keratin based bricks with lipids as mortar [97].

(a) (b)

Figure 5-2 (a) skin like brick wall without enough mortar (b) Brick wall is strong and water tight with mortar [99].

5.1.1 Material and structure

In epithelial tissue of human skin keratin is composed of intermediate filament (IF) containing Type I keratin with molecular weight 40-50 kDa, Type II keratin molecular weight 55-65 kDa, matrix proteins (10-20 kDa) (high cysteine) and 6-9 kDa proteins. The final keratin structure is complex and has cross linking with disulfide bonds [94]. For laser processing of keratin it is important to extract solid keratin from the hard parts of the body and generate a liquid form for the preparation of keratin samples with required thicknesses. A scheme for cross linking due to cystine in keratin is shown in Figure 5-3 .

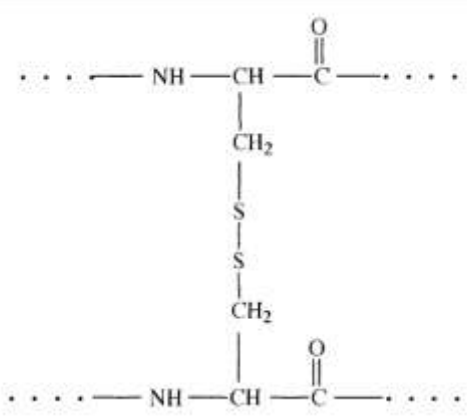

Figure 5-3 A scheme of cross linking due to cysteine in keratin [93]

5.1.2 Sample preparation

Liquid keratin was prepared from keratin powder extracted from wool and was supplied by TCI, Europe containing a quoted protein content of 85%. In order to prepare samples for keratin ablation, 250 μl of a mixed solution containing 1 mg ml^{-1} keratin protein and 2.5 wt% H_2O_2 is placed on a quartz plate of 25 × 25 mm^2, and dried in a thermostatically controlled box at 35 ^oC for an hour after pouring excess liquid from the substrate. The thickness of the sample was measured using a stylus profilometer (DektakTX) and was found to be 70nm. In order to prepare thicker keratin films, 150μl of liquid keratin was put on the quartz substrate of the same size and was allowed to become dry without pouring it from the substrate. The thickness of the sample was found to be approximately 250nm.

5.1.3 Experimental setup for femtosecond laser ablation

In order to study the threshold energy and threshold fluence for laser processing of the keratin film, the procedure derived at the beginning of this chapter was used. Figure 5-4 shows the experimental setup comprising of the femtosecond laser source. Keratin films with different thicknesses were ablated at 800 and 400nm wavelength. A Ti: sapphire femtosecond laser system (Spectra Physics) Hurricane X with a wavelength of 800 nm and pulse energies up to 560 μJ was used for ablation experiments.

The laser pulses at 400nm wavelength in the energy range 310nJ to 37nJ were applied to the front side of the target via a 0.25 N.A lens using a direct focusing technique. Keratin films were also ablated at 800nm wavelength with pulse

energies in the range1µJ to 400nJ. The pulse power of the laser incident on the keratin film at the rate of 1 kHz was measured after focus using a Newport (model 840 IRVINE CA) optical power meter. The pulse duration of the incident laser was measured and found to be 160fs. The keratin film was prepared on a quartz substrate with different thicknesses by putting 250µl and 150µl liquid keratin and was dried as described in section 5.1.2. The keratin sample was mounted normal to the optical axis on an x-y-z translational stage and for each pulse energy selected by neutral density filters, single pulses were used to irradiate the film. Five repeats were made at a spacing of 0.5mm with the same pulse energy. The ablated areas were analysed with the help of a Leica DM LM optical microscope and the average diameter was calculated for the same pulse energy. In order to study the morphological characteristics of surface damage structure, the samples were also analysed using a scanning electron microscope. The thicknesses of the keratin films had been measured with the help of a stylus using DektakTX and were found to be 250nm and 70nm as stated earlier.

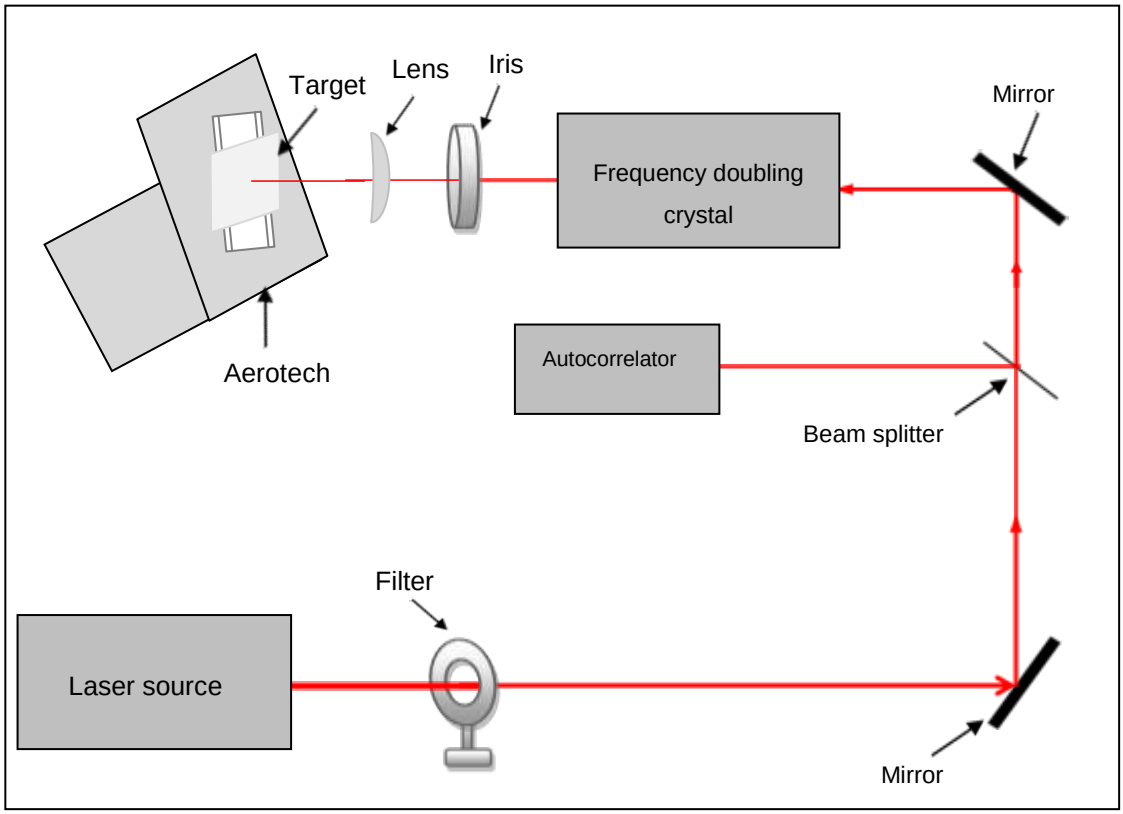

Figure 5-4: Schematic diagram showing experimental arrangement for the ablation of keratin films. The frequency doubling crystal was used for second harmonic generation (400nm) for some of the experiments.

5.1.4 Femtosecond thin film interactions at 800nm

Laser pulses from the Ti:sapphire regenerative amplifier system at 800nm wavelength with pulse duration of 160fs were focussed on the keratin sample using a 0.25N.A. lens. Keratin films with different thicknesses were ablated with laser pulses in the energy range 1µJ to 400nJ. It was possible to remove the thick keratin film with a single pulse. Examples at different pulse energies are shown in Figure 5-5 and thin film ablation is shown in Figure 5-6. The area ablated with 1mW power is shown in Figure 5-5(a) along with the detail of the damaged surface. Holes in the surface of the substrate appear and molten keratin material in the central, high-fluence region and [100] the high temperature region is deposited. At low power, such as 670µW, the keratin film has been completely ablated without any damage to the surface as shown in Figure 5-5(c).

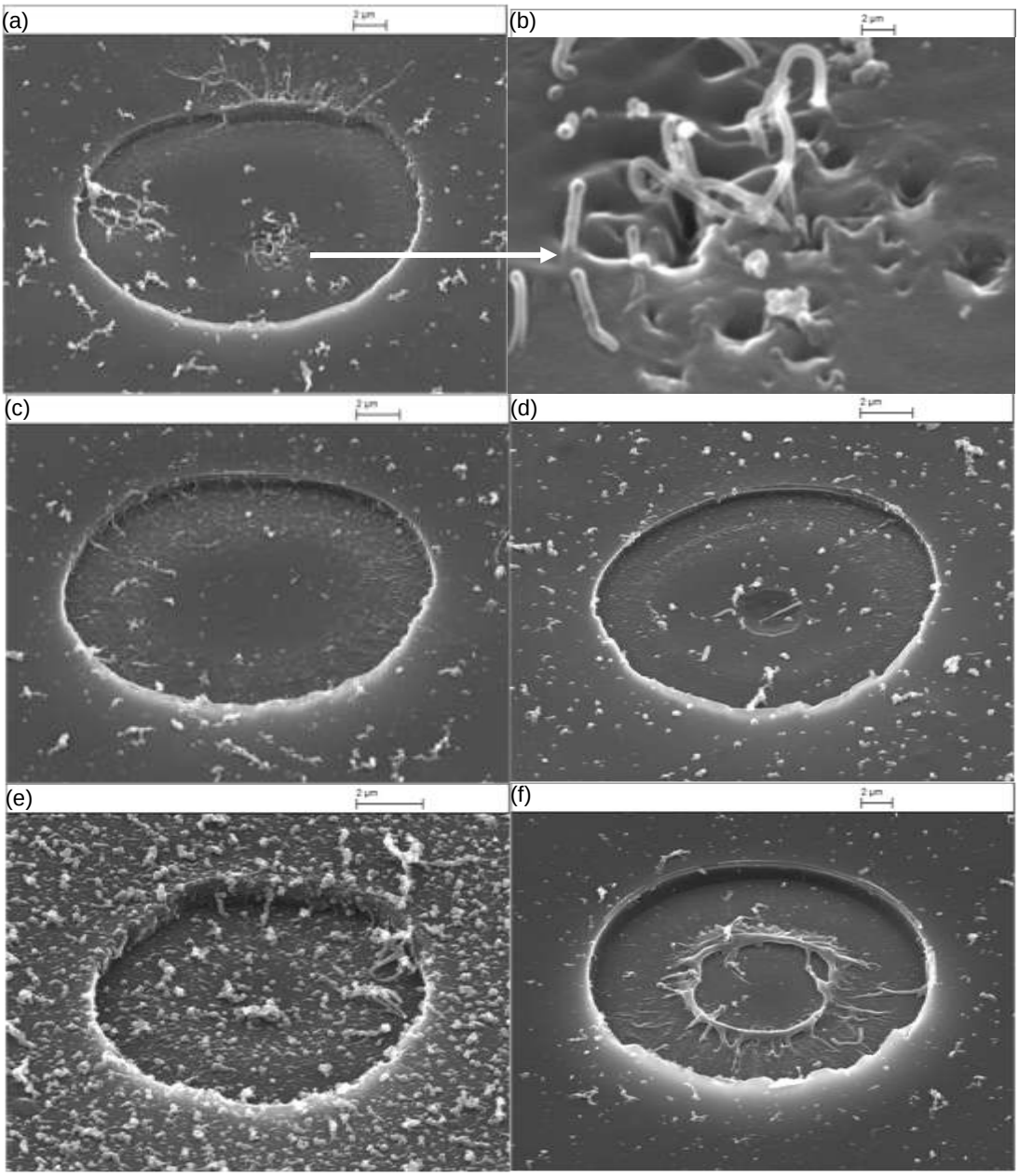

Figure 5-5 SEM image (viewed at 45^{o}) of a thick layer of keratin ablated by single pulse at 800nm wavelength using energy (a) 1µJ (b) detailed structure of the damaged substrate surface(c) 670nJ (d) 547nJ (e) 410nJ (f) ablated area with large power.

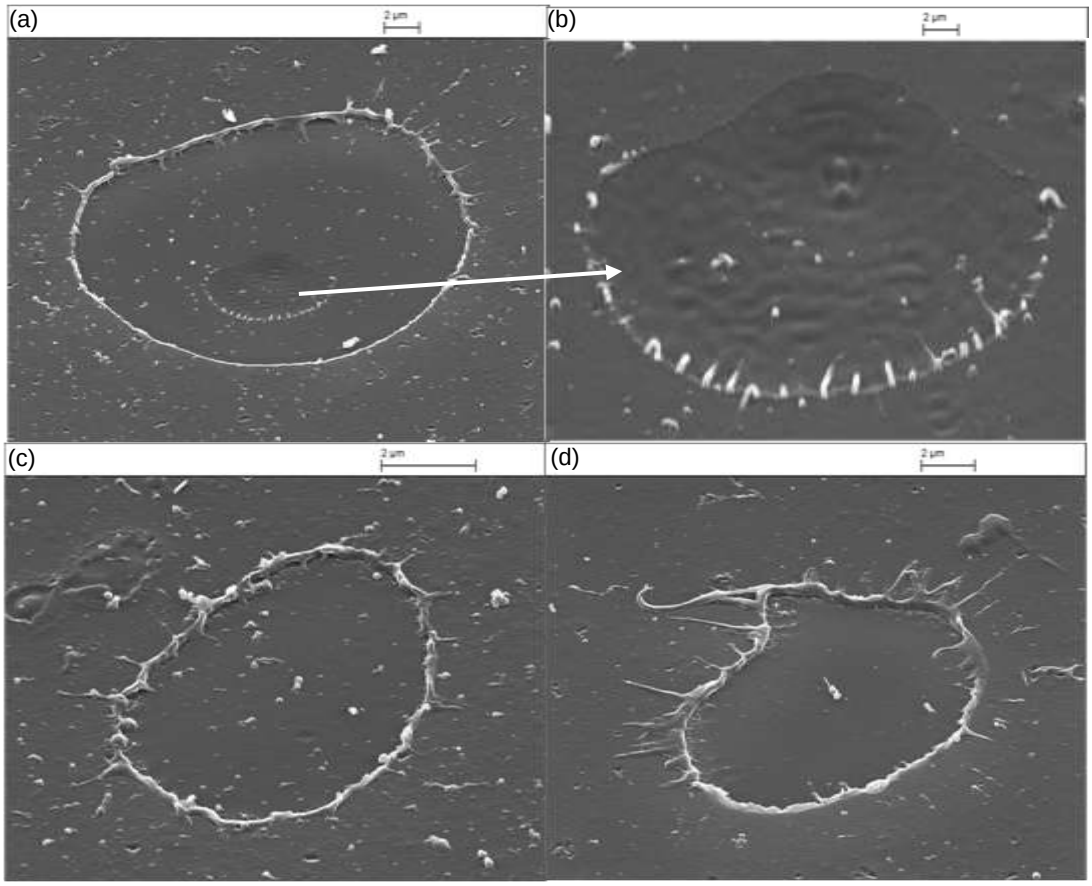

Figure 5-6 SEM image of a thin layer of keratin ablated by single pulse at 800nm wavelength. (viewed at 45^{o}) SEM image of the ablated area at (a) 1µJ (b) shows detail structure of the damage area (c) 450nJ (d) 410nJ

The threshold energy E_{th} was estimated by extrapolation of the fits to squared diameter $D^2=0$ as shown in Figure 5-7 and Figure 5-8. The slope of the linear fit gives a Gaussian beam radius $\omega_{o.}$ for thick film of approximately 12µm and the threshold energy E_{th} was found to be 247nJ. The area of the semi elliptical spot was calculated as $\pi (a+b)^2$ where "a" denotes major axis and "b" denotes minor axis. The threshold fluence was found to be 120mJ/cm^2. For the thin film, the Gaussian beam radius ω_o was found to be approximately 14µm and the threshold energy was found to be 350.7nJ while threshold fluence was found to be 100mJ/cm^2. As the optical system was not altered between these two samples it is to be expected that the laser spot size should be constant. This can be seen to be the case if experimental errors (e.g. repositioning the sample in the focal plane) are taken into account.

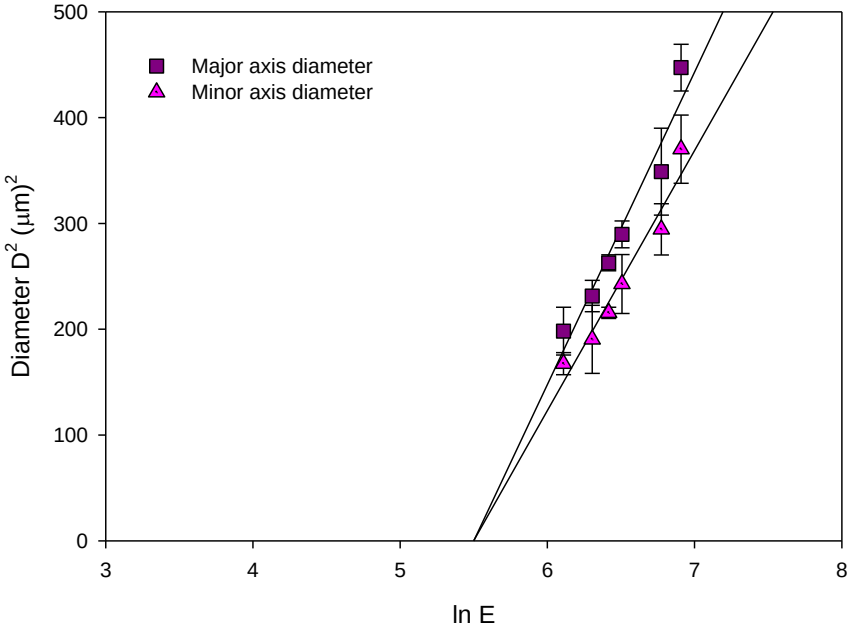

Figure 5-7 Keratin thick layer ablation. The thickness of the film is approximately 250nm measured by DektakTX. Threshold energy was 247nJ while the threshold fluence was 120mJ/cm^2 at 800nm wavelength. The error bars indicate average diameter of the area ablated with single pulse at same pulse energy.

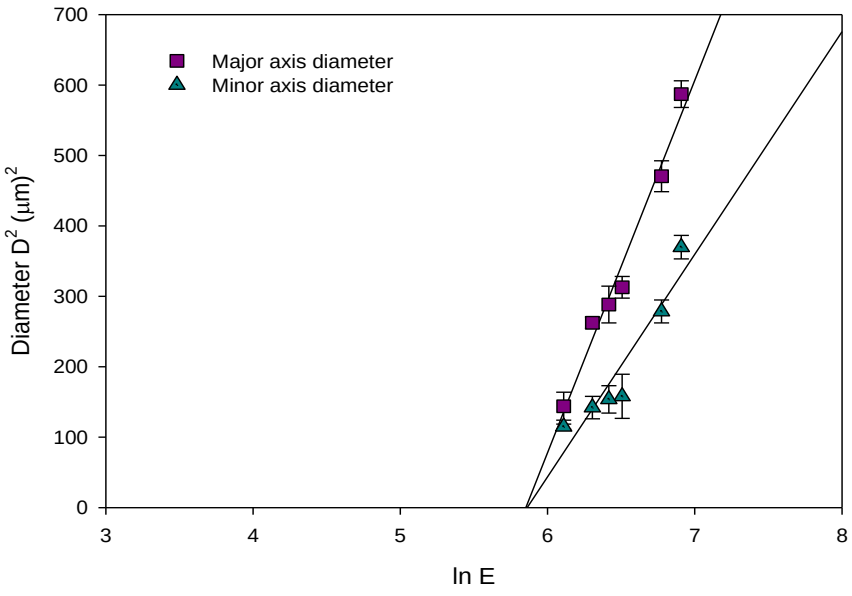

Figure 5-8 Keratin thin layer ablation. The thickness of the film is approximately 70nm measured with the help of DektakTX. Threshold energy was 350.7nJ while the threshold fluence was 100mJ/cm^2 at 800nm wavelength. The error bars indicate average diameter of the area ablated with single pulse at same pulse energy.

5.1.5 Femtosecond thin film interactions at 400nm

For further investigation, keratin films were ablated from the same source at 400nm wavelength using a frequency doubling crystal. Laser pulses at 400nm wavelength generated by second-harmonic conversion of the femtosecond laser output were allowed to focus on the keratin sample using a 0.25N.A. lens as stated earlier. The sample was ablated by single pulses in the energy range 37nJ to 310nJ. The major axis and minor axis of the ablated spots were measured with the help of optical microscopy and areas of the slightly elliptical ablated spots were calculated. The sample was analysed with a scanning electron microscope to study the morphological characteristics of surface damaged structures and the change in spot size with change in pulse energy. The sample was analysed at an angle of 45^{o}. The ablated sites shown in Figure 5-9 indicates that the size of the ablated spots decreases with decrease in energy and that the keratin film was removed from the quartz substrate at pulse energy greater than the threshold energy. At high beam intensity bubbles can be seen in Figure 5-9 (a) in the centre of the ablated area. At a pulse energy slightly greater than the threshold energy, the keratin film is completely removed without damaging the substrate and no bubble formation was found as shown in Figure 5-9(b, c). When the sample was processed with pulse energy close to the threshold energy, the film was removed completely in the centre and was partially removed along the periphery of the damaged spots as shown in Figure 5-9(d).

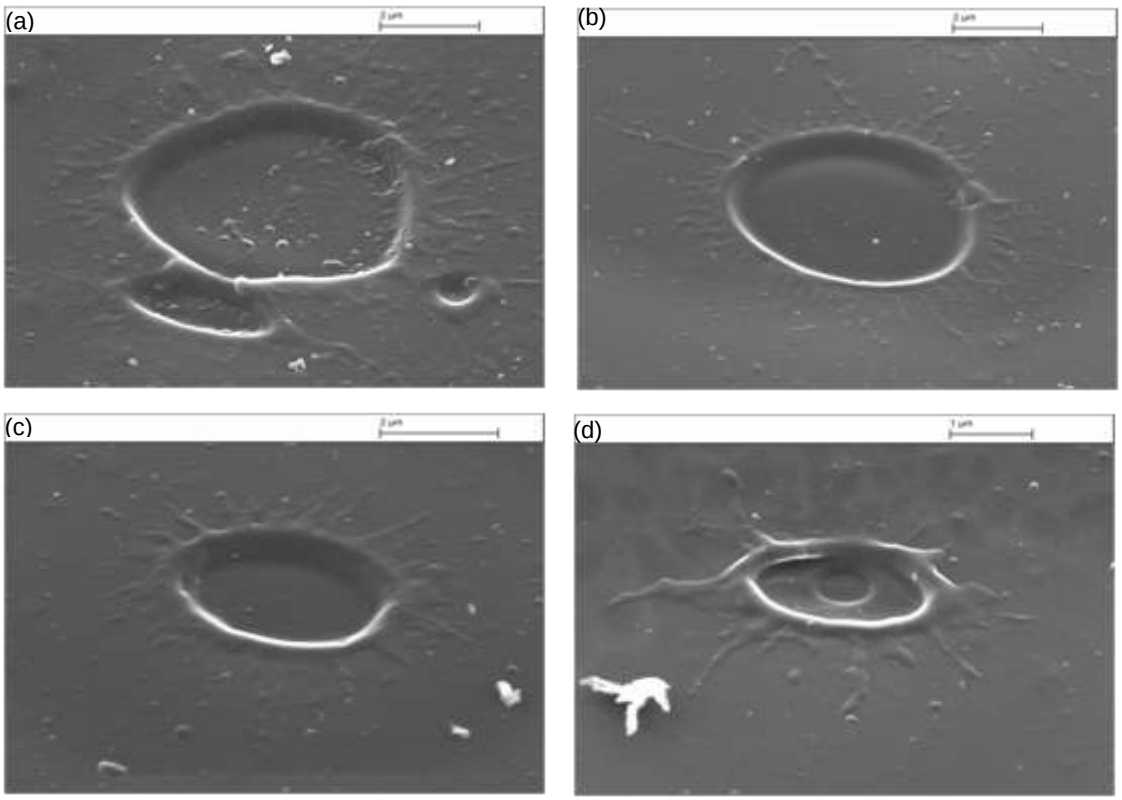

Figure 5-9 SEM images of keratin thick layer ablated by single pulse at 400nm wavelength generated by using second-harmonic conversion of the femtosecond laser output. (viewed at 45^{o}) SEM image of ablated area at (a) 310nJ (b) 250nJ (c) 41.5nJ (d) 39nJ

The natural logarithm of energies was plotted against squared diameter of the ablated area D^2 as shown in Figure 5-10 and Figure 5-11. The error bars in the figure represents slight variation in the measured diameters of the area ablated with single pulses but with the same pulse energy. The threshold energy was obtained from the intercept of Figure 5-10 and Figure 5-11. The Gaussian beam radius from the gradient of the graph for the thick film was found to be approximately 5.5µm. This is smaller than the result for the 800nm interaction but is to be expected as the size of the beam waist depends linearly on the laser wavelength. The threshold energy measured for the thick keratin film with thickness 250nm was found to be 36.5nJ while the threshold fluence was found to be $80mJ/cm^2$ when ablated at 400nm wavelength. The Gaussian beam radius for the thin film experiment was found to be approximately 9µm which is somewhat larger than the thick film case. While the threshold fluence for the keratin thin film with thickness 70nm when ablated at 400nm wavelength

femtosecond laser was found to be 35.65nJ and the threshold fluence was found to be 30mJ/cm^2

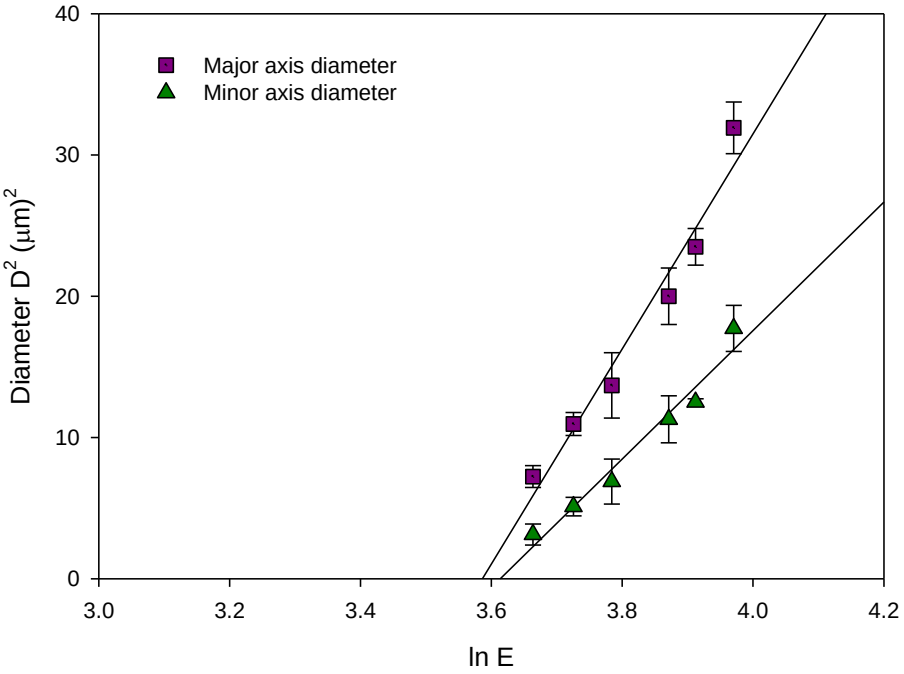

Figure 5-10 Keratin thick layer ablation. The thickness of the film is approximately 250nm measured with the help of DektakTX. Threshold energy was 36.5nJ while the threshold fluence was 80mJ/cm^2 at 400nm wavelength. The error bars indicate average diameter of the area ablated with single pulse at same pulse energy.

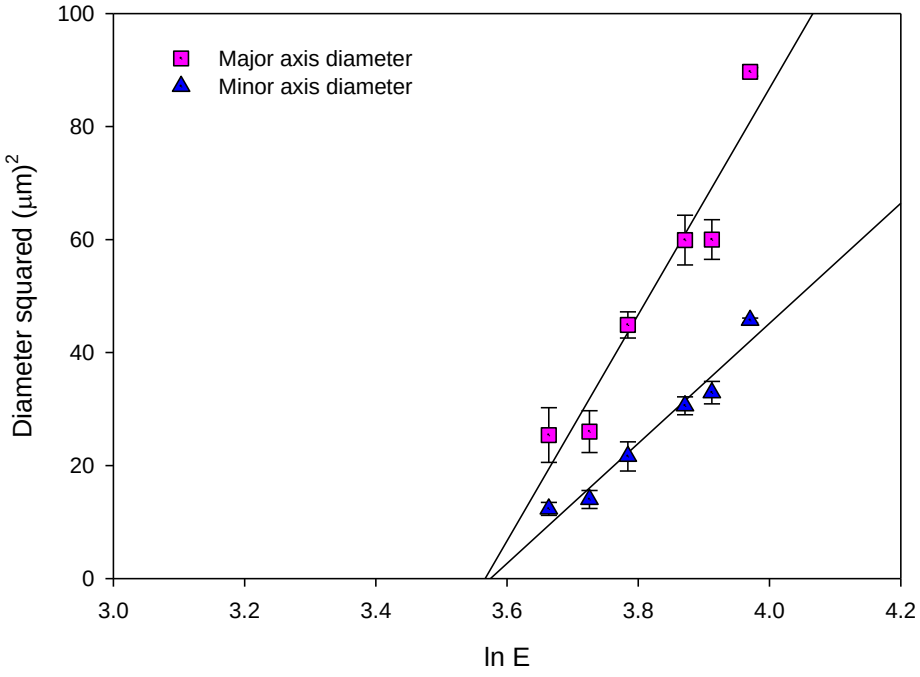

Figure 5-11 Keratin thin layer ablation. The thickness of the film is approximately 70nm measured with the help of DektakTX. Threshold energy was 36.65nJ while the threshold fluence was 30mJ/cm^2 at 400nm wavelength. The error bars indicate average diameter of the area ablated with single pulse at same pulse energy.

5.1.6 Brick-and-mortar structure fabrication

Laser processing of keratin has been used to investigate effects of cream on human skin by building a model skin structure. Keratin films with 250nm and 70 nm thicknesses were ablated to fabricate a bricks and mortar pattern structure. A near infrared mode-locked Ti: Sapphire femtosecond laser of wavelength 800nm with 160fs pulse duration and 1 kHz repetition rate has been used for the fabrication of structure. The sample was mounted on a computer controlled X-Y-Z translation stage (Aerotech linear motor stages with NPAQ controller) to allow translation of the sample through the laser beam with preset velocity. The computer controlled stage has a resolution of 10nm and a maximum travel of 50mm.The laser pulses at 800nm wavelength with 41mW average power and with a stage velocity of 60mm/min were applied to the front side of the target focussed to small spots by a 0.25 N.A. lens using direct focusing technique. The power of the radiation incident on the sample at the rate of 1 kHz was measured after focus using a Newport (model 840 IRVINE CA) optical power meter.

Incident power on the sample was controlled with the help of attenuation filters and only 570nJ pulse energy was allowed to focus on the sample. In order to ablate keratin films in the bricks and mortar pattern, the laser pulses were made incident on the sample in the desired pattern by moving the computer controlled stage. Software Automation 3200 was used to control the movement of the stage in three dimensions. The sample was analyzed with a Leica DM LM optical microscope and scanning electron microscope (SEM). The brick and mortar structure fabricated in the thin keratin film at 800nm wavelength is shown in Figure 5-12. The threshold fluence for keratin ablation at 800nm wavelength is much larger and it can be seen that the quartz substrate is damaged during ablation process.

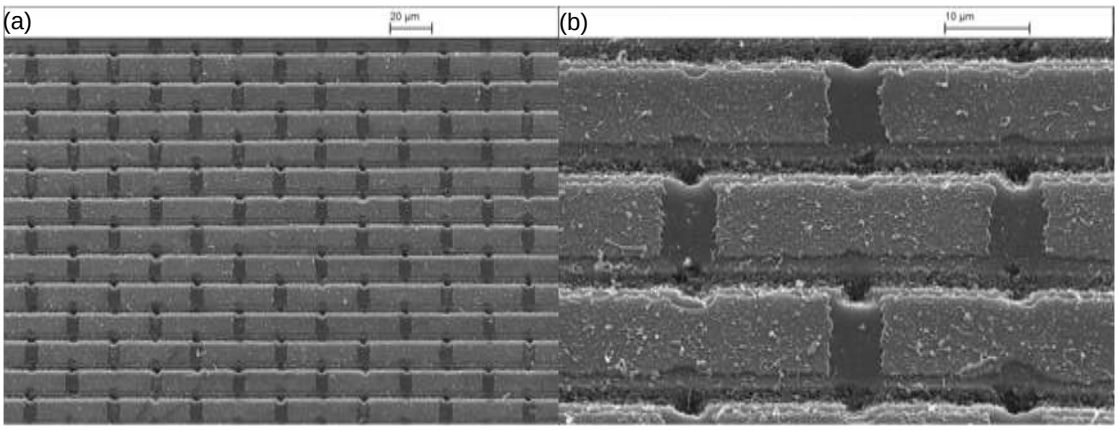

Figure 5-12 SEM images of brick and mortar structure in keratin ablated at 800nm wavelength. (a) Brick structures fabricated in film with thickness of 250nm with 41µJ pulse energy. (b) Detail of structure shown at higher magnification.

As the keratin film is quite transparent at 800nm it is difficult to localise the laser energy in the film and therefore damage to the substrate occurred. Changing to 400nm wavelength irradiation gave more reliable machining of the film without affecting the substrate integrity. The femtosecond laser beam at wavelength 800nm was made incident on the frequency doubling crystal to generate 400nm wavelength. The laser pulses at 400nm wavelength with 53µW average power were made incident on keratin films with 250nm and 70nmm thickness as shown in Figure 5-13.

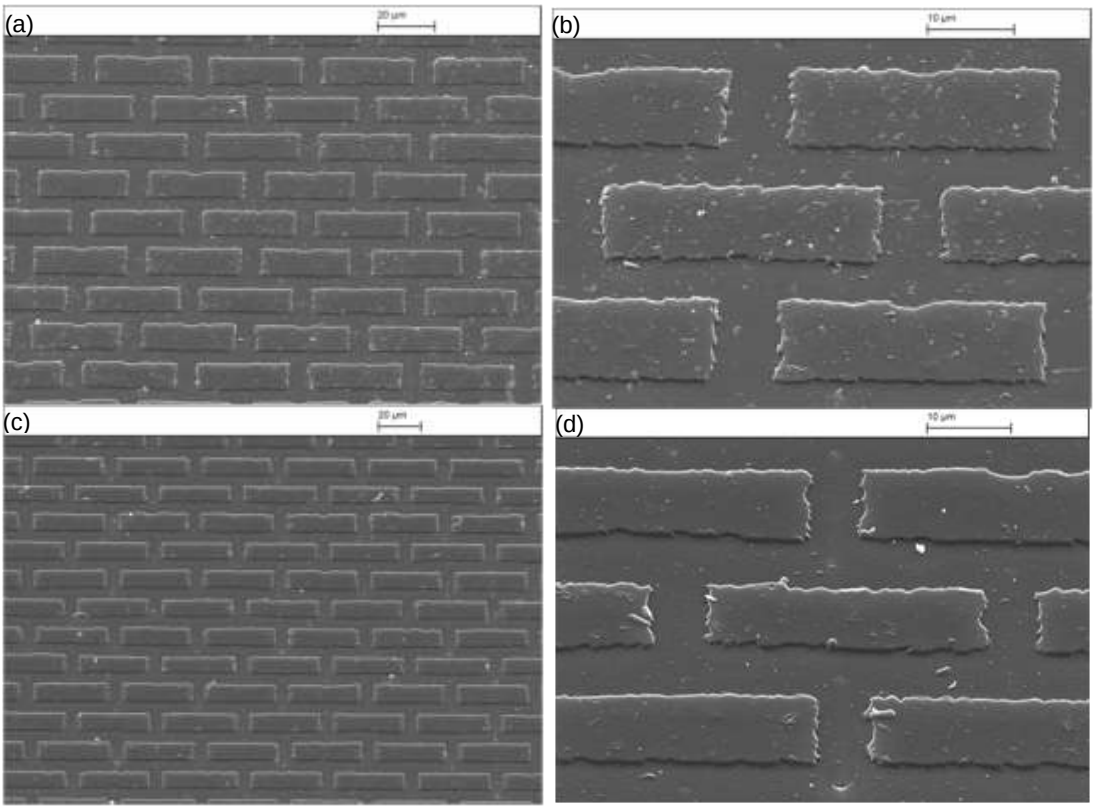

Figure 5-13 SEM brick and mortar structure in keratin film ablated at 400nm wavelength. (a), (b) shows bricks structures fabricated in thick film with thickness of 250nm with 53nJ pulse energy. (c), (d) shows bricks structures fabricated in thin film with thickness of 70nm with 53nJ pulse energy.

The structure was analysed using a white light interferometer to measure the surface topology and the result is shown in Figure 5-14. The depth has been found using DektakTX as shown in Figure 5-15.

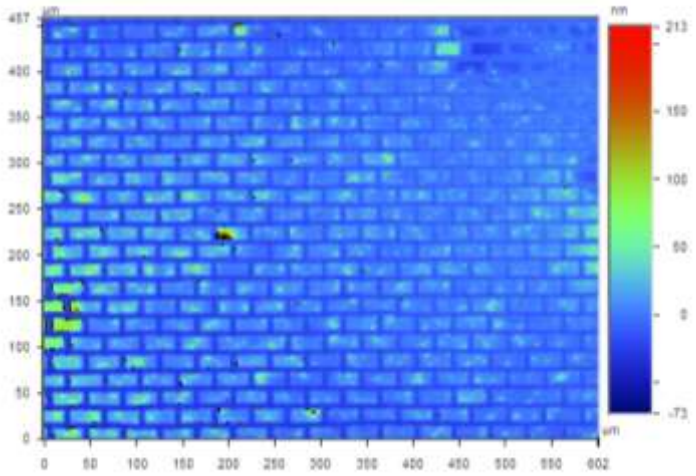

Figure 5-14 Brick and mortar structure fabricated in thin keratin film with 70nm thickness using femtosecond laser at 400nm wavelength as analysed by a white light interferometer for surface data.

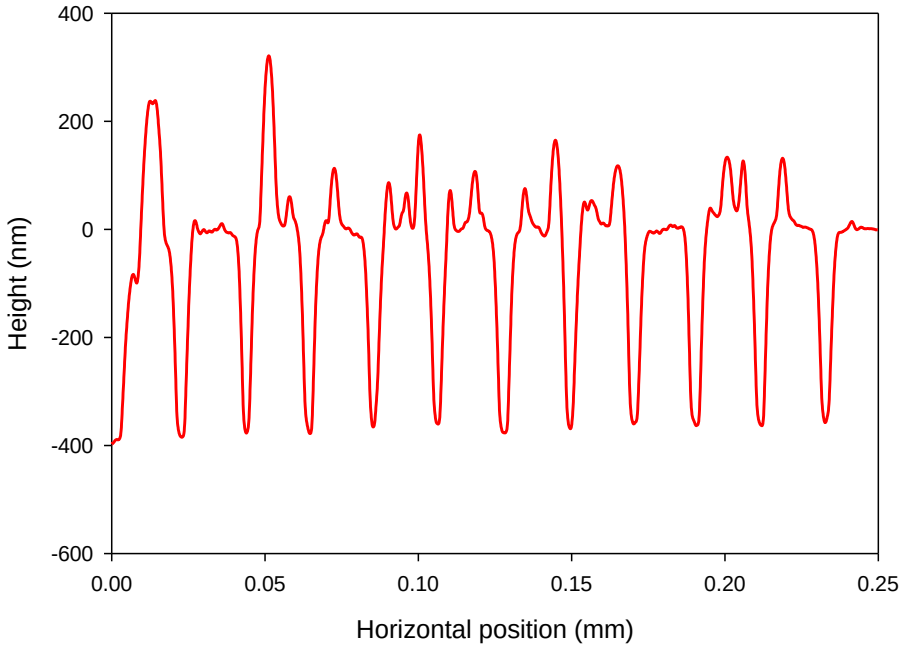

Figure 5-15 Stylus scan of the brick and mortar structure in thin keratin film with thickness of 70nm using DektakTX. The pulse energy was 53nJ and was ablated with 400nm wavelength generated by using second harmonic generator of the femtosecond laser system.

5.1.7 Comparison of interactions at 800nm and 400nm

The ablation of keratin films at 800nm and 400nm were compared and it was found that threshold fluence for keratin film ablation at 400nm is less than that

for 800nm and therefore for the fabrication of brick and mortar structure 400nm wavelength was used. Comparison of the results obtained for thick and thin film interactions at 400nm and 800nm wavelengths are shown in Table 5-1. The threshold fluence at 400nm wavelength for the thin film was 30mJ/cm^2 while it is 100mJ/cm^2 for 250nm thick film. This can be seen that thick film thickness is more than three times larger than the thin film and also the threshold fluence for thick film is more than three times than that of thin film. While for 800nm wavelength ablation the thick film ablation threshold was 120mJ/cm^2 and thin film ablation threshold was 80mJ/cm^2. This indicates that due to the higher penetration of 800nm wavelength, threshold fluence do not change as much according to the thickness of the material as shown below in Table 5-1.

Table 5-1 Comparison of threshold fluence at different wavelength using different thicknesses of keratin film

Wavelength	Film thickness	Threshold fluence	Beam radius (ω_o)
400nm	70nm	30mJ/cm^2	9µm
	250nm	100mJ/cm^2	5.5µm
800nm	70nm	80mJ/cm^2	14µm
	250nm	120mJ/cm^2	12µm

5.2 Projection etching of keratin thin films

5.2.1 Amplitude mask

For effective studies of skin treatments, large areas of model skin need to be generated. As the femtosecond system requires pulses to overlap the speed of the process depends on the spot size and laser repetition rate. The 10μm feature size (or smaller) specified for the model skin together with a maximum repetition rate of 1kHz meant that for square centimetre areas, several hours would be required. The use of an excimer laser with the ability to pattern square mm areas per pulse is therefore attractive even though the maximum repetition rates are typically an order of magnitude slower. As an initial investigation a contact mask was placed on the keratin film and the area flood illuminated with UV light. The argon fluoride laser was chosen as its short wavelength (193nm) is strongly absorbed in the film. The relatively transparent quartz substrate has a much higher ablation threshold and so damage to the substrate is unlikely. Figure 5-16 show ablation of keratin by the ArF laser using a simple contact mask. The sample, keratin film on quartz substrate, was ablated with one, two and five pulses with 173mJ energy.

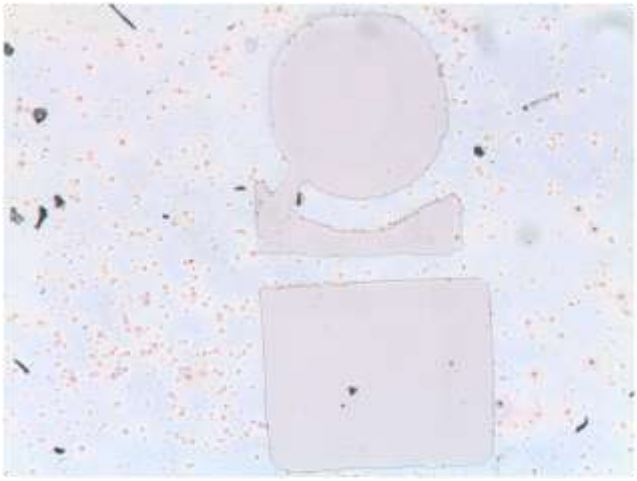

Figure 5-16 Keratin ablation by ArF Excimer laser at 193 nm wavelength using a contact mask. This image was obtained using an optical microscope. The size of the image can be seen in Figure 5-17.

The sample ablated at 193 nm wavelength was also analysed with the help of a white light interferometer WYKO NT1100. Surface data of the analysed sample is shown in Figure 5-17.

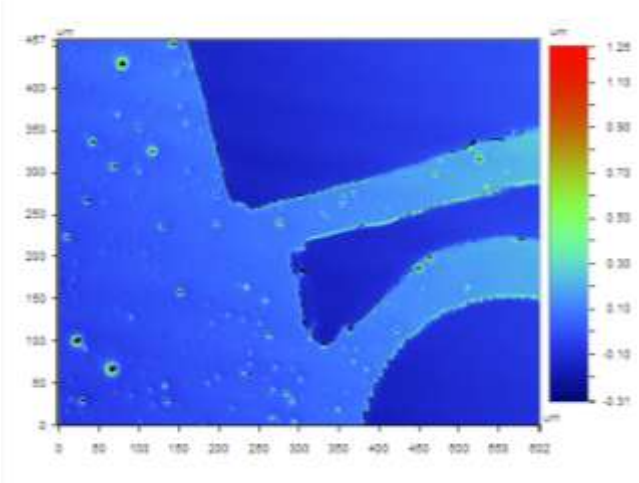

Figure 5-17 Surface data of the sample ablated by ArF Excimer laser at 193 nm wavelength using contact mask. The surface statistics of the ablated keratin sample have been analysed using a white light interferometer WYKO NT1100.

The depth of the ablated keratin layers with different pulses were also measured by scanning the sample using a Dektak KLA-Tencor. Figure 5-18 show ablation scan of the keratin sample. The sample was ablated with five pulses and the depth of the sample was found to be approximately 240 nm.

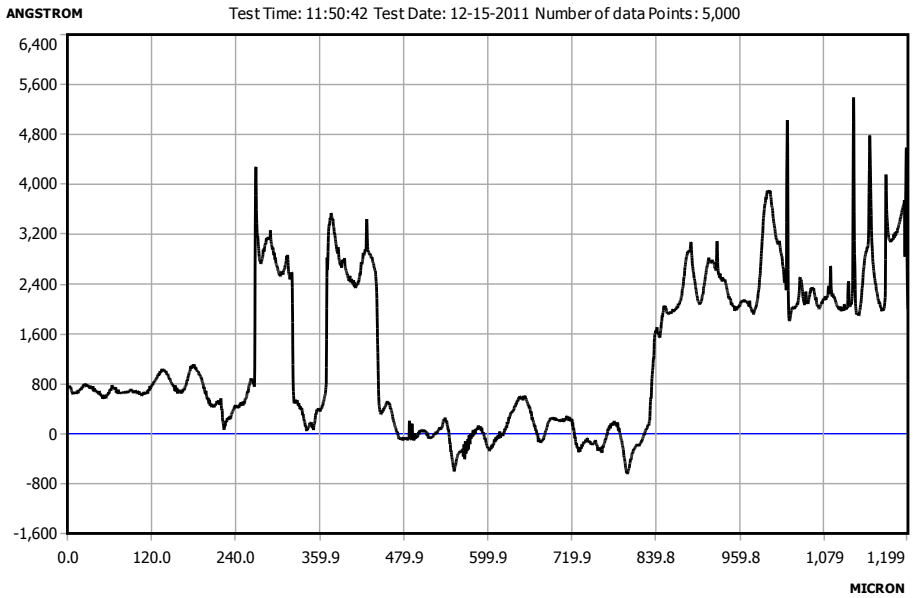

Figure 5-18 Scan of ablated areas on Keratin thick film irradiated with 5 pulses of Excimer ArF 193nm wavelength laser. The depth of the ablated layer is approximately 240nm.

The scan of the keratin sample ablated with 2 pulses is shown in Figure 5-19. The depth of the ablated layer was found to be approximately 190nm.

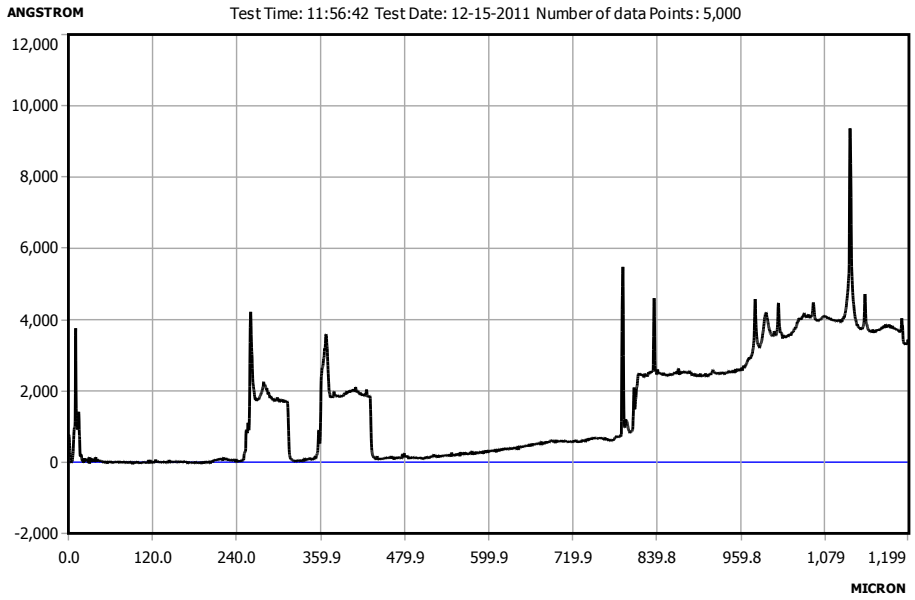

Figure 5-19 Scan of ablated areas on Keratin thick film irradiated with 2 pulses of Excimer ArF 193nm wavelength laser. The depth of the ablated layer is approximately 190nm.

Keratin samples with different film thicknesses were ablated with single pulse. The depth of the thick film with single pulse was found to be approximately 170 nm as shown in Figure 5-20 while the thin film ablation depth was found as 77nm as shown in Figure 5-21.

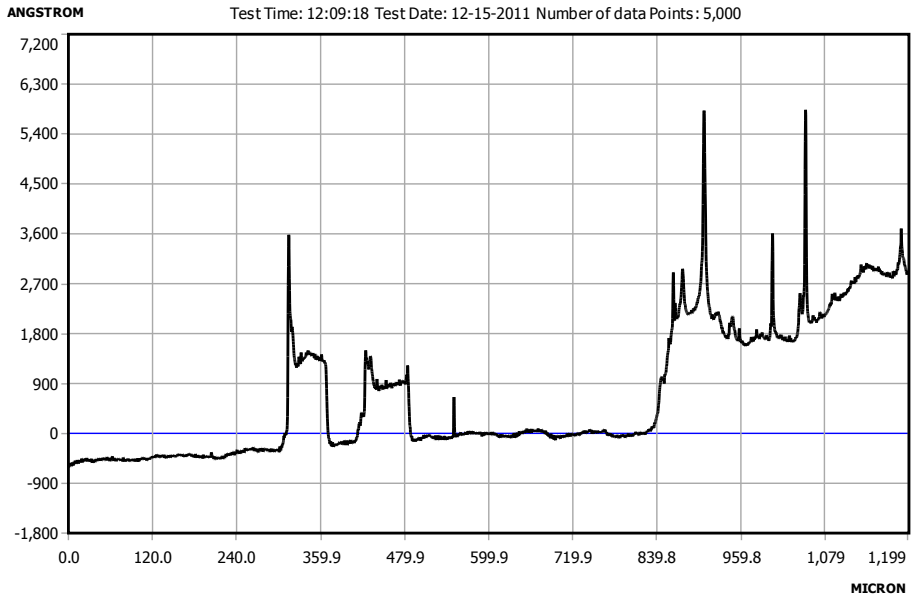

Figure 5-20 Scan of ablated areas on Keratin thick film irradiated with 1 pulse from the ArF 193nm wavelength laser. The depth of the ablated layer is approximately 170nm.

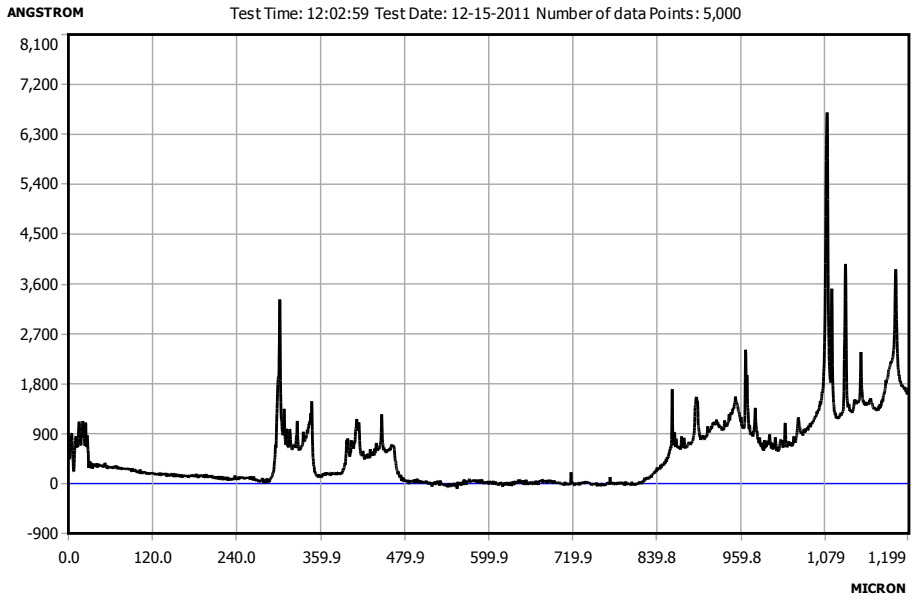

Figure 5-21 Scan of ablated area at the edge of the Keratin film irradiated with 1 pulse from the ArF laser. The depth of the ablated layer is approximately 77nm.

5.2.2 Phase mask

Ultimately, there may be a requirement to pattern the keratin at micron or sub-micron length scales. As the keratin can be fibrous in nature, it is not immediately possible to assert that the material itself can support such small features. Therefore, interference fringes were used to briefly explore if there is a limit to the resolution of patterns that could be generated due the film itself. A phase mask was placed in contact with the film and illuminated with the 193nm radiation. The mask was not optimised for this wavelength and so it was expected that considerable zero order light would be transmitted. This means that the fringe spacing was likely to have a strong irradiance at a period of 1μm. The resultant surface of the film after irradiation is shown in Figure 5-22. This SEM image indicates that approximately 1μm feature sizes can indeed be fabricated in the keratin material. More careful choice of mask and setup is required to see if this is the limit or not.

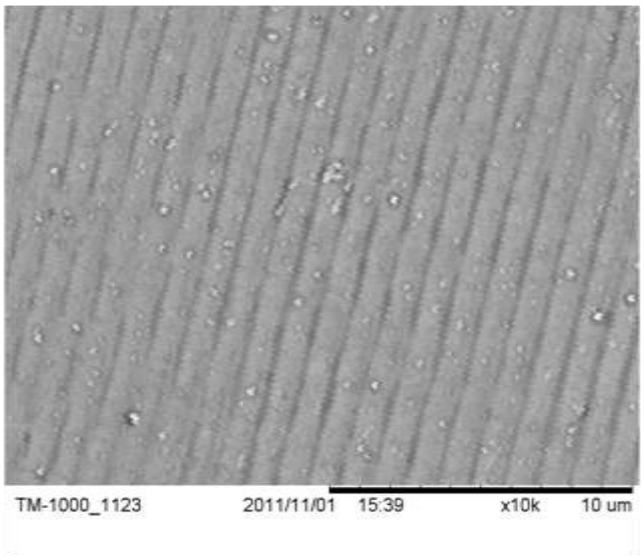

Figure 5-22 Keratin ablation using an ArF laser at 193 nm wavelength to illuminate a quartz phase mask placed in contact with the film.

5.3 Laser interactions at oblique angles

In this section ablation results of polyimide Kapton (HN) foils are presented. Processing of polyimide with high precision is required for electronics and industrial applications [92]. During laser ablation of polymers photochemical and photothermal effects can occur as compared to metal ablation where photothermal effects are prominent [91]. Polyimide, in this study, is considered as a model for corneal sculpting. Here we are concerned with affects that may occur when the beam is incident away from the surface normal. For nanosecond pulses, changes in the plume interaction have been cited as a mechanism for changes in ablation rate when the beam and plume are no longer aligned [101]. It is unlikely that this will be the case for femtosecond pulses as the plume expansion cannot be rapid enough to coexist with the incident laser pulse (assuming single pulse experiments). In order to measure the threshold fluence for ablation of polyimide (PI) the method presented earlier of measuring the damage diameter as a function of pulse energy was used but the setup modified to allow ablation at different angles of incidence.

A femtosecond laser system was employed to perform ablation experiments on Polyimide (Kapton HN) for single pulses at different angles. Polyimide (HN) is a general purpose film and can be used successfully at very low and very high temperatures due to its thermal stability and highly adaptable properties [92].

The chemical name for Kapton (HN) is poly (4,4'-oxydiphenylene-pyromellitimide) and its chemical structure is shown in Figure 5-23.

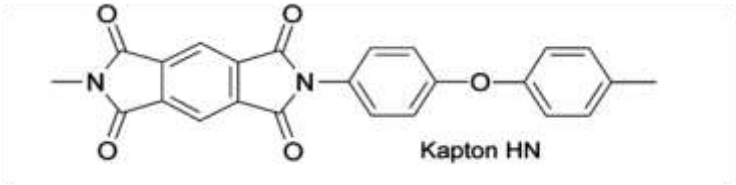

Figure 5-23 Chemical structure of polyimide Kapton (HN) [102]

5.3.1 Experimental Setup

The material used in this experiment is a thin film of polyimide Kapton (HN), Goodfellow, with 75µm thickness. The experimental set up is shown in Figure 5-24 and Figure 5-25.

A Spectra Physics, Hurricane X laser as previously described was used in these experiments. A 45mm focal length lens was used to focus laser light on a Polyimide (Kapton HN) sample. The laser pulses were focused through a hole on the front side of the sample mount onto the polymer attached to the back of the rotating holder. Laser pulses with different pulse energies were allowed to fall on the target at different angles. Careful alignment ensured that the pulses were incident at the rotation axis so that changes in angle did not also result in translation of the sample out of the focal plane. The pulse duration for the femtosecond laser was determined using an optical autocorrelator (PulseCheck APE ser.03/3A211) and was found to be 130fs at a repetition rate of 1 kHz.

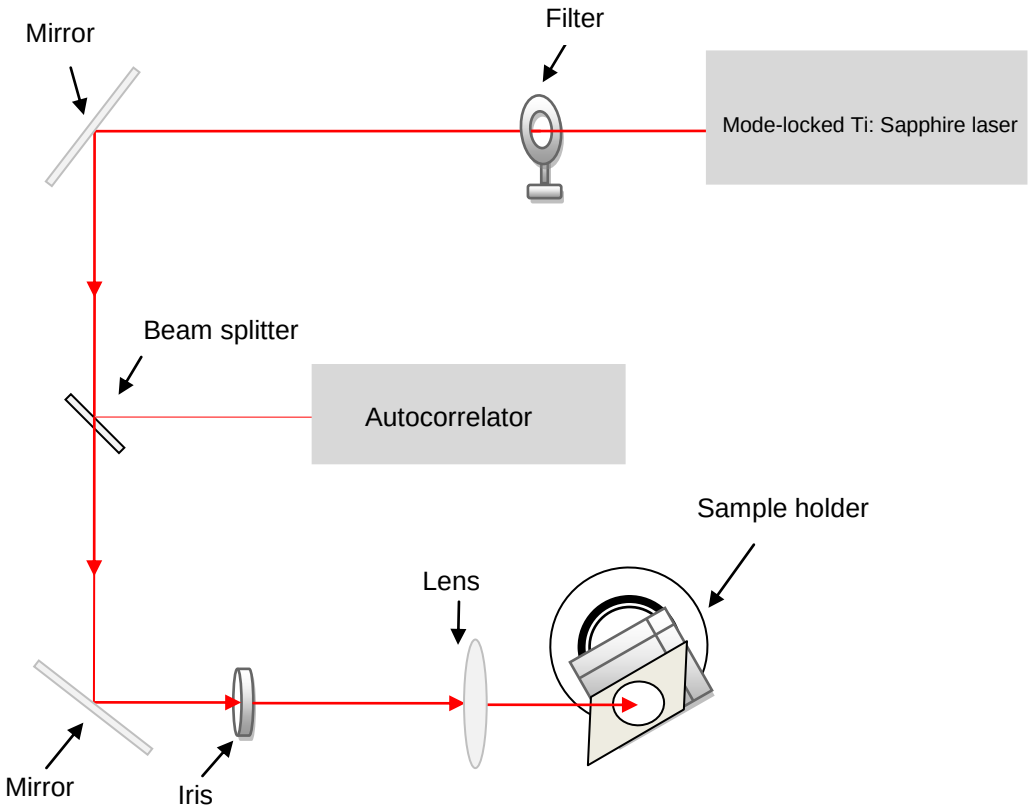

Figure 5-24 Schematic diagram of Polyimide (HN) ablation at different angles using Mode-locked Ti Sapphire femtosecond laser.

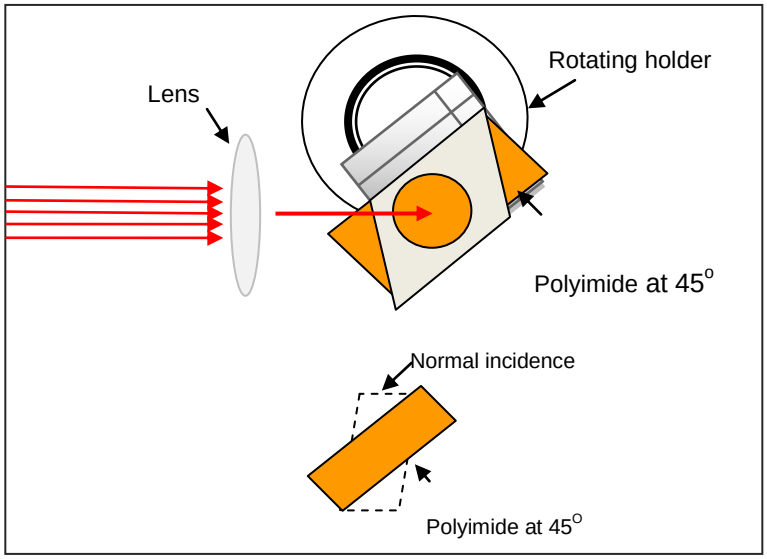

Figure 5-25 shows position of sample at normal incidence and 45° angle when a film of polyimide with 75µm thickness was processed with the femtosecond laser pulses.

By rotating the holder, the angle of the sample changes and the laser can be made incident on the sample with different angles. The power of the radiation

incident at the rate of 1 kHz was measured using a laser power meter, Molelectron (PM 500A-2). As single pulses were used in the experiment, the pulse energy was inferred from the average power by using E=P/f where f is the repetition rate used for the power measurement. The incident energy on the sample was controlled with the help of attenuation filters and energy in the range of 60µJ to 650 µJ was allowed to focus on the polyimide with single pulse on front side.

5.3.2 Results and discussion

The polyimide with 75µm thickness was mounted on the rotating holder and was ablated at different angles with single pulses at different pulse energies. The diameter of the ablated polymer was investigated by means of an optical microscope and scanning electron microscope (SEM). Figure 5-26 shows the SEM images of the polyimide film ablated at normal incidence with single pulses at different pulse powers. The diameters of the ablated areas were measured using the optical microscope. No burr or thermal deformation can be seen around the ablated spots shown in Figure 5-26(a) and (b). There is also evident from the figure that the diameter of the ablated area decreases with decreasing power. A graph between squared diameters as a function of the logarithm of the pulse energy was used to estimate the Gaussian beam radius ω_o due to its linear relation between pulse energy E and laser fluence F_o as given in equation 5.3.

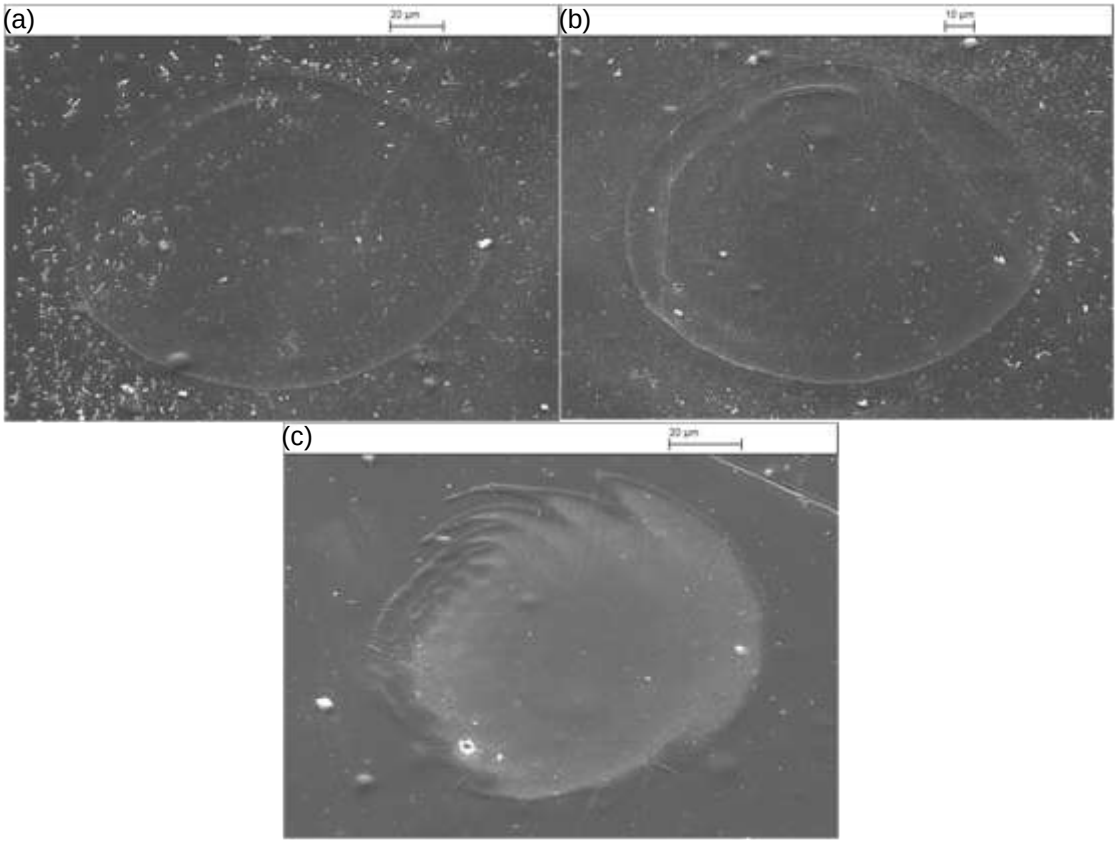

Figure 5-26 SEM images (viewed at 45^{o}) show polyimide ablated at normal incidence. Polyimide ablated with different power (a) 450mW (b) 240mW (c) 90mW.

Polyimide ablated with pulse energies from 60µJ to 650µJ at normal incidence were plotted verses squared diameter D^2 of the ablated area as shown in Figure 5-27. In order to obtain the threshold fluence, E_{th} was estimated from the graph. By extrapolation of the fits to D^2 =0, the threshold energy E_{th} can be determined. When the polyimide was ablated at normal incidence, the ablated area was nearly in the form of circle. Using optical microscopy the vertical and horizontal diameters were measured. Also the Gaussian beam radius ω_o and threshold energies were estimated both for vertical and horizontal diameters. Using equation 5.3 the Gaussian beam radius ω_o was calculated from the gradient of the graph. A value of ω_o=79µm at E_{th}=38µJ for horizontal diameter and ω_o =84µm at E_{th}=33.4µJ for vertical diameter was found. The threshold laser fluence can be calculated from the threshold pulse energy and Gaussian beam radius using equation 5.3. A value for threshold fluence F_{th} was found to be 0.38J/cm^2 and 0.3J/cm^2 for horizontal and vertical diameter respectively.

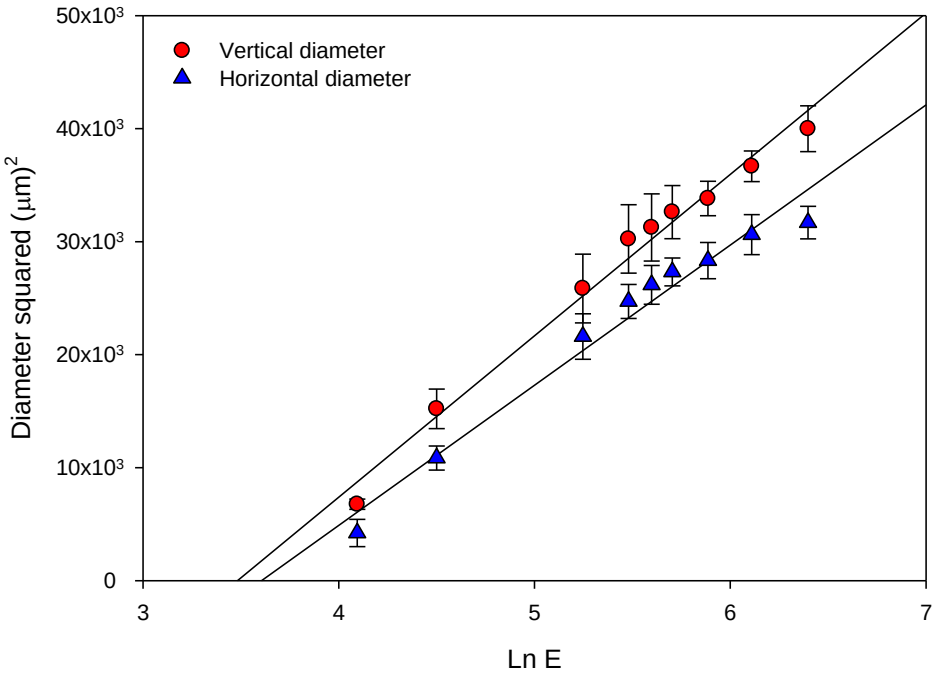

Figure 5-27 75μm thick Polyimide ablated at 0^o with single pulse at different laser fluences using the femtosecond laser. o Shows vertical diameter of the ablated spot while Δ shows the horizontal diameter of the ablated spot. (τ = 130 fs, λ = 800 nm, f = 45 mm)

For further investigation the sample on the rotating holder was rotated to give an angle of incidence of 20^o, 30^o, 45^o, and 50^o. Laser pulses from the same source were focussed on the polyimide sample using the same focal length lens. The diameter of the ablated areas were analysed and recorded with the help of the optical microscope. At large laser pulse power some cloudy areas and thermal effects can be seen around the ablated polyimide spots due to lens aberration as shown in Figure 5-28(a, b) and Figure 5-30(a). Graphs were drawn between D^2 and log of pulse energy E. The threshold energy E_{th} was estimated by extrapolation of the fits to squared diameter $D^2=0$ as shown in Figure 5-29 and Figure 5-31. The slope of the linear fit yielded Gaussian beam radius ω_o according to the Equation 5.3 as used in the previous calculations. Gaussian beam radius ω_o for polyimide ablation at 20^o angle was obtained from the linear fit as ω_o = 113μm at threshold energy, E_{th}=81μJ for horizontal diameter and ω_o = 131μm at E_{th}= 77.5μJ at vertical diameter. Threshold fluence

calculated for horizontal and vertical diameter at 20^o was calculated as $0.4J/cm^2$ and $0.3J/cm^2$ respectively.

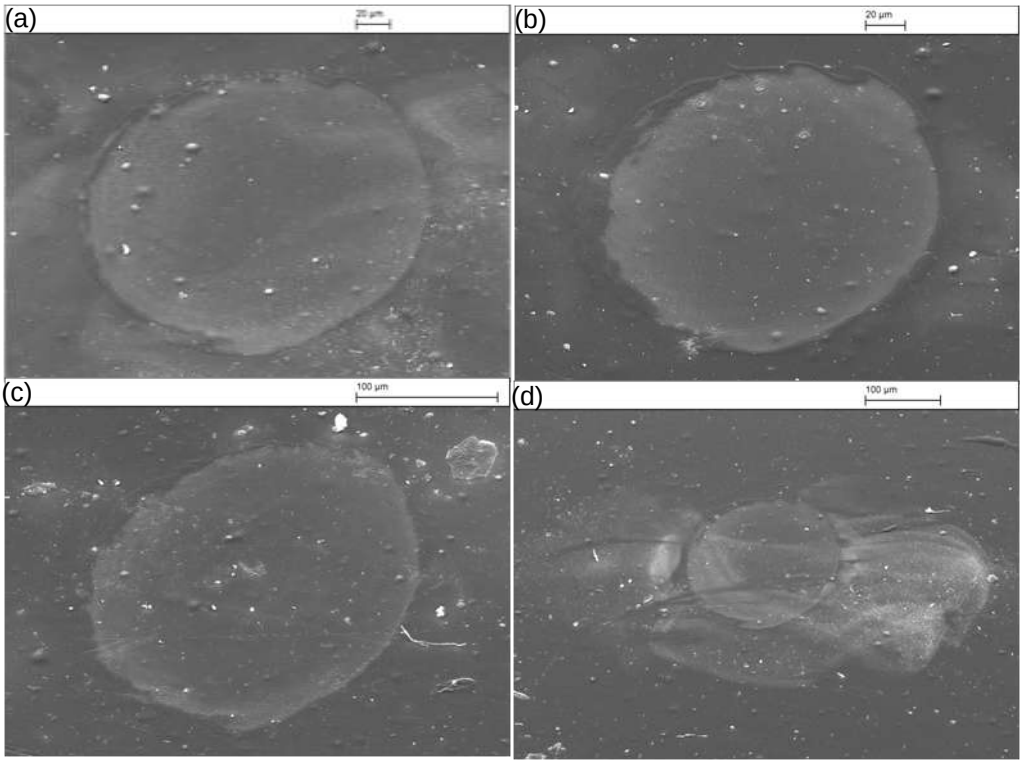

Figure 5-28 SEM images of polyimide ablated at 20^o and 30^o angles viewed at 45^o. Polyimide ablated with pulse power (a) 630mW at 20^o (b) 270mW at 20^o (c) 600mW at 30^o (d) 360mW at 30^o.

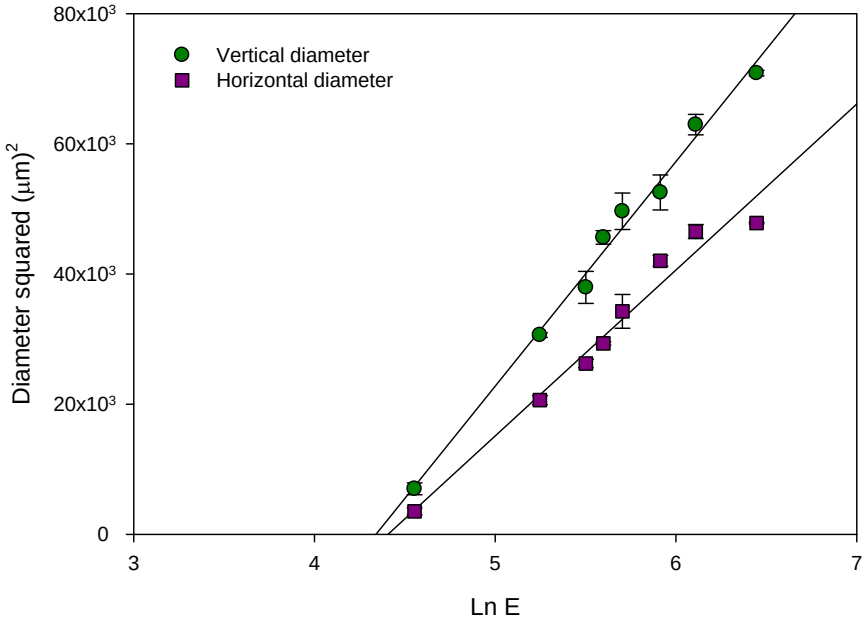

(a) Polyimide ablation at 20°

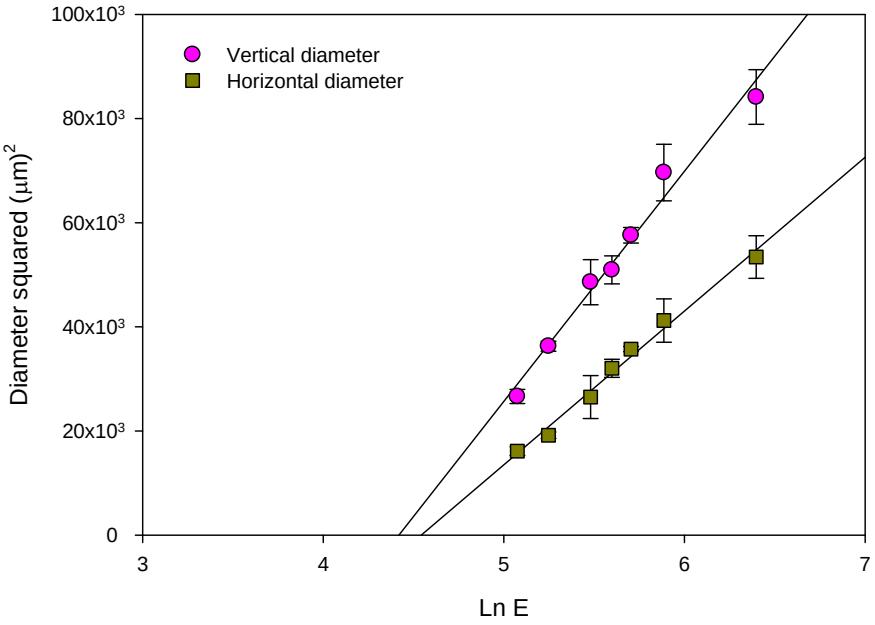

(b) Polyimide ablation at 30°

Figure 5-29 Polyimide ablated at 20° and 30° with single pulse at different fluence using femtosecond lasers. o Shows vertical diameter of the ablated spot while □ shows the horizontal diameter of the ablated spot. (τ = 130 fs, λ = 800 nm, f = 45 mm)

Similarly for polyimide ablation at 30°, the Gaussian beam radius ω_o from the gradient of the graph was found to be 121μm at 90μJ threshold energy for

horizontal diameter and 149µm at 82µJ threshold energy for vertical diameter. The threshold fluence when polyimide was ablated for 30^{o} was found to be 0.4J/cm^{2} for horizontal and 0.24J/cm^{2} for vertical diameter.

Visual analysis of the laser ablated spots indicates that as the ablation angle increases the vertical diameter increases while the horizontal diameter shows decrease in value as shown in Figure 5-30. In case of polyimide ablation at 45^{o}, value of Gaussian beam radius was found to be ω_o=128µm at E_{th}=152µJ for horizontal diameter and ω_o=186µm at E_{th}=132µJ for vertical diameter. The threshold fluence was found to be 0.6J/cm^{2} for horizontal diameter and 0.23J/cm^{2} for vertical diameter. In the case of ablation at 50^{o} the Gaussian beam radius ω_o was found to be 125µm for horizontal diameter with 0.7µJ/cm^{2} threshold fluence and 214µm for vertical diameter with 0.23µJ/cm^{2} at the same threshold energy E_{th}=164µJ as shown in Figure 5-31b. For 50^{o} the ablation experiment was repeated and it was found that at the same threshold energy it showed an increase in the vertical beam waist ω_o whilst a decrease in the horizontal beam waist.

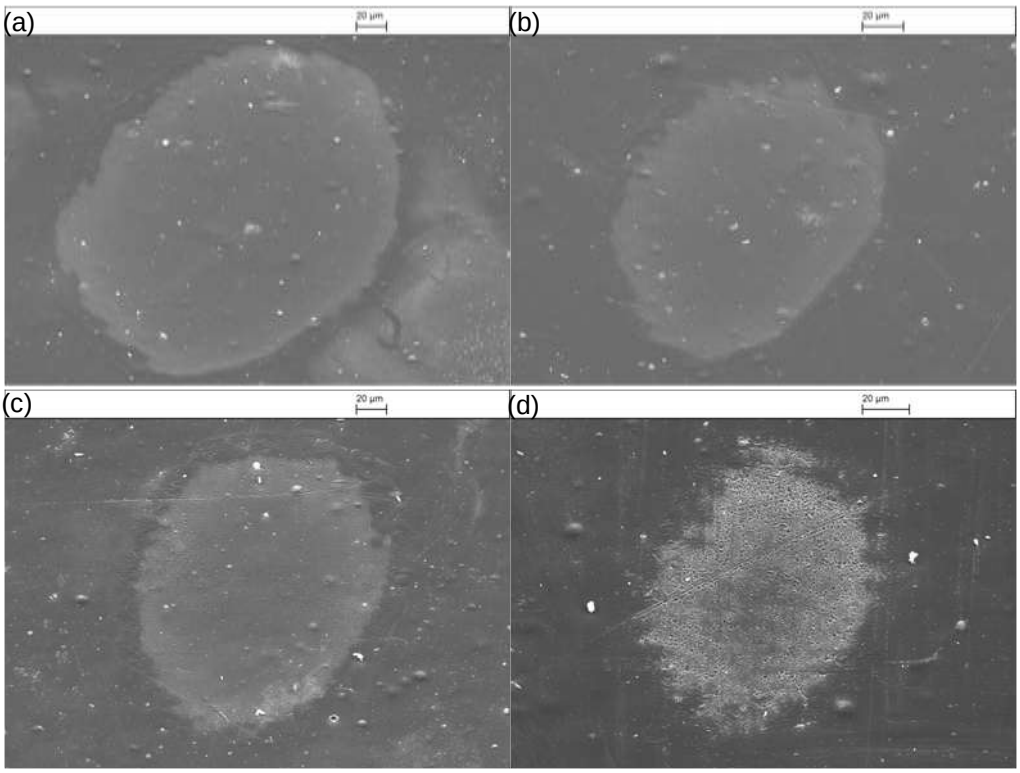

Figure 5-30 SEM images of polyimide ablated at 45^{o} and 50^{o} angles viewed at 45^{o}. Polyimide ablated with pulse power (a) 650mW at 45^{o} (b) 70mW at 45^{o} (c) 450mW at 50^{o} (d) 270mW at 50^{o}.

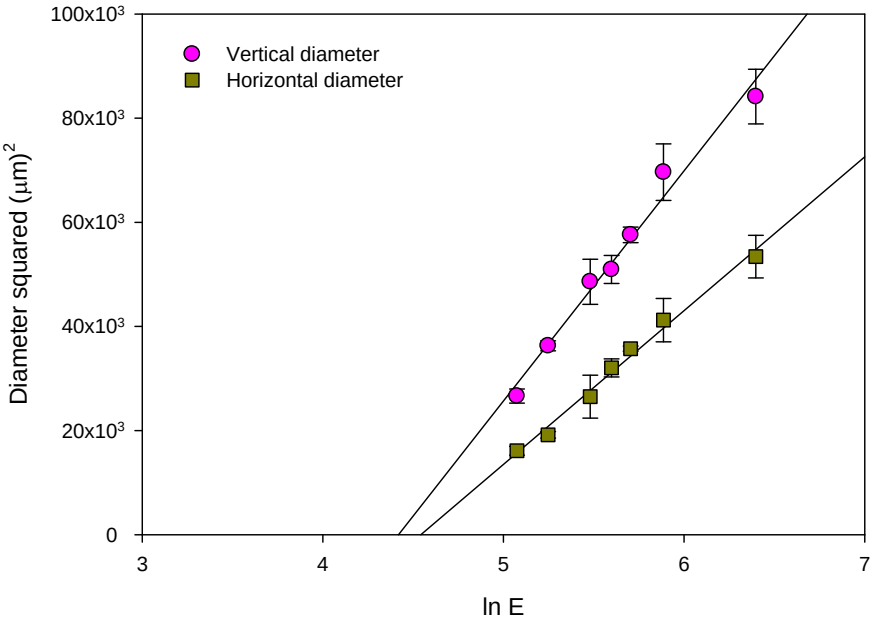

(a) Polyimide ablation at 45°

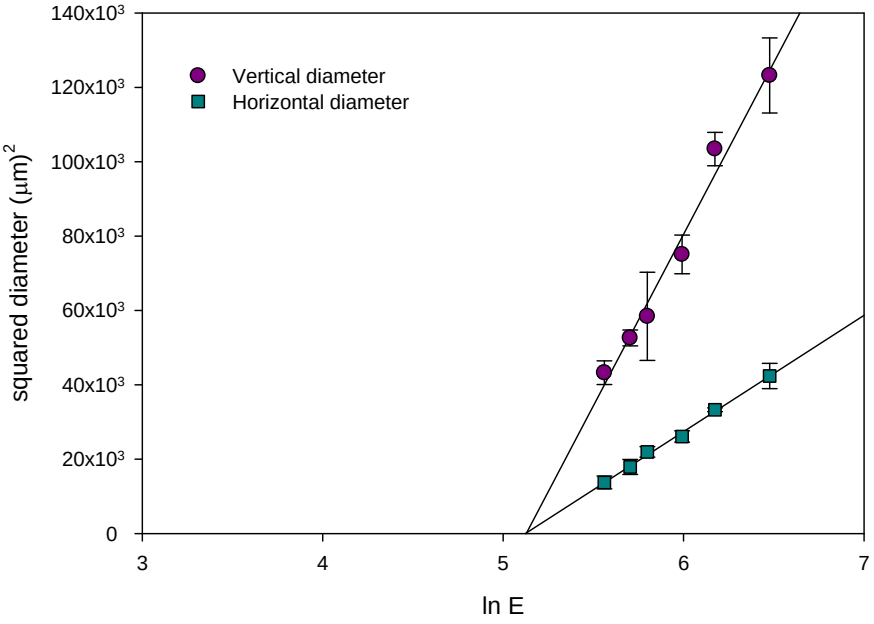

(b) Polyimide ablation at 50°

Figure 5-31 Polyimide ablated at 45° and 50° with single pulse at different laser fluence using femtosecond lasers. o Shows vertical diameter of the ablated spot while □ shows the horizontal diameter of the ablated spot. There is difference between the threshold fluence for vertical and horizontal diameter when ablated at 45° but they coincide at 50°. (τ = 130 fs, λ = 800 nm, f = 45 mm)

Polyimide (PI (Kapton), Goodfellow) with thickness 125µm was also ablated at normal incidence and the ablated area was in the form of circle. Vertical and horizontal diameters measured were approximately equal in size. The Gaussian beam radius ω_o and threshold energies were estimated both for vertical and horizontal diameters as shown in Figure 5-32. The Gaussian beam radius ω_o were found to be 126µm and 123µm for vertical and horizontal diameters respectively. The threshold laser fluence was also calculated from the threshold pulse energy and Gaussian beam radius. A value for threshold fluence F_{th} was found to be 0.52J/cm^2 and 0.45J/cm^2 for horizontal and vertical diameter respectively. Experiments with different thickness of the polymer foil results in different modification threshold fluences. The modification threshold fluences for large thickness foil was found to be more then the thin film. This might be expected due to the fact that more energy is required to modify thick surfaces.

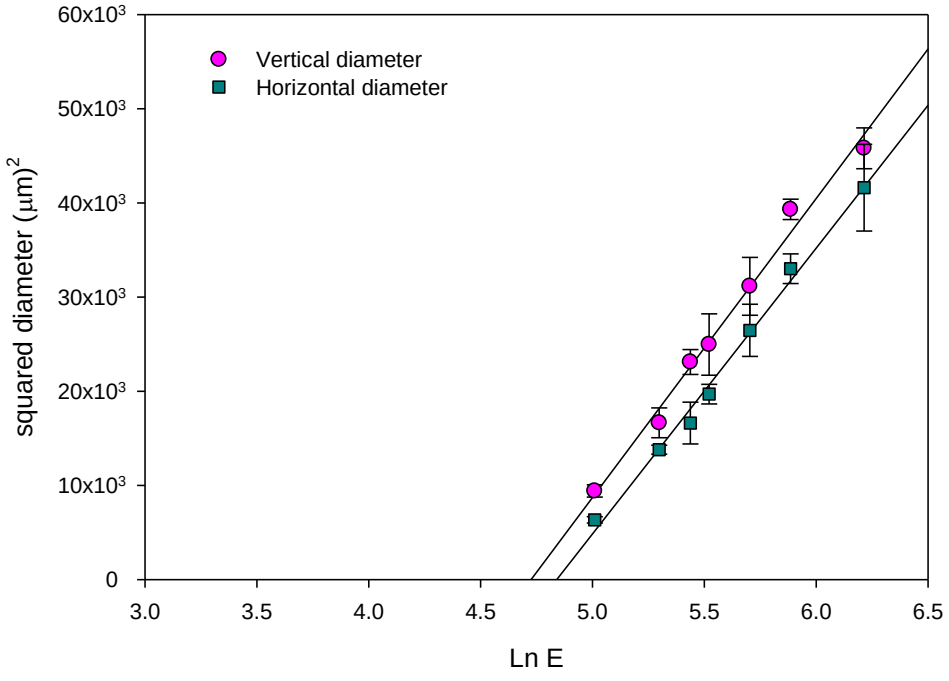

Figure 5-32 125µm thick Polyimide ablated at 0^o with single pulse at different laser fluence using femtosecond lasers. O shows vertical diameter of the ablated spot while □ shows the horizontal diameter of the ablated spot. Threshold fluence F_{th} was found to be 0.52J/cm^2 for horizontal diameter and 0.45J/cm^2 for vertical diameter. (τ = 130 fs, λ = 800 nm, f = 45 mm)

Significant differences were observed in the ablated pattern at large angle. The vertical diameter increases for large angles and the ablated spots on the polyimide surface changed from circular shape to an ellipse. As stated earlier threshold fluence F_{th}, threshold energy E_{th} and Gaussian beam radius ω_o has been calculated and compared at all laser fluence for vertical and horizontal diameters as given in Table 5-2.

Table 5-2. Threshold fluence, Threshold energy and beam radius for the ablation of polyimide Kapton (HN) at different angles.

Angle (θ)	Threshold fluence F_{th} (J/cm^2)		Threshold Energy E_{th} (μJ)		Beam radius ω_o (μm)	
	Vertical axis	Horizontal axis	Vertical axis	Horizontal axis	Vertical axis	Horizontal axis
0^o	0.3	0.38	33.4	38	79	84
20^o	0.3	0.4	77.5	81	113	131
30^o	0.24	0.4	82	90	121	149
45^o	0.23	0.6	132	152	128	186
50^o	0.23	0.7	164	164	214	125

A graph has been drawn to compare the calculated threshold fluence F_{th} for vertical and horizontal diameter at all angles used for ablation. As shown in Figure 5-33 the threshold fluence for vertical diameter increases with increase in angle while it decreases for horizontal diameter. This shows higher ablation rate in vertical direction i.e., along the direction of the incident laser radiation as compared to horizontal direction which is perpendicular to the incident radiation. This indicates that the threshold laser fluence depends in addition to the nature of material also on the angle of ablation θ.

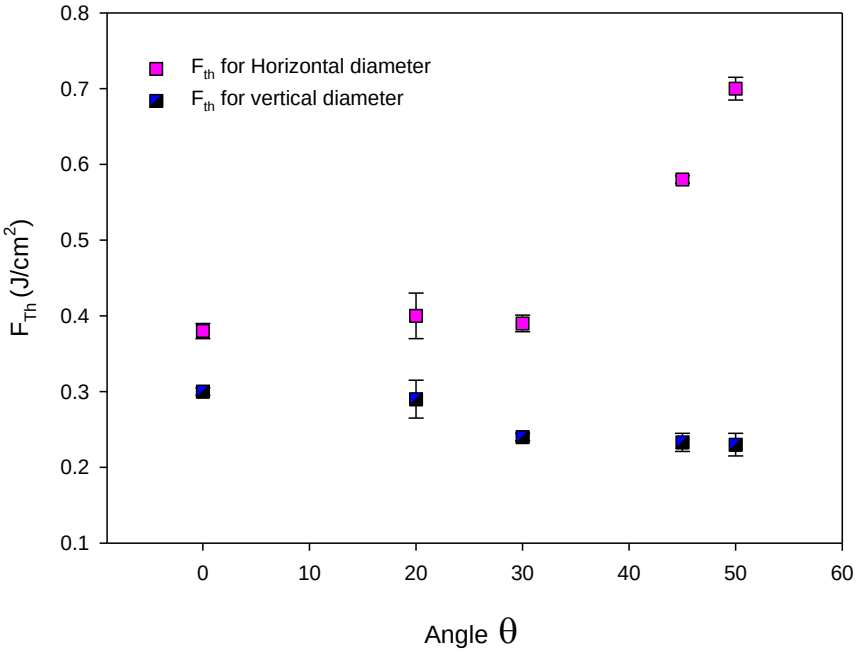

Figure 5-33 Shows a graph drawn for threshold fluence at different angles for horizontal and vertical diameter. Threshold fluence for vertical diameter increases while it decreases for horizontal diameter. (τ = 130 fs, λ = 800 nm, , f = 45 mm)

The results calculated for threshold energy E_{th} was plotted versus the angle of incidence θ as shown in Figure 5-34. The values of threshold energies calculated for vertical and horizontal diameter were found to be in excellent agreement with each other. For each ablated angle θ their values approximately coincide. An increase in the value of threshold energy was found with the increase in angle of ablation.

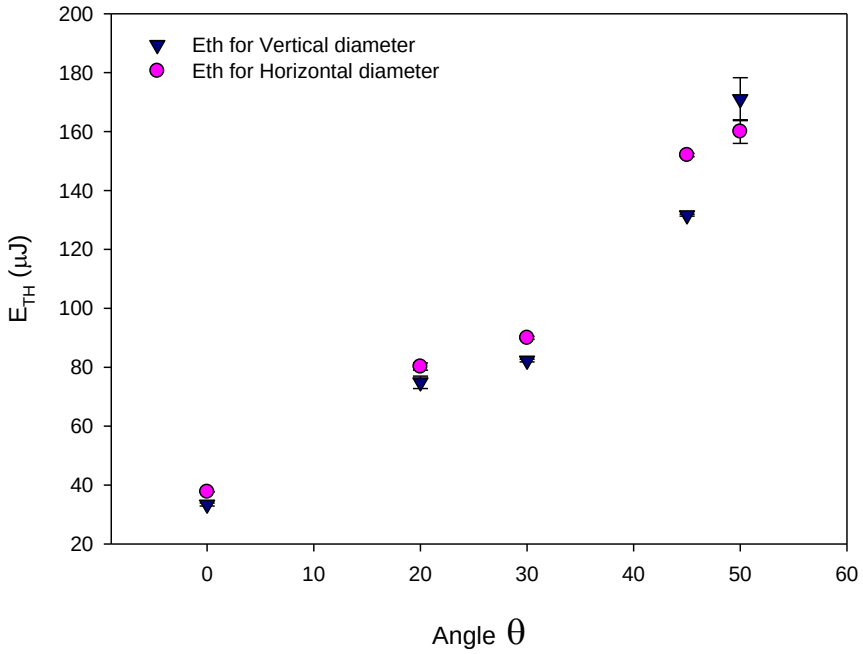

Figure 5-34 Graph for threshold energy E_{th} and angle θ which increases for both vertical and horizontal diameters in the same way (τ = 130 fs, λ = 800 nm, f = 45 mm)

The Gaussian beam radius ω_o was plotted against angle θ for vertical and horizontal diameter as shown in Figure 5-35. With an increase in angle of ablation different behaviour were seen in the vertical and horizontal diameter. Gaussian beam radius ω_o calculated for vertical diameter show increase with increase in angle θ while Gaussian beam radius calculated for horizontal diameter increases with angle and then suddenly after 45^o it starts decreasing.

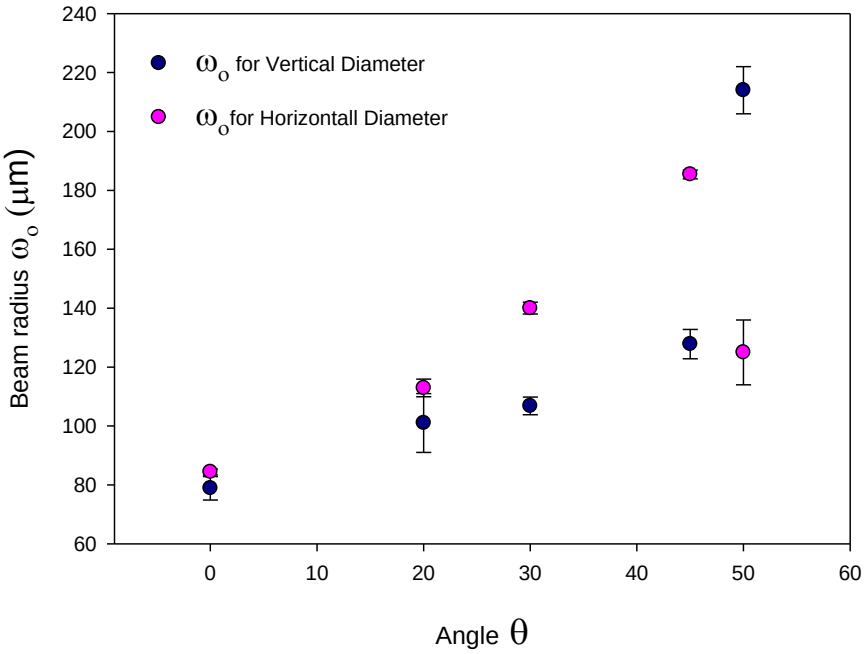

Figure 5-35 Graph showing Gaussian beam radius ωo obtained at different angles. The beam radius ω_o increases with angle θ both for vertical and horizontal diameter until 45^o after which the beam radius for vertical diameter increases in the same manner but beam radius calculated for horizontal diameter shows decrease. (τ = 130 fs, λ = 800 nm, f = 45 mm)

The focal irradiance distributions calculated earlier using the diffraction theory of aberrations indicates that there is often an oscillatory nature in this region. Placing a sample at an oblique angle through this distribution is likely to result in a complicated incident irradiance profile that may explain some of these observations. Modifications to the diffraction model have been made to allow plotting the irradiance distribution on an inclined plane [103] but more verification is required before reporting these results.

Chapter 6 Conclusions and future work

This work has reported the current research and future applications of additive and subtractive laser patterning for biomedical applications. A direct write method utilising two-photon polymerisation processes was demonstrated in this work and patterns in keratin films formed by laser ablation were produced. These findings are important for further development of 3D fabrication technology.

6.1 Conclusion

This research was aimed at using lasers for fabricating cell scaffolds for tissue engineering applications, to measure two-photon absorption cross sections of the photosensitizers used and to perform studies of material ablation for medical applications. Two-photon absorption process, applied to two-photon polymerisation is a technique used for the fabrication of 3D microstructures. The use of efficient TPA chromophores can contribute to the fabrication of fine 3-D patterns with high resolution using low laser power and short time periods. In this study the two-photon absorption cross sections of photoinitiators *4, 4'-Bis (diethylamino) benzophenon* and *Thioxanthone* have been determined by comparing the amplitude of the fluorescence of a sample under one and two photon excitation using a mode locked Ti: Sapphire laser. The second harmonic of this laser was used as the source of one photon excitation.

The molar absorption coefficient ε for *4, 4'-Bis (diethylamino) benzophenon* and *Thioxanthone* were determined in ethanol at 400nm wavelength and were found to be $11366M^{-1}cm^{-1}$ and $2870M^{-1}cm^{-1}$ respectively. The molar absorption coefficient for *4, 4'-Bis (diethylamino) benzophenon* was also measured in ethyl acetate and *Ethoxylated Bisphenol A Dimethacrylate* at 400nm wavelength. The molar absorption coefficient for *4, 4'-Bis (diethylamino) benzophenon* was found to be $4450M^{-1}cm^{-1}$ in the resin *Ethoxylated Bisphenol A Dimethacrylate* while in ethyl acetate its value was found to be $65.4M^{-1}cm^{-1}$. Using the molar absorption coefficient, single photon absorption cross sections were calculated for the photoinitiators under consideration. The single photon absorption cross section for *4, 4'-Bis (diethylamino) benzophenon* and *Thioxanthone in Ethanol* were found to be 43.4$X10^{-18}$ cm^2 $molecule^{-1}$ and $11X10^{-18}$ cm^2 $molecule^{-1}$respectively. On the basis of the single photon absorption cross sections, two-photon

absorption cross sections for *4, 4'-Bis (diethylamino) benzophenon* and *Thioxanthone* in Ethanol were calculated and were found to be $14X10^{-50}$ cm^4 *s photon*$^{-1}$ and $7X10^{-50}$ cm^4 *s photon*$^{-1}$ *respectively*. The two-photon absorption cross section of TPA chromophores were compared and 4, 4'-Bis (diethylamino) benzophenon was found to be more efficient for three dimensional microfabrication in the liquid resin Ethoxylated Bisphenol A Dimethacrylate.

Three dimensional micrometer size structures were polymerised on glass substrates using liquid resin *Ethoxylated Bisphenol A Dimethacrylate*. The dependence of the TPP properties on the writing power, speed and on the NA of the focusing lens were studied in detail. Changes in feature size observed when altering the aperture of the lens have been shown to be due to the spherical aberration introduced at large N.A. values. Three dimensional structures have been prepared using photo polymerization initiated by two-photon absorption process. The activated resin when exposed to a Ti: sapphire femtosecond laser having wavelength of 800nm with pulse duration of 170fs at different laser power, was polymerized. Polymerization reactions leading to the formation of solid structures were chemically activated when the photo initiators (chromophores) were excited by the nonlinear absorption of two photons. By moving the laser focus through the resin in three dimensions, 3D structures of different shapes and different pore sizes were fabricated. The reactivity of the sensitised resin was sufficient to achieve writing speeds up to 400 mm/min. Fabrications of various structures with different pore sizes and different heights show that the monomer is suitable for the fabrication of 3D complex structures for applications in biomedical engineering. High spatial resolution was achieved when the cell scaffolds were fabricated at low laser power close to the threshold and at low N.A. focusing using much high power. A two-photon polymerization threshold as low as 80μW at 10mm/min has been achieved for EBPDMA and has been tailored specifically for biological applications e.g., implants, where larger scale structures need to be manufactured quickly. The two-photon absorption cross section for *4, 4'-Bis (diethylamino) benzophenon* was found to be relatively small. By tailoring the optical system and making use of a relatively weak absorption cross-section we have been able to manufacture deep structures in a single pass of the laser light. The primary function of the scaffold structure is to provide a 3D environment for the cells to migrate and to

proliferate. Using this technique we have prepared deeper scaffolds more rapidly than that reported in previous two-photon photopolymerization studies. Tissue scaffolds have been prepared with different pore sizes suitable for application in different living tissues.

In the present study a bricks and mortar pattern in keratin films has been fabricated using an ArF excimer laser operating at 193 nm wavelength and femtosecond laser system at 800nm and 400nm wavelengths. The ablation efficiency and the phenomenology of the etched keratin patterns have been investigated and the surface modification was analysed.

Laser ablation of keratin, which is a representative of fibrous proteins, was investigated in terms of laser wavelength and energy fluence. The surface morphology of ablated areas was analyzed by means of optical microscopy and scanning electron microscope. Threshold energy and threshold fluence were determined for keratin films of 250nm and 70nm thicknesses. Using the D^2 fitting method, threshold fluence in the range of 30-80mJ/cm^2 were found for 400nm wavelength while the range of 100-120mJ/cm^2 was found for 800nm wavelength. However some uncertainties in the specific values of these fluences were found. Different spot sizes, pulse lengths at different wavelengths give rise to complication in fair comparison of the threshold fluence.

Thus we have demonstrated that laser light is capable of preparing keratin based bricks and mortar wall structure as in epidermis, the outer most layer of the human skin. Fabrication of model skin structures will help to produce effective moisturising products for the protection of skin from dryness, diseases and wrinkles. Due to the very low ablation threshold of keratin, femtosecond laser systems are practical for laser processing of proteins. However, the larger areas that can be processed by the excimer laser are likely to be needed for industrial trials.

For surface processing of organic polymer materials, pulsed laser ablation is a universal tool. Instead of using other conventional techniques, present study was focused in using laser ablation with ultra short laser pulses for surface modification of polyimide. The main advantage of using very short laser pulses, e.g. of fs duration, is that heat diffusion into the polymer material is negligible.

As a result high precision patterning of the sample, without thermal damage of the surroundings, becomes possible.

The modification threshold fluences for 75µm thick films of polyimide (Kapton HN) were determined at different incident angles (0^o, 20^o, 30^o, 45^o and 50^o) for vertical and horizontal diameters. Values between 0.23J/cm^2 and 0.7 J/cm^2 were obtained and the data show that the modification threshold fluences increase with increase in angle for vertical diameter while it significantly decreases with increase in angle in horizontal direction. The size of the beam radius ω_o increases with angle in vertical direction while in horizontal direction it shows increase until 45^o and at 50^o it suddenly drops. The threshold energy E_{th} shows increase with increase in angle both along vertical and horizontal direction. It is thought that these results will need a more detailed exploration of the irradiance across the inclined plane before they can be fully explained.

6.2 Future work

The work done to date in the laboratory for material processing and the theoretical investigation both are interesting and encouraging. At this stage polymerisation based on a direct write system to build up solid polymeric material for the fabrication of three dimensional scaffolds has been achieved. The material used is a photo-cross linkable Ethoxylated Bisphenol A Dimethacrylate (EBPADMA) (6EO) monomer, which was chosen for its biocompatibility and optical transparency. LIFT technique will be used to transfer organic and inorganic materials into and onto these structures but the work can be extended to other laser based techniques if required.

- Future goal is to investigate LIFT method for the deposition of antimicrobial material i.e., silver onto the scaffold to reduce the risk of infection.

- The development of complex three dimensional cell structures can be investigated with spatially controlled cell deposition onto it. The high resolution of the technique will provide control over the cell organization inside the scaffold and, consequently, over cell interactions. Laser Induced Forward Transfer (LIFT) will be used for the damage-free

transfer of living cells to the cell scaffolds. Post transfer proof of cell viability can also be investigated.

- Process for the rapid and reproducible complex three dimensional structures can be developed to reduce fabrication time for 3D microstructuring.
- Numerous 3D structures for biomedical applications and regenerative medicine devices can be produced by two-photon polymerization process including bone prosthetics, microneedles for Transdermal Drug Delivery, stents, and wound closure systems.
- Optimal sterilizing method and disinfecting techniques for fabricated 3D microstructures can be investigated to find less damaging methods.
- Because of the optical transparency of the material used, generation of optical structures e.g., micro lenses, micro lens arrays, moulded gratings and prisms can be explored in the future work.

References

[1] D. Bäuerle, *Laser Processing and Chemistry*, 2nd ed. Berlin: Springer, 1996.

[2] "Pulsed Laser Deposition of Thin Films," Douglas B. Chrisey and G. K. Hubler, Eds.: John Wiley & Sons, 1994.

[3] A. Pique, D.B. Chrisey, R.C.Y. Auyeung, J. Fitz-Gerald, H.D.Wu, R.A. McGill, S. Lakeou, P.K.Wu, V.Nguyen, and M. Duignan, "A novel laser transfer process for direct writing of electronic and sensor materials," *Appl. Phys. A* vol. 69, pp. S279–S284, 1999.

[4] Koji Sugioka, Michel Meunier, and A. Pique, *Laser Precision Micro Fabrication*, 135 ed: Springer Series in materials science, 2011.

[5] Hong-Bo Sun and S. Kawata, *Two-Photon Photopolymerization and 3D Lithographic Microfabrication*: Springer, 2004.

[6] Thomas Weix, Gerhard Hildebrand, Ronald Schade, and Klaus Liefeith, "Two-Photon polymerization for microfabrication of three-dimensional scaffolds for tissue engineering application," *Eng. Life Science*, vol. 9, pp. 384-390, 2009.

[7] En-Yea Pan, Nen-Wen Pu, Yuh-Ping Tong, and H.-F. Yau, "Scaffold-like Micro-well Structures Fabricated by Two-photon-absorption Photopolymerization," *Journal of Medical and Biological Engineering*, vol. 23,No.2, pp. 79-84, 2003.

[8] B. Chichkov, "Two-photon polymerization enhances rapid prototyping of medical devices," *SPIE—The International Society for Optical Engineering*, pp. 1-2, 2007.

[9] J. Bohandy, B. F. Kim, and F. J. Adrian, "Metal deposition from a supported metal film using an excimer laser," *J. Appl. Phys. 60*, pp. 1538, 1986.

[10] J. Bohandy, B. F. Kim, F. J. Adrian, and A. N. Jette, "Metal deposition at 532 nm using a laser transfer technique," *J. Appl. Phys. 63*, pp. 1158, 1988.

[11] V. Schultze and M. Wagner, "Laser-induced forward transfer of aluminium," *Applied Surface Science*, vol. 52, pp. 303, 1991.

[12] S. M. I. Zergioti, N.A. Vainos, C. Fotakis, S. Chen, and C. P. Grigoropoulos, "Microdeposition of metals by femtosecond excimer laser," *Applied Surface Science*, vol. 601-605, pp. 127-129, 1998.

[13] J. A. Greer, T. E. Parker, in: A.N. Pirri, and B. P. Piwczyk(Eds.), "Excimer Beam Applications," *Proc.SPIE* vol. 998, pp. 113, 1988.

[14] E. Fogarassy, C. Fuchs, and e. a. F. Kerherve, "Laser- induced forward transfer of high-Tc YBaCuO and BiSrCaCuO superconducting thin films," *J. Appl. Physics*, vol. 66, pp. 457, 1989.

[15] T. S. B. Hopp, Zs. Antal, N. Kresz, Zs. Bor, D.B.Chrisey, *Appl. Phys.96(6)*, pp. 3478, 2004.

[16] Craig B. Arnold, Pere Serra, and A. Pique, "Laser Direct-Write Techniques for Printing of Complex Materials," *MRS BULELETIN*, vol. 32, pp. 23-31, 2007.

[17] Ik-Bu Sohn, Myeong-Jin Ko, Young-Seop Kim, and Y.-C. Noh, "Direct femtosecond laser lithography for photoresist patterning " *Optical Engineering*, vol. 48(2), pp. 024301, 2009.

[18] G. Lemercier, J.-C. Mulatier, C. Martineau, R. Anémian, C. Andraud, I. Wang, O. Stéphan, N. Amari, and P. Baldeck, "Two-photon absorption: from optical power limiting to 3D microfabrication," *Comptes Rendus Chimie*, vol. 8, pp. 1308-1316, 2005.

[19] R. Liska, M. Schuster, R. Infuhr, C. Turecek, C. Fritscher, B. Seidl, V. Schmidt, L. Kuna, A. Haase, F. Varga, H. Lichtenegger, and J. Stampfl, "Photopolymers for rapid prototyping," *J. Coat. Technol. Res.*, vol. 4(4), pp. 505–510, 2007.

[20] A. Ovsianikov, A. Gaidukeviciute, B. N. Chichkov, M. Oubaha, B. D. MacCraith, I. Sakellari, A. Giakoumaki, D. Gray, M. Vamvakaki, M. Farsari, and C. Fotakis, "Two-Photon Polymerization of Hybrid Sol-Gel Materials for Photonics Applications," *Laser Chemistry*, vol. 2008, pp. 1-7, 2008.

[21] Irène Wang, Michel Bouriau, P. L. Baldeck, C. Martineau, and C. Andraud, "Three-dimensional microfabrication by two-photon-initiated polymerization with a low-cost microlaser," *Optics Letters*, vol. 27, pp. 1348-1350, 2002.

[22] Kwang-Sup Lee, D.-Y. Yang, Prem Prabhakaran, Jinsoon Park, S. H. Park, and R. H. Kim, "Recent developments in the use of two-photon polymerization in precise 2D and 3D microfabrications," *Polymers for advanced technologies*, vol. 17, pp. 72-82, 2006.

[23] S. Passinger, *Two-Photon Polymerization and application to Surface Plasmon Polaritons,*: Cuvillier Verlag, 2008.

[24] C. Xu and W. W. Webb, "Measurement of two-photon excitation cross sections of molecular fluorophores with data from 690 to 1050 nm," *Journal of the Optical Society of America B: Optical Physics*, vol. 13, pp. 481-491, 1996.

[25] J. M. Song, T. Inoue, H. Kawazumi, and T. Ogawa, "Determination of two photon absorption cross section of fluorescein using a mode locked titanium sapphire laser," *Analytical Sciences*, vol. 15, pp. 601-603, 1999.

[26] J. Liu, Y. W. Zhao, J. Q. Zhao, A. D. Xia, L. J. Jiang, S. Wu, L. Ma, Y. Q. Dong, and Y. H. Gu, "Two-photon excitation studies of hypocrellins for photodynamic therapy," *Journal of Photochemistry and Photobiology B: Biology*, vol. 68, pp. 156-164, 2002.

[27] Schafer, K. J., J. M. Hales, M. Balu, K. D. Belfield, E. W. Van Stryland, and D. J. Hagan, "Two-photon absorption cross-sections of common photoinitiators," *Journal of Photochemistry and Photobiology A: Chemistry*, vol. 162, pp. 497-502, 2004.

[28] Du Xia Cao, Zhi Qiang Liu, Qi Fang, Gui Bao Xu, Gang Xue, Guo Qun Liu, and W. T. Yu, "Blue two-photon excited fluorescence of several D-p-D, A-p-A, and D-p-A compounds featuring dimesitylboryl acceptor," *Journal of Organometallic Chemistry* vol. 689, pp. 2201–2206, 2004.

[29] Werts Martinus H. V., N. Nerambourg, D. Pelegry, Y. L. Grand, and M. Blanchard-Desce, "Action cross sections of two-photon excited luminescence of some Eu(iii) and Tb(iii) complexes," *Photochemical & Photobiological Sciences*, vol. 4, pp. 531-538, 2005.

[30] M. Atif, P. E. Dyer, T. A. Paget, H. V. Snelling, and M. R. Stringer, "Two-photon excitation studies of m-THPC photosensitizer and photodynamic activity in an epithelial cell line," *Photodiagnosis and Photodynamic Therapy*, vol. 4, pp. 106-111, 2007.

[31] R. Signorini, C. Ferrante, D. Pedron, M. Zerbetto, E. Cecchetto, M. Slaviero, I. Fortunati, E. Collini, R. Bozio, A. Abbotto, L. Beverina, and G. A. Pagani, "Effective Two-Photon Absorption Cross Section of Heteroaromatic Quadrupolar Dyes: Dependence on Measurement Technique and Laser Pulse Characteristics," *The Journal of Physical Chemistry A*, vol. 112, pp. 4224-4234, 2008.

[32] C. Martineau, G. Lemercier, C. Andraud, I. Wang, M. Bouriau, and P. L. Baldeck, "New initiator for two-photon absorption induced polymerization with a microlaser at 1.06 µm.," *Synthetic Metals*, vol. 138, pp. 353-356, 2003.

[33] C. K. Chua, K. F. Leong, and C. S. Lim, *Rapid Prototyping: Principles and Applications*, 3rd ed. Singapure: World Scientific publishing Co., 2010.

[34] Houbertz, Ruth, Steenhusen, Sönke, Stiche, Thomas, Sext, and Gerhard, "Two-Photon Polymerization of Inorganic-Organic Hybrid Polymers as Scalable Technology Using Ultra-Short Laser Pulses, Coherence and Ultrashort Pulse Laser Emission," in *Coherence and Ultrashort Pulse Laser Emission*: InTech, 2010, pp. 583-608.

[35] A Ovsianikov, B Chichkov, O Adunka, H Pillsbury, A Doraiswamy, and R. Narayan, "Rapid prototyping of ossicular replacement prostheses," *Applied Surface Science* vol. 253 pp. 6603-6607, 2007.

[36] A. Ovsianikov, A. Gaidukeviciute, B. N. Chichkov, M. Oubaha, B. D. MacCraith, I. Sakellari, A. Giakoumaki, D. Gray, M. Vamvakaki, M. Farsari, and C. Fotakis, "Two-Photon Polymerization of Hybrid Sol-Gel Materials for Photonics Applications," *Laser Chemistry*, pp. 1-7 doi:10.1155/2008/493059, 2008.

[37] J. Serbin, A. Egbert, A. Ostendorf, B. N. Chichkov, R. Houbertz, G. Domann, J. Schulz, C. Cronauer, L. Fröhlich, and M. Popall,

"Femtosecond laser-induced two-photon polymerization of inorganic organic hybrid materials for applications in photonics," *Optics Letters*, vol. 28, pp. 301-303, 2003.

[38] B. Bhuian, R.J. Winfield, S. O'Brien, and G. M. Crean, "Investigation of the two-photon polymerisation of a Zr-based inorganic–organic hybrid material system," *Applied Surface Science*, vol. 252, pp. 4845–4849, 2006.

[39] A Ovsianikov, A Ostendorf, and B. N. Chichkov, "Three-dimensional photofabrication with femtosecond lasers for applications in photonics and biomedicine " *Applied Surface Science,* , vol. 253, pp. 6599-6602, 2007.

[40] T. Stichel, B. Hecht, R. Houbert, and G. Sextl, "Two-photon Polymerization as Method for the Fabrication of Large Scale Biomedical Scaffold Applications " *JLMN-Journal of Laser Micro/Nanoengineering*, vol. 5, pp. 209-212, 2010.

[41] F. A. Landis, J. S. Stephens, J. A. Cooper, M. T. Cicerone, and S. Lin-Gibson, "Tissue Engineering Scaffolds Based on Photocured Dimethacrylate Polymers for in Vitro Optical Imaging," *Biomacromolecules*, vol. 7, pp. 1751-1757, 2006.

[42] S. Lin-Gibson, J. A. Cooper, F. A. Landis, and M. T. Cicerone, "Systematic Investigation of Porogen Size and Content on Scaffold Morphometric Parameters and Properties," *Biomacromolecules*, vol. 8, pp. 1511-1518, 2007.

[43] Frederik Claeyssens, Erol A. Hasan, Arune Gaidukeviciute, Demetra S. Achilleos, Anthi Ranella, Carsten Reinhardt, Aleksandr Ovsianikov, Xiao Shizhou, Costas Fotakis, Maria Vamvakaki, Boris N. Chichkov, and Maria Farsari, "Three-Dimensional Biodegradable Structures Fabricated by Two-Photon Polymerization," *Langmuir*, vol. 25, pp. 3219-3223, 2009.

[44] Andreas Ostendorf and B. N. Chichkov, "Two photon polymerization: A new approach to micromachining; Femtosecond lasers enable microfabrication with resolution beyond the diffraction limit," in *Photonic spectra*, 2006.

[45] S D Gittard, R J Narayan, C Jin, A Ovsianikov, B N Chichkov, N A Monteiro-Riviere, S. Stafslien, and B. Chisholm, "Pulsed laser deposition of antimicrobial silver coating on Ormocer® microneedles," *Biofabrication*, vol. 1, 2009.

[46] J.-W. Choi, R. Wicker, S.-H. Lee, K.-H. Choi, C.-S. Ha, and I. Chung, "Fabrication of 3D biocompatible/biodegradable micro-scaffolds using dynamic mask projection microstereolithography," *Journal of Materials Processing Technology*, vol. 209, pp. 5494-5503, 2009.

[47] T. Lippert, "Interaction of photons with polymers: From surface modification to ablation," *Plasma Processes and Polymers*, vol. 2, pp. 525–546, 2005.

[48] P. E. Dyer, "Excimer laser polymer ablation: twenty years on," *Applied Physics A : Materials Science and Processing*, vol. 77, pp. 167-173, 2003.

[49] M. C. Gower, *Laser Processing in Manufacturing*, R. C. Crafer, P. J. Oakley. ed: Great Britain: Chapman and Hall, 1993.

[50] M. C. Gower, "Industrial applications of laser micromachining," *Optics Express*, vol. 7, pp. 56–67, 2000.

[51] N H. Rizvi, P T. Rumsby, and M. C. Gower, "New developments and applications in the production of 3D microstructures by laser micromachining " *Proc. SPIE 3898*, vol. 240, 1999.

[52] T.H.R. Crawford and H.K. Haugen, "Sub-wavelength surface structures on silicon irradiated by femtosecond laser pulses at 1300 and 2100 nm wavelength," *Applied Surface Science* vol. 253 pp. 4970–4977, 2007.

[53] Peter Osborne, *The Mercator Projections(chapter 5)*. Edinburgh, 2008.

[54] A.E.Siegman, *Lasers*, 1st ed. United States of America: University Science Books, 1986.

[55] A.E.Siegman, *New developments in laser resonators*: Proc.SPIE, 1990.

[56] A.E.Siegman, *Defining, measuring, and optimizing laser beam quality*, vol. 2: Proc. SPIE, 1993.

[57] D.R.Hall and P.E.Jackson, *The Physics and Technology of Laser Resonators*: IOP Publishing Ltd, 1989.

[58] C. Rulliere, *Femtosecond Laser Pulses: Principles and Experiments*, 2nd ed. New York: Springer, 2006.

[59] Emil Wolf, *Progress in optics*, vol. 46: Elsevier Science & Technology, 2004.

[60] Diels and W. Rudolf, *Ultrashort Laser Pulse Phenomena*, Second Edition ed: Massachusetts, Academic Press, 2006.

[61] K. Jain, C. G. Willson, and B. J. Lin, "Ultrafast Deep UV Lithography with Excimer Lasers," *IEEE ELECTRON DEVICE LETTERS*, vol. EDL-3, NO. 3, pp. 53-55, 1982.

[62] D. Basting and G. Marowsky, *Excimer Laser Technology*: Springer, 2005.

[63] www.uslasercorp.com/envoy/diverge.html, "Measuring laser beam divergence," 23/1/2009.

[64] O.Svelto, *Principles of lasers*. New York: Springer, Plenum press, 1998.

[65] W. T. Silfvast, *Laser Fundamentals*. Cambridge: Cambridge University Press, 2004.

[66] Shaun D Gittard and Roger J Narayan, "Laser direct writing of micro- and nano-scale medical devices," *Expert Rev Med Devices*, vol. 7(3), pp. 343–356, 2010.

[67] D.B. Chrisey, A. Pique, J. Fitz-Gerald, R.C.Y. Auyeung, R.A. McGill, H.D. Wu, and M. Duignan, "New approach to laser direct writing active and passive mesoscopic circuit elements," *Applied Surface Science*, vol. 154–155, pp. 593-600, 2000.

[68] Tobias C. Röder and J. R. Köhler, "Physical model for the laser induced forward transfer process " *Applied physics letters*, vol. 100(071603), pp. 3, 2012.

[69] A. Ovsianikov, J. Viertl, B. Chichkov, M. Oubaha, B. MacCraith, I. Sakellari, A. Giakoumaki, D. Gray, M. Vamvakaki, M. Farsari, and C. Fotakis, "Ultra-Low Shrinkage Hybrid Photosensitive Material for Two-Photon Polymerization Microfabrication," *ACS Nano*, vol. 2, pp. 2257-2262, 2008.

[70] D. X. Cao, Z. Q. Liu, Q. Fang, G. B. Xu, G. Xue, G. Q. Liu, and W. T. Yu, "Blue two-photon excited fluorescence of several D-[pi]-D, A-[pi]-A, and D-[pi]-A compounds featuring dimesitylboryl acceptor," *Journal of Organometallic Chemistry*, vol. 689, pp. 2201-2206, 2004.

[71] N. Kawatsuki, T. Tachibana, and K. Kamada, *Advanced Materials*, vol. 17, pp. 1886-1890, 2005.

[72] Forrest A. Landis, Jean S. Stephens, James A. Cooper, Marcus T. Cicerone, and S. Lin-Gibson*, "Tissue Engineering Scaffolds Based on Photocured Dimethacrylate Polymers for in Vitro Optical Imaging," *Biomacromolecules*, vol. 7, pp. 1751-1757, 2006.

[73] D. Karaca Balta, S. Keskin, F. Karasu, and N. Arsu, "Quinoxaline derivatives as photoinitiators in UV-cured coatings," *Progress in Organic Coatings*, vol. 60, pp. 207-210, 2007.

[74] Lakowicz and J. R, *Principles of Fluorescence Spectroscopy*, 3rd ed: Springer 2006.

[75] M. Atif, "Fluorescence dynamics studies of PDT photosensitiser," in *Department of physical Sciences (physics)*, vol. Ph.D. Hull: University of Hull, 2005.

[76] Chris Xu and W. W. Webb, "Measurement of two-photon excitation cross sections of molecular fluorophores with data from 690 to 1050 nm," *Journal of the Optical Society of America B*, vol. 13, pp. 481-491, 1996.

[77] Joseph R. Lakowicz, *Topics in fluorescence spectroscopy: Nonlinear and two photon induced fluorescence*, vol. 5. New York: Springer, 1997.

[78] M. K. Saroj., Neera Sharma, and R. C. Rastogi, "Solvent effect profiles of absorbance and fluorescence spectra of some indole based chalcones," *Journal of Fluorescence*, vol. 21, pp. 2213–2227, 2011.

[79] C. Phipps, *Laser ablation and its applications.* Santa Fe New Mexico: Springer 2007.

[80] Nitin Uppal, "A mathematical model development and sensitivity analysis of two photon polymerization for 3D micro/nano fabrication," in *Mechanical Engineering*, vol. Ph.D. Arlington: The University of Texas, 2008, pp. 1-156.

[81] Fengjie Qi, Yan Li, Dengfeng Tan, Hong Yang, and Qihuang Gong, "Polymerized nanotips via two-photon photopolymerization," *Optics. Express*, vol. 15, pp. 971-976, 2007.

[82] S. Hong-Bo, T. Tomokazu, and K. Satoshi, *Three-dimensional focal spots related to two-photon excitation*, vol. 80: AIP, 2002.

[83] J.-F. Xing, X.-Z. Dong, W.-Q. Chen, X.-M. Duan, N. Takeyasu, T. Tanaka, and S. Kawata, "Improving spatial resolution of two-photon microfabrication by using photoinitiator with high initiating efficiency," *Applied Physics Letters*, vol. 90, pp. 131106-131106-3, 2007.

[84] Anthony S, Kewitsch, and Amnon Yariv, "Self-focusing and self-trapping of optical beams upon photopolymerization," *Optics. Letters*, vol. 21, pp. 24-26, 1996.

[85] Theodor Asavei, Timo A. Nieminen, Norman R. Heckenberg, and H. Rubinsztein-Dunlop, "Fabrication of micro-structures for optically driven micromachines using two-photon photopolymerization of UV curing resins," *Journal of Optics A: Pure and Applied Optics*, vol. 11(034001), pp. 7, 2009.

[86] M Born and E. Wolf, *Principles of Optics*, 6th ed. Cambridge: pub Cambridge University Press, 1998.

[87] J. J. Stamnes, *Waves in focal regions*. Bristol pub Adam Hilger Imprint (IoP Publishing Ltd) 1986.

[88] J M Aaron, C L M Ireland, and C. Grey-Morgan, "Aberration effects in the interaction of focused laser beams with matter," *J Phys D*, vol. 7, pp. 1907, 1974.

[89] M. Polyanskiy, "Refractive index database," http://refractiveindex.info 2008-12.

[90] D. Skrtic and J. M. Antonucci, "Dental composites based on amorphous calcium phosphate – resin composition/physicochemical properties study," *Journal of Biomaterials Applications*, vol. 21, pp. 375–393, 2007.

[91] B. S. Shin, J. Y. Oh, and H. Sohn, "Theoretical and experimental investigations into laser ablation of polyimide and copper films with 355-nm Nd:YVO4 laser," *Journal of Materials Processing Technology*, vol. 187-188, pp. 260-263, 2007.

[92] S. Baudach, J. Bonse, and W. Kautek, "Ablation experiments on polyimide with femtosecond laser pulses," *Applied Physics A: Materials Science & Processing*, vol. 69, pp. S395-S398, 1999.

[93] Yasuyuki Tsuboi, Naohisa Kimoto, Masashi Kabeshita, and A. Itaya, "Pulsed laser deposition of collagen and keratin," *Journal of Photochemistry and Photobiology A: Chemistry*, vol. 145, pp. 209–214, 2001.

[94] Akira NAKAMURA, Makoto ARIMOTO, Keiji TAKEUCHI, and T. FUJII, "A Rapid Extraction Procedure of Human Hair Proteins and Identification of Phosphorylated Species," *Biol. Pharm. Bull.* , vol. 25, pp. 569—572, 2002.

[95] M. Richardson, "Understanding the structure and function of the skin," *Nursing Times.net,*, vol. 99, pp. 46, 2003.

[96] Janetta Bensouilah and P. Buck, "Skin structure and function," in *Aromadermatology:Aromatherapy in the Treatment and Care of Common Skin Conditions*. Abingdon: Radcliffe Publishing, 2006, pp. 264.

[97] "Understanding the causes of skin disease," www.hse.gov.uk, 6/3/2012.

[98] Z. Nemes and P.M. Steinert, "Bricks and mortar of the epidermal barrier.," *Experimental and molecular medicine*, vol. 31, pp. 5-19, 1999.

[99] "What is going on with my skin? Damaged skin barrier," www.eczemazones.co.uk, 23/3/2012.

[100] S. Lugomer, A. Maksimovića, B. Farkasb, Z. Geretovszkyb, T. Szörényic, A. L. Tóthe, Z. Zolnai, and I. Bársonye, "Multipulse irradiation of silicon by femtosecond laser pulses: Variation of surface morphology," *Applied Surface Science*, vol. 258(8), pp. 3589-3597, 2012.

[101] J. E. A. Pedder, A. S. Holmes, and P. E. Dyer, "Improved model for the angular dependence of excimer laser ablation rates in polymer materials," *Appl. Phys. Lett. 95, 174105* (2009); doi: 10.1063/1.3254236.

[102] K. Rasmussen, G. Grampp, M. v. Eesbeek, and T. Rohr, "Thermal and UV Degradation of Polymer Films Studied In situ with ESR Spectroscopy," *ACS Applied Materials & Interfaces*, vol. 2, pp. 1879-1883, 2010.

[103] H V Snelling, "Private communication," University of Hull, 2012.